

Human-Operator Identification with Time-Varying ARX Models

Master of Science Thesis

H.A. van Grootheest

Human-Operator Identification with Time-Varying ARX Models

Master of Science Thesis

H.A. van Grootheest

for obtaining the degree of

Master of Science
in
Aerospace Engineering

at
Delft University of Technology

Cover design by H.A. van Grootheest.



Copyright © 2017 by H.A. van Grootheest and Delft University of Technology, Faculty of Aerospace Engineering, Delft, The Netherlands.
All rights reserved.

The undersigned hereby certify that they have read, and recommend to the Faculty of Aerospace Engineering at Delft University of Technology for acceptance, a thesis entitled: **Human-Operator Identification with Time-Varying ARX Models**, submitted by **H.A. van Grootheest** in partial fulfillment of the requirements for the award of the degree of **Master of Science**.

Dated: 10 April 2017

Assessment committee

Professor:

Prof.dr.ir. M. Mulder

Supervisors:

Dr.ir. M.M. van Paassen

Dr.ir. D.M. Pool

External examiner:

Dr.ir. D.A. Abbink

Preface

This thesis summarizes the work of the final graduation project for my Master of Science (MSc) degree in Aerospace Engineering at Delft University of Technology. This work was carried out at the Section Control and Simulation (C&S).

The thesis is set out as follows. Part I contains the scientific paper with the most relevant information and results on the conducted research. Readers that are interested in the preliminary work are referred to Part II. Part III contains additional results that were not included in the scientific paper.

The graduation project experience I had at C&S was a great chance for learning and professional development. Prior to my graduation project I was quite unfamiliar with the concept of system identification, so I was rather thrown in at the deep end. Along the way it was particularly the guidance of my supervisors that helped to push me through the barriers. I am very proud of the end result.

Daan, thank you very much for putting so much effort and time in supervising me. Your constructive feedback was very useful to make progress. René, thank you for the guidance you gave me and the time you made available to discuss breakthrough ideas. Max, thanks for your help and for giving me the opportunity to do this graduation project. You made me enthusiastic to finish my studies at C&S.

Furthermore, I would like to thank all the people at the C&S Upper House group who made the graduation project an enjoyable ride. I would like to thank my brother who kept faith in me. A special thank to my girlfriend, you have been a tremendous support and your love always motivates me. Finally, I would like to give special thanks to my parents for their support throughout my education and life.

Andries van Grootheest
Delft, 10 April 2017

Table of contents

Preface	v
List of figures	ix
List of tables	xiii
Nomenclature	xv
1 Introduction	1
1.1 Reason for the research	1
1.2 Aim of the research and research design	1
1.3 Thesis's structure	3
I Paper	5
II Preliminary report	23
2 State-of-the-art in time-varying human-operator identification	25
2.1 Fundamentals of compensatory manual control	25
2.1.1 Adaptive behavior	26
2.1.2 Compensatory tracking tasks	26
2.1.3 Quasi-linear models	26
2.2 Relevant research fields	27
2.3 Areas of controversy	28
2.4 Synthesis	29
3 Compensatory manual-control model	31
3.1 Single-loop target-following control task	31
3.2 Parametric models	32
3.3 Time variations	33
4 Identification framework	37
4.1 Identification loop	37
4.2 Proposed identification method	38
4.2.1 Data generation	38
4.2.2 Data preprocessing	39
4.2.3 Further steps	39
4.3 ARX models	40
4.3.1 ARX-model structure	40
4.3.2 ARX model and human-operator model	41
4.3.3 Linear regression	41
4.3.4 ARX-model orders	41
4.4 Fit criterion	42
4.4.1 Ordinary least-squares estimation	42
4.4.2 Recursive least-squares estimation	43
5 Preliminary simulation analysis	45
5.1 Compensatory manual-control model simulations	45
5.1.1 General simulation setup	45
5.1.2 Toward more realistic simulations	48
5.2 Identification-framework implementation and application	51
5.2.1 Theoretical selection of the ARX-model orders and delay integer	51
5.2.2 OLS estimation of ARX models and selection using VAF-contour plots	52
5.2.3 RLS estimation of ARX models	55

6	Further research proposal	57
6.1	Compensatory manual-control model simulation with time-varying dynamics	57
6.2	Further steps in ARX-model selection and RLS estimation	58
6.3	Verification and validation procedure	58
6.4	Recommended future research	58
7	Conclusions	59
A	Simulation setup of the compensatory manual-control model with time-invariant dynamics	61
B	Remnant-free simulation of the compensatory manual-control model with time-invariant dynamics	63
C	VAF-contour plots	67
III	Final report appendices	77
D	Simulation setup of the compensatory manual-control model	79
D.1	Human-operator dynamics	79
D.2	Controlled-element dynamics	80
D.3	SIMULINK implementation	80
E	Remnant-free simulations of the compensatory manual-control model	83
E.1	Measurement window	84
E.2	Transition window	85
F	ZOH discretization of the analytical human-operator dynamics	87
G	Influence of the remnant-filter type on ARX-model estimation	91
G.1	Variable delay estimation	92
G.1.1	Condition 1	92
G.1.2	Condition 2	93
G.2	Relative bias	94
G.2.1	Condition 1	94
G.2.2	Condition 2	97
H	Frequency-response statistics and accuracies	101
H.1	Ensemble statistics	101
H.2	Frequency-response accuracies	102
I	Frequency-response estimation with FCs, and batch and recursive ARX models	103
J	VAF-results	107
J.1	Estimation data VAFs	108
J.2	Validation data VAFs	109
J.3	Overfit measures	110
J.4	Tracking ability versus noise sensitivity	111
K	Time traces of the ARX-model parameters	113
L	Time traces of the human-operator model parameters	157
M	Real measurements	161
	References	169

List of figures

1.1	Research framework for researching the adaptive human operator in compensatory tracking tasks.	2
II Preliminary report		
2.1	Variables affecting the manual-control behavior, adapted from McRuer and Jex (1967).	26
2.2	A compensatory tracking task, adapted from McRuer (1980).	27
2.3	Quasi-linear human-operator model structure.	27
3.1	Block diagram of a single-loop compensatory target-following control task with time-varying dynamics, adapted from Zaal (2016)	32
3.2	“Values of the time-varying simulation parameters” (Zaal and Sweet, 2011).	34
3.3	“Time evolution of the control mode” (Olivari et al., 2016).	34
3.4	“Sigmoid function parameter variation” (Zaal, 2016).	34
4.1	Identification loop, adapted from Ljung (1999) and Verhaegen and Verdult (2007).	38
4.2	Proposed identification method.	39
4.3	Equivalent representations of the ARX-model structure.	40
4.4	Representation of the ARX-model structure and the human-operator model.	41
4.5	RLS estimation from the viewpoint of feedback control, adapted from Tangirala (2015).	44
5.1	Forcing-function signal.	46
5.2	Bode plots of the controlled-element dynamics and the analytical human-operator dynamics.	47
5.3	Bode plots of the analytical system dynamics.	47
5.4	Block diagram of a single-loop compensatory target-following control task with time-invariant dynamics.	48
5.5	Remnant signal.	49
5.6	Error signal.	49
5.7	Control-output signal.	49
5.8	System-output signal.	50
5.9	Bode plots of the analytical human-operator dynamics and frequency responses identified with the FC method.	50
5.10	Bode plots of the analytical system dynamics and frequency responses identified with the FC method.	50
5.11	Bode plots of the analytical human-operator dynamics and frequency responses identified with the FC method and an ARX model (remnant free).	53
5.12	High-valued VAF-contour plots: input-output signals decimated with $d = 16$	53
5.13	Bode plots of the analytical human-operator dynamics and frequency responses identified with the FC method and with the most suitable ARX models for different preprocessed data sets.	54
5.14	RLS parameter estimations for different initial scaled covariance matrices with $\lambda = 1$	55
5.15	Influence of different constant forgetting factors on the memory horizon and the RLS weight.	56
5.16	RLS parameter estimations for different forgetting factors.	56
A.1	Block diagram of a single-loop compensatory target-following control task with time-invariant dynamics. Figure 5.4 repeated.	61

A.2	SIMULINK implementation of the compensatory manual-control model with time-invariant dynamics.	61
B.1	Block diagram of a single-loop compensatory target-following control task with time-invariant dynamics excluding remnant.	63
B.2	Remnant-free error signal.	64
B.3	Remnant-free control-output signal.	64
B.4	Remnant-free system-output signal.	64
B.5	Bode plots of the analytical human-operator dynamics and frequency responses identified with the FC method (remnant free).	65
B.6	Bode plots of the analytical system dynamics and frequency responses identified with the FC method (remnant free).	65
C.1	VAF-contour plots: input-output signals decimated with $d = 2$	68
C.2	VAF-contour plots: input-output signals filtered and decimated with $d = 2$	70
C.3	VAF-contour plots: input-output signals decimated with $d = 4$	72
C.4	VAF-contour plots: input-output signals filtered and decimated with $d = 4$	73
C.5	VAF-contour plots: input-output signals decimated with $d = 8$	74
C.6	VAF-contour plots: input-output signals filtered and decimated with $d = 8$	74
C.7	VAF-contour plots: input-output signals decimated with $d = 16$	75
C.8	VAF-contour plots: input-output signals filtered and decimated with $d = 16$	75
C.9	High-valued VAF-contour plots: input-output signals decimated with $d = 8$	75
C.10	High-valued VAF-contour plots: input-output signals filtered and decimated with $d = 8$	76
C.11	High-valued VAF-contour plots: input-output signals decimated with $d = 16$	76
C.12	High-valued VAF-contour plots: input-output signals filtered and decimated with $d = 16$	76
 III Final report appendices		
D.1	Block diagram of a single-loop compensatory manual-control model.	79
D.2	Equivalent block diagrams of a part of the controlled-element dynamics.	80
D.3	SIMULINK implementation of the compensatory manual-control model with the possibility to simulate both time-invariant and time-varying dynamics.	81
E.1	Block diagram of the single-loop compensatory target-following control task excluding remnant.	83
E.2	Time traces of the forcing function.	83
E.3	Measurement-time traces for condition C1.	84
E.4	Measurement-time traces for condition C2.	84
E.5	Measurement-time traces for condition C3.	84
E.6	Measurement-time traces for condition C4.	84
E.7	Measurement-time traces for condition C5.	85
E.8	Measurement-time traces for condition C6.	85
E.9	Transition-time traces for condition C1.	85
E.10	Transition-time traces for condition C2.	85
E.11	Transition-time traces for condition C3.	86
E.12	Transition-time traces for condition C4.	86
E.13	Transition-time traces for condition C5.	86
E.14	Transition-time traces for condition C6.	86
F.1	Comparison of the ARX model and the human-operator model.	88
F.2	Bode plots of the continuous-time human-operator model $H_{HOe,1}(j\omega)$ and the discrete-time human-operator models $H_1(z)$ including the time delay for different decimation factors d	89
G.1	Variable n_k^* estimation for condition C1.	92
G.2	Variable n_k^* estimation for condition C2.	93
G.3	Relative bias in ARX-model parameters for condition C1 for $f_s = 50$ Hz.	94

G.4	Relative bias in ARX-model parameters for condition C1 for $f_s = 100$ Hz.	95
G.5	Relative bias in ARX-model parameters for condition C1 for $f_s = 200$ Hz.	96
G.6	Relative bias in ARX-model parameters for condition C2 for $f_s = 50$ Hz.	97
G.7	Relative bias in ARX-model parameters for condition C2 for $f_s = 100$ Hz.	98
G.8	Relative bias in ARX-model parameters for condition C2 for $f_s = 200$ Hz.	99
H.1	Standard deviations $\sigma_{ \bar{H} }$ and $\sigma_{\angle\bar{H}}$ in the complex plane, adapted from van der Vaart (1992).	102
I.1	Bode plots for condition 1.	104
I.2	Bode plots for condition 2.	105
J.1	Estimation data VAFs.	108
J.2	Validation data VAFs.	109
J.3	Overfit as subtraction.	110
J.4	Overfit as ratio.	110
J.5	Ratio to trade off between tracking ability and noise sensitivity.	111
K.1	Time traces of ARX-model parameters for condition C1.	114
K.2	Time traces of ARX-model parameters for condition C2.	121
K.3	Time traces of ARX-model parameters for condition C3.	128
K.4	Time traces of ARX-model parameters for condition C4.	135
K.5	Time traces of ARX-model parameters for condition C5.	142
K.6	Time traces of ARX-model parameters for condition C6.	149
L.1	Human-operator model parameters for condition C1.	158
L.2	Human-operator model parameters for condition C2.	158
L.3	Human-operator model parameters for condition C3.	159
L.4	Human-operator model parameters for condition C4.	159
L.5	Human-operator model parameters for condition C5.	160
L.6	Human-operator model parameters for condition C6.	160
M.1	Estimated ARX-model parameters and HO-model parameters for condition C1.	162
M.2	Estimated ARX-model parameters and HO-model parameters for condition C2.	163
M.3	Estimated ARX-model parameters and HO-model parameters for condition C3.	164
M.4	Estimated ARX-model parameters and HO-model parameters for condition C4.	165
M.5	Estimated ARX-model parameters and HO-model parameters for condition C5.	166
M.6	Estimated ARX-model parameters and HO-model parameters for condition C6.	167

List of tables

II Preliminary report

4.1	Signal-processing quantities for different decimation factors.	39
5.1	Target forcing-function properties adapted from Zaal (2016).	46
5.2	Bounds of ARX-model integers n_a and n_b , and delay integer n_k for different decimation factors.	53
5.3	Most suitable combinations of ARX-model integers n_a and n_b , and delay integer n_k for the different preprocessed data sets based on VAF-contour plots and Bode plots.	54
C.1	Bounds of ARX-model integers n_a and n_b , and delay integer n_k for different decimation factors. Table 5.2 repeated.	67

III Final report appendices

E.1	Simulated conditions and overview of figures.	83
F.1	Values of the ARX-model coefficients for different sampling times T_s once ZOH discretization is employed.	88
F.2	VAF values when using ARX-model coefficients for different sampling times T_s once ZOH discretization is employed, $f_s = 100$ Hz, $n_k^0 = 29$	88
F.3	Values of the ARX-model coefficients for different sampling times T_s once ZOH discretization is employed.	88
G.1	Optimized K_n values for different remnant-filter types $H_n^m(s)$, for conditions C1 and C2.	91
K.1	Simulated conditions and overview of figures.	113
M.1	Experiment conditions.	161

Nomenclature

List of acronyms

ARX	Autoregressive exogenous
CE	Controlled element
DFT	Discrete Fourier transform
FC	Fourier coefficient
HO	Human operator
LPV	Linear parameter varying
LTI	Linear time invariant
mBIC	Modified Bayesian information criterion
MLE	Maximum-likelihood estimation
OLS	Ordinary least squares
PSD	Power-spectral density
RegRLS	Regularized recursive least squares
RK4	Fourth-order Runge-Kutta formula
RLS	Recursive least squares
SRS	SIMONA Research Simulator
VAF	Variance accounted for
ZOH	Zero-order hold

List of symbols

Greek

$\beta(t, k)$	Weight (forgetting profile)	
δ	Large positive constant	
$\epsilon(t)$	White noise	deg
$\varepsilon(t)$	Prediction error	deg
ζ	Realization of a stochastic process	
ζ_{nm}	Neuromuscular-damping ratio	
$\Theta; \theta$	Parameter vector	
λ	Forgetting factor	
σ	Real component of s ; Standard deviation	
σ^2	Variance	
τ_e	Effective time delay	s
τ_v	Visual time delay	s
Φ	Regression matrix	
ϕ_m	Phase margin	deg
ϕ_t	Sinusoid phase shift	rad
$\varphi(t)$	Regression vector	
ω	Frequency	rad/s
ω_b	Break frequency	rad/s
ω_c	Crossover frequency	rad/s
ω_m	Measurement-base frequency	rad/s
ω_N	Nyquist frequency	rad/s
ω_{nm}	Neuromuscular frequency	rad/s
ω_s	Sampling frequency	rad/s
ω_t	Sinusoid frequency	rad/s

Latin

$A(q)$	ARX model's output polynomial	
A_t	Sinusoid amplitude	deg
a_0	Lead coefficient of $A(q)$ (fixed to 1)	
a_i	Coefficient i of $A(q)$	
a_{n_a}	Final coefficient of $A(q)$	
$B(q)$	ARX model's input polynomial	
b_0	Lead coefficient of $B(q)$ (direct transmission coefficient)	
b_i	Coefficient i of $B(q)$	
b_{n_b}	Final coefficient of $B(q)$	
$CM(t)$	Control-mode parameter	
C_r	Crest factor	
d	Decimation factor	
$E(j\omega)$	Fourier transform of $e(t)$	deg
$e(t)$	Error signal	deg
f_s	Sampling frequency	Hz
$f_t(t)$	Target forcing-function signal	deg
f_N	Nyquist frequency	Hz
G	Maximum rate of change	s ⁻¹
$G(q; \theta)$	Parametric plant model	
$G(z); H(z)$	Discrete-time transfer function	
$H(j\omega); H(s)$	Continuous-time transfer function	
$H(q; \theta)$	Parametric noise model	
h_k	Padé approximation coefficient at discrete instant k	
I	Identity matrix	
j	Imaginary unit	
$K(t)$	Gain vector	
K_{CE}	Controlled-element gain	
K_v	Visual gain	
k	Discrete-time sample	
k_t	Sinusoid index	
M	Time of maximum rate of change	s
m	Integer multiple of T_s	
N	Number of samples	
$N(j\omega)$	Fourier transform of $n(t)$	deg
N_t	Total number of sinusoids	
$n(t)$	Remnant signal	deg
n_a	Number of coefficients in $A(q)$	
n_b	Number of coefficients in $B(q)$	
n'_b	Highest order of $B(q)$ when using n_k : $n'_b = n_b + n_k - 1$	
n_k	ARX model's input-output delay integer	
n_t	Integer factor	
$n_w(t)$	Zero-mean Gaussian white-noise signal with unit variance	deg
P	Parameter	
$P(t)$	Scaled covariance matrix	
P_n	Remnant intensity (power ratio)	
p	Integer for setting up Φ with known input-output data: $p = \max(n_a + 1, n_b + n_k)$	
$Q(t)$	Matrix obtained by RLS criterion minimization	
q	Discrete-time shift operator	
$S(j\omega)$	Power-spectral density	deg ² /(rad/s)
s	Laplace variable, $s = \sigma + j\omega$	
T_0	Memory horizon	
T_L	Lead-time constant	s
T_m	Measurement time	s
T_n	Remnant-time constant	s
T_r	Run-in time	s

T_s	Sampling time/interval	s
T_t	Total recording time	s
t	Time	s
$U(j\omega)$	Fourier transform of $u(t)$	deg
$u(t)$	Control-output signal	deg
\mathbf{u}	Vector of $u(t)$	
$v(t)$	Stochastic disturbance signal	deg
$V(\theta, Z)$	Criterion function	
$x(t)$	System-output signal	deg
Z	Data set	
z	z-transform variable	

Other

$\mathbf{0}$	Zero vector	
$-$	Average	
\in	Element of	
$\hat{}$	Estimated; Predicted	
Im	Imaginary part	
$ \cdot $	Magnitude	
\angle	Phase angle	deg
Re	Real part	
\mathbb{Z}	Set of integers	

Subscripts

0	Initial; True
1	Initial; Single-integrator dynamics ($1/j\omega$)
2	Final; Double-integrator dynamics ($1/(j\omega)^2$)
ε	Prediction error
θ	Parameters
$CE; c$	Controlled element
CL	Closed loop
e	End; Error; Estimation
eq	Equalization
HO	Human operator
$L; l$	Lead
nm	Neuromuscular (actuation)
m	Measured
N	Number of samples
n	Remnant
OL	Open loop
s	Simulation; Start
t	Time
v	Validation

Superscripts

0	True
LS	Least squares
N	Number of samples
OLS	Ordinary least squares
RLS	Recursive least squares
t	Time

Introduction

1.1 Reason for the research

To date, cybernetic models are well capable to capture dynamic multimodal human manual-control behavior in stationary and time-invariant situations, where the human operator is assumed to be stationary and time-invariant too (Lone and Cooke, 2014; Grant and Schroeder, 2010; Mulder et al., 2006). In reality, however, the human operator is not only characterized as a multimodal controller, but also as an adaptive and learning controller “capable of exhibiting an enormous variety of behavior” (McRuer and Jex, 1967) varying over time and being nonlinear. In this context, adaptive refers to the behavioral ability of changing performance in new situations, while learning refers to the behavioral ability of changing performance in successive encounters with the same situation.

It is a desire to have system-theoretical models available that are capable to capture both the adaptive and learning characteristics of the human operator’s manual-control behavior in the various situations (Young, 1969). For instance, it would be interesting how novice and experienced human operators manage themselves to respond differently to sudden changes in important task variables (Zaal and Pool, 2014). A recent comprehensive research project, reviewed by Mulder et al. (2013), has shown that studying the time-varying and nonlinear characteristics of human-operator behavior requires an extension of the existing identification and modeling techniques.

As noted by Pool (2012), some argue that in the future, due to significant advances in automation technology, the role of human operators for skill-based manual-control tasks will diminish and that there will be only rule-based and knowledge-based supervisory-control tasks left for them to do. Subsequently, Pool refers to the still-valid statement by Young (1969) which reads that “man’s adaptability as a controller is frequently cited as the primary reason for incorporating him in the complex vehicle control loops.” In the near future, it is virtually impossible to imitate this ability by some sort of automation system. The need for ever-increasing levels of safety and economic efficiency in practically all socio-technical domains involving manual control, leads to the need to advance training methods and to further improve human-machine system performance. It is for these reasons that the role of the human operator as a manual controller ought to be investigated further.

1.2 Aim of the research and research design

This thesis aims to provide an overview of the conducted research for the thesis project focusing on the further characterization and understanding of adaptive human-operator behavior in manual-control systems. A cybernetic approach is taken which will be based on time-varying autoregressive exogenous (ARX) models, to be estimated using a recursive least-squares (RLS) algorithm equipped with forgetting factor. The application of compensatory tracking tasks with time-varying controlled-element dynamics will serve as a stepping stone toward meeting the challenge.

Research objective The research objective of the thesis project can be formulated as follows.

To further characterize and understand adaptive compensatory manual-control behavior, by implementing an identification method based on time-varying ARX models, which requires no prior definitions of specific human-operator parameter functions.

Research framework In order to reach the research objective, consecutive steps need to be taken during the research. A high-level schematic research framework representing these steps is drawn in Figure 1.1. An analysis of compensatory manual-control theory, together with a literature survey on the state-of-the-art in time-varying human-operator identification and on system identification, plus preliminary research, consisting of mathematical implementations and offline simulations, will lead to the research perspective, i.e., the identification scheme. The application of this research perspective to the research object, i.e., the human operator, intends to achieve the research objective.

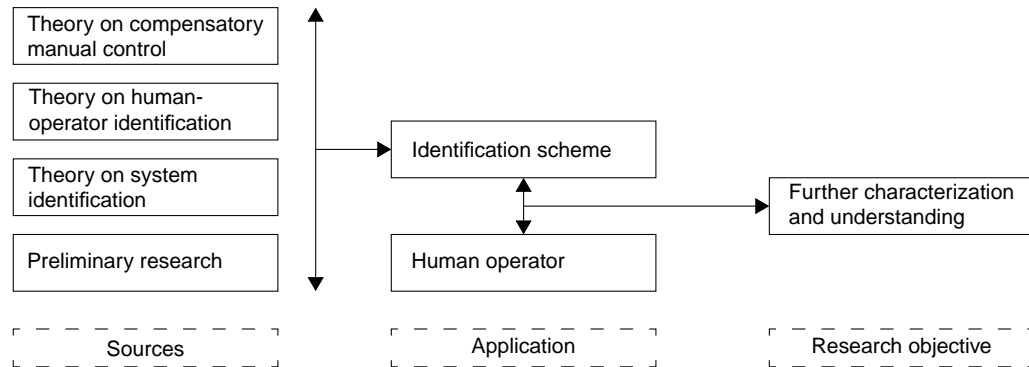


Figure 1.1 Research framework for researching the adaptive human operator in compensatory tracking tasks.

Research questions Based on the research framework, a set of research questions can be formulated. The central question that drives the thesis project asks the following.

To what extent is an identification method based on time-varying ARX models, which requires no prior definitions of specific human-operator parameter functions, able to quantitatively describe adaptive compensatory manual-control behavior, due to transitions in the controlled-element dynamics?

To provide an answer to this central question, the following subquestions are addressed.

- What are the fundamental considerations in human-operator modeling in compensatory tracking tasks?
- What are the likely time variations to be introduced in simulating manual-control behavior for both slow and fast parameter transitions in the controlled-element dynamics?
- Which preprocessing steps are needed for transforming human-operator input-output data to model inside the operator's frequency range of interest?
- What are the relevant criteria for selecting the appropriate ARX-model orders so that the adaptive human-operator behavior due to parameter transitions in the controlled-element dynamics can be captured?
- What are the relevant criteria for assessing the performance of the resulting time-varying ARX models in relation to the input-output data, to prior knowledge, and to their intended use?
- What are the promising RLS forgetting-factor tuning techniques to capture human-operator behavior for both slow and fast parameter transitions in the controlled-element dynamics?
- Which verification and validation procedures should be employed to analyze the robustness of the proposed identification method to different intensity levels and realizations of remnant?
- To what extent are other time-varying identification methods in development able to quantitatively describe adaptive human-operator behavior compared to the proposed identification method?

Research subgoals From the above subquestions, the following research subgoals are set. These need to be accomplished in order to reach the research objective.

- To perform a literature survey on compensatory manual control, methods for estimating time-varying ARX models, other methods in development for time-varying human-operator identification, and related verification and validation procedures.
- To set up compensatory tracking task simulations using software in which time variations can be applied to both the dynamics of the human operator and the controlled element.
- To set up preprocessing steps to subject human-operator input-output data sets before presenting them to identification algorithms.

- To determine suitable ARX-model orders so that typical human-operator adaptations in compensatory tracking tasks can be described based on a selection criterion.
- To decide on an assessment criterion for evaluating the performance of time-varying ARX models in relation to the input-output data, to prior knowledge, and to their intended use.
- To implement and to tune an RLS algorithm equipped with forgetting factor so that human-operator behavior can be described for both slow and fast parameter transitions in the controlled-element dynamics.
- To analyze and to verify the capability of the novel time-varying ARX-model identification method for capturing time-varying human-operator behavior by simulating different intensity levels and realizations of remnant.
- To validate the novel identification method by gathering and analyzing real time-varying experimental manual-control data from a fixed-base simulator operation.

The theoretical basis of the thesis project work to be undertaken is as follows. In order to meet the external goal, i.e., the further characterization and understanding of adaptive human-operator behavior in compensatory tracking tasks, a cybernetic approach will be adopted. The internal goal, i.e., the implementation of an identification method based on time-varying ARX models, is attempted to be achieved by using the concept of system identification. In this research context, cybernetics studies the fundamental properties of human-machine interaction centered around information used for manual control (Mulder, 1999). System identification can be described as the process of building mathematical models of dynamic systems from observed input-output data (Ljung, 1999). In this project, the cybernetic approach consists of two stages:

1. the analysis of the compensatory tracking task with time-varying controlled-element dynamics to be completed by the human operator;
2. the capture of the time-varying manual-control behavior characteristics in a system-theoretical model.

It should be emphasized that the resulting identification method will just serve as a tool for the further human-operator characterization and understanding. However, in order to investigate the application possibilities of the time-varying ARX models, a strong emphasis is put on the mathematical development and the low-level implementation of the identification scheme.

The research objective will be facilitated by drawing on TU Delft's Control and Simulation chair's knowledge of and experience with ARX models for human-operator identification. Because the accuracy of the identification method should be evaluated properly before using it in laboratory experiments or real-life applications, extensive implementation testing with offline simulations is required. Real experimental manual-control data will not be used until the identification method has realized its full potential. The scope of the research project is limited, due to time constraints, in the sense that it only focuses on compensatory tracking tasks. More specifically, single-axis target-following tasks are considered with different time variations in the parameters of the controlled-element dynamics and with different levels of remnant intensity.

1.3 Thesis's structure

This thesis is structured as follows.

- Part I contains the scientific paper with the most relevant information and results on the conducted research.
- Part II lists the chapters and appendices that are related to the preliminary work. Chapter 2 critically surveys the existing knowledge regarding adaptive human-operator identification. It lists some fundamentals on compensatory manual control, addresses the relevant research fields requiring further investigation of manual-control behavior, discusses the different approaches on time-varying human-operator identification, and identifies the knowledge gap and the information needed to fill that gap. From Chapter 3 on, a more mathematical approach is taken. In Chapter 3, a setup of the compensatory manual-control model is given. Next, this chapter gives parametric models for both the controlled-element and human-operator dynamics. It also compares different time variations to be introduced in these dynamics. The setup of the identification framework is described in Chapter 4. It outlines the identification loop, explains the proposed identification method, provides a description of ARX models, and highlights the least-squares parameter estimations. A preliminary simulation analysis, conducted with The MathWorks, Inc.'s MATLAB[®] and

SIMULINK[®] R2016b, is presented in Chapter 5. The further research proposal for the remainder of the thesis project is described in Chapter 6. Lastly, conclusions are drawn in Chapter 7.

- Additional results that are not documented in the scientific paper can be found in the appendices in Part III.



Paper

Identification of Time-Varying Manual-Control Adaptation with Recursive ARX Models

H. A. van Grootheest, D. M. Pool, M. M. van Paassen, and M. Mulder

Abstract—The time-varying adaptation ability of human operators in basic manual-control tasks is barely understood. Most identification methods do not explicitly take into account any time variations. An identification procedure based on both batch and recursive autoregressive exogenous (ARX) models is presented for capturing the operator’s controlled-element adaptation in compensatory tracking tasks. The operator’s time delay was assumed to be constant and estimated beforehand. Conditions with constant controlled-element dynamics, matching recent experimental work, and gradual and sudden transitions in the controlled-element dynamics were considered. This study introduces a procedure to fine-tune forgetting strategies for these different conditions and for different remnant intensities. Both the use of a constant scalar forgetting factor λ and a constant forgetting matrix Λ , containing separate forgetting factors for each ARX-model parameter, was analyzed. Batch ARX-model identifications applied on conditions with constant dynamics, indicate that a high bias results when the operator’s remnant is not coupled to the linear operator dynamics. By means of Monte Carlo simulations, an optimal forgetting factor is found for all conditions. For the human-operator model considered, the use of a forgetting matrix did not result in an improvement over the use of a scalar forgetting factor. An evaluation of real experimental manual-control data shows that the method has potential to capture the operator’s adaptive control characteristics.

Index Terms—ARX model, forgetting factor, human operator, manual control, recursive least squares, time-varying system identification.

I. INTRODUCTION

HUMAN manual-control behavior inherently varies over time, across different situations, and between operators. Identification methods have been developed that are able to describe the dynamic characteristics of human operators (HOs) in skill-based manual-control tasks [1]. These are, however, mostly restricted in their use to cases where the control behavior is assumed to be time invariant. A long-standing desire is to have control-theoretic models available that are capable of capturing both the adaptive and learning characteristics of manual-control behavior [2]–[4]. State-of-the-art cybernetics cannot explain, in depth, how HOs adapt themselves to cope with control-task transitions. Rapid advancement of understanding how humans interact with dynamic control systems requires the further development of time-varying identification methods [5].

Most research on identifying time-varying manual-control behavior focuses on induced changes in the task variables and, in particular, on transitions in the controlled-element (CE)

dynamics [2], [6]. For these variables, substantial and highly noticeable adaptation changes are expected. Many studies start with investigating single-axis compensatory control tasks and are based on the well-known crossover model [6], bearing in mind that extensions to multiple axes of control or even the usage of other classes of inputs to the HO should not pose fundamental difficulties [4]. Previous investigations make clear that, before using a novel identification method in laboratory experiments or real-life tasks, its accuracy should be evaluated thoroughly by means of Monte Carlo simulations [7]–[9]. In addition to task variables, manual-control behavior depends on a myriad of other factors, e.g., suffering fatigue or alterations in motivation are directly related to the human operator. Usually, these factors are lumped together as remnant, taking into account different remnant intensities.

Literature shows that different approaches have been taken to mathematically model time-varying manual-control behavior. Identification using wavelet transforms [10], [11] is not mature yet and very sensitive to HO remnant. The identification method based on genetic maximum-likelihood estimation [8] is less sensitive to remnant and can provide accurate estimations, but requires restrictive definitions about how certain parameters will change [12]. Recently, the viability of linear parameter varying (LPV) predictor-based subspace identification was assessed [13]. To study the human-in-the-loop problem, this framework requires precise scheduling functions. Recursive identification methods, however, are beneficial in that they are able to analyze the evolution of parameters over time. They can even track time-varying dynamics in real time, i.e., online. Initial results in [14] make the recursive least-squares (RLS) algorithm equipped with forgetting factor a promising candidate to consider. No previous study has investigated in detail the tuning of this type of algorithm for the identification of manual control.

In manual-control cybernetics, very few studies have yet attempted to make use of recursive autoregressive exogenous (ARX) models. In contrast to autoregressive moving average exogenous (ARMAX), output-error (OE), or Box-Jenkins (BJ) model structures, the structure of ARX models allows direct linear regression estimation. This convenience is particularly relevant in identifying manual-control behavior as the real process is of infinite order. This study aims to extend the works in [9] and [7] with recursive estimation, i.e., to take the ARX-model structure and to recursively estimate the model parameters using RLS. Contrary to [12], this study opts to set up an identification method able to capture time variations in manual-control behavior without making explicit assumptions on how these will evolve over time.

This paper investigates the use and feasibility of a recursive

The authors are with the Section Control and Simulation, Department of Control and Operations, Faculty of Aerospace Engineering, Delft University of Technology, 2600 GB Delft, The Netherlands (e-mail: H.A.vanGrootheest@student.TUdelft.nl; D.M.Pool@TUdelft.nl; M.M.vanPaassen@TUdelft.nl; M.Mulder@TUdelft.nl).

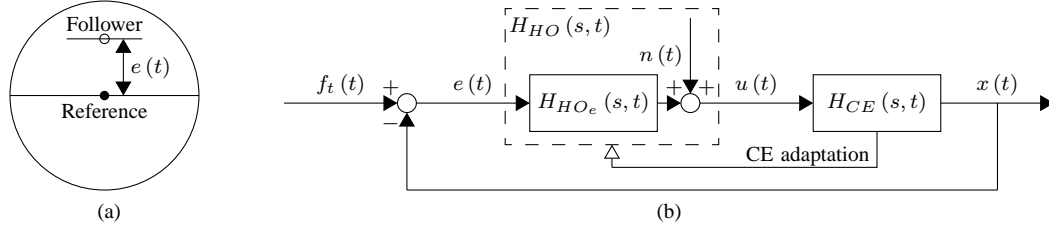


Fig. 1. Single-axis compensatory manual-control task with time-varying dynamics. (a) Compensatory display: $e(t)$ acts as stimulus. (b) Block diagram.

ARX-model identification method for capturing time-varying manual-control adaptations. RLS algorithms equipped with a constant scalar forgetting factor and a constant forgetting matrix are considered. To ensure the robustness of the identification method, a Monte Carlo simulation analysis with $M = 100$ replications is performed, considering different remnant-filter orders ($m = 1-4$) and remnant intensity levels (0–30%, in increments of 5%). The emphasis is placed on identifying the operator's adaptive responses in a compensatory tracking task when faced with gradual and sudden transitions in the CE dynamics, as studied by Zaal [12]. For reference, the quality of the obtained results is explicitly compared with batch (i.e., nonrecursive) ARX-model estimation of the operator's responses to constant CE dynamics.

The paper is structured as follows. The compensatory manual-control task is described in Section II. Section III outlines the ARX-model identification approach. The setup of the Monte Carlo simulation analysis is given in Section IV. Section V provides example results. An evaluation of the identification method on real experimental manual-control data is presented in Section VI. Section VII discusses the identification scheme and its limitations. Conclusions are drawn in Section VIII.

II. COMPENSATORY MANUAL-CONTROL TASK

Based on research by Zaal [12], this study concentrates on the single-axis compensatory manual-control task shown in Fig. 1. The HO, modeled as $H_{HO}(s, t)$, observes and acts, with a control output $u(t)$, upon the error $e(t)$ between a target $f_t(t)$ (e.g., a multisine) and the output $x(t)$ of the CE dynamics $H_{CE}(s, t)$. The HO dynamics consist of deterministic responses $H_{HO_e}(s, t)$ and remnant $n(t)$ accounting for control nonlinearities [6]. Changes over time in the CE dynamics require control-strategy adaptations in the HO [2].

A. Controlled-Element Dynamics

In [12], the following second-order CE dynamics were taken for analysis, which parametrically approximate many dynamic control systems [6]:

$$H_{CE}(s, t) = \frac{K_c(t)}{s(s + \omega_b(t))} \quad (1)$$

The CE parameters are the control gain $K_c(t)$ and the break frequency $\omega_b(t)$, which can both vary in time. Around $\omega_b(t)$ the CE dynamics shift between single- and double-integrator

dynamics (i.e., $1/s \leftrightarrow 1/s^2$). Convenient functions to introduce different types of time variations in a parameter $p(t)$ are sigmoids:

$$p(t) = p_i + \frac{p_f - p_i}{1 + e^{-G(t-t_M)}} \quad (2)$$

The initial and final parameter values are set by p_i and p_f , respectively. Fig. 2 clarifies the tuning of the maximum rate of transition G and the time t_M at which this change happens. For all G , $p(t_M)$ equals $p_i + \frac{p_f - p_i}{2}$. Gradual transitions are obtained for low values of G . Around $G = 10 \text{ s}^{-1}$, the sigmoid already approaches a step function.

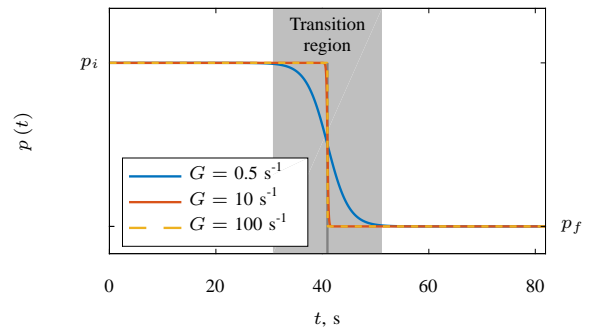


Fig. 2. Sigmoid-function variation with G .

B. Human-Operator Dynamics

A suitable HO model for the time-varying CE dynamics to be controlled [12], based on the precision model [15], is defined by:

$$H_{HO_e}(s, t) = \overbrace{K_e(t) [T_L(t) s + 1]}^{\text{Equalization}} \overbrace{e^{-s\tau_e} H_{nm}(s)}^{\text{Limitations}}, \quad (3)$$

with:

$$H_{nm}(s) = \frac{\omega_{nm}^2}{s^2 + 2\zeta_{nm}\omega_{nm}s + \omega_{nm}^2} \quad (4)$$

Equation (3) is split into equalization dynamics $H_{eq}(s, t)$ and operator limitations, which include the neuromuscular dynamics $H_{nm}(s)$. The equalization parameters are the error gain $K_e(t)$ and the lead-time constant $T_L(t)$. The limitation parameters are the time delay τ_e , the natural frequency ω_{nm} , and the damping ratio ζ_{nm} , which are assumed to be time invariant [12]. If the HO's equalization-model structure in (3) is used and the pure response to the error rate $\dot{e}(t)$ has to be determined, an ambiguity arises between $K_e(t)$ and $T_L(t)$. An equivalent alternative parametrization for $H_{eq}(s, t)$, easing

identification [13], can be obtained with the error-rate gain $K_{\dot{e}} = K_e(t) T_L(t)$:

$$H_{eq}(s, t) = K_{\dot{e}}(t) s + K_e(t) \quad (5)$$

III. ARX-MODEL IDENTIFICATION

A. ARX-Model Structure

Transfer-functions models with a rational polynomial structure provide high flexibility in describing the HO dynamics. Computationally efficient polynomial estimation is offered by the ARX-model structure. Fig. 3 represents this structure, which is equivalent to the HO-model structure in Fig. 1. The process dynamics $\frac{B(q)}{A(q)}$ relate $e(t)$ to $u(t)$. The disturbance signal $v(t)$, obtained by filtering the white-noise signal $\epsilon(t)$ using disturbance dynamics $\frac{1}{A(q)}$, is similar to the remnant signal $n(t)$. The coupling of the process and disturbance dynamics is a shortcoming of the ARX-model structure. However, in practice, the ease of estimation outweighs this disadvantage significantly.

Denoting q as the discrete-time shift operator, the ARX model's difference equation is:

$$A(q) u(t) = B(q) e(t) + \epsilon(t) \quad (6)$$

with the output and input polynomials $A(q)$ and $B(q)$, having orders n_a and $n_b - 1$, respectively:

$$A(q) = 1 + a_1 q^{-1} + \dots + a_{n_a} q^{-n_a} \quad (7)$$

$$B(q) = (b_0 + b_1 q^{-1} + \dots + b_{n_b} q^{-n_b+1}) q^{-n_k} \quad (8)$$

The integers n_a and n_b set the number of parameters a_i for $i \geq 1$ and b_j for $j \geq 0$, respectively. The adjustable parameters are thus:

$$\theta = [a_1 \ a_2 \ \dots \ a_{n_a} \ b_0 \ b_1 \ \dots \ b_{n_b}]^T \quad (9)$$

The integer n_k models a discrete input delay, leading to exponent shifts in $B(q)$. To ease notation, $n'_b = n_b + n_k - 1$ can be used. If n_k is zero, parameter b_0 provides direct transmission.

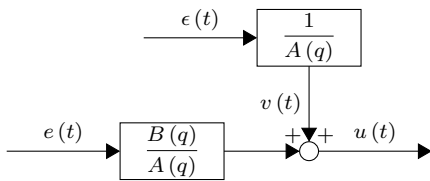


Fig. 3. ARX-model structure.

B. OLS and RLS Estimation

As the ARX-model structure allows the application of linear regression [16], ordinary least-squares (OLS) and recursive-least squares (RLS) estimation of the parameter vector θ in (9) is straightforward. OLS estimation acts in batch mode, while RLS estimation updates the parameter estimation for each new measurement sample that becomes available, and is, therefore, able to track time variations with appropriate use of forgetting. In both least-squares estimations, the regression vector $\varphi(t)$

plays a central role. For the input-output data set $\{e(t), u(t)\}$, it is defined as:

$$\varphi(t) = [-u(t-1) \ -u(t-2) \ \dots \ -u(t-n_a) \\ e(t-n_k) \ e(t-n_k-1) \ \dots \ e(t-n'_b)]^T \quad (10)$$

The least-squares methods and their implementation can be explained as follows.

1) *OLS Estimation*: From the input-output data set consisting of N samples, a regression matrix Φ and output vector \mathbf{u} should be constructed from $\varphi(t)$ and $u(t)$, respectively. In order to consider only known input-output data, regressors $\varphi(t)$ cannot be fully constructed at instants less than the critical instant $k_c = \max(n_a + 1, n_b + n_k)$, unless assumptions are made. OLS estimates $\hat{\theta}^{\text{OLS}}$ can be obtained using QR factorization provided that Φ is full rank [16].

2) *RLS Estimation*: The RLS algorithm is provided by (11) to (16) [16]. By adjusting the gain vector $K(t)$, the prediction error $\varepsilon(t)$ between $u(t)$, i.e., the observed output at time t , and $\hat{u}(t)$, i.e., the prediction of $u(t)$ based on observations up to time $t-1$, can be minimized. The computation of $Q(t)$ makes use of the scaled covariance matrix $P(t)$.

$$\hat{\theta}(t) = \hat{\theta}(t-1) + K(t) \varepsilon(t) \quad (11)$$

$$\varepsilon(t) = u(t) - \hat{u}(t) \quad (12)$$

$$\hat{u}(t) = \varphi^T(t) \hat{\theta}(t-1) \quad (13)$$

$$K(t) = Q(t) \varphi(t) \quad (14)$$

$$Q(t) = \frac{P(t-1)}{\lambda(t) + \varphi^T(t) P(t-1) \varphi(t)} \quad (15)$$

$$P(t) = \frac{P(t-1)}{\lambda(t)} (I - K(t) \varphi^T(t)) \quad (16)$$

The design variable of the RLS algorithm is the forgetting factor $\lambda(t) \in (0, 1)$, which assigns less weight to older measurements and, more importantly, affects the variance of $\hat{\theta}(t)$. In essence, $\lambda(t)$ sets the trade-off between noise sensitivity (i.e., $\lambda(t)$ close to 1, slow adaptation, and low variance in $\hat{\theta}(t)$) and tracking ability (i.e., lowered $\lambda(t)$, fast adaptation, and high variance in $\hat{\theta}(t)$). Numerous strategies exist for implementing and tuning the forgetting strategy. Particularly in the area of research of manual-control cybernetics, it is essential “to look for the simplest possibility of making estimators reliably adaptive, within a rigorous framework” [17]. Hence, a conservative approach is taken here. Only constant forgetting factors $\lambda(t) \equiv \lambda$ are used. A scalar forgetting factor λ and a forgetting matrix Λ are considered. The latter may use different λ values for different parameters, with possible different timescales of variations [18]. For the parameter vector θ in (9), Λ is defined as:

$$\Lambda = \text{diag} \left(\lambda_{a_1}, \lambda_{a_2}, \dots, \lambda_{a_{n_a}}, \lambda_{b_0}, \lambda_{b_1}, \dots, \lambda_{b_{n_b}} \right)^{-1/2} \quad (17)$$

It is a diagonal matrix with inverse square roots of forgetting factors matching specific parameters. When using Λ , (15) and (16) are changed into:

$$Q(t) = \frac{\Lambda P(t-1) \Lambda}{1 + \varphi^T(t) \Lambda P(t-1) \Lambda \varphi(t)} \quad (18)$$

$$P(t) = \Lambda P(t-1) \Lambda (I - K(t) \varphi^T(t)) \quad (19)$$

This ensures that all entries in $P(t-1)$ are weighted properly, e.g., if $n_a = n_b = 2$ (omitting $(t-1)$ for readability):

$$\Lambda P \Lambda = \begin{bmatrix} \frac{P_{a_1}}{\lambda_{a_1}} & \frac{P_{a_1,a_2}}{\sqrt{\lambda_{a_1}\lambda_{a_2}}} & \frac{P_{a_1,b_0}}{\sqrt{\lambda_{a_1}\lambda_{b_0}}} & \frac{P_{a_1,b_1}}{\sqrt{\lambda_{a_1}\lambda_{b_1}}} \\ \frac{P_{a_1,a_2}}{\sqrt{\lambda_{a_1}\lambda_{a_2}}} & \frac{P_{a_2}}{\lambda_{a_2}} & \frac{P_{a_2,b_0}}{\sqrt{\lambda_{a_2}\lambda_{b_0}}} & \frac{P_{a_2,b_1}}{\sqrt{\lambda_{a_2}\lambda_{b_1}}} \\ \frac{P_{a_1,b_0}}{\sqrt{\lambda_{a_1}\lambda_{b_0}}} & \frac{P_{a_2,b_0}}{\lambda_{a_2}} & \frac{P_{b_0}}{\lambda_{b_0}} & \frac{P_{b_0,b_1}}{\sqrt{\lambda_{b_0}\lambda_{b_1}}} \\ \frac{P_{a_1,b_1}}{\sqrt{\lambda_{a_1}\lambda_{b_1}}} & \frac{P_{a_2,b_1}}{\sqrt{\lambda_{a_2}\lambda_{b_1}}} & \frac{P_{b_0,b_1}}{\lambda_{b_0}} & \frac{P_{b_1}}{\lambda_{b_1}} \end{bmatrix} \quad (20)$$

As only constant forgetting factors λ are considered, old measurements are discounted exponentially [16]. A measurement that is $N_0 = 1/(1-\lambda)$ samples old has a weight equal to $\lambda^{N_0} \approx e^{-1} \approx 37\%$ times the weight of the most recent observation. The memory horizon N_0 is easier to interpret than the value of λ , e.g., if $\lambda = 0.9375$, N_0 equals 16 samples. Alternatively, denoting T_s as the sampling time in seconds, a memory horizon is expressible in seconds: $T_0 = T_s/(1-\lambda)$, e.g., if $T_s = 0.01$ s and $\lambda = 0.9375$, T_0 equals 0.16 s.

The RLS algorithm is completed by specifying the initial parameter estimate $\hat{\theta}_0$, and the initial scaled covariance matrix P_0 (typically set equal to δI , with δ a positive constant). The actual covariance matrix of the parameters, i.e., $P_\theta(t)$, can be obtained by multiplying $P(t)$ with $\sigma_\varepsilon^2(t)/2$, where $\sigma_\varepsilon^2(t)$ denotes the variance of $\varepsilon(t)$ [16, pp. 381–382]. Similar as described in Section III-B1, if only known input-output data is considered, RLS estimation starts at instant k_c .

C. HO Model and ARX Model

As shown by Hess [19], the discrete-time transfer function $G(z)$ of the continuous-time HO-model structure in (3), without considering τ_e , and assuming zero-order hold (ZOH) discretization would be:

$$G(z) = z^{-1} \frac{b_0 + b_1 z^{-1}}{1 + a_1 z^{-1} + a_2 z^{-2}} \quad (21)$$

Except for the unit-sample delay z^{-1} caused by ZOH discretization, this function corresponds to the ARX model's transfer function from $e(t)$ to $u(t)$ with $n_a = n_b = 2$ and $n_k = 0$.

For easier interpretation, ARX models can also be converted back to the HO-model structure under consideration. If $n_a = n_b = 2$, this conversion to the rational continuous-time ZOH equivalent model is straightforward:

$$H(s) = \frac{b_1^c s + b_0^c}{s^2 + a_1^c s + a_0^c} \quad (22)$$

The HO-model parameters are then retrieved as:

$$\begin{aligned} \hat{K}_e &= \frac{b_0^c}{a_0^c}, & \hat{T}_L &= \frac{b_1^c}{b_0^c}, & \hat{K}_\varepsilon &= \frac{b_1^c}{a_0^c}, \\ \hat{\omega}_{nm} &= \sqrt{a_0^c}, & \hat{\zeta}_{nm} &= \frac{a_1^c}{2\sqrt{a_0^c}} \end{aligned} \quad (23)$$

Estimation complexity increases if n_a and n_b are not both equal to 2 and the identified ARX model is fit to the specific

HO model. Then model order reduction techniques should be applied. It means that a nonlinear optimization problem based on a certain frequency-domain criterion should be solved.

The poles of (21) and (22) are mapped according $z = e^{sT_s}$. For the mapping of zeros, such an expression does not exist. From (23) it can be observed that the HO's neuromuscular parameters are only related to the ARX model's output polynomial $A(q)$. Inspecting again Fig. 3, the ARX-model estimation thus compromises between the estimating these neuromuscular parameters and the remnant characteristics using $A(q)$.

Methods are available to capture τ_e as fractional delay [20], however, this would mean that extra parameters a_i and b_i are needed. The study aims to identify time-varying CE adaptations in the HO, as unambiguously as possible. Therefore, n_a and n_b are both fixed to 2 and τ_e is modeled as an integer multiple of the sampling interval T_s , taking into account the additional ZOH unit-sample delay.

From an identification perspective, time variations in the input-output data are best captured if the sampling time T_s is as low as possible. It might be, however, that the ARX model's transfer function from $\varepsilon(t)$ to $u(t)$ cannot properly explain the HO remnant characteristics. Typically, there are noise disturbances in the data, above the frequencies of interest. Then, a remedy is to decimate the input-output data [7], [16]. To circumvent the issue of decreased resolution in capturing the integer time delay, the input signal $e(t)$ can be shifted with the assumed interval steps n_k^* of time delay before decimating.

Furthermore, it should be noted that the closed-loop identification problem considered here will be tackled by means of the direct identification approach. In [21] it was found that the direct identification approach with ARX models is able to provide more accurate estimates in the frequency range of interest for manual control than the indirect approach. Hence, closed-loop identification issues are not explicitly taken into account.

D. Identification Approach

The general identification approach taken in this study is shown in Fig. 4. The gray blocks indicate the user's main tuning options. In order to fine-tune the procedure, two input-output data sets are considered, one for estimation $\{e_e(t), u_e(t)\}$, and one for validation $\{e_v(t), u_v(t)\}$, both sampled with frequency f_s . The procedure has 9 steps.

- 1) *Discard run-in time data.* Discard the transients present in the beginning of the recordings $e_e(t)$, $u_e(t)$, $u_v(t)$ and obtain the measurement signals $e_{e,m}(t)$, $u_{e,m}(t)$, $u_{v,m}(t)$, respectively, all of length T_m and containing $N_m = f_s T_m$ samples.
- 2) *ARX-model setup.* Select the integers n_a and n_b , and the range of integers $n_{k,\min}^*$ and $n_{k,\max}^*$ to be tested for estimating the time delay $\hat{\tau}_e$ with n_k^*/f_s . The initial choice is to use physical insight, and by applying the principle of parsimony select n_a and n_b as low as possible. Insights could also be gained from nonparametric analysis, e.g., using Fourier coefficients [22], for cases where the HO can be characterized as time invariant.
- 3) *Input-delay estimation.* Simultaneously estimate the selected ARX models, all with different n_k^* , using OLS.

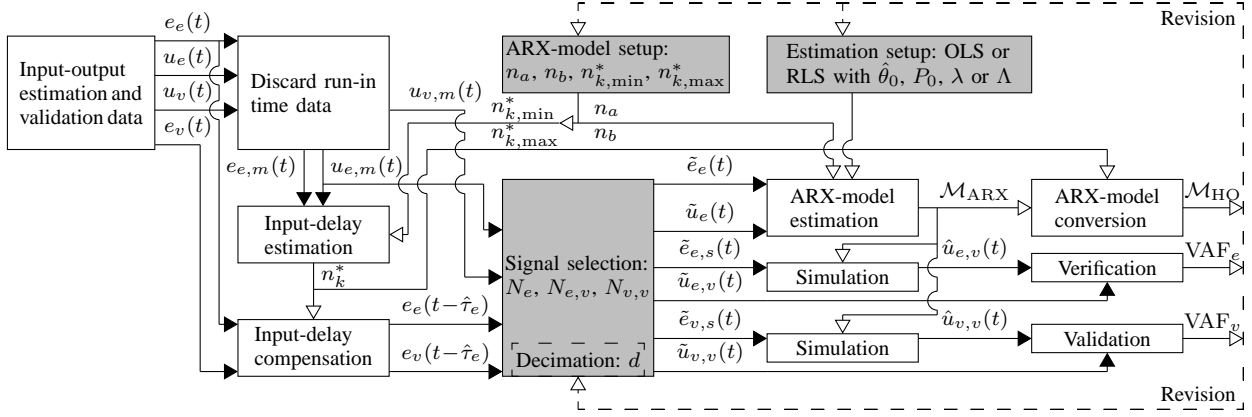


Fig. 4. Flow chart of the ARX-model identification method.

Pick out the n_k^* that results in the lowest loss function V of the one-step-ahead prediction $\hat{u}_{e,p}(t)$. This V is defined as:

$$V = \frac{1}{N} \sum_{t=1}^N (u_{e,m}(t) - \hat{u}_{e,p}(t)) \quad (24)$$

- 4) *Input-delay compensation.* Shift the recordings $e_e(t)$ and $e_v(t)$ with n_k^* samples, and obtain the signals $e_e(t - \hat{\tau}_e)$ and $e_v(t - \hat{\tau}_e)$, respectively.
- 5) *Signal selection.* Select the number of samples N_e for estimation, $N_{e,v}$ for verification, and $N_{v,v}$ for validation. Obtain from $e_e(t - \hat{\tau}_e)$ and $u_{e,m}(t)$ the signals $\tilde{e}_e(t)$ and $\tilde{u}_e(t)$, respectively, for the actual ARX-model estimation; from $e_e(t - \hat{\tau}_e)$ and $e_v(t - \hat{\tau}_e)$ the signals $\tilde{e}_{e,s}(t)$ and $\tilde{e}_{v,s}(t)$, respectively, for simulation; from $u_{e,m}(t)$ the signal $\tilde{u}_e(t)$ for verification; and from $u_{v,m}(t)$ the signal $\tilde{u}_{v,v}(t)$ for validation.
- 6) *Estimation setup.* This includes the choice between OLS and RLS estimation. The latter requires specifications for $\hat{\theta}_0$, P_0 , and the forgetting strategy, i.e., λ or Λ .
- 7) *ARX-model estimation.* Estimate the ARX model \mathcal{M}_{ARX} . Note that here the structure is defined with integers n_a and n_b .
- 8) *Verification, validation, and optional revision.* Simulate using the ARX-model equations with zero initial output condition. Obtain the verification output $\hat{u}_{e,v}(t)$ and validation output $\hat{u}_{v,v}(t)$. Verify and validate \mathcal{M}_{ARX} using the variance accounted for metrics VAF_e and VAF_v , respectively. The VAF measures the quality of fit and requires the (preprocessed) measured output $\tilde{u}(t)$ and (preprocessed) simulated output $\hat{u}(t)$:

$$VAF = \max \left(0, \left(1 - \frac{\sum_{t=1}^N |\tilde{u}(t) - \hat{u}(t)|^2}{\sum_{t=1}^N |\tilde{u}(t)|^2} \right) \cdot 100\% \right) \quad (25)$$

If the VAF ratio VAF_e/VAF_v is larger than 1, overfit occurs [9]. If $VAF_e/VAF_v \gg 1$, it means that \mathcal{M}_{ARX} provides a high model quality on the estimation data, but it cannot be generalized to other data. The user should specify the acceptable range of VAF ratios, e.g., accept

a VAF ratio of 1.1 for all remnant intensities. A revision of \mathcal{M}_{ARX} is made possible by the following options.

- a) *Data decimation.* Return to Step 5 and select a decimation factor d , for convenience a power of two.
- b) *Estimation setup adjustment.* Return to Step 6, actually only applicable for RLS.
- c) *ARX-model setup adjustment.* Return to Step 2.

Example decimators include a downsampler, an ideal noncausal filter, or piecewise aggregate approximation. These decimators consider the first sample and then every d th sample of the input-output data. For a proper decimation, the first sample of a shifted input signal requires an offset of $\lceil n_k^*/d \rceil d - n_k^*$, i.e., an integer between 0 and $d-1$.

- 9) *ARX-model conversion.* Obtain the continuous-time HO model \mathcal{M}_{HO} by converting \mathcal{M}_{ARX} and n_k^* . Retrieve the HO-model parameters as described in Section III-C.

IV. METHOD

To study the functionality and feasibility of the recursive ARX-model identification method, a Monte Carlo simulation analysis with $M = 100$ replications is set up. The compensatory manual-control model in Fig. 1 is simulated for different conditions. In particular, the sensitivity to remnant is investigated. The simulations will run with $f_s = 100$ Hz. The measurement window is set to $T_m = 81.92$ s. The total recording time is set to a multiple of eight times T_m to reduce the effects of transients.

A. Target-Forcing Function

The compensatory manual-control system will be excited by the same target-forcing function as in [12]:

$$f_t(t) = \sum_{k=1}^{N_t} A_t(k) \sin[\omega_t(k)t + \phi_t(k)], \quad (26)$$

for which a sum of $N_t = 10$ sinusoids is considered. Table I lists the amplitude $A_t(k)$, excitation frequency $\omega_t(k)$, and phase shift $\phi_t(k)$ of the k th sinusoid. All $\omega_t(k)$ are integer multiples n_t of the measurement-base frequency

TABLE I
TARGET FORCING-FUNCTION PROPERTIES [12]

$k_t, -$	$n_t, -$	$\omega_t, \text{rad/s}$	A_t, deg	ϕ_t, rad
1	3	0.230	1.186	-0.753
2	5	0.384	1.121	1.564
3	8	0.614	0.991	0.588
4	13	0.997	0.756	-0.546
5	22	1.687	0.447	0.674
6	34	2.608	0.245	-1.724
7	53	4.065	0.123	-1.963
8	86	6.596	0.061	-2.189
9	139	10.661	0.036	0.875
10	229	17.564	0.025	0.604

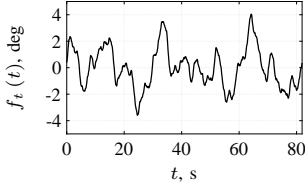


Fig. 5. Target forcing-function time trace.

$\omega_m = 2\pi/T_m = 0.0767 \text{ rad/s}$. Fig. 5 shows the time trace of $f_t(t)$. The amplitude distribution is varied and scaled to attain a variance of $\sigma_{f_t}^2 = 2.2490 \text{ deg}^2$ in T_m .

B. Parameter Variations and Conditions

Table II lists the two sets of parameter values that are considered for the CE dynamics and the assumed HO dynamics. These are based on experimental data. Bode plots of the corresponding states are shown in Fig. 6. State 1 mostly represents $1/s$ CE dynamics, while State 2 mostly represents $1/s^2$ dynamics in the frequency range 1–5 rad/s. For State 2, a strong increase in lead generation by the HO is observed, corresponding to the findings in [12].

TABLE II
CE AND HO PARAMETER VALUES FOR TWO STATES [12]

State	CE		HO					
	K_c	ω_b	K_e	T_L	K_e	τ_e	ω_{nm}	ζ_{nm}
	-	rad/s	-	s	s	s	rad/s	-
1	90	6	0.09	0.4	0.036	0.28	11.25	0.35
2	30	0.2	0.07	1.2	0.084			

Table III presents the six different conditions that will be simulated. The same conditions were also studied in [12]. Conditions C1 and C2 have constant dynamics and are associated with States 1 and 2, respectively. Such dynamics were also considered in [7], in which HO dynamics were successfully identified using batch ARX models. Conditions C1 and C2 could thus be used as reference conditions for the identification with recursive ARX models. Conditions C3–C6 include time-varying dynamics. Here, the sigmoid's t_M value is set around $T_m/2$. Both gradual and sudden transitions are considered from C1 to C2, and vice versa. The time variations introduced in the HO's equalization parameters are equivalent to the sigmoid function used to vary the CE dynamics. The parameter functions for these equalization parameters can be expanded with deterministic perturbations [13]. This will be

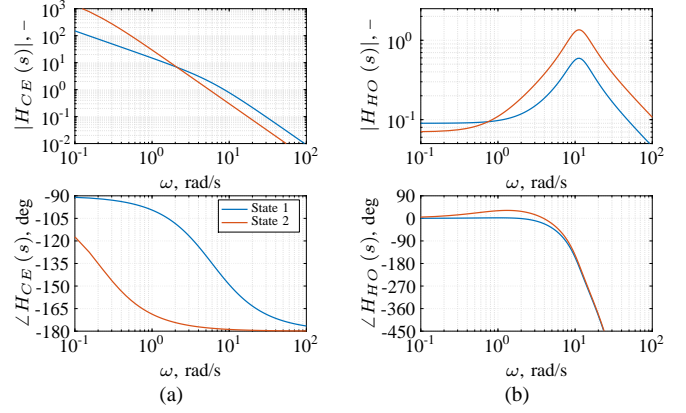


Fig. 6. Bode plots corresponding to the two states listed in Table II. (a) Set of CE dynamics. (b) Set of assumed HO dynamics.

more realistic than assuming that the HO's equalization parameters are prescribed by the same sigmoid function introduced for the variation in the CE parameters. This study, however, focuses on algorithm performance and the question is whether it could capture such transitions at all. Example remnant-free input-output measurement-time traces for conditions C3 and C4 are shown in Fig. 7. The gray line indicates the time instant t_M of the maximum transition rate G . Around t_M , small, but noticeable, differences between the two conditions can be seen.

TABLE III
CONDITIONS TO SIMULATE

Condition	$H_{CE}(s)$	G, s^{-1}
C1	$H_{CE,1}(s)$	n/a
C2	$H_{CE,2}(s)$	n/a
C3	$H_{CE,1}(s) \rightarrow H_{CE,2}(s)$	0.5
C4	$H_{CE,1}(s) \rightarrow H_{CE,2}(s)$	100
C5	$H_{CE,2}(s) \rightarrow H_{CE,1}(s)$	0.5
C6	$H_{CE,2}(s) \rightarrow H_{CE,1}(s)$	100

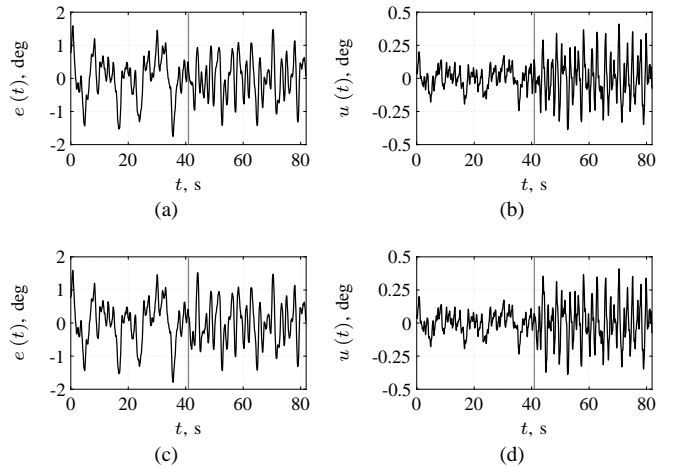


Fig. 7. Remnant-free input-output measurement-time traces. (a) and (b) Condition C3. (c) and (d) Condition C4.

ZOH equivalent parameter values for the two assumed HO models listed in Table II (without considering the delay) are presented in Table IV. These values are considered as the

TABLE IV
ARX-MODEL PARAMETER VALUES FOR ZOH DISCRETIZATION OF
ASSUMED HO DYNAMICS

T_s, s	States 1 and 2		State 1		State 2	
	a_1^0	a_2^0	b_0^0	b_1^0	b_0^0	b_1^0
0.01	-1.9121	0.9243	0.0443	-0.0432	0.1024	-0.1016

true ARX-model parameters $\theta^0 = [a_1^0 \ a_2^0 \ b_0^0 \ b_1^0]^T$. A range of these true parameters at each time instant is also obtainable for conditions C3–C6.

C. Remnant Model

In manual-control literature, there is no clear agreement on how HO remnant $n(t)$ should be represented [7], [8], [23]–[25]. Here, it is modeled as a zero-mean Gaussian white-noise signal $n_w(t)$, with unit variance, passed through a low-pass filter. The following m th-order remnant-filter structure is considered:

$$H_n^m(s, t) = \frac{K_n(t)}{(T_n s + 1)^m}, \quad (27)$$

where the remnant gain $K_n(t)$ could vary in time. The remnant-time constant T_n will be set equal to 0.06 s [26], resulting in a cutoff frequency of 16.67 rad/s. A key issue of ARX models is that the disturbance dynamics $\frac{1}{A(q)}$ are completely tied to the process dynamics $\frac{B(q)}{A(q)}$. Hence, the remnant characteristics cannot be parametrized independently and the estimation of the parameters in the linear HO dynamics becomes biased. This aspect was not fully investigated in [9] and [7]. Therefore, this study will check to what extent the ARX model constrains parametrization of the linear HO dynamics by examining different remnant filters. Integer orders of $m = 1, 2, 3,$ and 4 are tested. In addition, a special remnant filter, similar to $H_{nm}(s)$, is considered ($m = nm$), with the values of the neuromuscular parameters listed in Table II:

$$H_n^{nm}(s, t) = K_n(t) H_{nm}(s) \quad (28)$$

It is expected that the $H_n^{nm}(s, t)$ filter least constrains the estimation of the parameters in the process dynamics.

For the different $H_n^m(s, t)$, $K_n(t)$ can be set to induce remnant-intensity levels $P_n = \sigma_n^2 / \sigma_u^2$ in the measurement window. Seven levels of P_n are selected: 0.00 (i.e., no remnant), 0.05, 0.10, 0.15, 0.20, 0.25, and 0.30. By means of the nonlinear programming solver `fmincon` [27], a constant K_n is tuned for the constant dynamics conditions C1 and C2, based on 10 $n_w(t)$ realizations. For conditions C3–C6, $K_n(t)$ can then be varied according a sigmoid analogous to the HO equalization and CE parameters. After tuning K_n , another 110 independent $n_w(t)$ are generated. To simulate estimation data sets, 100 of these were used, and 10 were used to create validation data sets. So, different remnant signals $n(t)$ are obtained by filtering exactly the same realizations $n_w(t)$ through the different $H_{n,t}^m(s)$ for which only $K_n(t)$ varies. This allows the fairest comparison.

Fig. 8 shows an overview of the different types of constant $H_n^m(s)$ filters with different tuned K_n to induce a P_n of 0.15 for condition C1. Equivalent Bode plots can be obtained

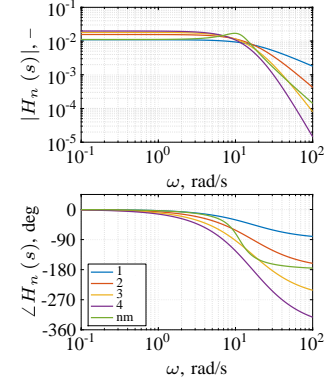


Fig. 8. Bode plots of the different remnant-filter models with different tuned K_n to induce a P_n of 0.15 for condition C1.

for other P_n and for condition C2. Over a wide frequency range, $H_n^1(s)$ has the lowest magnitude and $H_n^4(s)$ has the highest magnitude. The opposite can be seen at the highest frequencies. For all $H_n^m(s)$, the phase angle becomes more negative as the magnitude drops.

TABLE V
FORGETTING FACTORS TAKEN BASED ON N_0

$N_0, -$	$\lambda, -$	$N_0, -$	$\lambda, -$
2	0.5	256	0.99609
4	0.75	512	0.99805
8	0.875	1024	0.99902
16	0.9375	2048	0.99951
32	0.96875	4096	0.99976
64	0.98438	8192	0.99988
128	0.99219	∞	1

D. Estimation Setup

As shown in Figs. 2 and 7, if t_M is set around $T_m/2$, the initial and final 30.72 s of the measurement traces for conditions C3–C6 can be assumed to include only constant dynamics. In essence, if the dynamics to be identified are constant, the RLS algorithm will recursively approximate the OLS estimate. Therefore, in these particular regions ARX models can be estimated with OLS serving as a reference for the RLS estimation.

The main interest is concentrated on the recursive estimation in the transition region of 20.48 s around t_M (see again Fig. 2). The implementation with the scalar forgetting factor λ and the forgetting matrix Λ and corresponding results will be explored. All conditions listed in Table III will be assessed with a range of forgetting factors, that correspond to a matching range of memory horizons N_0 , of integer powers of two (see Table V). Also, the case of no-forgetting is considered, i.e., $\lambda = 1$ so $N_0 = \infty$. For each recursive estimation, the RLS algorithm will be initialized with $\hat{\theta}_0 = \hat{\theta}^{\text{OLS}}$ estimated on the initial 30.72 s, and with $P_0 = I$.

As can be interpreted from Table IV, the ARX model's output parameters $a_1(t)$ and $a_2(t)$ remain constant in all conditions with time-varying dynamics. These parameters are closely linked to the HO's neuromuscular parameters ω_{nm} and

ζ_{nm} which were not varied in the offline simulations. Therefore, $a_1(t)$ and $a_2(t)$ can be assumed to be time invariant throughout the whole estimation. On the contrary, the ARX model's input parameters $b_0(t)$ and $b_1(t)$ are not constant. These parameters are closely linked to the HO's equalization parameters $K_e(t)$ and $K_{\dot{e}}(t)$, which were varied according the same sigmoid function. Hence, the forgetting matrix can provide more accurate results as it is able to discount distinct information for each ARX-model parameter. The forgetting factors λ_{a_1} and λ_{a_2} in the forgetting matrix Λ will be set equal to 1, while the range of forgetting factors listed in Table V is tested for $\lambda_{b_0} = \lambda_{b_1}$.

E. Identification-Tuning Criteria

Prior to commencing the analysis of the recursive ARX-model estimation, the effects of the order of the remnant filter on the resulting estimation accuracy with the selected ARX-model structure, i.e., $n_a = n_b = 2$, is assessed for conditions C1 and C2 using batch ARX-model estimation. First, the estimation of n_k^* is compared to n_k^0 , i.e., the true integer value of 29 samples based on $\tau_e f_s$ plus a unit-sample delay from the ZOH discretization. The use of n_k^* can be justified by calculating the difference in validation data VAFs for n_k^0 and n_k^* :

$$\Delta \text{VAF}_v^{n_k^0} = \text{VAF}_v^{n_k^0} - \text{VAF}_v^{n_k^*} \quad (29)$$

If $\Delta \text{VAF}_v^{n_k^0}$ is close to zero, the model qualities are practically the same. Second, the batch ARX-model parameter estimates will be compared to the ZOH parameter values listed in Table IV. For this, the metric of relative bias B_r is used, which accounts for the sign of the bias:

$$B_r = \frac{\hat{\theta} - \theta_0}{\theta_0} \quad (30)$$

An objective metric to trade off the tracking ability and remnant-level sensitivity is introduced by calculating the difference between the validation data VAFs for $\lambda = 1$ (highest robustness against noise) and for $\lambda < 1$ for a range of λ (ability to capture time variations). The metrics for the scalar forgetting factor λ and forgetting matrix Λ implementation are defined as:

$$\Delta \text{VAF}_v^{\lambda=1} = \text{VAF}_v^{\lambda} - \text{VAF}_v^{\lambda=1} \quad (31)$$

$$\Delta \text{VAF}_v^{\Lambda=I} = \text{VAF}_v^{\Lambda} - \text{VAF}_v^{\Lambda=I} \quad (32)$$

As indicated in Section IV-D, the calculation of the above VAF metrics in the transition region are of particular importance.

V. RESULTS

A. Influence of Remnant-Filter Type and Delay Estimation

Fig. 9 shows, for condition C1, a box plot of the variable input-delay estimation n_k^* for the different types of $H_n^m(s)$ and intensity levels P_n , for $M = 100$ replications. For condition C2, equivalent results were obtained. In Fig. 9, the dotted gray line represents the true fixed integer delay n_k^0 of 29 samples. In the remnant-free case, i.e., $P_n = 0$, $n_k^* = n_k^0$ is indeed found. A clear distinction can be made between remnant-filter orders 1 and 2 that overestimate n_k^0 , and orders 3 and 4 that

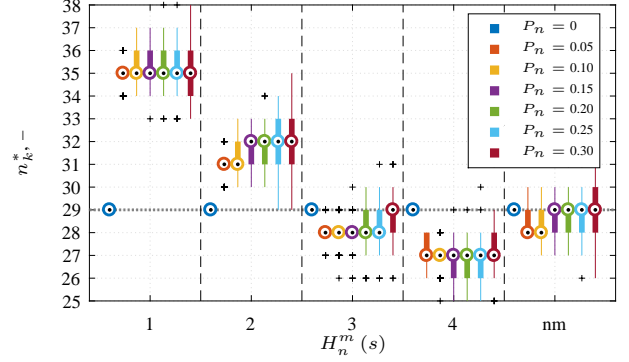


Fig. 9. Variable n_k^* estimation, for condition C1, for different $H_n^m(s)$.

underestimate n_k^0 . The n_k^* for the $H_n^{nm}(s)$ filter are centered around n_k^0 . Furthermore, it is apparent that the n_k^* for the $H_n^1(s)$ filter, deviate, on average, for all P_n , seven samples from n_k^0 . Focusing for a moment on the higher frequency range in the Bode phase-angle plots in Fig. 8, a clear trend can be seen with the results in Fig. 9. The ARX-model estimations on data simulated with the $H_{nm}(s)$ filter result in the best estimates of n_k^0 . An increase in delay is needed for the orders 1 and 2, while less delay is needed for the orders 3 and 4.

To further assess how the ARX-model estimates vary with the different remnant-filter types, it is important to look at the relative bias B_r . Fig. 10 shows, again for condition C1, box plots for all ARX-model parameters a_1 , a_2 , b_0 , and b_1 , estimated with the true delay integer n_k^0 and the variable delay integer n_k^* . Equivalent results were found for condition C2. The B_r of all parameters in the remnant-free case is zero. It stands out that the B_r in all parameters for $H_n^1(s)$ is more than ten times larger compared to the other $H_n^m(s)$. Similar to the results in Fig. 9, a clear difference can be seen between orders 1 and 2, and the other remnant-filter types. The output parameters a_1 and a_2 are overestimated for $H_n^1(s)$ and $H_n^2(s)$, while an underestimation of the input parameters b_0 and b_1 occurs. The opposite can be seen for the other $H_n^m(s)$. The lowest relative bias is seen for $H_n^{nm}(s)$. Except for $H_n^1(s)$, the difference between B_r when estimating with n_k^0 and n_k^* is negligible.

To gain a better understanding of the differences and commonalities between the considered remnant filters, Figs. 11(a) and (b) show, for conditions C1 and C2, Bode plots of the batch ARX models, estimated with the true integer delay n_k^0 , for a single remnant realization with $P_n = 0.15$. Equivalent Bode plots are obtained for the other P_n . Figs. 11(a) and (b) also provide Bode plots of the ZOH equivalent dynamics, for conditions C1 and C2, for the values listed in Table IV and n_k^0 . For both conditions, the batch ARX-model estimations on data sampled with $f_s = 100$ Hz and generated with $H_n^1(s)$ cannot provide a good description of the HO dynamics in frequency range of interest for manual control (0.2–18 rad/s). There is a large misfit at the high frequencies and the peak value is not even captured. The above results clearly express the ARX model's compromise between minimizing the bias in the parameters of the process dynamics and explaining the disturbance dynamics. In fact, this bias minimization is

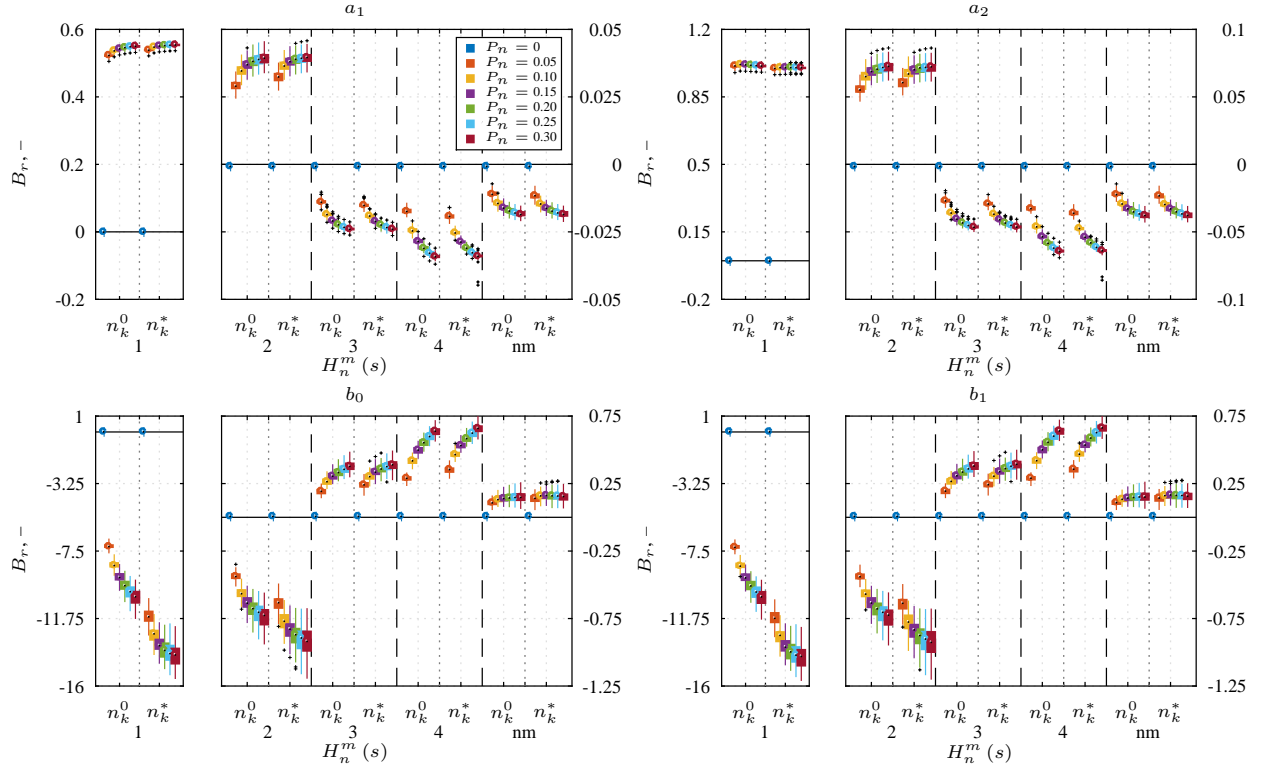


Fig. 10. Relative bias in the ARX-model parameters, for condition C1, for the different $H_n^m(s)$ when using n_k^0 and n_k^* .

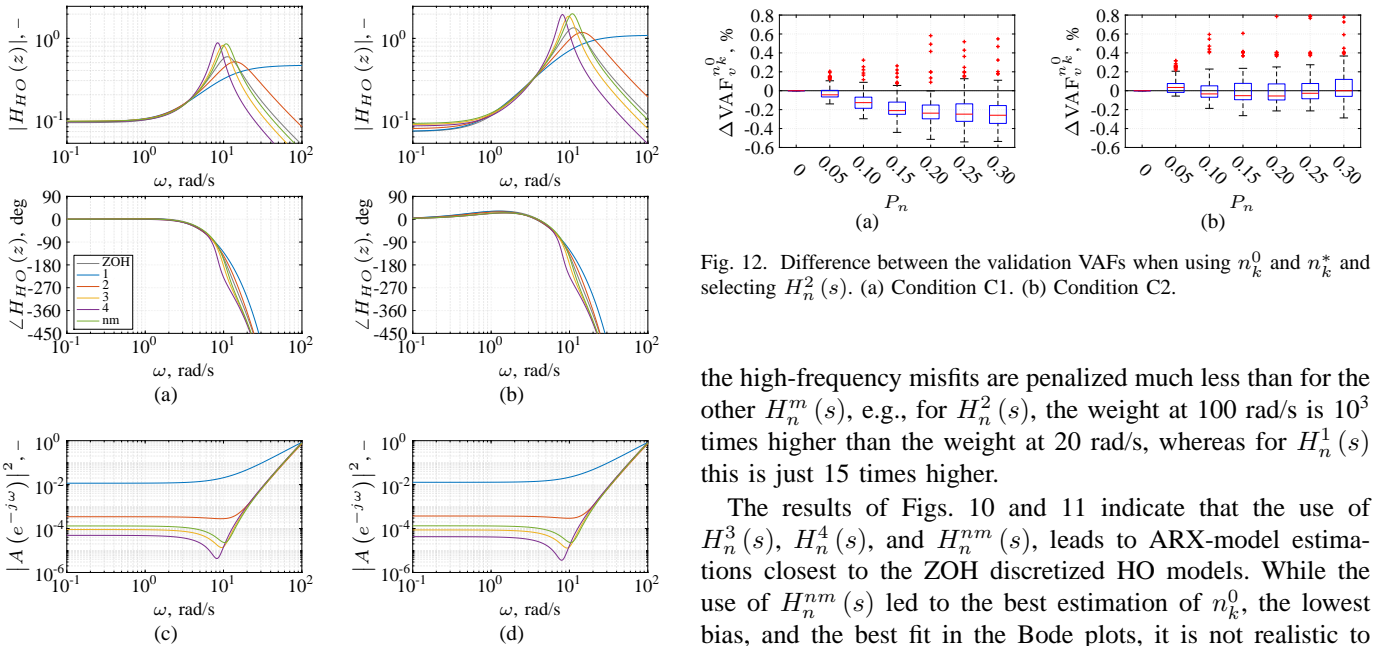


Fig. 11. Bode plots of the batch ARX-model estimations for different $H_n^m(s)$ for a single realization with $P_n = 0.15$ and using n_k^0 . (a) HO dynamics for condition C1. (b) HO dynamics for condition C2. (c) Weighting function for condition C1. (d) Weighting function for condition C2.

weighted with $|A(e^{-j\omega})|^2 = |1 + a_1 e^{-j\omega} + a_2 e^{-2j\omega}|^2$ [16]. Figs. 11(c) and (d) present Bode magnitude plots of the weighting functions, for conditions C1 and C2, in correspondence with the Bode plots of the HO dynamics. For $H_n^1(s)$,

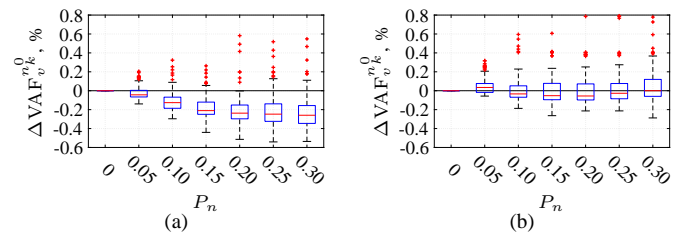


Fig. 12. Difference between the validation VAFs when using n_k^0 and n_k^* and selecting $H_n^2(s)$. (a) Condition C1. (b) Condition C2.

the high-frequency misfits are penalized much less than for the other $H_n^m(s)$, e.g., for $H_n^2(s)$, the weight at 100 rad/s is 10^3 times higher than the weight at 20 rad/s, whereas for $H_n^1(s)$ this is just 15 times higher.

The results of Figs. 10 and 11 indicate that the use of $H_n^3(s)$, $H_n^4(s)$, and $H_n^{nm}(s)$, leads to ARX-model estimations closest to the ZOH discretized HO models. While the use of $H_n^m(s)$ led to the best estimation of n_k^0 , the lowest bias, and the best fit in the Bode plots, it is not realistic to assume that the HO's remnant dynamics are equivalent to the HO's neuromuscular dynamics—these were only considered as a reference. The second and third best candidates serving as appropriate remnant models for the further analysis are then $H_n^3(s)$ and $H_n^4(s)$. However, to better assess the potential feasibility of the ARX-model estimation, the further analysis will be based on the second-order remnant filter $H_n^2(s)$. The use of this filter is considered as the compromise limit between bias in the ARX-model parameters and the fitting of the remnant by the ARX model.

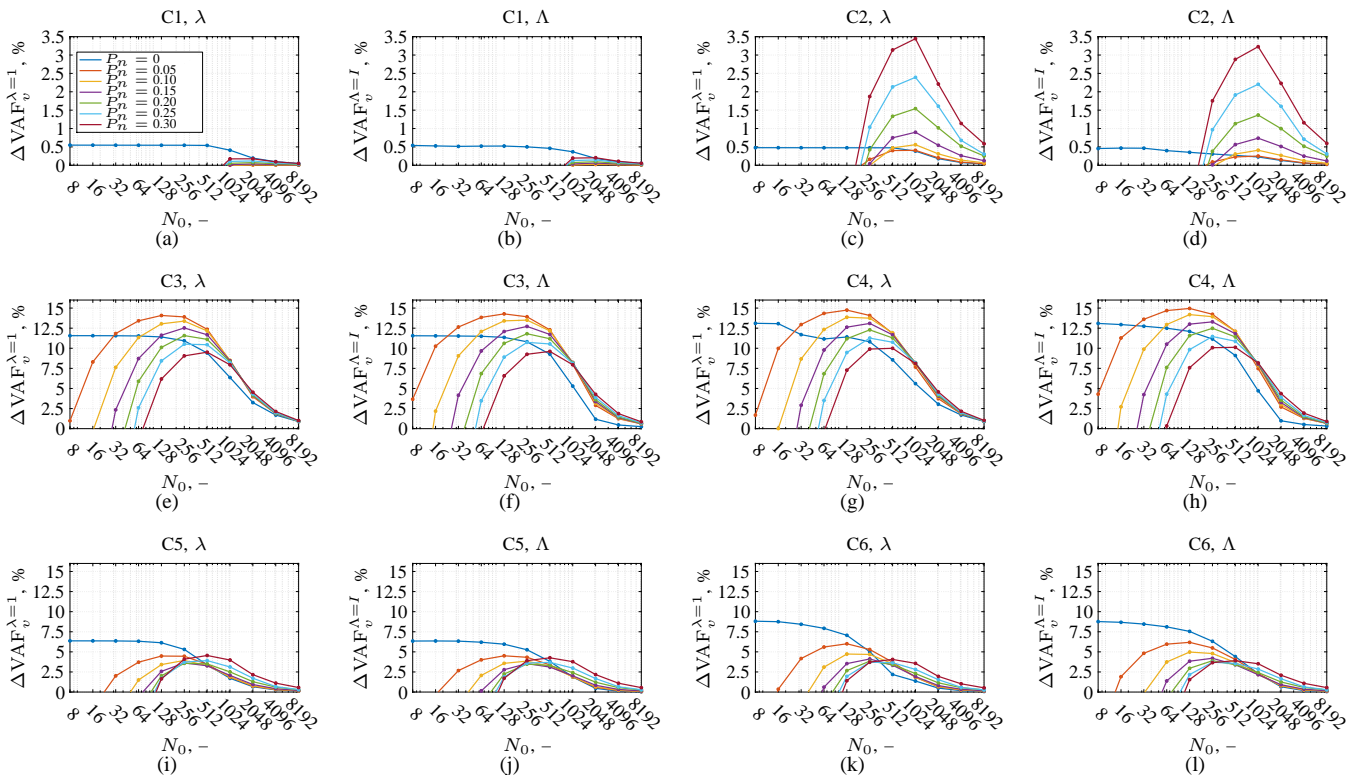


Fig. 13. Overview for all conditions to trade off between tracking ability and noise sensitivity for the two forgetting strategies λ and Λ , with P_n ranging between 0 and 0.30 in increments of 0.05. (a) to (d) Conditions with constant dynamics. (e) to (l) Conditions with time-varying dynamics.

To give a final justification of using n_k^* and the selection of $H_n^2(s)$, Fig. 12 shows box plots of the metric $\Delta\text{VAF}_v^{n_k^0}$, for conditions C1 and C2. These results indicate that negligible differences in model quality are obtained when using n_k^* compared to n_k^0 , for all remnant intensities P_n .

B. Forgetting-Factor Tuning

This section includes the results of recursive ARX-model estimation. Fig. 13 visualizes, for all conditions listed in Table III and tested remnant intensities P_n , the calculations of the metrics defined in (31) and (32), based on 1000 simulations. Data for the scalar forgetting factor λ and the forgetting matrix Λ are shown side by side. The validation data VAFs are calculated on the transition region window of 20.48 s around t_M . For both implementations, the range of memory horizons N_0 listed in Table V are compared with the case of no-forgetting, i.e., $\lambda = 1$ and $\Lambda = I$. What stands out in Fig. 13 is that no significant differences can be seen between the two different forgetting-factor implementations. Apparently, the quality of fit in the transition region data is not improved by changing the forgetting strategy. More interesting, per P_n and condition, an optimal N_0 can be observed from Fig. 13. Data with lower P_n require the selection of lower N_0 . In particular, this can be seen for the remnant-free cases. Higher forgetting factors for the constant dynamics conditions C1 and C2 should be selected, as the corresponding data are less variable compared to the data of the conditions with time-varying dynamics. For the different P_n , the values of $\Delta\text{VAF}_v^{\lambda=1}$ and $\Delta\text{VAF}_v^{\Lambda=I}$ differ more for

condition C2 compared to condition C1. The variability in the data increases more with higher P_n for condition C2 than for condition C1. Furthermore, a comparison between conditions C3 and C4 (i.e., $1/s \rightarrow 1/s^2$) and conditions C5 and C6 (i.e., $1/s^2 \rightarrow 1/s$) reveals that differences between no-forgetting and forgetting are notably smaller for the latter. In conditions C5 and C6, the estimations are influenced more by the data based on $1/s^2$ dynamics than $1/s$ dynamics. Hence, the effect of variability in the data is flattened. Overall, the one-optimal forgetting factor, for all conditions, for this data, is observed for $N_0 = 256$ samples, i.e., $\lambda = 0.99609$. So, for data sampled with $f_s = 100$ Hz, the RLS algorithm requires 2.56 s to come up with accurate parameter estimates.

While Fig. 13 did not show significant differences between the implementation of the scalar λ and the matrix Λ , the matching recursive estimates of $a_1(t)$, $a_2(t)$, $b_0(t)$, and $b_1(t)$ show that there is in fact a benefit of making use of Λ . Fig. 14 shows in black the time evolutions of the recursive ARX-model parameters for condition C4, based on the 100 different estimation data sets, for a scalar forgetting factor λ and for a forgetting matrix Λ . The results for three different remnant-intensity levels are shown, i.e., $P_n = 0$ (no remnant), 0.15 and 0.30. A similar pattern was observed for P_n between 0.05 and 0.30. For $P_n = 0.15$ and 0.30, standard deviations are included. The red lines in Fig. 14 represent the true ZOH parameter values. The green lines, at the beginning and the end, indicate batch ARX-model estimations (mean and standard deviations). The gray lines indicate the sigmoid's instant t_M . For all P_n , the black lines clearly show that

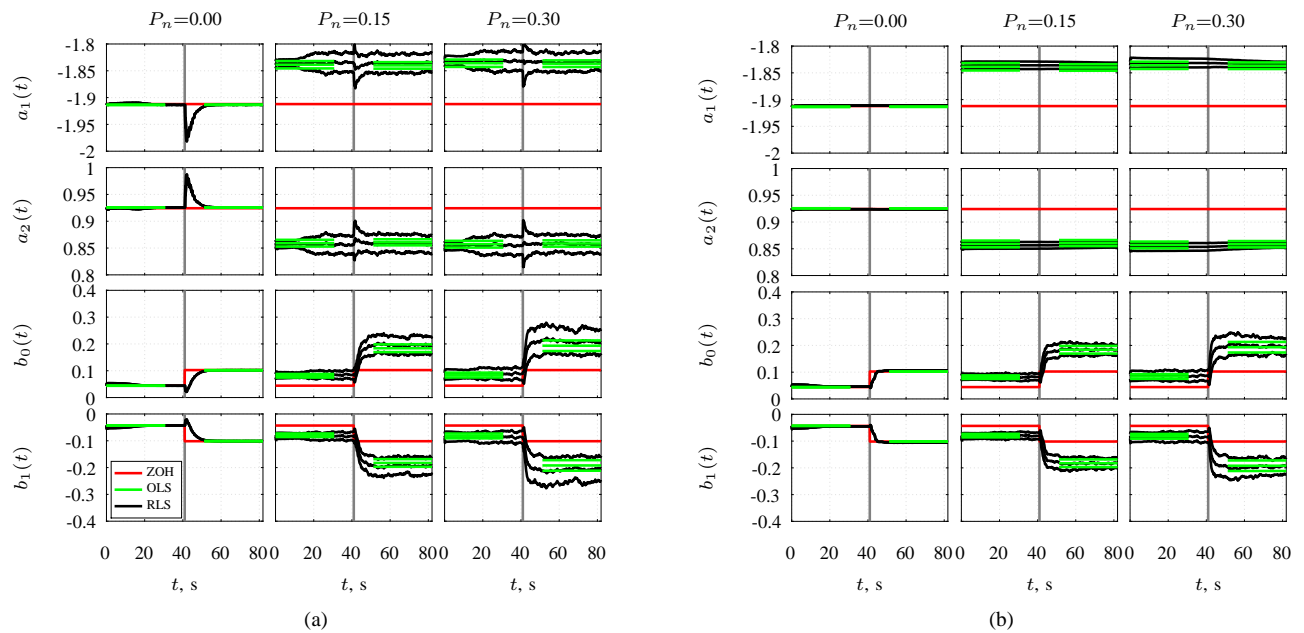


Fig. 14. ARX-model parameters for condition C4 for three different P_n . (a) λ with $N_0 = 256$. (b) Λ with $N_0^{a_1, a_2} = \infty$ and $N_0^{b_0, b_1} = 256$.

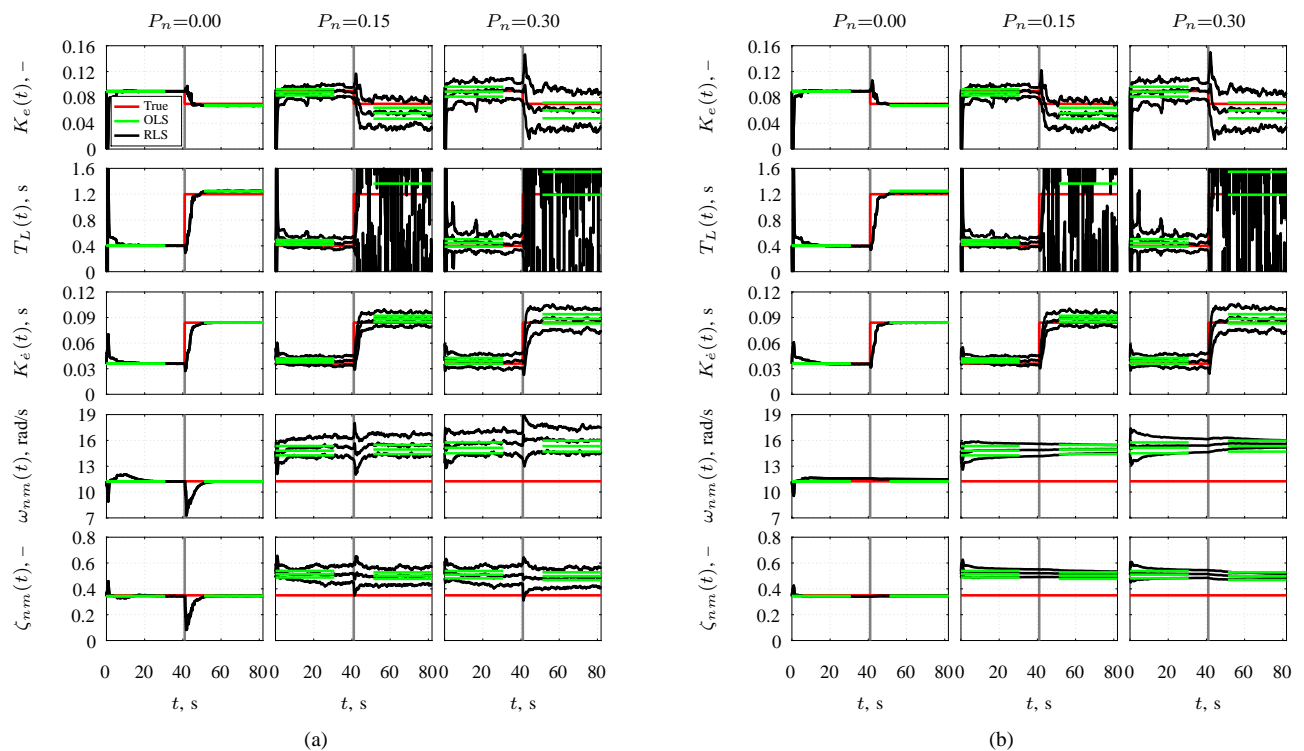


Fig. 15. HO-model parameters for condition C4 for three different P_n . (a) λ with $N_0 = 256$. (b) Λ with $N_0^{a_1, a_2} = \infty$ and $N_0^{b_0, b_1} = 256$.

$a_1(t)$ and $b_0(t)$ are negatively correlated with $a_2(t)$ and $b_1(t)$, respectively. In accordance with the results shown in Section V-A, for $P_n > 0$, a high bias with respect to the true parameters is obtained for both the batch and recursive ARX models as the simulation was set up with $H_n^2(s, t)$. For $P_n = 0$, it can be noted that $N_0 = 256$ samples is not the best choice. In this case, the estimation is not driven by remnant

and the tracking ability can be increased by decreasing N_0 . From Fig. 14(b), a significant reduction in the variability of the ARX-models parameters is observed for all P_n . This becomes clear, in particular, when looking at the ARX-model output parameters. Better fits are obtained by using the matrix Λ .

Turning now to \mathcal{M}_{HO} by converting \mathcal{M}_{ARX} with integers $n_a = n_b = 2$, the HO parameters can be retrieved using (23).

Only instants of \mathcal{M}_{ARX} with pairs of complex-conjugate poles are considered. In accordance with Fig. 14, Fig. 15 is presented for condition C4 for both forgetting-factor implementations. The black lines represent the HO parameters based on the recursive ARX models, and the green lines at the beginning and end are based on batch ARX-model estimations. Standard deviations are included for $P_n = 0.15$ and 0.30 . The red lines are the true HO parameters, of which the equalization parameters vary according the sigmoid function. The gray lines represent t_M . Similar patterns as in Fig. 14 can be seen in Fig. 15 for the two different forgetting-factor implementations. While for $K_e(t)$ and $K_\epsilon(t)$ acceptable estimation results are obtained, the estimation of $T_L(t)$ is seen to be problematic in the $1/s^2$ dynamics region. This can be explained by examining the definition of $T_L(t)$ in (23) and drawing the analogy with the negative correlation between the ARX-model parameters $b_0(t)$ and $b_1(t)$. If the continuous-time coefficient $b_1^c(t)$ increases, $b_0^c(t)$ decreases, and vice versa. The variability in the data related to $1/s^2$ dynamics increases, hence the negative correlation effect is stronger. Therefore, no stable estimates for $T_L(t)$ are obtained. High deviations from the true values are observed in $\hat{\omega}_{nm}$ and $\hat{\zeta}_{nm}$. This clearly demonstrates that the ARX model not only captures the dynamics of the system but also those of the remnant filter $H_n^2(s, t)$. Both $\omega_{nm}(t)$ and $\zeta_{nm}(t)$ are overestimated.

VI. EXPERIMENTAL EVALUATION

A. Method

An experiment was conducted in the SIMONA Research Simulator at Delft University of Technology, in fixed-base setting. Three subjects, with an average age of 24 years, performed the single-axis compensatory manual-control task (see Fig. 1) for all the conditions listed in Table III. In each condition seven runs were performed. The length of the runs was set to 90.00 s. A measurement time T_m of 81.92 s was used for the identification. The maximum rate of transition t_M in conditions C3–C6 was set at 42.93 s in the measurement window (i.e., at 50.00 s in the recording window). For the actual identification, only the five last runs were considered.

The ARX-model identification approach, as outlined in Fig. 4, was adopted. Input-output data were recorded with $f_s = 100$ Hz, and $f_t(t)$ was set up with the properties listed in Table I. Similar to the Monte Carlo analysis, the ARX-model structure was set to $n_a = n_b = 2$. Visual delay was assumed to be constant and estimated using n_k^* . Batch ARX models were fit on the initial and final 30.72 s of the measurement window. The recursive ARX-model estimations were initialized with the initial $\hat{\theta}^{\text{OLS}}$ and P_0 set to I . In accordance with the results from the Monte Carlo analysis in Section V, N_0 was set to 256 samples. Both the scalar forgetting factor λ and the forgetting matrix Λ (with $\lambda_{a_1} = \lambda_{a_2} = 1$) were considered.

B. Results

Example identification results are presented for condition C4, for all three subjects. Equivalent results are obtained for the other conditions. Condition C4 is taken as this allows a comparison with the results of Monte Carlo simulation

analysis in Section V. In accordance with Figs. 14 and 15, Figs. 16 and 17 are presented, respectively. The latter two figures include ensemble averages based on batch and recursive ARX-model estimation. These batch ARX-model estimates fit on the initial and final 30.72 s are indicated with thick green lines, and these recursive ARX-model estimates are shown with thick black lines. The sigmoid's instant t_M is indicated with the gray line. Both Figs. 16 and 17 also include the five recursive single-run ARX-model estimates (thin colored lines). No extreme outliers are observed in these single-run estimates.

In addition to these results, Table VI lists the average performance scores for each subject in different time windows. The scores include the root-mean-square of the error signal $\text{rms}_e(t)$, the tracking score defined by $\sigma_e^2(t)/\sigma_{f_t}^2(t)$, and the control activity expressed as the variance of the control signal $\sigma_u^2(t)$. Four time windows are considered: the measurement window T_m , the initial region of 30.72 s (ini), the transition region of 20.48 s (tran), and the final region of 30.72 s (fin). The results clarify that all subjects executed a different control strategy. On average Subject 1 has the highest scores for $\text{rms}_e(t)$ and $\sigma_e^2(t)/\sigma_{f_t}^2(t)$, and it has a low control activity. On contrary, Subject 3 has the lowest scores for $\text{rms}_e(t)$ and $\sigma_e^2(t)/\sigma_{f_t}^2(t)$, and it has a higher control activity. The highest control activity is observed for Subject 2. All subjects have more difficulty in controlling the $1/s^2$ dynamics.

The ARX-model identification results in Fig. 16 show that Subject 3 strongly adapts to the step transition in the CE dynamics. In particular, this becomes clear when focusing on the evolution of $b_0(t)$, and $b_1(t)$. Such strong adaptations are not seen in the results for Subjects 1 and 2. In all cases, the ensemble averages of the recursive ARX-model estimates approach the initial and final ensemble averages of the batch ARX-model estimates. Furthermore, a comparison between the initial and final batch ARX-model estimates and the recursive ARX-model estimates in the transition region gives an indication if some ARX-model parameters have distinct rates of changes, and if the use of the forgetting matrix Λ is reasonable. For Subject 3, a low variability in $a_1(t)$ and $a_2(t)$ is seen. Hence, there seems to be a justification in using Λ .

The matching conversion of the ARX-model parameters to HO-model parameters is presented in Fig. 17. Focusing on the evolutions of $K_e(t)$, a generation of lead is seen for Subjects 2 and 3. This is not the case for Subject 1. Furthermore, it can be noted that the values of $\omega_{nm}(t)$ for Subject 1 remain low compared with Subjects 2 and 3. It is questionable whether the selected ARX-model structure $n_a = n_b = 2$ is appropriate for Subject 1. Similar as observed in the Monte Carlo simulation analysis, the estimation of $T_L(t)$ is problematic in the region with $1/s^2$ dynamics. However, clear patterns are observed in the evolution of $K_e(t)$ and $K_\epsilon(t)$. In general, the results are consistent with the findings in Section V.

VII. DISCUSSION

An identification method based on recursive ARX models is described that requires the user to specify the orders of the ARX model and to set up a forgetting strategy. The orders are defined using the integers n_a and n_b , and the sum of these

TABLE VI
AVERAGE PERFORMANCE SCORES FOR FIVE RUNS

	rms _e (t)				$\sigma_e^2(t)/\sigma_{f_t}^2(t)$				$\sigma_u^2(t)$			
	T_m	ini	tran	fi	T_m	ini	tran	fi	T_m	ini	tran	fi
Subject 1	1.037	0.978	0.900	1.159	0.420	0.310	0.293	0.458	0.009	0.005	0.006	0.016
Subject 2	0.944	0.640	0.920	1.180	0.373	0.151	0.350	0.499	0.037	0.027	0.037	0.048
Subject 3	0.774	0.622	0.817	0.871	0.259	0.142	0.284	0.286	0.022	0.018	0.021	0.026

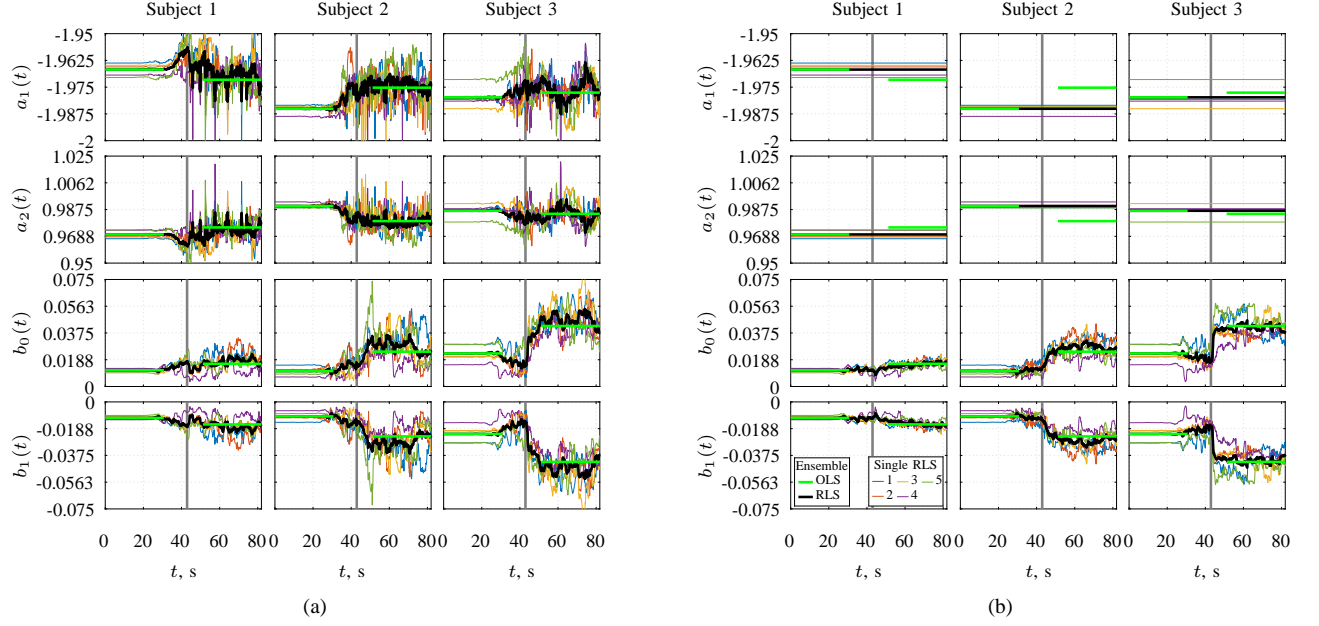


Fig. 16. ARX-model parameters for condition C4 for three different subjects. (a) λ with $N_0 = 256$. (b) Λ with $N_0^{a_1, a_2} = \infty$ and $N_0^{b_0, b_1} = 256$.

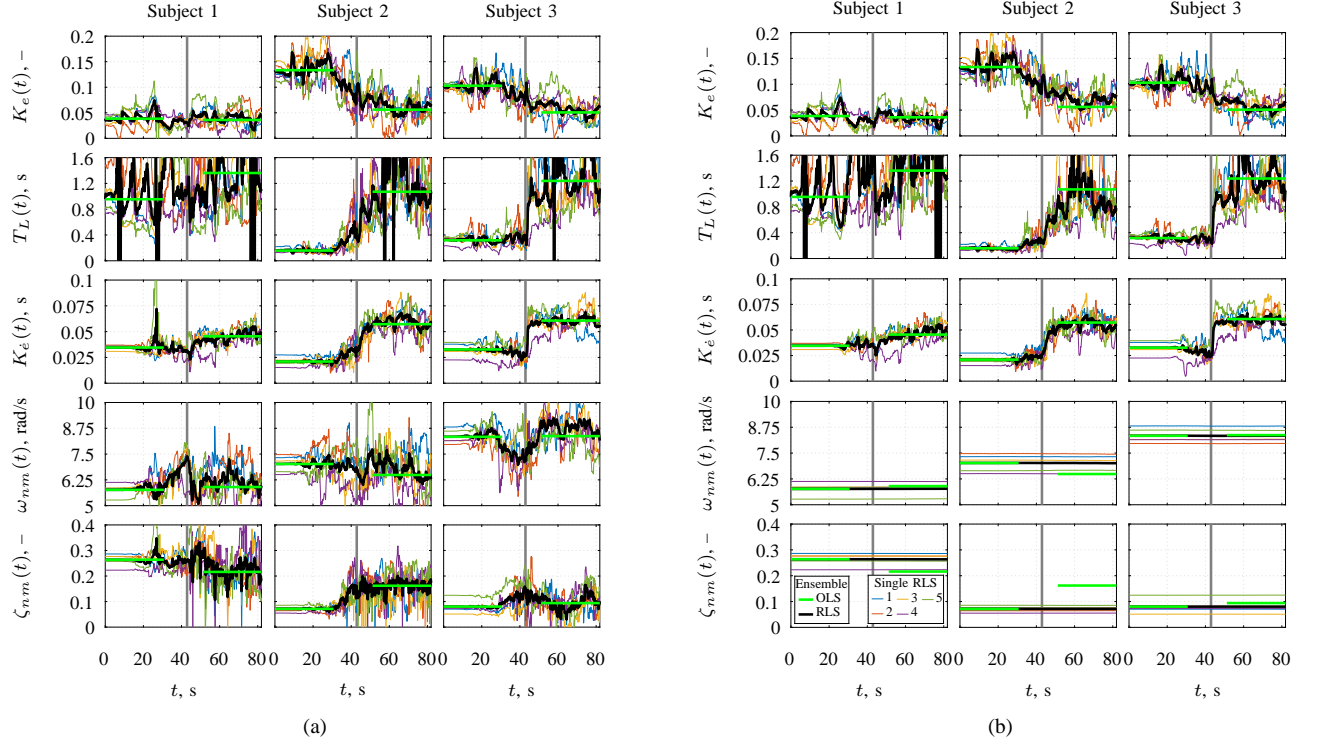


Fig. 17. HO-model parameters for condition C4 for three different subjects. (a) λ with $N_0 = 256$. (b) Λ with $N_0^{a_1, a_2} = \infty$ and $N_0^{b_0, b_1} = 256$.

integers sets the number of parameters to be estimated. The choice of the forgetting strategy in the recursive parameter estimation affects the trade-off between tracking ability and noise sensitivity. This study considered the implementation of a constant scalar forgetting factor λ , and a constant forgetting matrix Λ comprising forgetting factors for each parameter. Through testing on simulation data, an understanding is gained of the identification method's capability to quantitatively describe time-varying compensatory manual-control adaptation if the operator is faced with transitions in the CE dynamics matching Zaal's experiment [12].

Assuming that the considered HO model, consisting of a visual gain, a lead term, a delay and neuromuscular dynamics, is the suitable representation for the control of second-order CE dynamics, the results indicate that ARX models can only be used, directly, if the remnant dynamics are sufficiently similar to the (second-order) neuromuscular dynamics. The results presented in this paper show that the bias in the HO parameters becomes very high if the remnant is first-order low-pass filtered Gaussian white noise. Therefore, direct ARX-model estimation on measured input-output data cannot be used to identify the specific type of HO model if the remnant dynamics characterizes to first order. However, it was found that the remnant dynamics of orders 2, 3 or 4 are suitable.

For manual-control tasks, where the HO is better represented by for example an extra lead or lag term, the ARX model defined by the integers n_a and n_b can be easily adapted [19]. Furthermore, it is straightforward to convert the resulting ARX model to the (easier to interpret) HO-model parameters. The computational burden increases, however, if the conversion relationship is applicable, e.g., if extra ARX-model parameters are added to capture delay as a fraction. Then, model-order reduction approximations should be carried out, or nonlinear optimization problems should be solved to retrieve the physical HO-model parameters.

This study demonstrated, by means of simulated estimation and validation data, a tuning procedure for an optimal forgetting strategy for different conditions and different remnant intensities. These findings are not trivial given the high levels of remnant present in manual-control data. On average, for data sampled with 100 Hz, it can be said that the use of the scalar forgetting factor $\lambda = 0.99609$, corresponding to a memory horizon of 256 samples, is a satisfactory point of departure for the identification of time-varying compensatory manual-control behavior. In general, higher levels of remnant are present in single experimental runs. It means that for this application the value of λ should be increased. For ensemble-averaged experimental runs, the remnant levels will alleviate, so lower values of λ can be taken.

In addition to the constant scalar forgetting factor λ , the constant forgetting matrix Λ was considered as forgetting strategy for capturing time-varying compensatory manual-control behavior. It was found that the use of a forgetting matrix did not increase the model quality. However, the variance in the parameter estimates over time will notably lower. The use of a constant forgetting matrix should be considered, only if there is a strong evidence that HO parameters vary with different temporal scales, or certain parameters are constant.

To further improve the obtained results, further research could concentrate on time-varying forgetting strategies [16], [28]. Instead of using a constant forgetting strategy, time variations in the forgetting factors can be introduced to locally adapt the forgetting profile. This means that the scalar forgetting factor turns into a vector of forgetting factors. Instead of a constant forgetting matrix, a time-varying forgetting matrix can be used. This can be very useful for identification purposes, if the remnant levels vary during a measurement run.

The ARX-model delay estimation method based on the loss function of the one-step-ahead prediction seems to be useful. However, a drawback of the current identification approach is that it does not work for capturing time-varying delay. This issue can be circumvented by means of a sliding window approach, and by updating the input entries of the regression vector $\varphi(t)$ at different time instants. In essence, this results in a switched regression problem, which can be approached by means of piecewise ARX models [29].

Further investigations are needed to explore whether the recursive ARX-model identification method is also capable to detect time-varying manual-control adaptation due to changes in other task variables. The properties of the forcing function can be altered over time, e.g., to represent different command inputs to the HO or time-varying disturbances on the CE dynamics [2]. In [7] and [9], batch ARX-model identification was also used to determine the operator's vestibular motion and feedforward responses, respectively. Future work is needed to determine if the recursive ARX-model identification method is also able to capture, in addition to the visual response, these two multimodal characteristics of manual-control behavior.

The identification method is computationally efficient. Therefore, online implementation of the proposed approach is relatively straightforward. Furthermore, an experimental evaluation of real manual-control data indicates that the identification method is ready to use in future laboratory-control experiments.

VIII. CONCLUSION

A recursive ARX-model identification method was developed that is able to capture time-varying CE adaptation of the HO in compensatory tracking tasks. The method is practical since no stringent assumptions are required on how manual-control behavior will vary over time. A procedure was shown for the determination of the optimal forgetting factor for different conditions and different remnant intensities. For the considered application, the advice is to select a forgetting factor λ of 0.99609, if input-output data is sampled with 100 Hz. A Monte Carlo simulation analysis with remnant intensities of up to 30% shows that the method is then accurate in tracking time variations in adaptive manual-control behavior. The λ value can be slightly decreased for lower remnant intensities. If parameters have distinct rates of variations, the variance in parameter estimates can be lowered by using a forgetting matrix Λ with different forgetting factors.

As was shown by the experimental evaluation, the method has potential to become a novel cybernetic tool for further HO characterization and understanding. In the field of scientific studies of time-varying HO behavior, it may lead to

better investigations of how human respond, make decisions, and perceive the environment. The method could also serve as building block for the improvement of adaptive human-machine systems in practically all social-technical domains. Key applications include HO monitoring and adaptive support systems.

REFERENCES

- [1] M. Mulder, P. M. T. Zaal, D. M. Pool, H. J. Damveld, and M. M. van Paassen, "A cybernetic approach to assess simulator fidelity: Looking back and looking forward," in *AIAA Modeling and Simulation Technologies Conference*, ser. Guidance, Navigation, and Control and Co-located Conferences, no. AIAA 2013-5225, Boston, MA, 2013.
- [2] L. R. Young, "On adaptive manual control," *Ergonomics*, vol. 12, no. 4, pp. 635–674, 1969.
- [3] R. A. Hess, "Modeling pilot control behavior with sudden changes in vehicle dynamics," *Journal of Aircraft*, vol. 46, no. 5, pp. 1584–1592, 2009.
- [4] —, "Modeling human pilot adaptation to flight control anomalies and changing task demands," *Journal of Guidance, Control, and Dynamics*, vol. 39, no. 5, pp. 655–666, 2016.
- [5] M. Mulder, D. M. Pool, D. A. Abbink, E. R. Boer, and M. M. van Paassen, "Fundamental issues in manual control cybernetics," *IFAC-PapersOnLine*, vol. 49, no. 19, pp. 1–6, 2016, 13th IFAC Symposium on Analysis, Design, and Evaluation of Human-Machine Systems, Kyoto, Japan.
- [6] D. T. McRuer and H. R. Jex, "A review of quasi-linear pilot models," *IEEE Transactions on Human Factors in Electronics*, vol. HFE-8, no. 3, pp. 231–249, 1967.
- [7] F. M. Nieuwenhuizen, P. M. T. Zaal, M. Mulder, M. M. van Paassen, and J. A. Mulder, "Modeling human multichannel perception and control using linear time-invariant models," *Journal of Guidance, Control, and Dynamics*, vol. 31, no. 4, pp. 999–1013, 2008.
- [8] P. M. T. Zaal, D. M. Pool, Q. P. Chu, M. Mulder, M. M. van Paassen, and J. A. Mulder, "Modeling human multimodal perception and control using genetic maximum likelihood estimation," *Journal of Guidance, Control, and Dynamics*, vol. 32, no. 4, pp. 1089–1099, 2009.
- [9] F. M. Drop, D. M. Pool, M. M. van Paassen, M. Mulder, and H. H. Bühlhoff, "Objective model selection for identifying the human feedforward response in manual control," *IEEE Transactions on Cybernetics*, 2016, advance online publication.
- [10] P. M. Thompson, D. H. Klyde, and M. J. Brenner, "Wavelet-based time-varying human operator models," in *AIAA Atmospheric Flight Mechanics Conference and Exhibit*, ser. Guidance, Navigation, and Control and Co-located Conferences, no. AIAA 2001-4009, Montreal, Canada, 2001.
- [11] P. M. T. Zaal and B. T. Sweet, "Estimation of time-varying pilot model parameters," in *AIAA Modeling and Simulation Technologies Conference*, ser. Guidance, Navigation, and Control and Co-located Conferences, no. AIAA 2011-6474, Portland, OR, 2011.
- [12] P. M. T. Zaal, "Manual control adaptation to changing vehicle dynamics in roll-pitch control tasks," *Journal of Guidance, Control, and Dynamics*, vol. 39, no. 5, pp. 1046–1058, 2016.
- [13] R. F. M. Duarte, D. M. Pool, M. M. van Paassen, and M. Mulder, "Experimental scheduling functions for global LPV human controller modeling," 2017, in press.
- [14] M. Olivari, J. Venrooij, F. M. Nieuwenhuizen, L. Pollini, and H. H. Bühlhoff, "Identifying time-varying pilot responses: a regularized recursive least-squares algorithm," in *AIAA Modeling and Simulation Technologies Conference*, ser. AIAA SciTech Forum, no. AIAA 2016-1182, San Diego, CA, 2016.
- [15] D. T. McRuer, D. Graham, and E. S. Krendel, "Manual control of single-loop systems: Part I & II," *Journal of the Franklin Institute*, vol. 283, no. 1;2, pp. 1–29;145–168, 1967.
- [16] L. Ljung, *System Identification: Theory for the User*, 2nd ed. Upper Saddle River, NJ: Prentice Hall PTR, 1999.
- [17] R. Kulhavý and M. B. Zarrop, "On a general concept of forgetting," *International Journal of Control*, vol. 58, no. 4, pp. 905–924, 1993.
- [18] S. Sælid, O. Egeland, and B. A. Foss, "A solution to the blow-up problem in adaptive controllers," *Modeling, Identification and Control*, vol. 6, no. 1, pp. 39–56, 1985.
- [19] R. A. Hess and M. A. Mnich, "Identification of pilot-vehicle dynamics from in-flight tracking data," *Journal of Guidance, Control, and Dynamics*, vol. 9, no. 4, pp. 433–440, 1986.
- [20] E. R. Boer and R. V. Kenyon, "Estimation of time-varying delay time in nonstationary linear systems: an approach to monitor human operator adaptation in manual tracking tasks," *IEEE Transactions on Systems, Man and Cybernetics, Part A: Systems and Humans*, vol. 28, no. 1, pp. 89–99, 1998.
- [21] F. M. Drop, D. M. Pool, M. Mulder, and H. H. Bühlhoff, "Constraints in identification of multi-loop feedforward human control models," *IFAC-PapersOnLine*, vol. 49, no. 19, pp. 7–12, 2016, 13th IFAC Symposium on Analysis, Design, and Evaluation of Human-Machine Systems, Kyoto, Japan.
- [22] M. M. van Paassen and M. Mulder, "Identification of human operator control behaviour in multiple-loop tracking tasks," in *Analysis, Design and Evaluation of Man-Machine Systems*, K. Inoue and S. Nishida, Eds. Pergamon Press, Oxford, England, 1998, pp. 515–520, 7th IFAC/IFIP/IFORS/IEA Symposium, Kyoto, Japan.
- [23] M. Lone and A. Cooke, "Review of pilot models used in aircraft flight dynamics," *Aerospace Science and Technology*, vol. 34, pp. 55–74, 2014.
- [24] W. H. Levison, S. Baron, and D. L. Kleinman, "A model for human controller remnant," *IEEE Transactions on Man-Machine Systems*, vol. 10, no. 4, pp. 101–108, 1969.
- [25] L. D. Metz, "A time-varying approach to the modeling of human control remnant," *IEEE Transactions on Systems, Man and Cybernetics*, vol. 12, no. 1, pp. 24–35, 1982.
- [26] D. M. Pool, A. R. Valente Pais, A. M. de Vroome, M. M. van Paassen, and M. Mulder, "Identification of nonlinear motion perception dynamics using time-domain pilot modeling," *Journal of Guidance, Control, and Dynamics*, vol. 35, no. 3, pp. 749–763, 2012.
- [27] The MathWorks, Inc., *Optimization Toolbox™ User's Guide*, 2016, R2016b. [Online]. Available: https://mathworks.com/help/releases/R2016b/pdf_doc/optim/optim_tb.pdf
- [28] T. R. Fortescue, L. S. Kershenbaum, and B. E. Ydstie, "Implementation of self-tuning regulators with variable forgetting factors," *Automatica*, vol. 17, no. 6, pp. 831–835, 1981.
- [29] H. Ohlsson and L. Ljung, "Identification of switched linear regression models using sum-of-norms regularization," *Automatica*, vol. 49, no. 4, pp. 1045–1050, 2013.

NOMENCLATURE

Greek Symbols

δ	Positive constant.
$\epsilon(t)$	White noise, deg.
$\varepsilon(t)$	Prediction error, deg.
ζ_{nm}	Neuromuscular damping ratio.
θ	Parameter vector.
$\hat{\theta}_0$	Initial parameter estimate.
Λ	Forgetting matrix.
λ	Forgetting factor (scalar).
σ^2	Standard deviation.
τ_e	Visual time delay, s.
Φ	Regression matrix.
ϕ_t	Sinusoid phase shift, rad.
$\varphi(t)$	Regression vector.
ω	Frequency, rad/s.
$\omega_b(t)$	Break frequency, rad/s.
ω_t	Sinusoid frequency, rad.
ω_m	Measurement-base frequency, rad/s.
ω_{nm}	Neuromuscular frequency, rad/s.

Latin Symbols

$A(q)$	ARX model's output polynomial
A_t	Sinusoid amplitude, deg.
a_i	Coefficient i of $A(q)$.
$B(q)$	ARX model's input polynomial
b_j	Coefficient j of $B(q)$.
d	Decimation factor.
$e(t)$	Error signal, deg.
$\dot{e}(t)$	Error-rate signal, deg/s.
f_s	Sampling frequency, Hz.
$f_t(t)$	Target forcing-function signal, deg.
G	Maximum rate of change, s ⁻¹ .
$G(z)$	Discrete-time transfer function.
$H_{CE}(s, t)$	Time-varying CE dynamics.
$H_{eq}(s, t)$	Time-varying equalization dynamics.
$H_{HO}(s, t)$	Time-varying HO dynamics.
$H_{HO_e}(s, t)$	Time-varying HO's linear response to the error.
$H_n(t)$	Time-varying remnant filter.
$H_{nm}(s)$	Neuromuscular dynamics.
I	Identity matrix.
k_c	= $\max(n_a + 1, n_b + n_k)$. Critical instant.
$K_{\dot{e}}(t)$	Error-rate gain.
$K(t)$	Gain vector.
$K_c(t)$	Control gain.
$K_e(t)$	Error gain.
$K_n(t)$	Remnant gain.
M	Monte Carlo replications.
m	Order of remnant filter.
N	Number of samples.
N_0	Memory horizon in samples.
$n(t)$	Remnant signal, deg.
n_a	Number of coefficients in $A(q)$.
n_b	Number of coefficients in $B(q)$.
n'_b	= $n_b + n_k - 1$. Highest order of $B(q)$.
n_k	ARX model's integer delay.
n_k^*	Estimated ARX model's integer delay.

n_k^0	True ARX model's integer delay.
n_t	Integer multiple.
$n_w(t)$	Zero-mean Gaussian white-noise signal with unit variance, deg.
$P(t)$	Scaled covariance matrix.
P_0	Initial scaled covariance matrix.
$P_\theta(t)$	Actual covariance matrix of parameters θ .
$P_n(t)$	Remnant intensity.
$p(t)$	Parameter function.
$Q(t)$	Matrix obtained by RLS criterion minimization.
q	Discrete-time shift operator.
s	Laplace variable.
T_0	Memory horizon, s.
$T_L(t)$	Lead-time constant, s.
T_m	Measurement time/window, s.
T_n	Remnant-time constant, s.
T_s	Sampling time/interval, s.
t	Time, s.
t_M	Time of maximum rate of change, s.
$u(t)$	Control-output signal, deg.
V	Loss function.
VAF	Variance accounted for, %.
$v(t)$	Disturbance signal, deg.
$x(t)$	System-output signal, deg.
z	z-transform variable.

Other Symbols

$\hat{}$	Estimated; Predicted; Simulated.
$\tilde{}$	Preprocessed.
\mathcal{M}_{ARX}	ARX model.
\mathcal{M}_{HO}	HO model.

Subscripts

i	Initial.
e	Estimation.
f	Final.
m	Measurement
p	One-step-ahead prediction.
s	Simulation.
v	Validation; Verification.

Superscripts

0	True.
c	Continuous time.



Preliminary report

2

State-of-the-art in time-varying human-operator identification

The research on both the functioning and the structure of human-operator dynamics in manual-control systems has received considerable attention over the past few decades. Current research in manual-control cybernetics mainly focuses on the adaptive and learning behavior of human operators. In order to quantitatively describe these characteristics in compatible terms with the controlled element, time-varying and possibly nonlinear system-identification methods should be employed or extended. In general, the research vision is to first develop system-theoretical models that are able to capture adaptive manual-control behavior. The capture of the human operator's learning behavior is seen as a long-term challenge. Mulder et al. (2013) state that the abilities "to peek into the currently 'black box' of human adaptation and learning, and [to] quantify the dynamics of experience," will have "major scientific impact, for all domains where humans are trained to manually operate dynamic systems." This statement could even be extended, as the reason for modeling the human operator in manual-control tasks is not only motivated by the practical application but also by scientific interest in the general question of human behavior: experimental physiologists and psychologists can utilize manual-control tasks to investigate in more detail the "primitive sensing, decision making, and response characteristics of the human" (Sheridan and Ferrell, 1974).

This chapter aims to present an accurate overview of the state-of-the art in time-varying human-operator identification oriented toward the adaptive role of the human operator. From a historical perspective, the most well-known linear control-theoretic model for describing manual-control behavior is the crossover model. This model is validated for compensatory tracking tasks and still serves as a baseline in human-operator modeling. The survey discussed here is therefore primarily concerned with this successful approach.

The chapter starts off with Section 2.1 summarizing some fundamentals in modeling adaptive human-operator behavior in compensatory tracking tasks, essential for understanding the topic. The subsequent section, Section 2.2, addresses the relevant research fields where human-operator behavior needs to be investigated and where parts of the challenges can be traced back to the identification of the operator's behavior in compensatory tracking tasks. The areas of controversy in the literature on time-varying human-operator identification are considered in Section 2.3. This section also briefly touches upon the most successfully implemented identification methods of manual-control behavior based on the restrictive assumption that this is time invariant during the identification period. The chapter ends with Section 2.4 containing a synthesis of what is and is not known. The discovered knowledge gap was used to formulate the research objective, framework, questions, and subgoals in the preceding chapter, Chapter 1.

2.1 Fundamentals of compensatory manual control

The compensatory manual-control theory serves as a baseline for modeling human-operator behavior in manual-control tasks. This section starts with a consideration of some fundamentals in human-operator modeling in compensatory control systems.

2.1.1 Adaptive behavior

As mentioned earlier, in real manual-control tasks, time-varying adaptive behavior is virtually always present due to various changes of variables. For example, suffering fatigue or alterations in motivation are directly related to the human operator. The paper by McRuer and Jex (1967) includes a clear-cut classification of variables affecting manual-control behavior (see Figure 2.1). In addition to a class of operator-centered variables, classes of environmental, procedural and task variables can be distinguished. The task variables are considered most important as these are most explicit for the specific control task.

A set of constant classes of variables can be defined as a situation. A small variation in just one variable could change the situation, inducing adaptive behavior. This complexity, together with the fact that the behavior commonly has a closed-loop nature, makes it a challenge to develop useful models for engineering purposes that can describe manual-control behavior over a wide set of circumstances. However, in certain situations where, in particular, the task variables are kept constant, experiments have shown that this behavior can be described by quasi-linear models. The most successful quasi-linear models are able to describe manual-control behavior in compensatory tracking tasks.

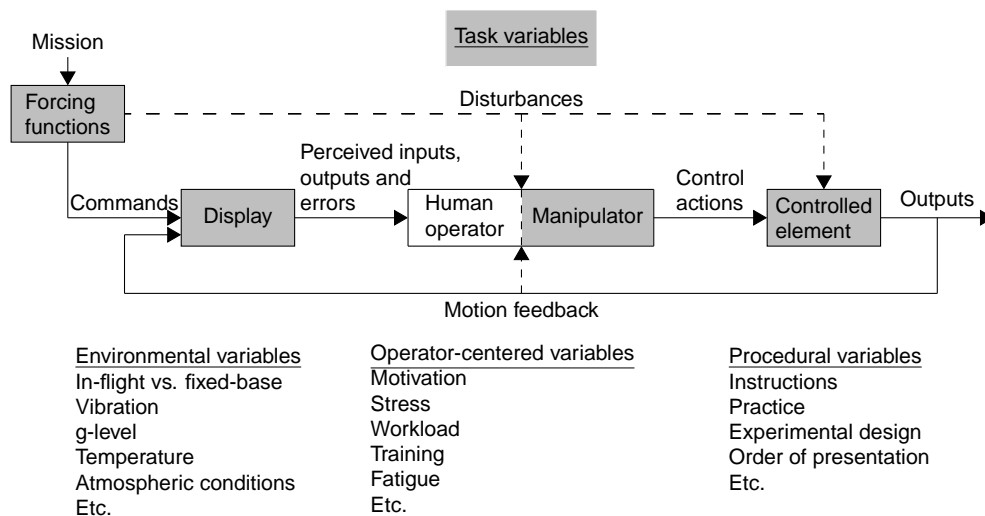


Figure 2.1 Variables affecting the manual-control behavior, adapted from McRuer and Jex (1967).

2.1.2 Compensatory tracking tasks

The simplest kind of manual-control task is single-axis compensatory tracking. In a classical sense, a compensatory tracking task is one in which the operator is presented a visual stimulus indicating the to be compensated difference between a stationary reference line or point and a moving line or point, while modern usage refers to situations where the human observes and acts upon errors irrespective of display details (McRuer, 1980). Figure 2.2 shows the archetypal compensatory display and a functional block diagram of a compensatory tracking task clarifying the operation. The operator output, often the displacement of a hand-joystick, drives the controlled element, which in effect, influences the system output. A closed loop is then formed by feeding back the system output to the input, imposing the human operator to act as a servo to compensate the error. Typically, the reference input is a target to be followed. The task could be challenged by rejecting disturbance inputs on the controlled element.

2.1.3 Quasi-linear models

The most well-known control-theoretic model, only validated for compensatory tracking tasks but still serving as a baseline in describing human-operator behavior in manual-control systems, is the crossover model (Mulder et al., 2006). This model was postulated in the 1960s (refer to McRuer and Jex, 1967), and states that human operators adjust their manual-control behavior to the controlled-element dynamics in such a way that the the open-loop dynamic characteristics around the crossover frequency approximate those of a single integrator. The crossover model was found by describing the human operator with a quasi-linear model structure. Figure 2.3 shows such a structure which consists

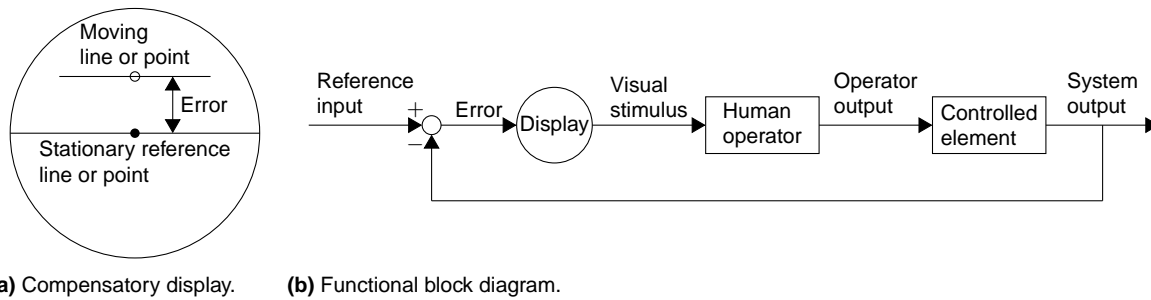


Figure 2.2 A compensatory tracking task, adapted from McRuer (1980).

of a linear part and a remnant part representing nonlinearities. Quasi-linear models are very suitable for analysis and system identification. They allow the use of control theory so the human operator can be quantitatively described in the same terms as the controlled element. On condition that laboratory experiments are designed properly, these types of models are capable of capturing the most important behavioral characteristics (McRuer and Krendel, 1974).

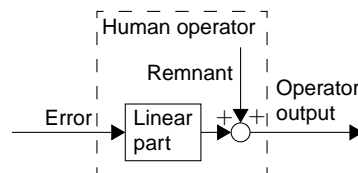


Figure 2.3 Quasi-linear human-operator model structure.

2.2 Relevant research fields

Previous research has primarily investigated the adaptive operator behavior for important changes in task variables, as this has the greatest practical interest (Hess, 2009; Phatak and Bekey, 1969). The prior investigations on the human operator's adaptive behavior have resulted in quantitative descriptions of different transition response phases, e.g., the steady-state and transient responses (Johnson and Weir, 1969; Miller and Elkind, 1967; Sheridan, 1960). Hess (2009) lists many more of such studies. What still remains unclear, however, is exactly how the human operators manage their "remarkable adaptation abilities" (Young, 1969). Partly, this is a result of the fact that early researchers were plagued by the then-existing recording and processing techniques of signals. However, these troubles no longer apply as advances have been made in the equipment of the modern control laboratories and in the simulation software. Another reason is that, after the 1960s, the focus in human-machine research has mainly shifted toward supervisory control (Sheridan, 1985).

Safety In recent years, the interest in characterizing and understanding the human operator is rekindled by the rise of reconfigurable and adaptive control systems in various applications and by the insistence on ever-increasing levels of safety (Hess, 2014). Several loss-of-control aviation incidents can, for instance, be attributed to unpredicted interactions between the adaptive human pilot and the adaptive flight-control system. Trujillo et al. (2014) hypothesized that the "reason for the adverse interactions with an adaptive controller in the loop is the pilot not realizing how the adaptive controller is changing aircraft dynamics." Another branch of research puts it the other way around. It approaches the adverse interactions with the concept of human-adaptive mechatronics. This concept was introduced by Harashima and Suzuki (2006) who define it as "an intelligent mechanical system that adapts themselves to human skill under various environments, improves human skill, and assists the operation to achieve best performance of the human-machine system."

Economic efficiency Tervo et al. (2010) point out that still, in many industrial processes, skilled manual control plays an important role in terms of fuel economy, productivity, and quality of the end product. They explain, for example, that productivity differences of over forty percent could exist between two professionally trained operators who work with similar machines in similar conditions. Therefore, in order to further improve the overall performance in the industrial processes, not only the opti-

mization of the machines should be considered, but also the limitations and the inherent capabilities of human-operator control (Xi and de Silva, 2015).

Current research is thus motivated by the quests of ever-increasing levels of safety and of economic efficiency. The alleged approaches, described above, require current identification techniques to be extended significantly for investigating manual-control behavior.

2.3 Areas of controversy

Before proceeding on to the different time-varying identification methods under development, a mention is made to the three most successfully implemented identification methods for cases where the operator can be characterized as quasi-linear and time invariant. These are the methods based on Fourier coefficients (FCs) (Stapleford et al., 1967; van Paassen and Mulder, 1998), linear time-invariant (LTI) ARX models (Nieuwenhuizen et al., 2008), and genetic maximum-likelihood estimation (MLE) (Zaal et al., 2009). They are very important to consider, because, despite significantly different dimensionality and complexity, some of them form basic building blocks for the development of the time-varying identification methods.

As already noted, research on identifying time-varying adaptive manual-control behavior primarily concentrates on adaptation due to changes in tasks variables. This section first gives account of studies toward ad hoc logic on this kind of adaptation. It then presents studies where the time-varying identification is performed with the genetic MLE procedure. Also the identification with wavelet transforms is highlighted. Next, it describes attempts of using recursive identification. In addition, a connection is made to identifying time-varying neuromuscular responses.

Adaptive logic Research by Hess (2009, 2016) has brought forward an adaptive logic as a tractable framework to approach the problem of operator adaptation for changes in the controlled-element dynamics which is not only applicable to single-axis but also to dual-axis control tasks. His most important guideline is as follows: “the post-adapted pilot models must follow the dictates of the crossover model of the human pilot” (Hess, 2016).

Maximum-likelihood estimation and wavelets Zaal (2016) investigated in a real experiment how human operators adapt to time-varying changes (transitions) in the controlled-element dynamics in a multi-axis closed-loop control task. The time-varying behavior was characterized by employing the genetic MLE procedure to estimate operator-model parameters with generalized time-dependent logistic models (sigmoid functions). In another study, performed by Zaal and Pool (2014), a multi-axis multi-loop control-task experiment was investigated by employing an identical identification procedure, although here the time variations were applied to motion-filter gains, also using sigmoid functions. A third study which used the MLE procedure to identify time-varying behavior was carried out by Zaal and Sweet (2011). They simulated a compensatory target-following tracking task where the controlled-element dynamics varied linearly over time. Here, also wavelet transforms were used to characterize time-varying operator behavior. This wavelet approach was particularly based on prior research by Thompson et al. (2001).

Recursive identification Recently, Olivari et al. (2016) attempted to identify time-varying operator responses to visual and force feedback during a compensatory tracking task using a regularized recursive least-squares (RegRLS) algorithm equipped with forgetting factor. In this case, time-varying human-operator dynamics were simulated according a control mode parameter representing abrupt and slow linear changes between different control device dynamics. Several more attempts were made in the past to identify the human in the loop using recursive identification. Ameyoe et al. (2015), for example, investigated a real-time identification of a linear parameter-varying (LPV) cybernetic driver model using the unscented Kalman filter. Boer and Kenyon (1998) made use of an extended Kalman filter to recursively identify time-varying human-operator delay. Trujillo and Gregory (2016) explored three different recursive estimation methods to analyze experimental manual-control data on the effects of an adaptive controller and on the use of vision system technologies, with the main purpose to develop a real-time indicator of manual-control behavior. Their considered estimators were based on gradient descent, least squares with exponential forgetting, and least squares with bounded gain forgetting.

Neuromuscular responses The RegRLS method was initially developed for estimating time-varying neuromuscular responses in human-in-the-loop experiments (Olivari et al., 2015a). In fact, such investigations are more specific, but they form a basis for identifying the completer models. Wavelet transforms (Mulder et al., 2011) and LPV subspace methods (van Wingerden and Verhaegen, 2009) are also under development for this specific problem. However, these applications are very immature.

2.4 Synthesis

By synthesizing the various studies on developing identification methods for time-varying manual-control behavior, relevant commonalities and differences in the research approaches are observed. Next, by delving into the details of the various studies, i.e., the setups and algorithms used, some potential advantages and disadvantages can be found.

- Most research on identifying time-varying adaptive manual-control behavior in the loop focuses on changes in the task variables and, in particular, on transitions in the controlled-element dynamics as for these variables the biggest adaptation changes are expected (McRuer and Jex, 1967).
- As a baseline, many studies start with investigating single-axis compensatory control tasks and keep reference to the famous crossover model, bearing in mind that extensions to multiple axes of control or even the usage of other classes of inputs to the human operator should not pose fundamental difficulties.
- Previous investigations make clear that, before using a novel identification method in laboratory experiments or real-life tasks, the accuracy of it should be evaluated thoroughly by means of Monte-Carlo simulations for different remnant levels.
- The identification method using wavelet transforms is not mature yet. Initial results have shown that this method is very sensitive to human-operator remnant (Zaal and Sweet, 2011).
- The MLE identification method is less sensitive to remnant and is able to provide accurate estimations, However, it requires a restrictive definition about how certain parameters will change (Zaal, 2016).
- Recursive identification methods have the big advantage that they are able to analyze the evolution of parameters over time. In addition, the main benefit of recursive identification is that time-varying dynamics can be tracked in real time, i.e., online. The initial results of the study by Olivari et al. (2016) make the RLS algorithm equipped with forgetting factor a promising candidate to consider.
- Apparently, in manual-control cybernetics, very few studies have yet attempted to make use of LPV models. There is a great temptation to extend the work by Nieuwenhuizen et al. (2008) with time-varying estimation, i.e., to take the representation of ARX models as a basic building block and then to employ a time-varying estimation method on the model parameters. The ARX-model structure is preferred as this is a linear regression-model structure which eases computations.

These points clarify, to some extent, which research approach should be adopted. As there is still a serious lack of knowledge to explain and to understand how human operators manage their ability of adaptation, the proposed thesis project opts to set up an identification method able to capture time variations in manual-control behavior without making explicit assumptions on how these will evolve over time. Based on the state-of-the-art literature survey, it seems most promising to bridge the knowledge gap by making use of an ARX-model structure and an RLS estimation method. The application of compensatory tracking tasks with time-varying controlled-element dynamics is considered as a stepping stone toward meeting the challenge.

3

Compensatory manual-control model

A complete identification scheme requires clear-cut specifications of the particular application to be modeled and the identification framework to be used. In this study, the human operator is the application to be considered. The operator is modeled as a compensatory controller in such a way that the manual-control behavior can be characterized in the same quantitative terms as the element to be controlled. Compensatory manual-control theory has been described extensively in the past. Many different approaches have been taken to mathematically model this type of manual control. The approaches range from the application of classical to optimal control theory (McRuer, 1980). More recently, also emerging approaches have been applied such as artificial neural networks and fuzzy logic (e.g., Celik and Ertugrul, 2010). As was already addressed in Chapter 2, the most solid basis for describing manual-control behavior, in many situations, is provided by the crossover model (i.e., a result of applying classical control theory) (Mulder et al., 2006). On this basis, attempts have been made to parameterize manual-control behavior. It has led to the successful buildup of structural-isomorphic models. Widely known are the extended crossover model and the precision model, both covering a broad frequency range (McRuer et al., 1967). However, despite their success in characterizing some of the human operator's capabilities and limitations, these models are not able to capture short-term adaptations, learning and time-varying behavior (McRuer and Jex, 1967).

In line with the procedure laid down in Chapter 1, this chapter takes a more mathematical approach in modeling the human operator compared to the previous chapter. A compensatory manual-control model is set up with the possibility to introduce time variations in both the human-operator and the controlled-element dynamics. More specifically, single-axis target-following control tasks will be considered. The dynamics of the human operator will be modeled using a modified version of the precision model by McRuer et al. (1967). As there is less common ground on how human operators manage their abilities of adaptation to time-varying controlled-element dynamics, prior definitions are required in simulating the time variations in control behavior. The setup described here is primarily based on the study by Zaal (2016).

This chapter begins with Section 3.1 which provides a mathematical description of the single-axis target-following control task to be considered. A block diagram clarifies the functioning of the human operator as a compensatory controller. In addition, the type of forcing function to excite the operator and the crossover model are explained in mathematical terms. Section 3.2 presents parametric models for both the controlled-element and the operator dynamics. Lastly, Section 3.3 discusses the various suggestions found in literature for simulating time-varying control behavior. Essentially, the operator's input-output data resulting from simulating the proposed compensatory manual-control model will be used by the identification algorithms presented in Chapter 4. More specific details and results of the simulation are given in Chapter 5.

3.1 Single-loop target-following control task

A block diagram of the compensatory manual-control model to be simulated with time-varying dynamics is shown in Figure 3.1. The figure was adapted from Zaal (2016). As was explained in Chapter 2, in compensatory tracking tasks, the human operator can only directly (visually) perceive the tracking

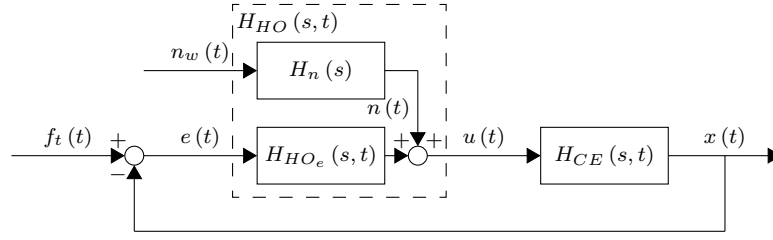


Figure 3.1 Block diagram of a single-loop compensatory target-following control task with time-varying dynamics, adapted from Zaal (2016).

error signal $e(t)$ in time t . This signal is the input to the operator. In Figure 3.1, the operator dynamics are represented, in the corner-aligned dashed rectangle, with the transfer function $H_{HO}(s, t)$. The operator output is the control signal $u(t)$ serving as input to the controlled element whose dynamics are expressed by $H_{CE}(s, t)$. As indicated by t , both these dynamics can be considered as time varying. In this control task, the operator aims to minimize $e(t)$ which is defined as the difference between a target forcing-function signal $f_t(t)$ and the system-output signal $x(t)$:

$$e(t) = f_t(t) - x(t) \quad (3.1)$$

Taking a closer look at Figure 3.1, $H_{HO}(s, t)$ is modeled with a quasi-linear model. It is an addition of a linear response to the error $H_{HO_e}(s, t)$, and a remnant signal $n(t)$ accounting nonlinearities. The latter signal is modeled by passing a zero-mean Gaussian white-noise signal $n_w(t)$ with unit variance through a time-invariant remnant filter $H_n(s)$. In reality, however, the remnant characteristics would also be time-varying. This study focuses on a proper examination of the linear time-varying operator responses. In order to avoid complications, $H_n(s)$ is assumed to be time invariant.

As the human operator is embedded in a closed loop, a crucial point for identification is that the remnant will be circulated, resulting in a correlation between $e(t)$ and $n(t)$. Accordingly, care should be taken in identifying the operator only on the basis of $e(t)$ and $u(t)$ as they will be biased estimates.

Forcing functions For executing human-in-the-loop simulations or experiments, van Paassen and Mulder (1998) provide useful guidelines to be taken into account. Usually, the forcing functions to excite the operator are multisinusoidal signals. They have a quasi-random appearing but are completely deterministic. In the tracking task to be simulated, $f_t(t)$ is described by

$$f_t(t) = \sum_{k_t=1}^{N_t} A_t[k_t] \sin(\omega_t[k_t]t + \phi_t[k_t]) \quad (3.2)$$

where $A_t[k_t]$, $\omega_t[k_t]$, and $\phi_t[k_t]$ are the amplitude, frequency, and phase shift of the k_t th sinusoid in $f_t(t)$, respectively, and N_t is the total number of sinusoids. All excitation frequencies $\omega_t[k_t]$ are integer multiples n_t of the measurement-base frequency ω_m . In designing the forcing functions, care should be taken that the signal-to-noise ratios are high.

Crossover model The crossover model was already discussed in Chapter 2. Mathematically, it can be expressed as follows. First, denote the open-loop transfer function $H_{OL}(j\omega)$, in the frequency domain, in Figure 3.1, relating $x(t)$ to $e(t)$, as

$$H_{OL}(j\omega) = H_{HO}(j\omega) H_{CE}(j\omega) \quad (3.3)$$

Around the crossover frequency ω_c , i.e., where $|H_{OL}(j\omega)|_{\omega=\omega_c}$ equals one, $H_{OL}(j\omega)$ approximates integrator-like dynamics ($1/j\omega$). Taking into account the operator's effective time delay τ_e (e.g., due to information-processing lags), the crossover model is mathematically represented as (McRuer and Jex, 1967)¹

$$H_{OL}(j\omega) \doteq \frac{\omega_c}{j\omega} e^{-j\omega\tau_e}, \quad \text{when } \omega \approx \omega_c \quad (3.4)$$

If $H_{CE}(j\omega)$ is known, the model allows to predict $H_{HO}(j\omega)$ in the crossover region.

3.2 Parametric models

This study will investigate manual-control behavior for time-varying controlled-element dynamics, which could approximate both single- and double-integrator dynamics ($1/j\omega$ and $1/(j\omega)^2$) in the crossover

¹The frequency operator $j\omega$ (with $j^2 = -1$) is used instead of the general Laplace variable $s = \sigma + j\omega$. The validity is only in the frequency domain and the existence is only under essentially stationary conditions.

region. They are defined parametrically by (Zaal, 2016)

$$H_{CE}(j\omega, t) = \frac{K_{CE}(t)}{s^2 + \omega_b(t)s} \quad (3.5)$$

where $K_{CE}(t)$ and $\omega_b(t)$ are the time-varying controlled-element gain and time-varying break frequency, respectively.

In order to parameterize $H_{HO_e}(s, t)$, the following model is taken from Zaal (2016) which is a modified version of the precision model. In this report, it will be referred to as the analytical human-operator model.

$$H_{HO_e}(s, t) = \underbrace{\underbrace{K_v(t)}_{\text{Gain}} \underbrace{[T_L(t)s + 1]}_{\text{Lead term}}}_{\text{Equalization dynamics: } H_{eq}(s, t)} \underbrace{\underbrace{e^{-s\tau_v}}_{\text{Time delay}} \underbrace{\frac{\omega_{nm}^2}{s^2 + 2\zeta_{nm}\omega_{nm}s + \omega_{nm}^2}}_{\text{Neuromuscular-actuation dynamics: } H_{nm}(s)}}_{\text{Limitations}} \quad (3.6)$$

It is split up into equalization dynamics and operator limitations. The equalization dynamics $H_{eq}(s, t)$ for the controlled-element dynamics to be considered, consist of a time-varying visual gain $K_v(t)$ and a lead term $T_L(t)s + 1$, where $T_L(t)$ is a time-varying lead-time constant. The operator's limitations include the time delay τ_v , incurred in the central nervous system's perception and processing of visual information, and the neuromuscular-actuation dynamics $H_{nm}(s)$ due to the operator's control actions. The latter ones are defined by a second-order system yielding the (undamped natural) neuromuscular frequency ω_{nm} and the neuromuscular-damping ratio ζ_{nm} . Generally, K_v and T_L are called the equalization parameters, while τ_v , ω_{nm} and ζ_{nm} are termed the limitation parameters.

Compared with the precision model by McRuer et al. (1967), the above model does not take into account an additional low-frequency lag-lead term and it lacks an additional neuromuscular-lag term. Pool et al. (2011a) refer to previous investigations indicating that models like the one in Eq. (3.6) have sufficient capability to capture manual-control behavior in similar tracking tasks over a wide frequency range. The limitation parameters are not considered to be time-varying in this study. Zaal (2016) argues, on the basis of previous research, that they are not significantly different for the proposed dynamics to be controlled.

3.3 Time variations

As was explained in Chapter 2, there is no clear agreement on how human operators adapt their manual-control behavior over time. The literature survey has led to the conclusion that some high-level guiding principles of adaptation are available, but no reliable identification frameworks exist to capture the time-varying adaptive human-operator dynamics for abrupt or gradual changes in for instance the task variables. In fact, in order to perform offline simulations, a priori information is needed on how human operators adapt. However, the availability of such a priori information is the external goal of the research here. It leads to a causality dilemma.

This study attempts to resolve the dilemma on the basis of earlier proposals for simulating time variations in manual-control behavior. The survey in Chapter 2 addressed different attempts: time variations were introduced by means of linear parameter changes, a control-mode parameter, and sigmoid functions. The paragraphs below explain them in more mathematical detail. Conclusive remarks are given at the end of this section.

Linear parameter changes In the work by Zaal and Sweet (2011), a similar control task as described above was set up and linear time variations were introduced in both the parameters of the controlled element and the operator. Figure 3.2 shows a visualization of their proposed time variations in the parameters (Θ). Changes happen at two time instants (t_1 and t_2) They were introduced in both the controlled element's gain (K_c) and time constant (T_c), and both the operator's visual gain (K_v) and lead-time constant (T_l). Both time-varying lead-time constants were assumed to be equal throughout the runs. The operator's limitation parameters were set to fixed values. In this simulation, the open-loop dynamics had single-integrator dynamics over the entire range. While some of the parameters changed linearly over time, the responses of the controlled element and the human operator did not change linearly.

Control-mode parameter A slightly different manual-control task was modeled in the study by Olivari et al. (2016). Their aim was to capture not only time-varying responses to visual but also force feedback. Instead of the controlled-element dynamics, control-device dynamics were changed over

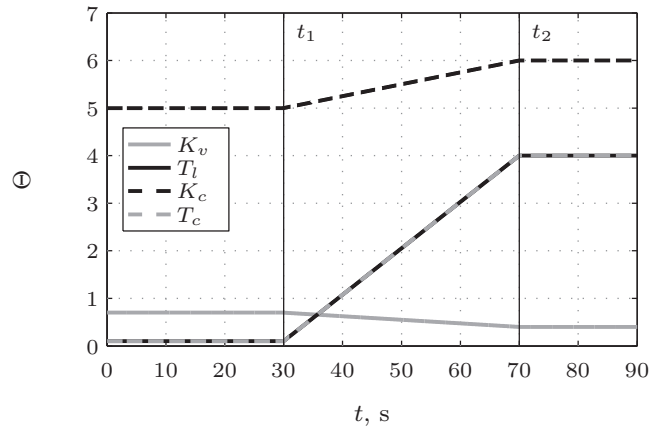


Figure 3.2 “Values of the time-varying simulation parameters” (Zaal and Sweet, 2011).

time via a control-mode parameter $CM(t)$ varying between values of zero and one. The transfer functions $H(s)$ of both the control device and the operator’s visual and force responses were equally varied in time between two parameter sets (1 and 2) according

$$H(s, t) = (1 - CM(t)) H_1(s) + CM(t) H_2(s) \tag{3.7}$$

The used pattern of $CM(t)$ is shown in Figure 3.3. It consists of two step and two ramp transitions.

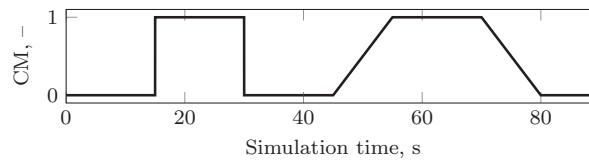
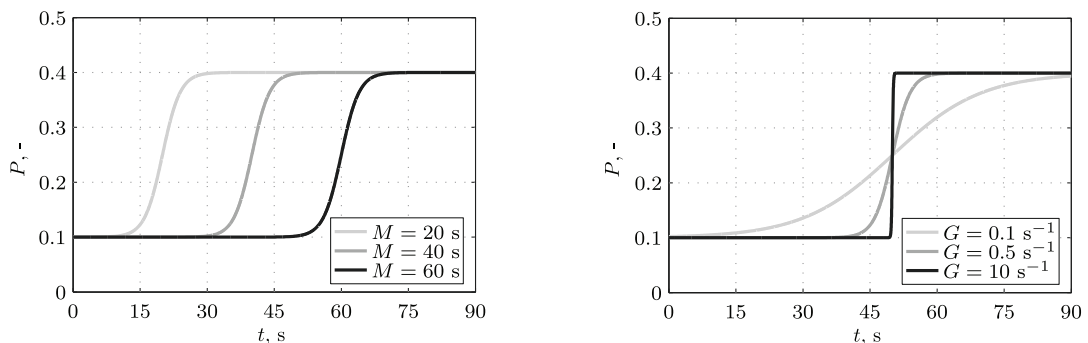


Figure 3.3 “Time evolution of the control mode” (Olivari et al., 2016).

Sigmoid functions Zaal (2016) introduced time variations in the parameters of both the controlled-element dynamics and the operator’s equalization dynamics by means of (nonlinear) sigmoid functions. The type of sigmoid functions used by Zaal to vary a parameter P in time is mathematically defined as

$$P(t) = P_1 + \frac{P_2 - P_1}{1 + e^{-G(t-M)}} \tag{3.8}$$

where P_1 and P_2 are the initial and final parameter values, respectively. The maximum rate of change is denoted by G and the time at which this happens is set by M . Actually, similar sigmoid functions were used in the study by Zaal and Pool (2014). Figure 3.4 clarifies the tuning of the variables M and G . The legends in this figure indicate the values used for M and G in order to generate the various sigmoid curves. It can be seen that the sigmoid functions allow the modeling of both abrupt and gradual transitions.



(a) M variation ($P_1 = 0.1, P_2 = 0.4, G = 0.5 \text{ s}^{-1}$).

(b) G variation ($P_1 = 0.1, P_2 = 0.4, M = 50 \text{ s}$).

Figure 3.4 “Sigmoid function parameter variation” (Zaal, 2016).

Conclusive remarks In reality, manual-control behavior is nonlinear. Although the resulting operator responses in the study by Zaal and Sweet (2011) varied nonlinear over time, the operator's equalization parameters were changed linearly. It would be better to directly introduce nonlinear time variations in the operator's parameters. Hence, the use of sigmoid functions for such variations, as suggested by Zaal (2016), possibly reflects more realistic control behavior. In contrast to the work by Olivari et al. (2016), where four transitions in the control-mode parameter were considered to introduce time-varying operator responses in one simulation run, Zaal (2016) just modeled one transition in a set of parameters in a run of similar length. The identification of manual-control behavior for even one transition during a run is already a challenge. Taken together, it seems to be fruitful to make use of a similar setup as in Zaal (2016) for introducing the time variations.

4

Identification framework

In recent years, identification frameworks based on parametric LTI models have been successfully applied in characterizing manual-control behavior, under the assumption that this behavior is time-invariant during the identification period. Commonly, these types of models are built by using time-domain data. Early experimental investigations utilizing time-series analysis for modeling the operator in the loop are described, for instance, by Stanković and Kouwenberg (1973), Shinnars (1974), Balakrishna (1976), Osafo-Charles et al. (1980), Jategaonkar et al. (1982), Balakrishna et al. (1983), Hanson and Jewell (1983), Biezdad and Schmidt (1985), Hess and Mnich (1986), Hess (1990), and Goto and Matsuo (1988). The work by Nieuwenhuizen et al. (2008) lists many more studies covering such investigations. The actual research by Nieuwenhuizen et al. (2008) has led to the buildup of the currently most successful identification framework based on LTI models for the characterization of compensatory manual-control behavior. Compared to preceding studies, they were able to take the step forward in employing parametric LTI models through advances made in simulation software. More recent investigations of manual-control behavior, partly relying on this work, can be found in the studies by Drop et al. (2013, 2016a,b), Olivari et al. (2014, 2015b), and Roggenkämper et al. (2016). As concluded in Chapter 2, very few attempts have been taken to make use of LTI models with time-varying parameters, i.e., LPV models, in the identification of manual-control behavior.

The aim of this chapter is to present the setup of an identification framework based on ARX models. It focuses on the kind of knowledge, information, and insights needed to establish the framework. Similarly to Chapter 3, a mathematical approach is taken here. In order to develop the framework, reference is primarily made to Ljung (1999). In essence, the framework is only going to make use of time-domain data sets containing the operator's error signal serving as input and control signal serving as output. In this chapter, some common notations used in system identification are adopted to notations introduced in Chapter 3.

The chapter's structure is as follows. Section 4.1 outlines the system-identification loop that will serve as basis for the development of the identification framework. Steps to be taken in the data generation and preprocessing, and in the estimation, simulation and validation are presented in Section 4.2. Section 4.3 provides a description of ARX models. Lastly, Section 4.4 highlights the parameter estimation. The estimation methods of ordinary least squares and recursive least squares equipped with forgetting factor are considered.

4.1 Identification loop

As introduced in Chapter 3, the identification scheme needs clear specifications of the application to be analyzed (i.e., in this research, the operator in a compensatory tracking task) and the identification framework to be used. The setup of the application was described in Chapter 3. This chapter specifies the identification framework. Ljung (1999) and Verhaegen and Verdult (2007) provide clever visualizations of the iterative identification procedure. An adapted version of these is shown in Figure 4.1. The procedure requires both basic principles from a statistical nature as well as prior knowledge about the application to be modeled.

It is important to gather maximally informative data from the application. However, it is very likely

that the data sets require preprocessing steps to avoid identification problems. In this project, the model structure is set to be ARX, but the real crux is the decision on the model orders. In deciding, not only physical insight must be considered, but also the principle of parsimony should be applied. The latter says that “when describing a dynamic process one should not use extra parameters if not necessary” (Niedźwiecki, 2000). In order to assess candidate models, a criterion of fit must be chosen. In general, it is usually a trade-off between the model complexity and the model quality-of-fit. So before estimating the ARX models with the proposed time-varying estimation method, all the preceding should be carefully thought out. Presumably, multiple revisions are needed before the “best” model is obtained with the correctly tuned estimation algorithm. Once this is done, Monte-Carlo testing should be employed for different intensity levels and realizations of remnant to verify the procedure. Eventually real experimental data will be used to completely validate the procedure. As can be inferred, the identification procedure is thus an iterative process with a lot of interdependencies.

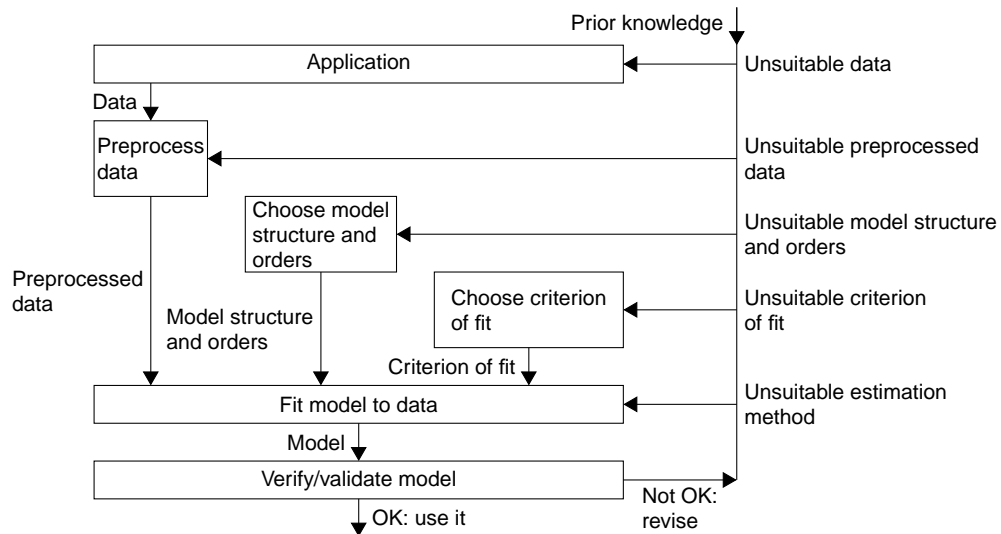


Figure 4.1 Identification loop, adapted from Ljung (1999) and Verhaegen and Verdult (2007).

4.2 Proposed identification method

Based on the general identification procedure, this section specifies the workflow that will be used in producing the “best” ARX models by identification. It starts with discussing how the input-output data sets will be generated. Next, it considers the data-preprocessing procedure. Lastly, the steps of estimation, simulation and validation are explained.

4.2.1 Data generation

The time-domain input-output data sets are generated using guidelines proposed by van Paassen and Mulder (1998). The total recording time T_t should consist of a run-in time T_r , e.g., for discarding transients in the manual-control behavior at the start of the recording, and a measurement time T_m . Very often, e.g., see Zaal (2016), the data is sampled with a frequency f_s of 100 Hz ($\omega_s = 628.32$ rad/s), i.e., with a sampling time or interval T_s of 0.01 s. It is usually fixed by the simulation software or the laboratory equipment. Commonly, the generated data sets are not only considered in the time domain but also in the frequency domain. In order to calculate the discrete Fourier transforms (DFTs) using the fast Fourier transform algorithm, it is most efficient that the number of samples N is an integer power of two. Typically, e.g., see again Zaal (2016), T_m is set to 81.92 s, resulting in measured data signals whose discrete-time samples range from $k = 1$ to $k = 2^{13}$, hence N equals 8192. The corresponding measurement-base frequency $\omega_m = 2\pi/T_m$ and frequency resolution f_s/N then become 0.0767 rad/s and 0.0122 Hz, respectively. In reconstructing signals, aliasing effects are avoided if the Nyquist-Shannon sampling theorem is obeyed. The maximum frequency that the signals can contain is determined by the Nyquist frequency $f_N = f_s/2$, which equals 50 Hz in this case ($\omega_N = 314.16$ rad/s).

4.2.2 Data preprocessing

In general before using input-output data sets in identification algorithms, data need to be subjected to preprocessing steps (Ljung, 1999). Typically, there are noise disturbances in the data, above the frequencies of interest. Nieuwenhuizen et al. (2008) mention that the typical frequency range of interest for identifying human-operator dynamics in compensatory tracking tasks covers 0.3 to 17 rad/s. Furthermore, they explain that, in general, recorded data need to be resampled or filtered, or both. Their most important note is that “the cutoff frequency of the filter should be higher than or equal to the Nyquist frequency of the resampled signal.”

In this study, the type of filter that will be used in the data preprocessing is the ideal noncausal filter. In line with the advice stated above, the cutoff frequency of this filter will be set equal to the Nyquist frequency. In order to decimate the data signals, a decimation factor d is used. As explained by Verhaegen and Verdult (2007), decimated signals are obtained by taking the first sample and then every subsequent d th sample (for $d \in \mathbb{Z}_{>0}$) from the original recordings. Consequently, signal-processing quantities will change. Table 4.1 shows an overview of these quantities for different values of d . Only values of d that are a power of 2 are considered so that the number of samples in the resampled signals also stays a power of 2. For clarity's sake, $d = 1$ is included, i.e., the case of no resampling.

Table 4.1 Signal-processing quantities for different decimation factors ($\omega_m = 0.0767$ rad/s, $f_s/N = 0.0122$ Hz).

d	T_s , s	f_s , Hz	ω_s , rad/s	f_N , Hz	ω_N , rad/s	N_m	N_e	N_v	$k_{e,s}$	$k_{e,e}$	$k_{v,s}$	$k_{v,e}$
1	0.01	100	628.32	50	314.16	8192	4096	4096	1	4096	4097	8192
2	0.02	50	314.16	25	157.08	4096	2048	2048	1	2048	2049	4096
4	0.04	25	157.08	12.5	78.54	2048	1024	1024	1	1024	1025	2048
8	0.08	12.5	78.54	6.25	39.27	1024	512	512	1	512	513	1024
16	0.16	6.25	39.27	3.125	19.63	512	256	256	1	256	257	512

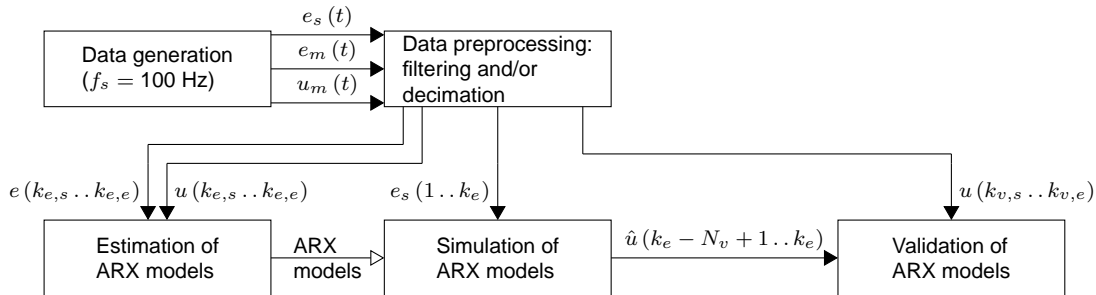


Figure 4.2 Proposed identification method. Denoting k_e as the end sample, the measurement signals $e_m(t)$ and $u_m(t)$ are obtained by taking the samples $k_e - N + 1 \dots k_e$ from the total recordings $e(t)$ and $u(t)$, respectively.

4.2.3 Further steps

In addition to the number of measurement samples N_m , when using different values of d , Table 4.1 provides the number of samples of a (re)sampled signal that will be used for estimation (N_e) and validation (N_v) in the order selection of ARX models. The start and end samples range from $k_{e,s}$ to $k_{e,e}$ for the estimation data subset, and from $k_{v,s}$ to $k_{v,e}$ for the validation data subset. The proposed identification method is schematized in Figure 4.2. It partly originates from the works of Drop et al. (2016a,b). The signals without subscript m indicate that they are preprocessed, and that they are used for the estimation and the validation. In the simulation of ARX models, decimated versions of the simulated input signal $e_s(t)$ are used. The modeled estimates of the true output are denoted by $\hat{u}(k)$.

An intuitive metric for validating an estimated model is the variance accounted for (VAF) (Nieuwenhuizen et al., 2008). It measures the model's quality of fit. For single-output signals the VAF is defined as (Verhaegen and Verdult, 2007)

$$\text{VAF}(u(t), \hat{u}(t)) = \max \left(0, \left(1 - \frac{\frac{1}{N_v} \sum_{t=k_{v,s}}^{k_{v,e}} |u(t) - \hat{u}(t)|^2}{\frac{1}{N_v} \sum_{t=k_{v,s}}^{k_{v,e}} |u(t)|^2} \right) \cdot 100\% \right) \quad (4.1)$$

The computation requires the measured output $u(t)$ and the simulated output $\hat{u}(t)$. The resulting percentage says how well the ARX model is able to simulate the measured output.

4.3 ARX models

This study considers the use of LTI ARX models for the identification. This section describes the ARX-model structure, its suitability for human-operator identification, the application of linear regression, and the determination of the ARX-model orders.

4.3.1 ARX-model structure

Equivalent representations of the signal flow of the ARX-model structure are presented in Figure 4.3. The notation of the input and output signals corresponds to the notation used in Chapter 3. To clarify, the input signal is the preprocessed error signal $e(t)$, and the output signal is the preprocessed control signal $u(t)$. As shown in Figure 4.3(a), the LTI ARX-model structure can be described by

$$\underbrace{u(t)}_{\text{Output}} = \underbrace{\overbrace{G(q; \theta)}^{\text{Deterministic process}} \underbrace{e(t)}_{\text{Input}}}_{\text{Plant model}} + \underbrace{\overbrace{H(q; \theta)}^{\text{Stochastic disturbance: } v(t)}}_{\text{Noise model}} \underbrace{\epsilon(t)}_{\text{White noise}} \quad (4.2)$$

$$= \frac{B(q)}{A(q)} e(t) + \frac{1}{A(q)} \epsilon(t) \quad (4.3)$$

It is thus a superposition of a deterministic process, in which a parametric (indicated by θ) plant model operates on the input, and a stochastic disturbance signal $v(t)$, obtained by letting a parametric noise model operate on a white-noise signal $\epsilon(t)$. Equation (4.2) can be written more compactly as (see also Figure 4.3(b))

$$A(q) u(t) = B(q) e(t) + \epsilon(t) \quad (4.4)$$

The argument q in Eqs. (4.2) to (4.4) and Figure 4.3 denotes the discrete-time shift operator, e.g., $q^{-1}u(t) = u(t-1)$. The ARX model makes use of the following two shift polynomials:

$$A(q) = 1 + a_1 q^{-1} + \dots + a_{n_a} q^{-n_a} \quad (4.5)$$

$$\begin{aligned} B(q) &= (b_0 + b_1 q^{-1} + \dots + b_{n_b} q^{-n_b+1}) q^{-n_k} \\ &= b_0 q^{-n_k} + b_1 q^{-n_k-1} + \dots + b_{n_b} q^{-n_k-n_b+1} \\ &= b_0 q^{-n_k} + b_1 q^{-n_k-1} + \dots + b_{n_b} q^{-n'_b} \end{aligned} \quad (4.6)$$

The complete ARX-model structure is defined by three integers: $n_a \in \mathbb{Z}_{>0}$, $n_b \in \mathbb{Z}_{>0}$, and $n_k \in \mathbb{Z}_{\geq 0}$. The number of coefficients a_i for $i \geq 1$ in the output polynomial $A(q)$ is set by n_a , while n_b defines the number of coefficients b_j for $j \geq 0$ in the input polynomial $B(q)$. The final coefficients of $A(q)$ and $B(q)$ are denoted by a_{n_a} and b_{n_b} , respectively. A delay (i.e., a dead time) from the input to the output in terms of the number of samples is set using n_k . The orders of polynomials $A(q)$ and $B(q)$ are set by n_a and by $n_b - 1$, respectively. Similarly, n_a and $n_b - 1$ set the number of poles and the number of finite zeros, respectively. Using n_k , the highest order of $B(q)$ is changed to $n'_b = n_b + n_k - 1$.

As shown in Eqs. (4.5) and (4.6), the formulations of $A(q)$ and $B(q)$ are slightly different. It can be observed that the lead coefficient of $A(q)$, i.e., a_0 , is fixed to 1 and that a direct transmission coefficient b_0 is used in $B(q)$. In this way, there will be no ambiguity in the definition of $G(q; \theta)$. Also, the monic property of $H(q; \theta)$ is preserved. Furthermore, it is straightforward to compute the output.

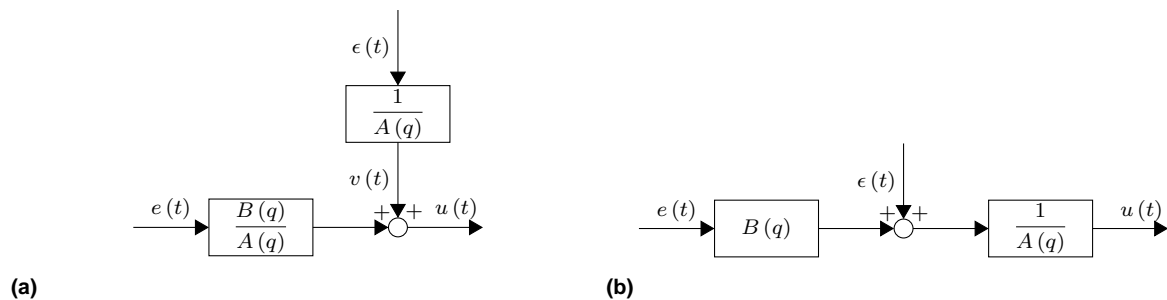


Figure 4.3 Equivalent representations of the ARX-model structure.

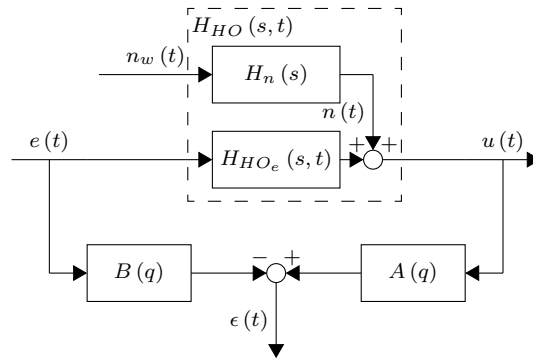


Figure 4.4 Representation of the ARX-model structure and the human-operator model.

4.3.2 ARX model and human-operator model

In order to better understand how the ARX model takes the human-operator input-output data, the block diagram in Figure 4.4 is drawn. It can be seen that the operator's blocks and signals are adapted from Figure 3.1 and incorporated in the ARX-model structure. The ARX model takes as input $e(t)$ and as output $u(t)$. The mismatch between $B(q)e(t)$ and $A(q)u(t)$ is modeled by $\epsilon(t)$.

It must be pointed out that the identification method based on ARX models considered here does not explicitly take into account closed-loop identification issues. Feedback is ignored and an open-loop system is identified using measured input-output data. Drop et al. (2016a) also utilized ARX models for the identification of manual-control behavior and compared this direct identification method with an indirect (two-stage) method that does explicitly take into account closed-loop identification. They concluded that the direct method is able to provide more accurate estimates in the frequency range of interest for manual control than the indirect method. Hence, there seems to be little resistance against using the direct method in identifying manual-control behavior with ARX models.

Considering again Figure 4.3(a), it can be noted that the deterministic block $G(q; \theta)$ is equivalent to the operator's linear response to the error $H_{HO_e}(s, t)$. Using the definition of $B(q)$, the operator's time delay τ_v can be approximated with n_k . In fact, n_k is an integer multiple of the sampling time T_s . Consequently, the higher the decimation factor, the rougher the approximation of τ_v with n_k . The remnant $n(t)$ is modeled by the stochastic disturbance $v(t)$, obtained by passing the white noise $\epsilon(t)$ through $H(q; \theta)$. Thus, $H(q; \theta)$ is tied to $G(q; \theta)$. However, as will be explained below, the ARX-model parameters θ can be obtained by applying linear regression.

4.3.3 Linear regression

As shown by Ljung (1999), the one-step-ahead predictor $\hat{u}(t|t-1)$ can be denoted by $\hat{u}(t|\theta)$ to emphasize its dependence on θ . It is computed as

$$\hat{u}(t|t-1) = \underbrace{[1 - A(q)]u(t)}_{\text{Past outputs}} + \underbrace{B(q)e(t)}_{\text{Current and past inputs}} \quad (4.7)$$

The above, which only involves known terms, can be written in the convenient linear regression format

$$\hat{u}(t|\theta) = \varphi^T(t)\theta \quad (4.8)$$

where $\varphi(t)$ is the regression vector of known past outputs, and current and past inputs:

$$\varphi(t) = [-u(t-1) \quad -u(t-2) \quad \cdots \quad -u(t-n_a) \quad e(t-n_k) \quad e(t-n_k-1) \quad \cdots \quad e(t-n'_b)]^T \quad (4.9)$$

and θ is the unknown parameter vector:

$$\theta = [a_1 \quad a_2 \quad \cdots \quad a_{n_a} \quad b_0 \quad b_1 \quad \cdots \quad b_{n_b}]^T \quad (4.10)$$

4.3.4 ARX-model orders

One of the biggest questions in setting up the identification framework, is how the right ARX-model orders, i.e., how the two integers n_a and n_b , can be selected. In addition, there is the integer n_k to be set. A combination of the integers should be found that will serve as basic building block in the identification. Time-variations can then be captured by the proposed time-varying estimation method.

Mathematically, this approach can be clarified as follows

$$H(s) = \frac{1}{1 + a_1 s} \rightarrow H(s, t) = \frac{1}{1 + a_1(t) s} \quad (4.11)$$

Above transfer functions have the same model structure. They differ in that the left one is time invariant, while the right one is time varying. The time-invariant model structure, however, is used for the initial order selection.

The problem of model-order determination for time-domain models of human-operator dynamics in compensatory tracking tasks was already investigated decades ago by Jategaonkar et al. (1982). Several model (order) selection criteria were tested by them for this application. A more up-to-date overview of such criteria is given by Raol et al. (2004, pp. 130–137). Although these criteria have been available for a number of years, to date, no well-accepted objective ARX-model selection criterion exists for identifying human-operator behavior in compensatory tracking tasks. Recent research by Drop et al. (2016a,b), however, has established a potential objective procedure for identifying human feedforward responses in manual control. The study uses a modified Bayesian information criterion (mBIC) which trades off between model complexity and model's quality of fit.

As research is ongoing, this study will not directly make use of the mBIC to determine the ARX-model orders. Instead, it considers the use of the VAF. This metric was also used in the work by Nieuwenhuizen et al. (2008). Numerous ARX models will be computed for the different preprocessed data sets. In the end, the “best” model for a preprocessed data set is obtained based on physical insight and the parsimony principle.

4.4 Fit criterion

As the ARX-model structure allows the application of linear regression, the criterion of fit is based on the one-step-ahead prediction error,

$$\varepsilon(t, \theta) = u(t) - \hat{u}(t|\theta) \quad (4.12)$$

In order to estimate the parameter vector θ , the least-squares method can be used:

$$\min_{\theta} V(\theta, Z) \quad (4.13)$$

Here, $V(\theta, Z)$ denotes the criterion function (also called the least-squares criterion) to be minimized on the data set Z . The least-squares estimate $\hat{\theta}^{LS}$ is then provided by

$$\hat{\theta}^{LS} = \arg \min_{\theta} V(\theta, Z) \quad (4.14)$$

Several least-squares estimation methods are available that differ with respect to their definition of $V(\theta, Z)$. In this study, the estimation methods of ordinary least squares (OLS) and recursive least squares (RLS) equipped with forgetting factor will be considered. These are explained below.

4.4.1 Ordinary least-squares estimation

In general, the OLS criterion is defined as

$$V_N^{OLS}(\theta, Z^N) = \sum_{t=1}^N (u(t) - \varphi^T(t)\theta)^2 \quad (4.15)$$

for which the OLS estimate becomes

$$\hat{\theta}_N^{OLS} = \arg \min_{\theta} \frac{1}{N} \sum_{t=1}^N (u(t) - \varphi^T(t)\theta)^2 \quad (4.16)$$

The minimum can be found, assuming that the indicated inverse exists, using

$$\hat{\theta}_N^{OLS} = \left[\frac{1}{N} \sum_{t=1}^N \varphi(t) \varphi^T(t) \right]^{-1} \frac{1}{N} \sum_{t=1}^N \varphi(t) u(t) \quad (4.17)$$

With matrix-vector formulation, Eq. (4.17) can be written as

$$\hat{\theta}_N^{OLS} = (\Phi^T \Phi)^{-1} \Phi^T \mathbf{u} \quad (4.18)$$

where Φ is the regression matrix:

$$\Phi = \begin{bmatrix} \varphi^T(1) \\ \varphi^T(2) \\ \vdots \\ \varphi^T(N) \end{bmatrix}$$

$$= \begin{bmatrix} -u(0) & -u(-1) & \cdots & -u(1-n_a) & e(1-n_k) & e(0-n_k) & \cdots & e(1-n'_b) \\ -u(1) & -u(0) & \cdots & -u(2-n_a) & e(2-n_k) & e(1-n_k) & \cdots & e(2-n'_b) \\ \vdots & \vdots & \ddots & \vdots & \vdots & \vdots & \ddots & \vdots \\ -u(N-1) & -u(N-2) & \cdots & -u(N-n_a) & e(N-n_k) & e(N-1-n_k) & \cdots & e(N-n'_b) \end{bmatrix} \quad (4.19)$$

and \mathbf{u} is the vector of control-output signals:

$$\mathbf{u} = \begin{bmatrix} u(1) \\ u(2) \\ \vdots \\ u(N) \end{bmatrix} \quad (4.20)$$

Usually, the data for $t < 1$ is unknown. Then, before computing $\hat{\theta}_N^{OLS}$, all rows in Φ and \mathbf{u} with an unknown data sample should be removed.

A limitation of the OLS estimation method is that it acts in batch mode, i.e., on the whole time series at once. This method assumes that the system to be modeled is time invariant. On the contrary, as will be discussed next, the RLS estimation method is capable to track time variations of the system.

4.4.2 Recursive least-squares estimation

In recursive identification, the parameter estimation is updated for each new measurement sample that becomes available. It is, therefore, also referred to as online or real-time identification, or adaptive parameter estimation. Actually, the RLS algorithm is a special case of the Kalman filter algorithm.

RLS algorithm The criterion of fit for RLS estimation is in general defined as

$$V_t^{RLS}(\theta, Z^t) = \sum_{k=1}^t \beta(t, k) (u(k) - \varphi^T(k) \theta)^2 \quad (4.21)$$

containing the weight (also called the forgetting profile)

$$\beta(t, k) = \prod_{j=k+1}^t \lambda(j) \quad (4.22)$$

where $|\lambda(j)| \leq 1$ denotes the forgetting factor. The corresponding RLS estimate then becomes

$$\hat{\theta}_t^{RLS} = \arg \min_{\theta} \sum_{k=1}^t \beta(t, k) (u(k) - \varphi^T(k) \theta(k))^2 \quad (4.23)$$

The t in the above equations emphasizes that the criterion and the estimate are based on t data (i.e., Z^t). In order to compute $\hat{\theta}_t^{RLS}$, the following recursive algorithm will be used. For easier notation, $\hat{\theta}(t) = \hat{\theta}_t^{(t)}$ is introduced, denoting the parameter estimate at time t .

$$\hat{\theta}(t) = \hat{\theta}(t-1) + K(t) \varepsilon(t) \quad (4.24)$$

$$\varepsilon(t) = u(t) - \hat{u}(t) \quad (4.25)$$

$$\hat{u}(t) = \varphi^T(t) \hat{\theta}(t-1) \quad (4.26)$$

$$K(t) = Q(t) \varphi(t) \quad (4.27)$$

$$Q(t) = \frac{P(t-1)}{\lambda(t) + \varphi^T(t) P(t-1) \varphi(t)} \quad (4.28)$$

$$P(t) = \frac{P(t-1)}{\lambda(t)} (I - K(t) \varphi^T(t)) \quad (4.29)$$

Equation (4.24) is seen as an update rule for the parameters, which can also be written with q :

$$\hat{\theta}(t) = \frac{K(t)}{1 - q^{-1}} \varepsilon(t) \quad (4.30)$$

The above can be clarified using Figure 4.5. Here, the RLS algorithm is casted as a feedback control problem. By adjusting the gain vector $K(t)$, the prediction error $\varepsilon(t)$ between $u(t)$, i.e., the observed output at time t , and $\hat{u}(t)$, i.e., the prediction of $u(t)$ based on observations up to time $t-1$, can be minimized. By multiplying the matrix $Q(t)$ with the regression vector $\varphi(t)$, defined in Eq. (4.9), $K(t)$ is computed. Actually, $Q(t)$ is obtained by minimizing the RLS criterion at time t . The computation of $Q(t)$ makes use of the scaled covariance matrix of the parameters $P(t)$. The I in the definition of $P(t)$ denotes the identity matrix. The algorithm is completed by specifying the initial parameter estimate $\hat{\theta}_0 = \hat{\theta}(0)$, the initial regression vector $\varphi(1)$, and the initial scaled covariance matrix $P_0 = P(0)$.



Figure 4.5 RLS estimation from the viewpoint of feedback control, adapted from Tangirala (2015).

The actual covariance matrix of the parameters, i.e., $P_\theta(t)$, can be obtained by multiplying $P(t)$ with $\sigma_\varepsilon^2(t)/2$, where $\sigma_\varepsilon^2(t)$ denotes the variance of $\varepsilon(t)$ (Ljung, 1999, pp. 381–382).

Forgetting factor The forgetting factor is considered as the design variable of the RLS algorithm: it is a trade-off between the ability to track and the sensitivity to noise. By taking a constant forgetting factor, i.e., $\lambda(t) \equiv \lambda$, old measurements are discounted exponentially: a measurement that is

$$T_0 = \frac{1}{1 - \lambda} \quad (4.31)$$

old has a weight equal to λ^{T_0} times the weight of the most recent observation. This T_0 is called the memory horizon of the algorithm. By setting $\lambda < 1$, the parameters can be estimated over time. Commonly, λ is set to a positive value ranging between 0.98 and 0.995 (Ljung, 1999). If a constant forgetting factor is used, the weight in Eqs. (4.21) to (4.23) becomes

$$\beta(t, k) = \lambda^{t-k} \quad (4.32)$$

Choosing a fixed value of λ is suitable for a system that “changes gradually and in a ‘stationary manner,’” (Ljung, 1999) and when it is persistently excited. The value of λ can also be selected in such a way that it depends on the variation rates of the system’s properties or parameters. Ljung (1999) argues that “if the system remains approximately constant over T_0 samples, a suitable choice of λ can then be made from [Eq. (4.31)]” as this “reflects the ratio between the time constants of variations in the dynamics and those of the dynamics itself.”

Numerous other strategies exist for choosing the forgetting profile. A theoretical account on the general concept of forgetting is given by Kulhavý and Zarrop (1993). Here, points of particular interest are given for classical exponential forgetting, regularized exponential forgetting, directional forgetting and mixed forgetting. It especially features a role for prior information. Their main objective has been “to look for the simplest possibility of making estimators reliably adaptive, within a rigorous framework.” Furthermore, they state that, in this particular context, a good estimation algorithm is expected to be:

- (a) effective — the adaptive estimator is to track both constant and time-varying parameters as closely as possible (some trade-off is clearly inevitable);
- (b) robust — whichever data are observed, parameter estimation must generate acceptable results;
- (c) simple — the resulting complexity must not go far beyond the complexity of a non-adaptive algorithm (more complex solutions can be justified perhaps for special applications, but not as a standard tool).

Tangirala (2015) refers to different investigations that consider the use of an adaptive forgetting factor based on levels of excitation and measurement noise. Next, he mentions studies that consider vector-type forgetting, i.e., “to choose different forgetting factors for each parameter because parameters may have significantly differing timescales of variations.” A more practical overview of various RLS algorithms with several forgetting-factor policies is given by Navrátil and Ivanka (2014). They provide brief descriptions for RLS estimation with exponential forgetting, variable exponential forgetting, fixed directional forgetting, adaptive directional forgetting, an exponential forgetting matrix, a constant trace algorithm, and an exponential forgetting and resetting algorithm.

Turning more specifically toward ARX models, Fraccaroli et al. (2015) proposed to split up the classic RLS algorithm into “the minimization of the current prediction error and the minimization of a quadratic function which penalizes the distance between the current and previous value of the estimate.” This allows the modeling of multiple forgetting factors. Hence, different change rates for the estimation parameters can be set. Qin et al. (2010) proposed a recursive penalized weighted least-squares method for estimating ARX models that uses discounted weights and a regularization parameter. They also introduce a general information criterion to select the proper weights, regularization parameters and ARX-model orders. However, both forgetting-factor strategies are only verified for simple case studies, incomparably different to modeling compensatory manual-control behavior.

5

Preliminary simulation analysis

The advances made in simulation software have allowed detailed setups of identification schemes and careful designs of laboratory experiments. This is especially useful in the research on identifying manual-control behavior, as the experiments can be quite intrusive for subjects. By means of offline simulations, significant savings in time and effort on answering specific research questions could be realized and typical pitfalls in identification-scheme setups and experiment designs will be avoided.

This chapter covers the preliminary simulation analysis of the proposed identification scheme. Off-line simulations of the compensatory manual-control model, introduced in Chapter 3, are conducted. In setting up this simulation, reference is made to the work by Zaal (2016). Next, a low-level implementation of the identification framework, set up in Chapter 4, is done. All this, will result in a solid foundation for the further development of the identification scheme based on time-varying ARX models.

The chapter is set out as follows. Section 5.1 describes the setup and the results of the offline simulation of the compensatory manual-control model. The implementation and application of the identification framework is covered in Section 5.2. This section contains a theoretical selection of the ARX-model structure. Numerous ARX models are then estimated on preprocessed data sets using the OLS estimation method. The selection is assessed by means of VAF-contour plots and the principle of parsimony. Lastly, a demonstration is given of the RLS algorithm. Although initial and final analytical expressions of the time-varying simulation are given, this preliminary simulation analysis is concerned with human-operator data sets obtained from simulations in which no time variations were introduced yet in the manual-control behavior. SIMULINK implementation details can be found in Appendix A.

5.1 Compensatory manual-control model simulations

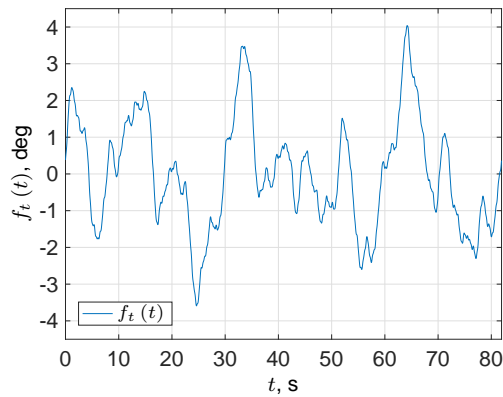
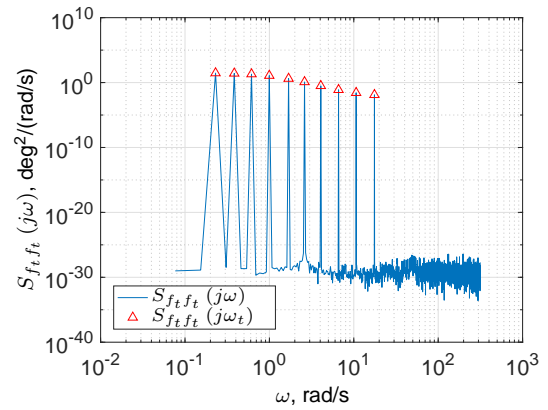
The simulations of the compensatory manual-control model (refer again to Figure 3.1) will be performed in a similar way as described in the work of Zaal (2016). Dynamics in this control model will change from an initial state to a final state. First, details of the type of forcing function are given. Then the results of the controlled-element dynamics, the analytical human-operator dynamics and the corresponding analytical system dynamics are provided for the initial and final state. Next, a step is made toward a more realistic modeling approach. By means of different noise realizations, human-operator remnant is simulated. The operator's input-output data resulting from these simulations can then be used in the identification algorithms.

5.1.1 General simulation setup

Forcing function The system is excited by the target forcing function $f_t(t)$ whose properties are summarized in Table 5.1. Its construction is based on $N_t = 10$ sinusoids. Figure 5.1(a) shows the measurement-time trace of $f_t(t)$. A frequency range of 0.2 to 17.6 rad/s is covered. As described in Section 4.2, the data is sampled with $f_s = 100$ Hz, resulting in a measurement-base frequency of $\omega_m = 0.0767$ rad/s which is used to calculate all ω_t . Furthermore, the amplitude distribution is varied and scaled to attain a variance of $\sigma_{f_t}^2$ of 2.2490 deg². The phase shifts are adjusted so that a crest factor C_r of 2.6930 is obtained. Figure 5.1(b) displays the auto-power-spectral density (PSD) estimates of $f_t(t)$. The peaks of $S_{f_t f_t}(j\omega)$ are located at ω_t .

Table 5.1 Target forcing-function properties adapted from Zaal (2016).

k_t	n_t	ω_t , rad/s	A_t , deg	ϕ_t , rad
1	3	0.230	1.186	-0.753
2	5	0.384	1.121	1.564
3	8	0.614	0.991	0.588
4	13	0.997	0.756	-0.546
5	22	1.687	0.447	0.674
6	34	2.608	0.245	-1.724
7	53	4.065	0.123	-1.963
8	86	6.596	0.061	-2.189
9	139	10.661	0.036	0.875
10	229	17.564	0.025	0.604

**(a)** Time trace.**(b)** Auto-power spectrum.**Figure 5.1** Forcing-function signal.

Controlled-element dynamics As was explained in Section 3.3, a set of initial (1) and a set of final (2) parameter values are considered to set up the sigmoid functions for the controlled-element parameters:

$$K_{CE,1} = 90.0, \quad \omega_{b,1} = 6.0 \text{ rad/s} \quad (5.1)$$

$$K_{CE,2} = 30.0, \quad \omega_{b,2} = 0.2 \text{ rad/s} \quad (5.2)$$

Bode plots of the corresponding controlled-element dynamics, expressible as

$$H_{CE}(j\omega) = \frac{K_{CE}}{(j\omega)^2 + \omega_b j\omega} \quad (5.3)$$

are shown in Figure 5.2(a). In the human operator's crossover-frequency range, in general running from 1 to 5 rad/s, $H_{CE,1}(j\omega)$ approximates single-integrator dynamics ($1/j\omega$), while $H_{CE,2}(j\omega)$ approximates double-integrator dynamics ($1/(j\omega)^2$).

Analytical human-operator dynamics In order to define the parameter functions for the analytical human-operator model, the following sets of initial and final equalization-parameter values are considered

$$K_{v,1} = 0.09, \quad T_{L,1} = 0.4 \text{ s} \quad (5.4)$$

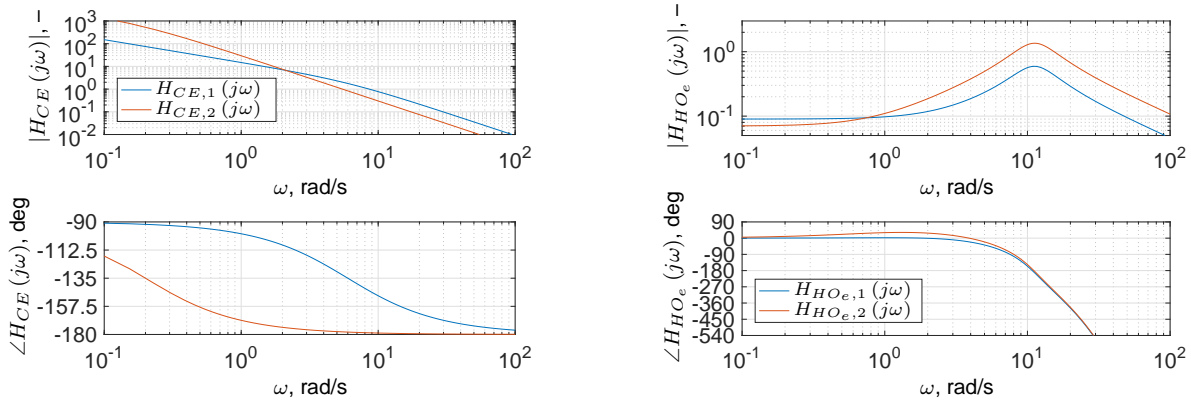
$$K_{v,2} = 0.07, \quad T_{L,2} = 1.2 \text{ s} \quad (5.5)$$

The fixed set of values that is considered for the operator's limitation parameters is

$$\tau_v = 0.28 \text{ s}, \quad \omega_{nm} = 11.25 \text{ rad/s}, \quad \zeta_{nm} = 0.35 \quad (5.6)$$

The above values were determined using data from a test experiment (Zaal, 2016). Bode plots of the resulting analytical human-operator dynamics $H_{HO_e}(j\omega)$ are shown in Figure 5.2(b). These were computed using the time-invariant version of the analytical human-operator model. From Eq. (3.6), this version is described as

$$H_{HO_e}(j\omega) = \underbrace{\underbrace{K_v}_{\text{Gain}} \underbrace{[T_L j\omega + 1]}_{\text{Lead term}}}_{\text{Equalization dynamics: } H_{eq}(j\omega)} \underbrace{\underbrace{e^{-j\omega\tau_v}}_{\text{Time delay}} \underbrace{\frac{\omega_{nm}^2}{(j\omega)^2 + 2\zeta_{nm}\omega_{nm}j\omega + \omega_{nm}^2}}_{\text{Neuromuscular-actuation dynamics: } H_{nm}(j\omega)}}_{\text{Limitations}} \quad (5.7)$$



(a) Controlled-element dynamics.

(b) Analytical human-operator dynamics.

Figure 5.2 Bode plots of the controlled-element dynamics and the analytical human-operator dynamics.

The magnitude Bode plots most clearly show, in the crossover-frequency range, the effect of the different lead-time constants. As dictated by the crossover model, in order to control $H_{CE,2}(j\omega)$ the operator generates more lead for compensating the double-integrator dynamics. Hence, the peak of the neuromuscular-actuation dynamics is lifted.

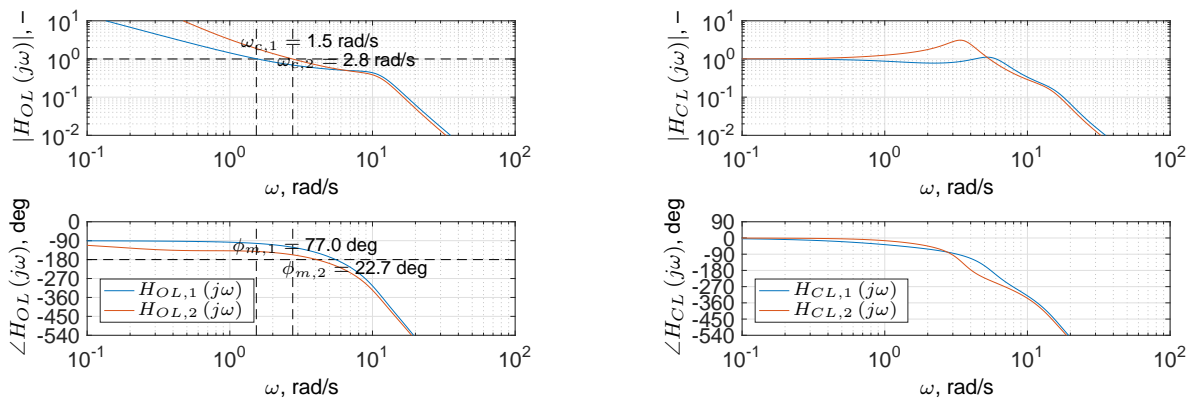
Analytical system dynamics Bode plots of the analytical open- and closed-loop dynamics corresponding to the initial and final sets of the parameter values are shown in Figures 5.3(a) and (b), respectively. Equation (3.3) is used to compute the analytical open-loop dynamics. The analytical closed-loop dynamics are computed by

$$\begin{aligned} H_{CL}(j\omega) &= \frac{H_{OL}(j\omega)}{1 + H_{OL}(j\omega)} \\ &= \frac{H_{HO}(j\omega) H_{CE}(j\omega)}{1 + H_{HO}(j\omega) H_{CE}(j\omega)} \end{aligned} \quad (5.8)$$

From the Bode plots of the analytical open-loop dynamics in Figure 5.3(a), the following crossover frequencies and phase margins can be determined

$$\omega_{c,1} = 1.5 \text{ rad/s}, \quad \phi_{m,1} = 77.0 \text{ deg} \quad (5.9)$$

$$\omega_{c,2} = 2.8 \text{ rad/s}, \quad \phi_{m,2} = 22.7 \text{ deg} \quad (5.10)$$



(a) Open-loop dynamics.

(b) Closed-loop dynamics.

Figure 5.3 Bode plots of the analytical system dynamics.

5.1.2 Toward more realistic simulations

Typically, data sets obtained from manual-control experiments contain high levels of remnant (Zaal et al., 2009). Therefore, the simulation of remnant should be taken into account too. A metric that characterizes the level of remnant in manual-control data is the remnant intensity (also called power ratio) P_n , defined as

$$P_n = \frac{\sigma_n^2}{\sigma_u^2} \quad (5.11)$$

Here, σ_n^2 and σ_u^2 denote the variances of the measurement-time traces of the remnant signal and the control signal, respectively. In order to simulate operator remnant, a zero-mean Gaussian white-noise signal $n_w(t)$ with unit variance is passed through the following first-order time-invariant remnant filter

$$H_n(j\omega) = \frac{K_n}{T_n j\omega + 1} \quad (5.12)$$

The remnant-time constant T_n is set equal to 0.2 s. In this preliminary simulation analysis, the remnant gain K_n is set to induce a certain average value of P_n , based on a set of ten realizations of $n_w(t)$. For this, the nonlinear programming solver `fmincon` in `MATLAB` was used with default options. The total recording time T_t of a simulation run is set to 819.2 s, i.e., a multiple of ten times T_m . A run-in time T_r of 737.28 s will be canceled to reduce the effects of transients in the operator's actions. In order to create the first noise realization for tuning K_n , the seed of the random number generator in `MATLAB` was set to 100. The corresponding K_n with these settings was found to be 0.0202.

Simulation with remnant Figure 5.4 displays the block diagram of a compensatory manual-control model in which no time variations are introduced in both the dynamics of the human operator and the controlled element. The model is referred to as the compensatory manual-control model with time-invariant dynamics. A simulation of this model with P_n set to 0.15 is performed using the sets of parameter values listed in Eqs. (5.1), (5.4) and (5.6). Figure 5.5(a) shows the measurement-time trace of $n(t; \zeta)$,¹ for which the seed was set to 110. The auto-power spectrum of this signal is shown in Figure 5.5(b). This figure also indicates the auto-PSD estimates at ω_t . It can be observed that the auto-power spectrum approximates the remnant-filter characteristics.

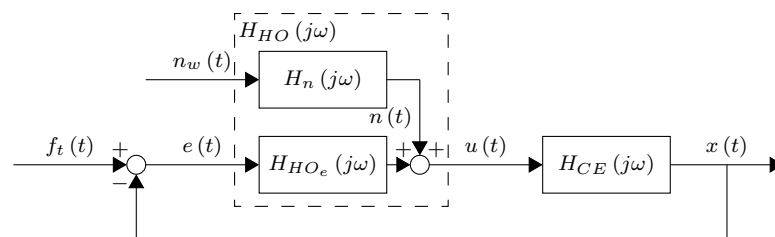


Figure 5.4 Block diagram of a single-loop compensatory target-following control task with time-invariant dynamics, adapted from Figure 3.1.

The corresponding measurement-time traces and the auto-power spectra of $e(t)$, $u(t)$, and $x(t)$ are shown in Figures 5.6 to 5.8, respectively. The signal-to-noise ratio is high for all auto-power spectra. From Figure 5.8, it can be noted that the system output closely follows $f_t(t)$. For this case, the performance score, defined as $\sigma_e^2/\sigma_{f_t}^2$, equals 0.1722.

In addition to the identification method based on ARX models, the nonparametric identification method based on Fourier coefficients (FCs) (van Paassen and Mulder, 1998) is considered as a means of reference. It is, however, only applicable if the dynamics to be identified are assumed to be time invariant during the identification method. The method dictates that “for each frequency response to be estimated an uncorrelated input signal, a forcing function, must be inserted in the closed loop” (Mulder, 1999). The forcing functions act like “black-box” identification inputs. Using the DFTs $U(j\omega; \zeta)$, $E(j\omega; \zeta)$, and $N(j\omega; \zeta)$, the following is obtained from the block diagram in Figure 5.4:

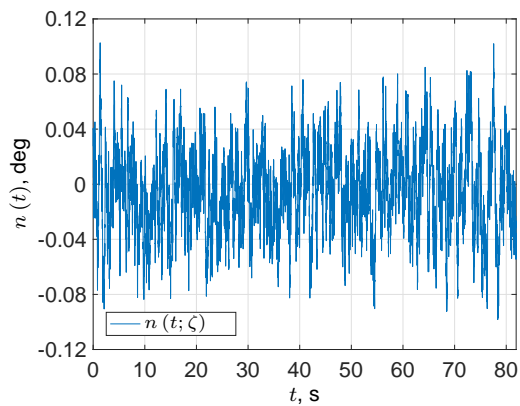
$$U(j\omega; \zeta) = H_{HO}(j\omega) E(j\omega; \zeta) + N(j\omega; \zeta) \quad (5.13)$$

Assuming that the signal-to-noise ratio is high, the frequency-response estimates of the human-operator dynamics can be identified at ω_t with

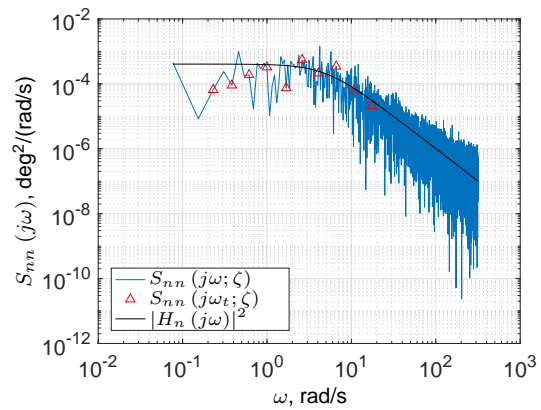
$$\hat{H}_{HO}(j\omega_t; \zeta) = \frac{U(j\omega_t; \zeta)}{E(j\omega_t; \zeta)} \quad (5.14)$$

¹The ζ reflects that the signal is a realization of a stochastic process.

Bode plots of the human-operator dynamics and system dynamics are provided in Figures 5.9 and 5.10. These also include the analytical dynamics. Most frequency responses are correctly estimated.

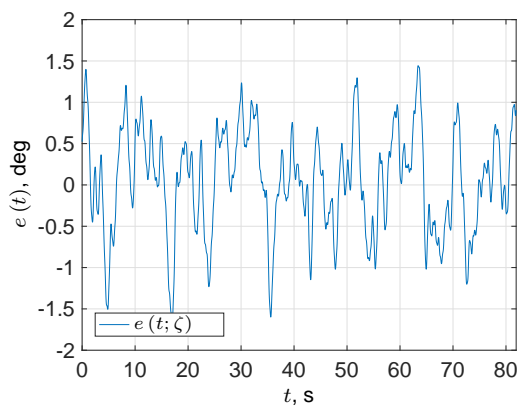


(a) Time trace.

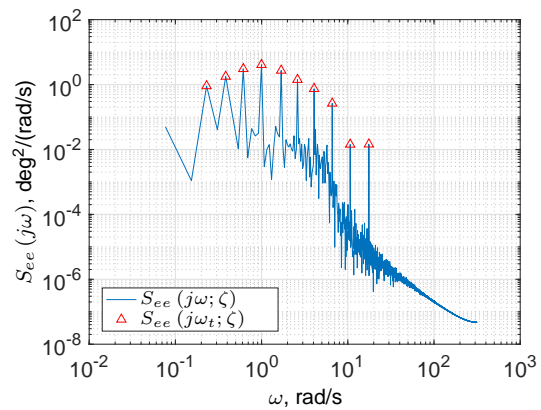


(b) Auto-power spectrum.

Figure 5.5 Remnant signal ($P_n = 0.15$).

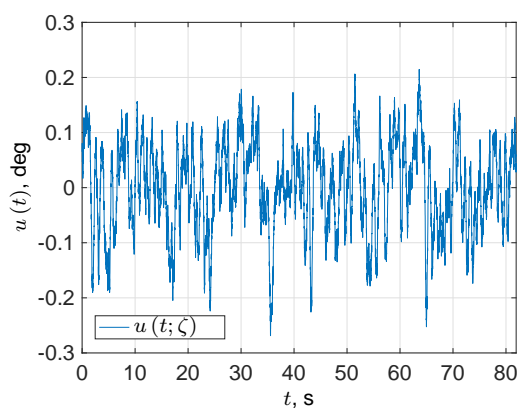


(a) Time trace.

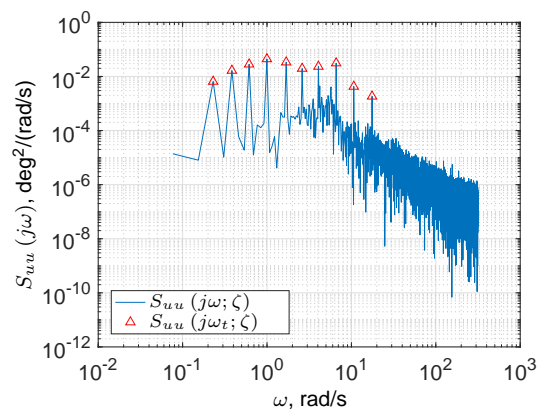


(b) Auto-power spectrum.

Figure 5.6 Error signal ($P_n = 0.15$).

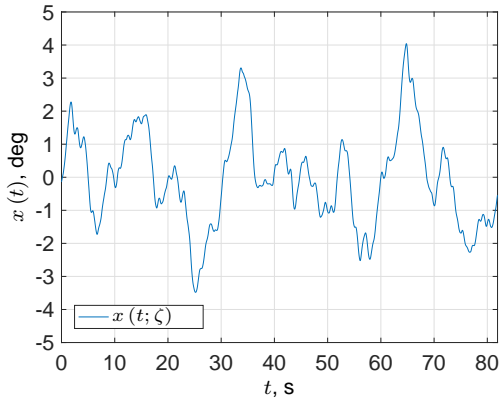


(a) Time trace.

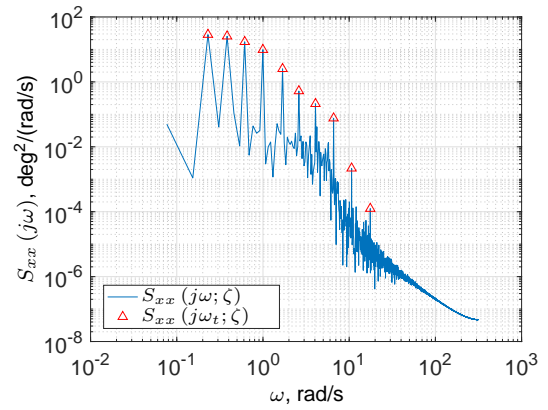


(b) Auto-power spectrum.

Figure 5.7 Control-output signal ($P_n = 0.15$).



(a) Time trace.



(b) Auto-power spectrum.

Figure 5.8 System-output signal ($P_n = 0.15$).

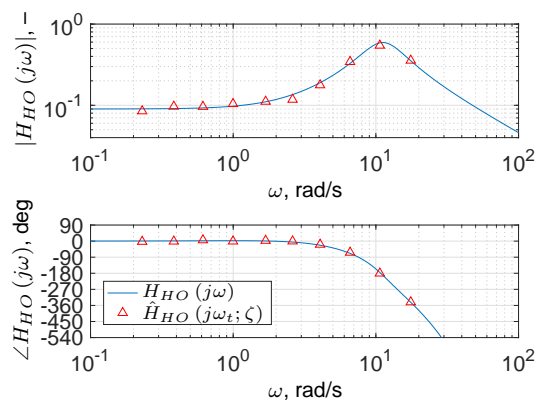
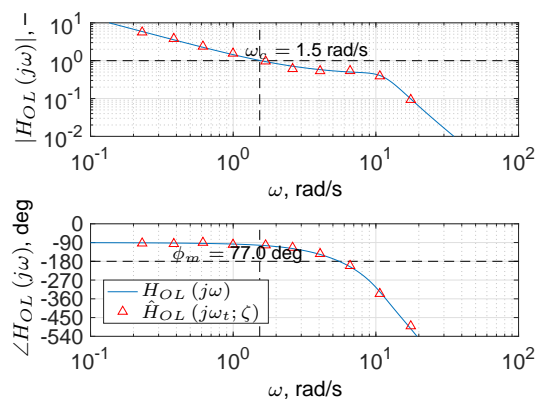
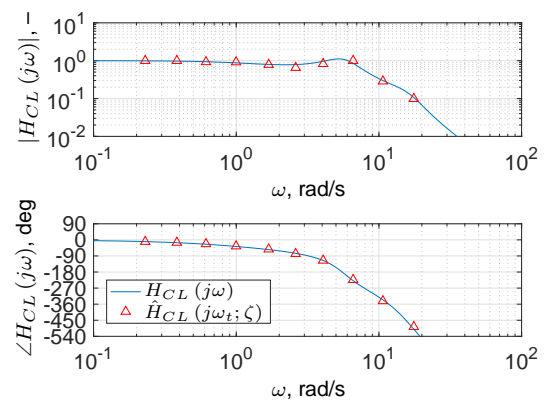


Figure 5.9 Bode plots of the analytical human-operator dynamics and frequency responses identified with the FC method ($P_n = 0.15$).



(a) Open-loop dynamics.



(b) Closed-loop dynamics.

Figure 5.10 Bode plots of the analytical system dynamics and frequency responses identified with the FC method ($P_n = 0.15$).

Remnant-free simulation Figures, similar to Figures 5.6 to 5.10, if remnant is excluded can be found in Appendix B. The same forcing function, with the properties listed in Table 5.1, and sets of parameter values, i.e., the ones listed in Eqs. (5.1), (5.4) and (5.6), are used for simulating the compensatory manual-control model displayed in Figure 5.4.

5.2 Identification-framework implementation and application

Low-level implementations of identification algorithms lead to a full understanding on how they work. This section discusses how the identification framework based on ARX models is implemented and how it will be applied on the different human-operator input-output data sets.

5.2.1 Theoretical selection of the ARX-model orders and delay integer

Care should be taken in the selection of the ARX-model orders, i.e., the integers n_a and n_b , and the delay integer, i.e., n_k . Setting the orders too high, leads to overfitting in the parameter estimation procedure. However, setting the orders too low leads to underfitting. As explained in Section 4.3, the order selection will be based on time-invariant ARX models. The resulting ARX-model transfer function for describing the operator's linear response to the error is expressed by

$$\begin{aligned} G(q; \theta) &= \frac{B(q)}{A(q)} \\ &= q^{-n_k} \frac{b_0 + b_1 q^{-1} + \dots + b_{n_b} q^{-n_b+1}}{1 + a_1 q^{-1} + \dots + a_{n_a} q^{-n_a}} \end{aligned} \quad (5.15)$$

The z-transform The selection of the ARX-model orders can be derived theoretically from the time-invariant version of the analytical human-operator model described in Eq. (5.7). In essence, this description is valid in the continuous-time domain. It is a continuous model of the human operator. ARX models, however, are discrete-time models which identify discrete-time transfer functions. By applying the z-transformation to $H_{HO_e}(j\omega)$, an equivalent discrete-time transfer function can be obtained. Hanson and Jewell (1983), Hess and Mnich (1986), and Hess (1990) provide tables with some common z-transforms of continuous systems. A prospective discrete-time transfer-function structure, in ascending powers of z^{-1} , for a system consisting of a gain, a first-order lead term, a pure time delay (modeled as $e^{-j\omega m}$, where m is an integer multiple of T_s), and a second-order system is:

$$G(z) = z^{-(1+m)} \frac{b_0 + b_1 z^{-1}}{1 + a_1 z^{-1} + a_2 z^{-2}} \quad (5.16)$$

Hence, without considering the time delay, there are four unknowns: two unknown b_i coefficients, i.e., b_0 and b_1 , and two unknown a_i coefficients, i.e., a_1 and a_2 .

Time delay The time delay $e^{-j\omega\tau_v}$ in the ARX models can be approximated with one of the following two methods.

- (1) Using the ARX model's discrete-time delay operator q^{-n_k} , similar to z^{-m} in Eq. (5.16).
- (2) Using extra coefficients a_i and b_i representing a Padé approximant, expressible as

$$e^{-j\omega\tau_v} \doteq \frac{1 - h_1 j\omega\tau_v + h_2 (j\omega\tau_v)^2 + \dots \pm h_k (j\omega\tau_v)^k}{1 + h_1 j\omega\tau_v + h_2 (j\omega\tau_v)^2 + \dots + h_k (j\omega\tau_v)^k} \quad (5.17)$$

with h_k the Padé approximation coefficient at discrete instant k .

As described in Section 4.3, n_k can only be an integer multiple of the sampling time, and consequently, the approximation of τ_v becomes less accurate once higher decimation factors are used. Turning to method (2), Zaal et al. (2009) point out that human-operator delays are typically approximated with fifth-order Padé approximations. This study, however, will make use of both methods (1) and (2). Part of the time delay will be captured using the input-output delay by setting the ARX-model integer n_k , primarily dependent on the decimation factor d . Another part of the time delay is captured by using extra coefficients a_i and b_i . A first attempt will be taken with a first-order variant of the Padé approximant:

$$e^{-j\omega\tau_v} \approx \frac{1 - h_1 j\omega\tau_v}{1 + h_1 j\omega\tau_v} \quad (5.18)$$

Bias term An aspect not yet addressed is the bias in the identification. As the human operator is embedded in a closed loop and the direct identification method will be used, bias will certainly be present. For this one extra numerator term is considered in the ARX model's transfer function.

Conclusive remarks From the above analysis, it is concluded that the number of unknowns for the $A(q)$ polynomial amounts to three, and the number of unknowns for the $B(q)$ polynomial amounts to four (or five) if closed-loop identification issues (with remnant) and a proper capture of the time delay are taken into account. However, a first attempt is to take $n_a = 2$ and $n_b = 2$, based on Eq. (5.16). Depending on the decimation factor d , the right n_k for approximating the time delay might be found

using the second column of Table 4.1 which lists the different sampling times. In order to model a time delay value τ_v of 0.28 s (Eq. (5.6)), the following integer values of $n_k(d)$ are prospected:

$$n_k(1) = 28, \quad n_k(2) = 14, \quad n_k(4) = 7, \quad n_k(8) = 3 \text{ or } 4, \quad n_k(16) = 2 \quad (5.19)$$

5.2.2 OLS estimation of ARX models and selection using VAF-contour plots

As the ARX-model structure allows linear regression, the OLS estimation method is used for the parameter estimation. For the complete input-output estimation data subset Z^{N_e} ,

$$Z^{N_e} = \{e(t), u(t)\}_{t=1}^{N_e} \quad (5.20)$$

the following regression matrix

$$\Phi = \begin{bmatrix} \varphi^T(p) \\ \varphi^T(p+1) \\ \vdots \\ \varphi^T(N_e) \end{bmatrix} = \begin{bmatrix} -u(p-1) & -u(p-2) & \cdots & -u(p-n_a) & e(p-n_k) & e(p-1-n_k) & \cdots & e(p-n'_b) \\ -u(p) & -u(p-1) & \cdots & -u(p+1-n_a) & e(p+1-n_k) & e(p-n_k) & \cdots & e(p+1-n'_b) \\ \vdots & \vdots & \ddots & \vdots & \vdots & \vdots & \ddots & \vdots \\ -u(N_e-1) & -u(N_e-2) & \cdots & -u(N_e-n_a) & e(N_e-n_k) & e(N_e-1-n_k) & \cdots & e(N_e-n'_b) \end{bmatrix} \quad (5.21)$$

and control-output vector

$$\mathbf{u} = \begin{bmatrix} u(p) \\ u(p+1) \\ \vdots \\ u(N_e) \end{bmatrix} \quad (5.22)$$

can be set up. The integer p is set to $\max(n_a + 1, n_b + n_k)$ in order to consider only known input-output data. By making use of the backslash operator “\” in MATLAB, $\hat{\theta}_{N_e}^{OLS}$ can be computed. This operation directly calls a computational efficient QR-factorization solver, provided that the regression matrix is nonsquare.² ARX models are only estimated if the regression matrix is full rank. A transfer function can then be constructed from the entries in $\hat{\theta}_{N_e}^{OLS}$.

Analysis without taking remnant into account Before using the different preprocessed input-output data sets which include remnant, the input-output data set resulting from the remnant-free simulation (Appendix B) is analyzed. Taking as first attempt the set of ARX-model integers $n_a = 2$, $n_b = 2$, and $n_k = 28$, results in the discrete-time frequency-response function shown in the Bode plot of Figure 5.11. In addition, Bode plots of the analytical human-operator model and the FC frequency responses are presented in this figure. The ARX model’s frequency responses almost perfectly fits the analytical transfer function of the human operator. The corresponding VAF-value is 99.9553%. The fit becomes a little bit worse at the higher frequencies. While the FC method only estimates frequency responses at the excitation frequencies of the forcing function, the method based on ARX models gives frequency responses over the full Nyquist frequency range. Figure 5.11 and the VAF-value indicate that the selection of a low ARX-model order and the right delay integer can be sufficient.

VAF-contour plots In order to check if the theoretical selection of the ARX-model orders and delay integers holds for the different preprocessed, i.e., filtered and/or decimated, data sets with remnant ($P_n = 0.15$) included, ranges of the integers n_a , n_b and n_k should be evaluated. The bounds of the ranges considered for different decimation factors are given in Table 5.2. The case of no resampling ($d = 1$) is also included. For all combinations (i.e., a total of 19 800), ARX models are estimated using the OLS method and validated using the VAF-metric. The results for $d = 2$ to $d = 16$ are summarized in VAF-contour plots which can be found in Appendix C. As an example, Figure 5.12 provides VAF-contour plots for ARX-model estimations on the input-output data set that was decimated with $d = 16$. The mesh is defined by the integers n_a and n_b . A VAF-contour plot is made per distinct value of n_k . Empty areas in the bottom-left corners indicate VAF-values less than or equal to 0%. The highest VAF-

²For reference, $\hat{\theta}_{N_e}^{OLS}$ can be compared to the output of the MATLAB function `arx`. Given the measured output and input signals u and e , sampled with time T_s , and the integers n_a , n_b , and n_k , the syntax required in MATLAB R2016b is: `data = iddata(u,e,Ts); data2 = nkshift(data,nk-1); m = arx(data2,[na nb 1]); m.nk = nk;`. In earlier MATLAB releases, the syntax `data = iddata(u,e,Ts); m = arx(data,[na nb nk])` can just be used.

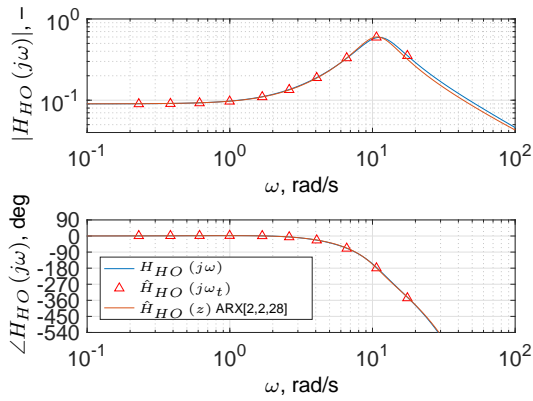


Figure 5.11 Bode plots of the analytical human-operator dynamics and frequency responses identified with the FC method and an ARX model (remnant free).

value in each contour plot is marked with an asterisk. More details can be found in Appendix C. From Figure 5.12 it becomes clear that the VAF-values do not necessarily increase for higher ARX-model orders. Instead, by applying the principle of parsimony, the ARX-model orders should be selected as low as possible. However, the selection cannot be completely based on VAF-contour plots and this principle. Potential combinations of n_a , n_b and n_k should always be compared in Bode plots.

Table 5.2 Bounds of ARX-model integers n_a and n_b , and delay integer n_k for different decimation factors.

d	n_a	n_b	n_k
1	[1..10]	[1..10]	[1..50]
2	[1..10]	[1..10]	[1..25]
4	[1..10]	[1..10]	[1..13]
8	[1..10]	[1..10]	[1..7]
16	[1..10]	[1..10]	[1..4]

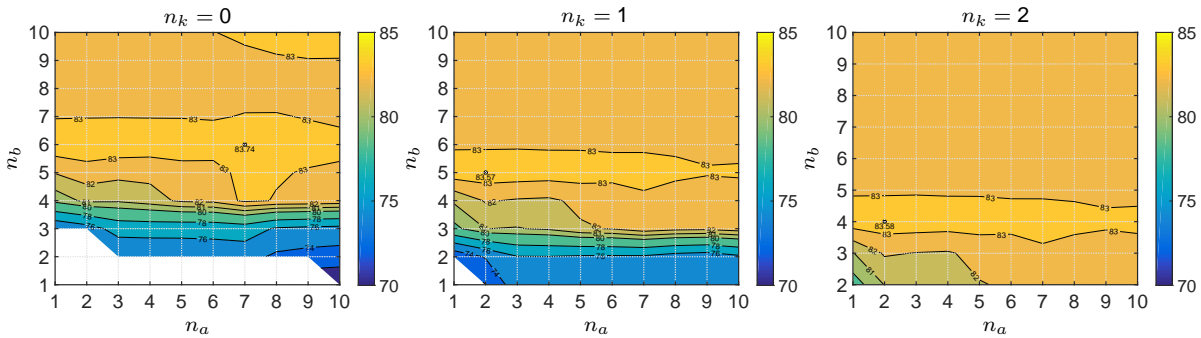


Figure 5.12 High-valued VAF-contour plots: input-output signals decimated with $d = 16$.

Most suitable ARX models Table 5.3 presents an overview of the most suitable integer combinations for the different preprocessed data sets. The case of no resampling ($d = 1$) is considered too. The table also lists the VAF-values, which are all around 80% to 85%. These values are quite reasonable for $P_n = 0.15$. Bode plots of the frequency responses constructed from the ARX models are shown in Figure 5.13. These are compared with the ones of the analytical human-operator model and the FC frequency responses. The most striking feature is that the frequency ranges on which the ARX models are valid differ per decimation factor. The maxima of these ranges are the Nyquist frequencies $\omega_N(d)$ (i.e., the vertical dashed lines). From the Bode phase-angle plots, it can be observed that the ARX models do not differ much. Up until a frequency of 10 rad/s they are very similar and approach the analytical human-operator model. On the contrary, the Bode magnitude plots show big differences. Especially, the ARX models, estimated on data sets that were decimated with $d = 2$ or 4, or that were not resampled ($d = 1$), have great difficulty in describing the peak of the neuromuscular-actuation dy-

namics. Interestingly, for $d = 1, 2$, and 4 , low values for n_a and n_b can be selected. In the analysis it was found that using higher values for these integers did not result in meaningful Bode plots. As shown in Table 5.3 the values of n_k , for $d = 1, 2$, and 4 , correspond to the ones in Eq. (5.19). Hence, in these cases, the time delay τ_v of 0.28 s is captured properly with n_k . However, by making use of $d = 8$ and 16 , higher values for n_a and n_b should be selected. In these cases, τ_v cannot be captured properly by n_k alone. Therefore, two extra coefficients of a_i and b_i are needed to capture a part of it using a Padé approximant like Eq. (5.18). One more coefficient b_i is used to account for the closed-loop bias.

Table 5.3 Most suitable combinations of ARX-model integers n_a and n_b , and delay integer n_k for the different preprocessed data sets based on VAF-contour plots and Bode plots ($P_n = 0.15$).

d	F/NF*	$[n_a, n_b, n_k]$	VAF, %
1	F	[2,2,28]	77.3841
2	NF	[2,2,14]	77.9174
2	F	[2,2,14]	78.5233
4	NF	[2,2,7]	79.0345
4	F	[2,2,7]	80.4681
8	NF	[3,4,4]	82.5968
8	F	[3,4,4]	83.9417
16	NF	[3,4,2]	83.5605
16	F	[3,4,2]	86.0262

*filtered (F); not filtered (NF)

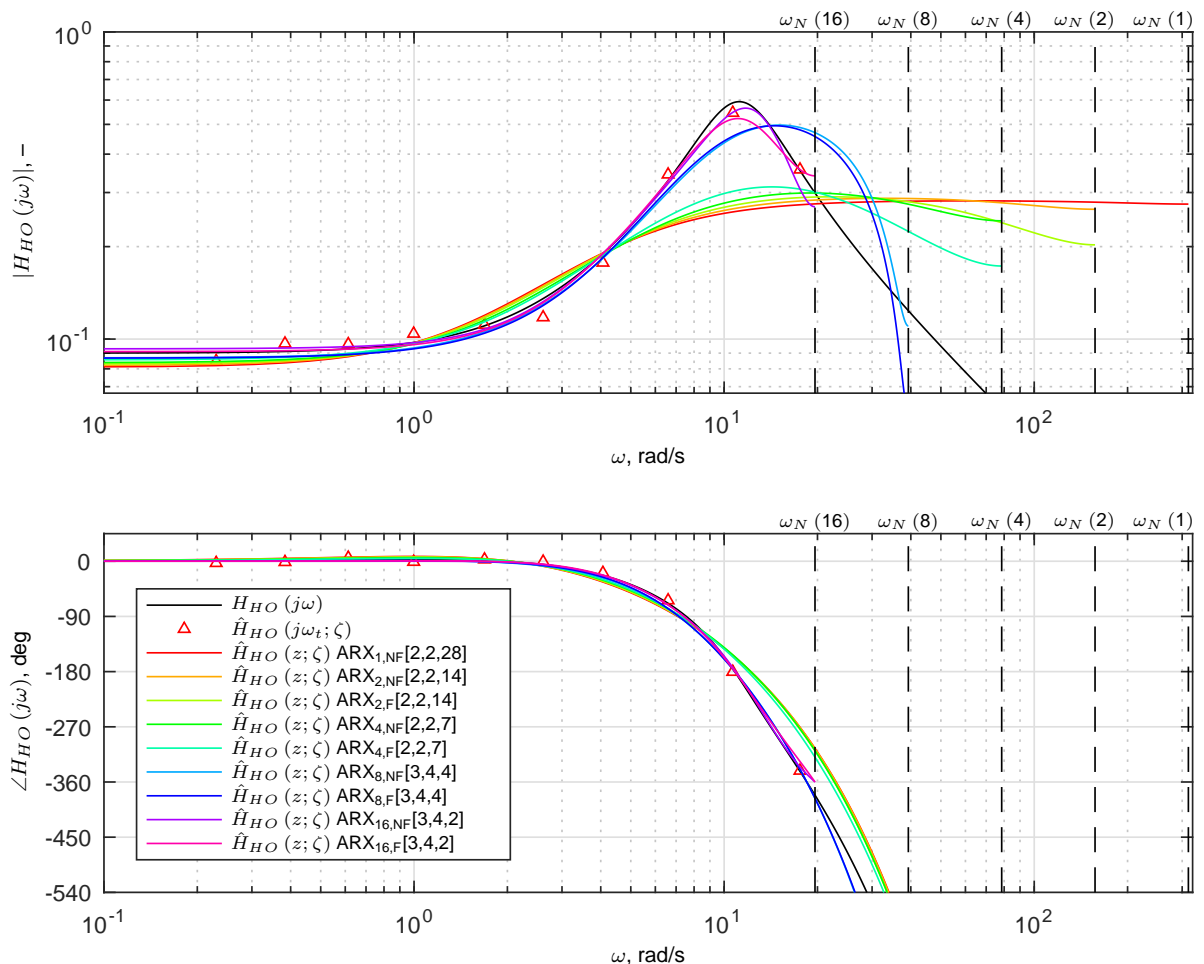


Figure 5.13 Bode plots of the analytical human-operator dynamics and frequency responses identified with the FC method and with the most suitable ARX models for different preprocessed data sets ($P_n = 0.15$).

In essence, Table 5.3 shows that filtering the input-output data sets results in higher VAF-values compared to decimating only. However, the corresponding Bode plots in Figure 5.13 are not necessarily much better. This becomes clear, in particular, when focusing on the Bode magnitude plots of the models $ARX_{16,NF}[3,4,2]$ and $ARX_{16,F}[3,4,2]$. The peak of the neuromuscular-actuation dynamics is better described by the former model. Overall, the results indicate that the human-operator dynamics in the operator's frequency range of interest are best described by the model $ARX_{16,NF}[3,4,2]$.

Conclusive remarks In general, it seems sufficient to only decimate the input-output data sets, at least for the ARX-model structure selection. The further analysis will, therefore, mainly consider decimation as the one and only step in data preprocessing. Next, it is very important to capture the time delay properly. Otherwise, higher orders of n_a and n_b are needed. Taken together, it seems that the theoretical selection holds.

5.2.3 RLS estimation of ARX models

In contrast to the OLS estimation method, the RLS estimation method equipped with forgetting factor is able to track time variations. The following presents a demonstration of the RLS algorithm and provides some details on how it should be implemented and applied. Input-output signals which contain time variations in the dynamics of the human operator and the controlled element are not considered yet. Light is shed on how the RLS algorithm works.

RLS algorithm initialization and OLS method comparison Before the RLS algorithm can be used, the initial parameter estimate $\hat{\theta}_0$, the initial regression vector $\varphi(1)$ and the initial scaled covariance matrix P_0 need to be set. Theoretically, if no information is available about $\hat{\theta}_0$, $\varphi(1)$, and P_0 , the RLS estimation method will only give the same results as the OLS estimation method when an infinite number of samples is used, the forgetting factor λ is fixed to one, and P_0 equals ∞I . In practice, a nearly perfect match between $\hat{\theta}_t^{RLS}$ and $\hat{\theta}_{N_e}^{OLS}$ is obtained, if $\hat{\theta}_0 = \hat{\theta}_{N_e}^{OLS}$, $\lambda = 1$, and a P_0 similar to the covariance matrix of $\hat{\theta}_{N_e}^{OLS}$ are used. Then, the RLS algorithm does not adjust $\hat{\theta}_0$.

Turning more specifically toward the RLS algorithm, care should be taken with the definition of $\varphi(1)$. For regression at time t , the algorithm requires the vector $\varphi(t)$ expressed by Eq. (4.9). In the case that data for $t < 1$ is unknown, a zero vector $\mathbf{0}$ is used for initialization. Often, the vector $\hat{\theta}_0$ is also set equal to $\mathbf{0}$. In order to avoid numerical issues, $\hat{\theta}_0$ can also be initialized to a set of zero-mean unit-variance Gaussian random numbers. Typically, P_0 is set equal to δI , where δ represents a large positive constant. The higher the uncertainty of $\hat{\theta}_0$, the higher the value of δ should be chosen.

Initial scaled covariance matrix By making use of the particular preprocessed input-output estimation data subset and the proposed ARX-model structure, i.e., $ARX_{16,NF}[3,4,2]$, the working of RLS algorithm is demonstrated. Figure 5.14 compares RLS parameter estimations for different initializations of P_0 when $\lambda = 1$ is used. Values for δ of 10^2 , 10^4 , and 10^6 were considered. Zero vectors were used for $\hat{\theta}_0$ and $\varphi(1)$. In addition, Figure 5.14 shows the coefficients of $\hat{\theta}_{N_e}^{OLS}$ with dashed lines. It can be observed that the use of high values for δ will result in high initial responses in the RLS parameter estimation. However, the difference between setting δ equal to 10^4 or 10^6 appears to be small. In the further analysis, a δ value of 10^4 will be considered.

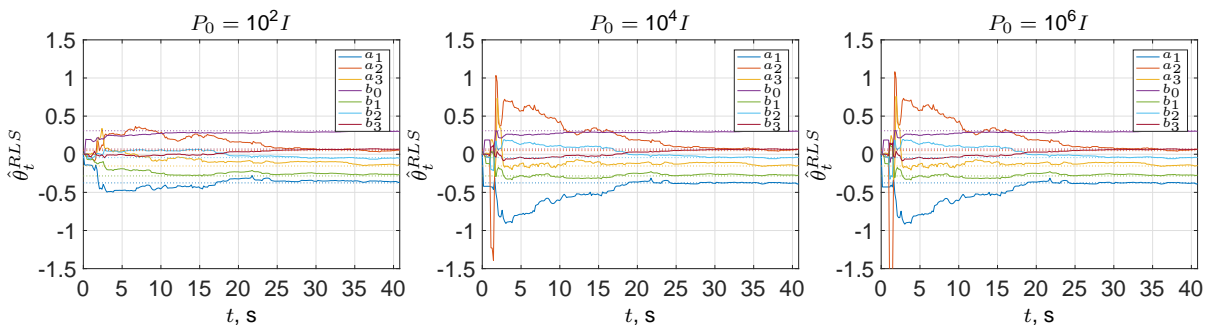
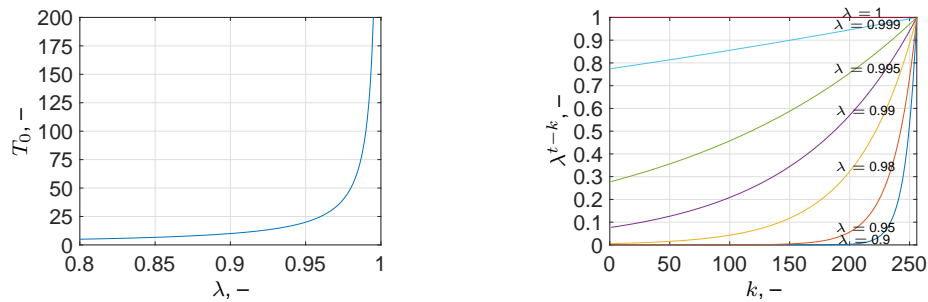


Figure 5.14 RLS parameter estimations for different initial scaled covariance matrices with $\lambda = 1$ ($\hat{\theta}_0 = \mathbf{0}$, $\varphi(1) = \mathbf{0}$, $P_n = 0.15$). Coefficients of $\hat{\theta}_{N_e}^{OLS}$ are indicated with the dashed-lines.

Influence of the forgetting factor Before trying out different forgetting factors, a view is given on the concept of the memory horizon ($T_0 = 1/(1 - \lambda)$) and the RLS weight in the case a constant forgetting factor is used (i.e., $\beta(t, k) = \lambda^{t-k}$). Figure 5.15(a) shows T_0 for different λ . Figure 5.15(b) shows the forgetting profiles for different constant forgetting factors. In this case, the t in λ^{t-k} was set to $N_e = 256$. It can be seen that for smaller λ , old data is discounted quicker.

A comparison of RLS parameter estimations with different forgetting factors is shown in Figure 5.16. Coefficients of the $\hat{\theta}_{N_e}^{OLS}$ are also displayed. Apparently, no reasonable RLS estimation results are obtained for values of $\lambda < 0.99$. Next, in almost all cases, the estimation rate of each coefficient is similar, e.g., b_0 approaches its final value very fast, while a_0 reaches its final value relatively slow. Furthermore, it can be seen that through the use of $\lambda < 1$ the initial estimate will become obsolete.



(a) Memory horizon.

(b) RLS weight ($t = 256$ samples).

Figure 5.15 Influence of different constant forgetting factors on the memory horizon and the RLS weight.

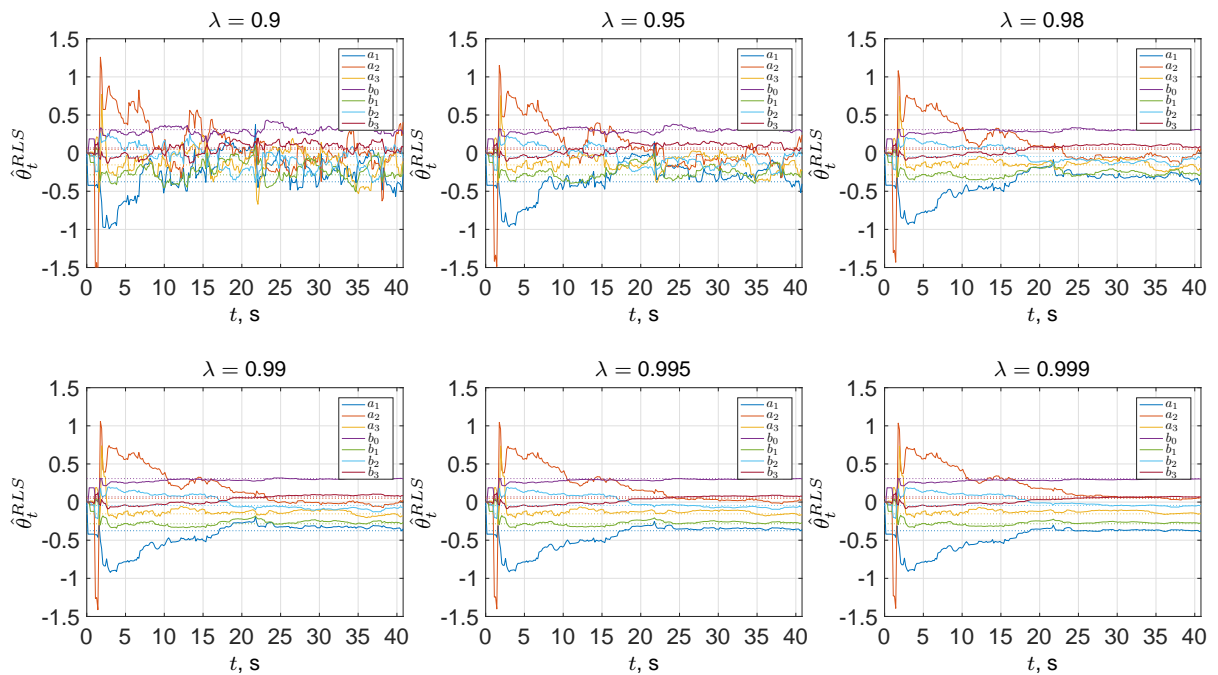


Figure 5.16 RLS parameter estimations for different forgetting factors ($P_0 = 10^4 I$, $\hat{\theta}_0 = \mathbf{0}$, $\varphi(1) = \mathbf{0}$, $P_n = 0.15$). Coefficients of $\hat{\theta}_{N_e}^{OLS}$ are indicated with the dashed-lines.

Conclusive remarks The input-output data analyzed with the RLS estimation method was obtained from a compensatory manual-control model simulation with time-invariant dynamics. No abrupt or gradual changes were considered in the system yet. It would be more interesting to analyze such data. For instance, the tracking ability and noise sensitivity of the RLS can then be investigated in more detail. However, some of the ins and outs of the algorithm have been demonstrated.

6

Further research proposal

By means of the literature survey and the preliminary simulation analysis, the majority of the research subquestions has been answered and most research subgoals have been accomplished. The proposed thesis project will not only deal with the remainder, but also with some new thoughts that resulted from the iterative-parallel research progression.

This chapter is concerned with the further steps to be taken in the proposed thesis project. In view of the cybernetic approach adopted in this project (refer to Chapter 1), these steps are related to the two stages. A number of steps belong to the further analysis of the compensatory manual-control model simulation with time-varying dynamics, and a number of steps correspond to the capture of time-varying manual-control behavior. Furthermore, this chapter highlights the steps needed for verification and validation of the identification method. In addition, some interesting future research is described.

The outline of the chapter is as follows. Section 6.1 discusses what is needed for the more advanced simulations. Section 6.2 explains how the estimation with time-varying ARX models can be improved. The procedure of verification and validation is addressed in Section 6.3. Lastly, the interesting recommended future research that is in line with the thesis project, but that will not be considered further, is listed in Section 6.4.

6.1 Compensatory manual-control model simulation with time-varying dynamics

The likely time variations to be introduced in simulating manual-control behavior for both slow and fast parameter transitions in the controlled-element dynamics were determined in Section 3.3. Sigmoid functions will be used for the parameter variations. Although Bode plots of the initial and final analytical dynamics of the human-operator and the system for the time-varying simulation were given, sigmoid functions were not yet analyzed in Chapter 5. In the further research, the sigmoid functions will be implemented in both the operator's equalization parameters as well as the controlled-element parameters. The initial type of sigmoid function to be implemented (refer to Eq. (3.8)) is one with a maximum rate of change G of 0.5 s^{-1} , which will be set on $M = T_m/2$. Using this value of G , the parameter transitions are then in between gradual and abrupt ones. The sigmoid functions for the operator's equalization parameters can be expanded with an additional perturbation. This will be more realistic than assuming that the values of M are equal for both the operator's equalization and the controlled-element parameters. Subsequently, lower and higher values of G can be selected to simulate gradual and abrupt parameter transitions, respectively.

In Chapter 5, only a remnant-free simulation and a simulation with a remnant intensity P_n of 0.15 have been analyzed. Higher and lower remnant intensities should also be examined in order to test the robustness of the identification method. This robustness testing will be explained further in Section 6.3. Anyway, the compensatory manual-control model with time-varying dynamics should also be simulated with remnant intensities of 0 (remnant free), 0.05, 0.10, 0.15, 0.20 and 0.25.

6.2 Further steps in ARX-model selection and RLS estimation

In the selection of the most suitable ARX models, it was found that problems occurred in capturing the time delay once higher decimation factors were used. The integer n_k can only be an integer multiple of the downsampling time after input-output data sets are decimated. In contrast to this, the input data could also be shifted by the number of time steps associated with the assumed time delay before the data set is decimated. This was also done in the research by Boer (1995).

Turning to the proposed time-varying RLS estimation method, it has been found that some promising forgetting-factor strategies are available. However, these are not specifically tuned for the identification of manual-control behavior. In the literature survey, it has been found that especially for this application, novel identification and estimation algorithms should be as effective, as robust and as simple as possible. Therefore, a conservative approach will be taken in the tuning of the forgetting factor in the RLS algorithm. A start will be made with the classic exponential forgetting factor. Gradually, more advanced forgetting-factor strategies, like exponential forgetting and resetting (refer again to Navrátil and Ivanka (2014)), will be implemented and tested.

6.3 Verification and validation procedure

In order to verify the sensitivity of the identification method based on time-varying ARX models to different remnant levels and realizations, extensive testing is needed, i.e., a Monte-Carlo analysis should be performed. Instead of using one white noise realization for the remnant modeling, numerous should be considered. Consecutively, variance, bias and other statistical calculations can be performed. The paper by Nieuwenhuizen et al. (2008) explains how the variance and bias of ARX models can be calculated. The paper by Zaal et al. (2009) provides a method to investigate average parameter bias for different remnant levels. Snapshots of Bode plots will be made in order to evaluate the time variations of the ARX models visually.

The identification method can be validated by analyzing real time-varying experimental manual-control data. This will be done once the verified identification method seems to be accurate. For instance, the data from an experiment described in the paper by Zaal (2016) could be requested and investigated.

6.4 Recommended future research

Some interesting research that is related to the thesis project, but that will not be considered further, can be described as follows.

- Focusing on time-varying manual-control behavior, in addition to changes in the controlled-element dynamics, two other types of time-varying control situations possible are (Phatak and Bekey, 1969):
 1. a change in the input characteristics, e.g., statistical or transient variations;
 2. a change in the display, e.g., compensatory to pursuit or vice versa and preview variations.
 The identification method based on time-varying ARX models might also be suitable to investigate the effects of such changing situations.
- Besides OLS and RLS estimation, a parametric estimation method not yet considered is the estimation based on smoothers. These can be seen as batch estimators that can handle time-varying system dynamics, as they can estimate model parameters at each time instance (Boer, 1995). They are only suitable for offline identification. The thesis project, however, focuses on online identification. Still, it might be interesting to compare all parametric estimation methods in the offline case.
- Decent comparisons should be made between the identification method based on time-varying ARX models and other novel time-varying identification methods for capturing adaptive manual-control behavior. The genetic MLE procedure by Zaal (2016) is already at hand. As surveyed in Chapter 1, attempts are undertaken to capture (part of the) manual-control behavior by means of wavelet transforms and LPV subspace methods. Very recently, Pronker (2016) studied changes in neuromuscular admittance with global LPV models based on local LTI models. Duarte (2016) assessed the viability of LPV predictor-based subspace identification on the time-varying human-in-the-loop problem. Active research is conducted by Rojer (2016) to identify time-varying manual control with the use of an unscented Kalman filter.

7

Conclusions

The literature survey has shown that there exists a great lack of knowledge on how human operators manage their ability of adaptation due to various changes of variables over time. The biggest adaptation changes are expected for changes in task variables, in particular for transitions in the controlled-element dynamics. Furthermore, it has become clear that well-established system identification techniques are not capable to capture such time-varying manual-control behavior of adaptation in system-theoretical models. However, most successful models developed so far for describing manual-control behavior make use of quasi-linear models that follow the dictates of the crossover model.

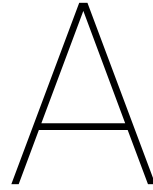
The proposed thesis project will contribute to fill up a part of the knowledge gap of how operators adapt their manual-control behavior, in compensatory tracking tasks, due to transitions in the controlled-element dynamics. A cybernetic approach and the concept of system identification will be used for this. Over the years, TU Delft's Control and Simulation chair has gained extensive knowledge of and experience with linear time-invariant (LTI) autoregressive exogenous (ARX) models for time-invariant human-operator identification. However, no attempts have been made to make use of linear parameter-varying models, i.e., to take the LTI model representation as basic building block and then to employ a recursive least-squares algorithm equipped with forgetting factor on the model parameters for capturing time-varying operator behavior. It seems, therefore, very promising to implement an identification method based on such time-varying ARX models.

The current state of knowledge in the field does not provide a universal approach to be taken in the simulating time-varying manual-control behavior. Guidelines are available on how to model the human operator in compensatory tracking tasks, but these are mainly based on the assumption that manual-control behavior can be considered as time invariant during the identification period. In this research, the time-variations in both the human-operator dynamics as well as the controlled-element dynamics will be introduced by making use of sigmoid functions. This can be seen as restrictive, however, no other reasonable justifications are available.

An identification scheme based on ARX models was set up and implemented. The direct approach for closed-loop identification was applied. Both filtering and decimation were selected as the preprocessing steps to subject human-operator input-output data. In order to make the crucial decision of the ARX-model structure, both physical insight and the principle of parsimony were considered. The intuitive variance accounted for (VAF) metric was selected as the assessment criterion to compare different ARX models. Both the estimation methods of ordinary least squares and recursive least squares equipped with forgetting factor were explained and demonstrated.

For the further development and tuning of the time-varying ARX-model identification method, extensive offline simulations will be performed. Monte-Carlo testing is employed to verify the method's sensitivity to different remnant levels and realizations and to give the method statistical significance. Real experimental manual-control data will only be used to validate the method once it has realized its full potential in the simulation environment.

Taken together, it can be concluded that a strong foundation is laid for the setup of compensatory manual-control model simulations with time-varying dynamics, and for the further development of the time-varying identification method based on ARX models.



Simulation setup of the compensatory manual-control model with time-invariant dynamics

A high-level block diagram of the compensatory manual-control model with time-invariant dynamics was given in Chapter 5 of Part II . This diagram is repeated in Figure A.1. Figure A.2 shows the corresponding SIMULINK block diagram. In order to compute the states of the model during the simulation, the fixed-step solver ode4 is selected with the step size set to $\Delta t = 0.01$. This solver uses the fourth-order Runge-Kutta (RK4) formula. The operator’s visual time delay is modeled with a “Transport Delay” block without using linearization.

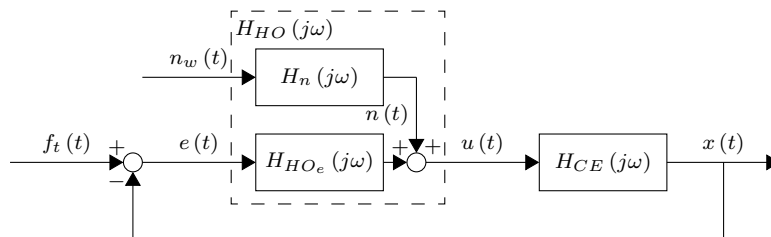


Figure A.1 Block diagram of a single-loop compensatory target-following control task with time-invariant dynamics. Figure 5.4 repeated.

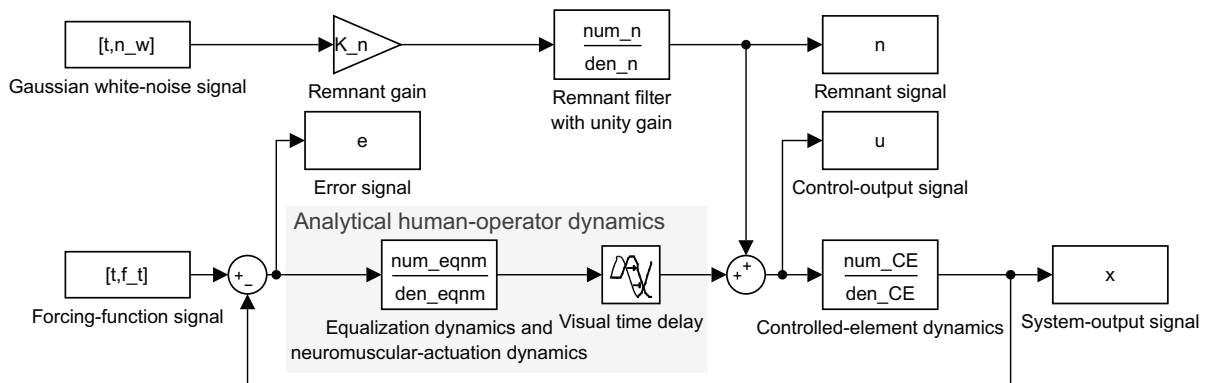


Figure A.2 SIMULINK implementation of the compensatory manual-control model with time-invariant dynamics.

B

Remnant-free simulation of the compensatory manual-control model with time-invariant dynamics

This appendix contains the set of figures for the remnant-free simulation of the compensatory target-following control task with time-invariant dynamics. A block diagram of this setup is shown in Figure B.1. The human operator is considered as a perfect controller, i.e., $H_{HO}(j\omega)$ equals $H_{HO_e}(j\omega)$, who responds, using control signal $u(t)$, on the error $e(t)$ between the target-forcing function $f_t(t)$ and the system output $x(t)$ of the controlled-element dynamics $H_{CE}(j\omega)$. Target-forcing function properties can be found in Table 5.1. The set of parameter values for $H_{HO_e}(j\omega)$ is

$$K_v = 0.09, \quad T_L = 0.4 \text{ s}, \quad \tau_v = 0.28 \text{ s}, \quad \omega_{nm} = 11.25 \text{ rad/s}, \quad \zeta_{nm} = 0.35 \quad (\text{B.1})$$

For $H_{CE}(j\omega)$, the set of parameter values is

$$K_{CE} = 90.0, \quad \omega_b = 6.0 \text{ rad/s} \quad (\text{B.2})$$

The red triangles in Figures B.2 to B.4 indicate auto-power-spectral density estimates at ω_t . Frequency-response estimates identified at ω_t with the Fourier-coefficient (FC) method are included in the Bode plots of Figures B.5 to B.6. The performance score $\sigma_e^2/\sigma_{f_t}^2$ for this simulation was found to be 0.1765.

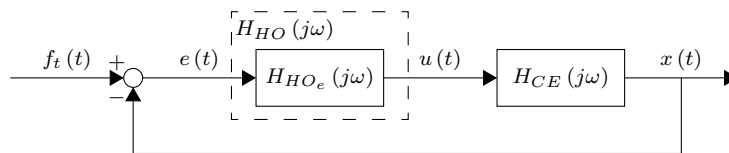
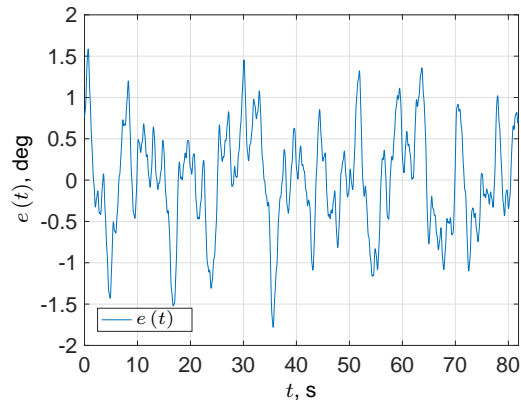
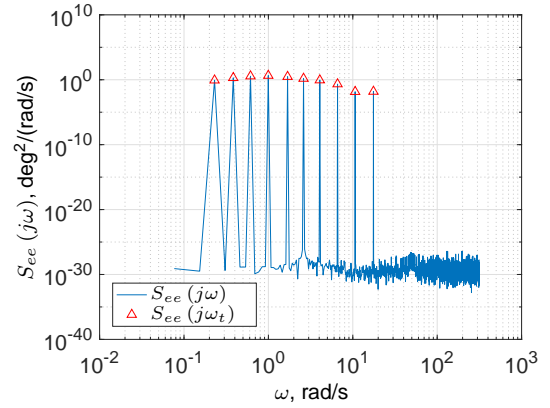


Figure B.1 Block diagram of a single-loop compensatory target-following control task with time-invariant dynamics excluding remnant.

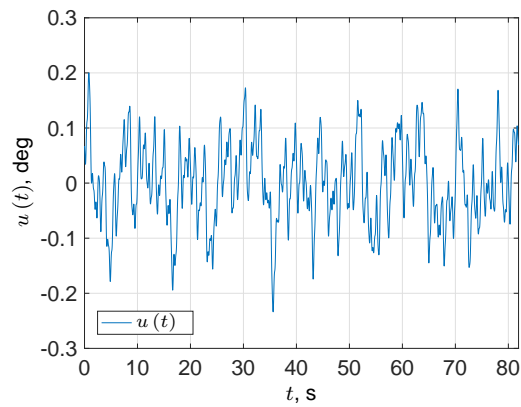


(a) Time trace.

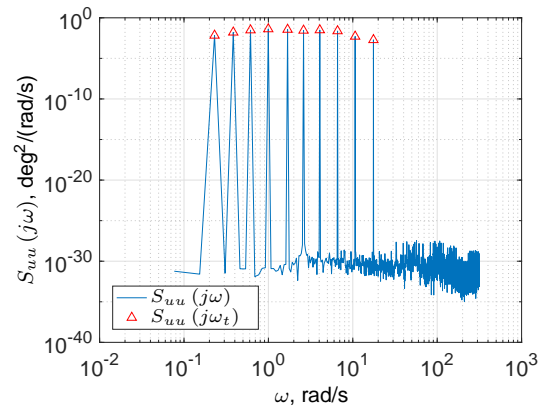


(b) Auto-power spectrum.

Figure B.2 Remnant-free error signal.

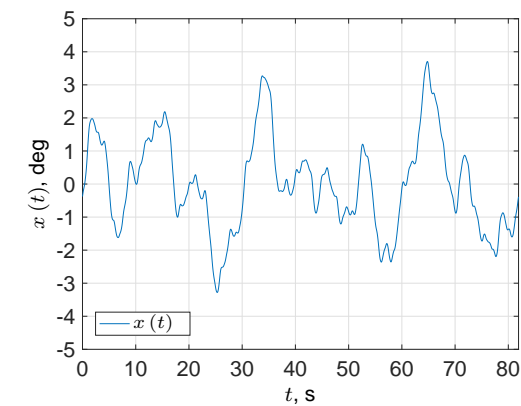


(a) Time trace.

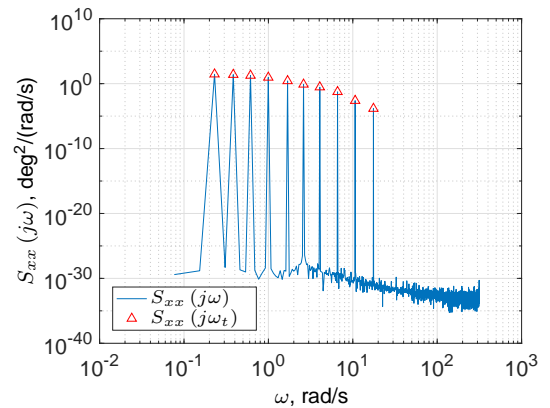


(b) Auto-power spectrum.

Figure B.3 Remnant-free control-output signal.



(a) Time trace.



(b) Auto-power spectrum.

Figure B.4 Remnant-free system-output signal.

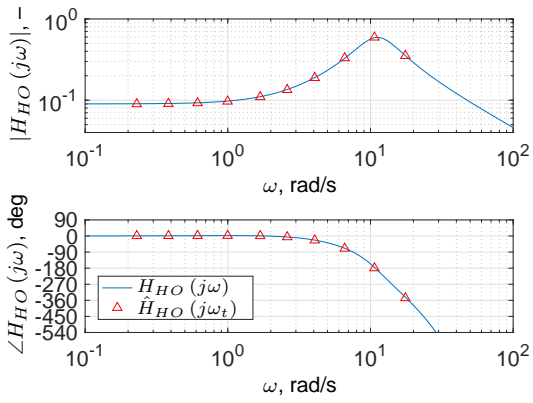
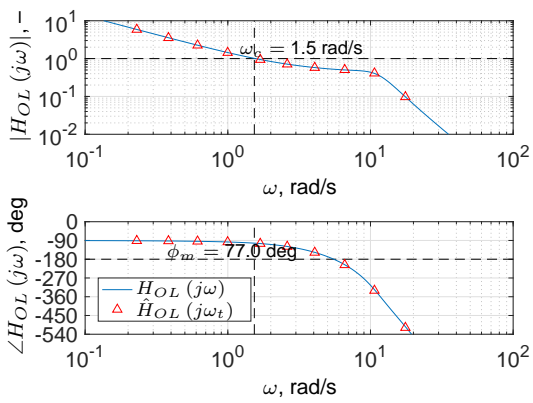
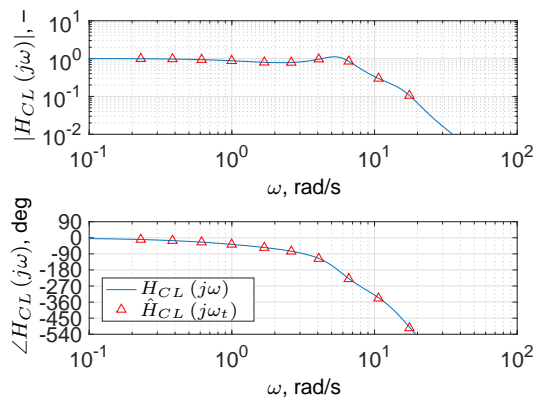


Figure B.5 Bode plots of the analytical human-operator dynamics and frequency responses identified with the FC method (remnant free).



(a) Open-loop dynamics.



(b) Closed-loop dynamics.

Figure B.6 Bode plots of the analytical system dynamics and frequency responses identified with the FC method (remnant free).

C

VAF-contour plots

The figures in this appendix display the contour plots of the variance accounted for (VAF) values for ARX-model estimations on different preprocessed input-output data sets. The original data sets had a remnant intensity P_n of 0.15. Using these contour plots parsimonious selections can be made on the ARX-model integers n_a and n_b and the delay integer n_k . Figures C.1 to C.8 each consider a data set that is filtered and/or decimated with a factor d of 2, 4, 8 or 16. The integers n_a and n_b both range from 1 to 10. Different ranges of the integer n_k are considered per decimation factor. The bounds of these ranges are listed in Table C.1.¹ The contour plots are created using vertices from the mesh defined by n_a and n_b . Each contour plot in a figure considers a different value for n_k . In Figures C.1 to C.8 the contour lines vary from 40% (“unreliable” model) to 80% (“good” model) in steps of 10% and a color-axis scaling is used with limits of 40% and 90%. Figures C.9 to C.12 again consider the input-output data sets decimated with a factor 8 or 16. The VAF-values in these contour plots are much higher and therefore the contour lines vary from 72% to 85% in steps of 1% and a color-axis scaling is used with limits of 70% and 85%. Empty areas in the bottom-left corners indicate that VAF-values are less than or equal to 0%. Empty areas in the upper-right corners indicate that the regression matrices were rank deficient. The corresponding integers were not considered in the estimation of the ARX models. The highest VAF-value in each contour plot is marked with an asterisk.

Table C.1 Bounds of ARX-model integers n_a and n_b , and delay integer n_k for different decimation factors. Table 5.2 repeated.

d	n_a	n_b	n_k
1	[1..10]	[1..10]	[1..50]
2	[1..10]	[1..10]	[1..25]
4	[1..10]	[1..10]	[1..13]
8	[1..10]	[1..10]	[1..7]
16	[1..10]	[1..10]	[1..4]

¹Meaningless VAF-contour plots for high values of n_k are not shown in this appendix.

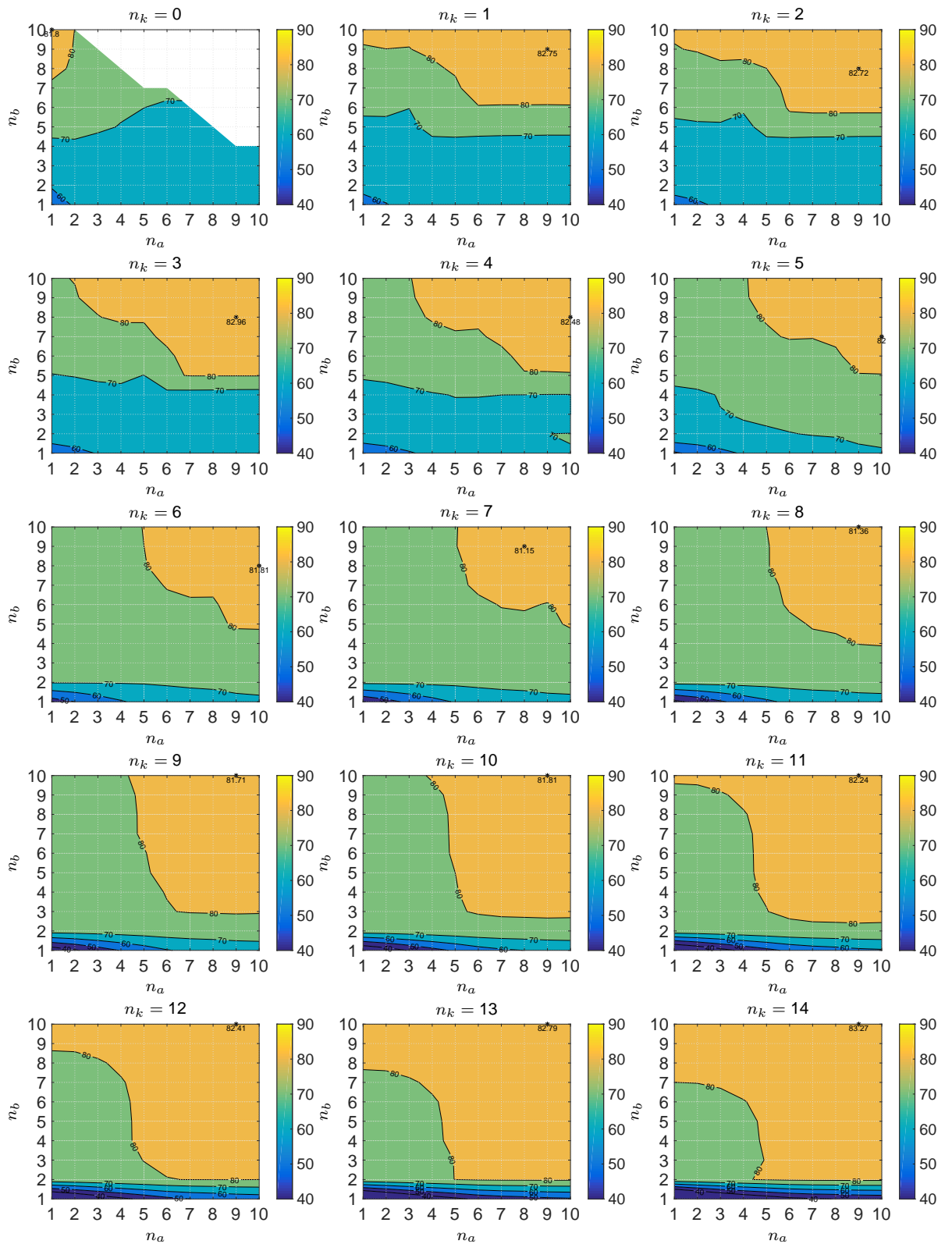


Figure C.1 VAF-contour plots: input-output signals decimated with $d = 2$ ($P_n = 0.15$).

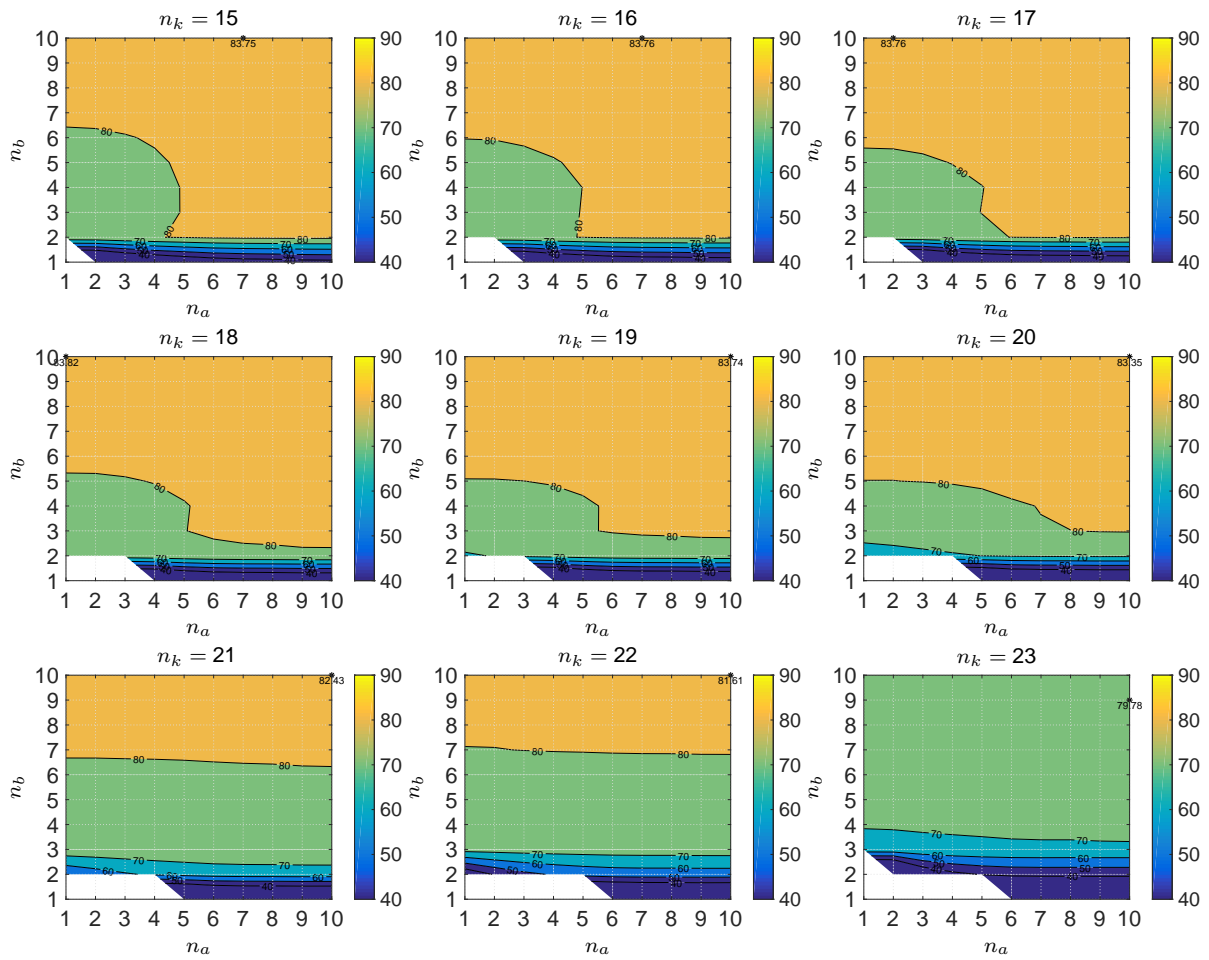


Figure C.1 (continued)

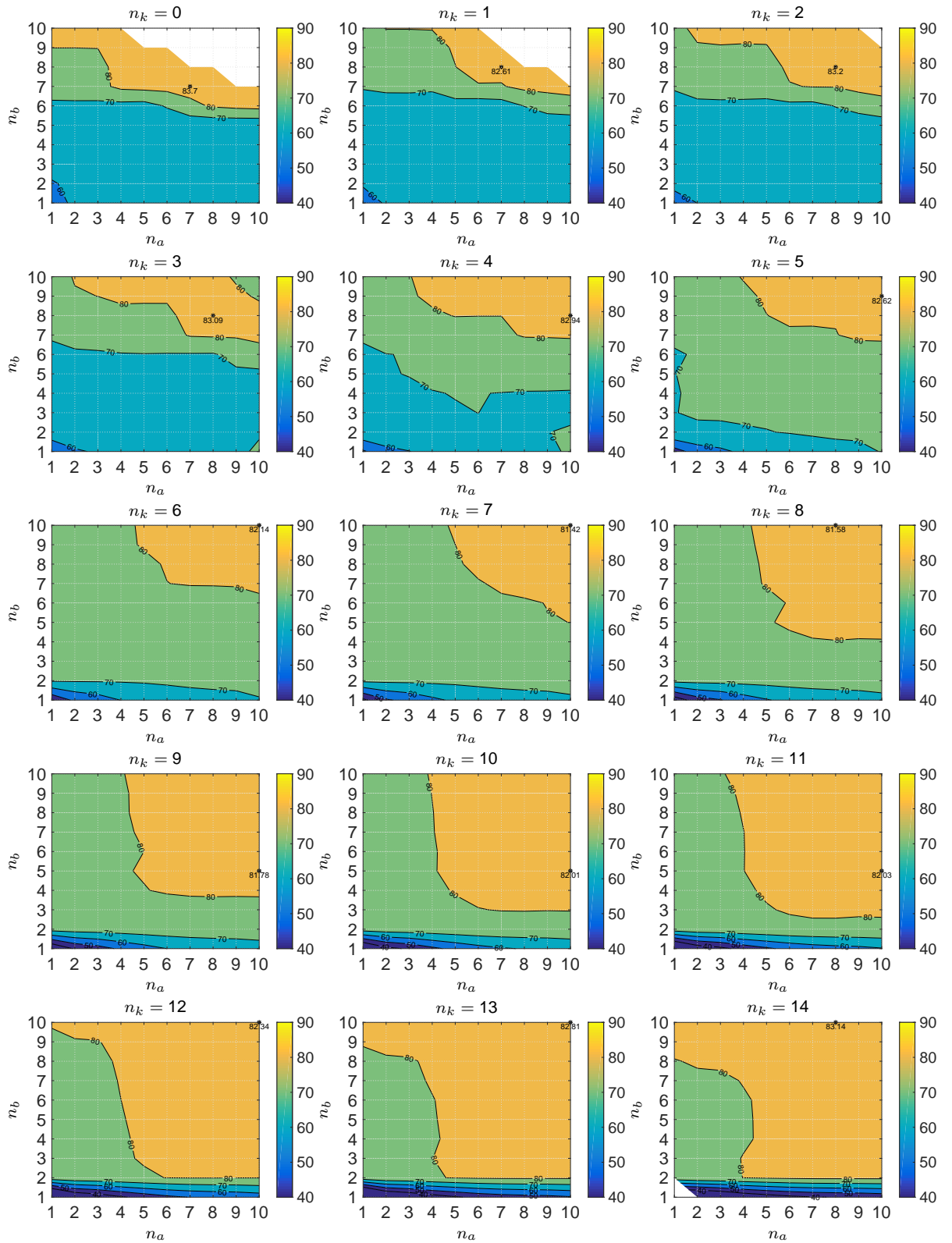


Figure C.2 VAF-contour plots: input-output signals filtered and decimated with $d = 2$ ($P_n = 0.15$).

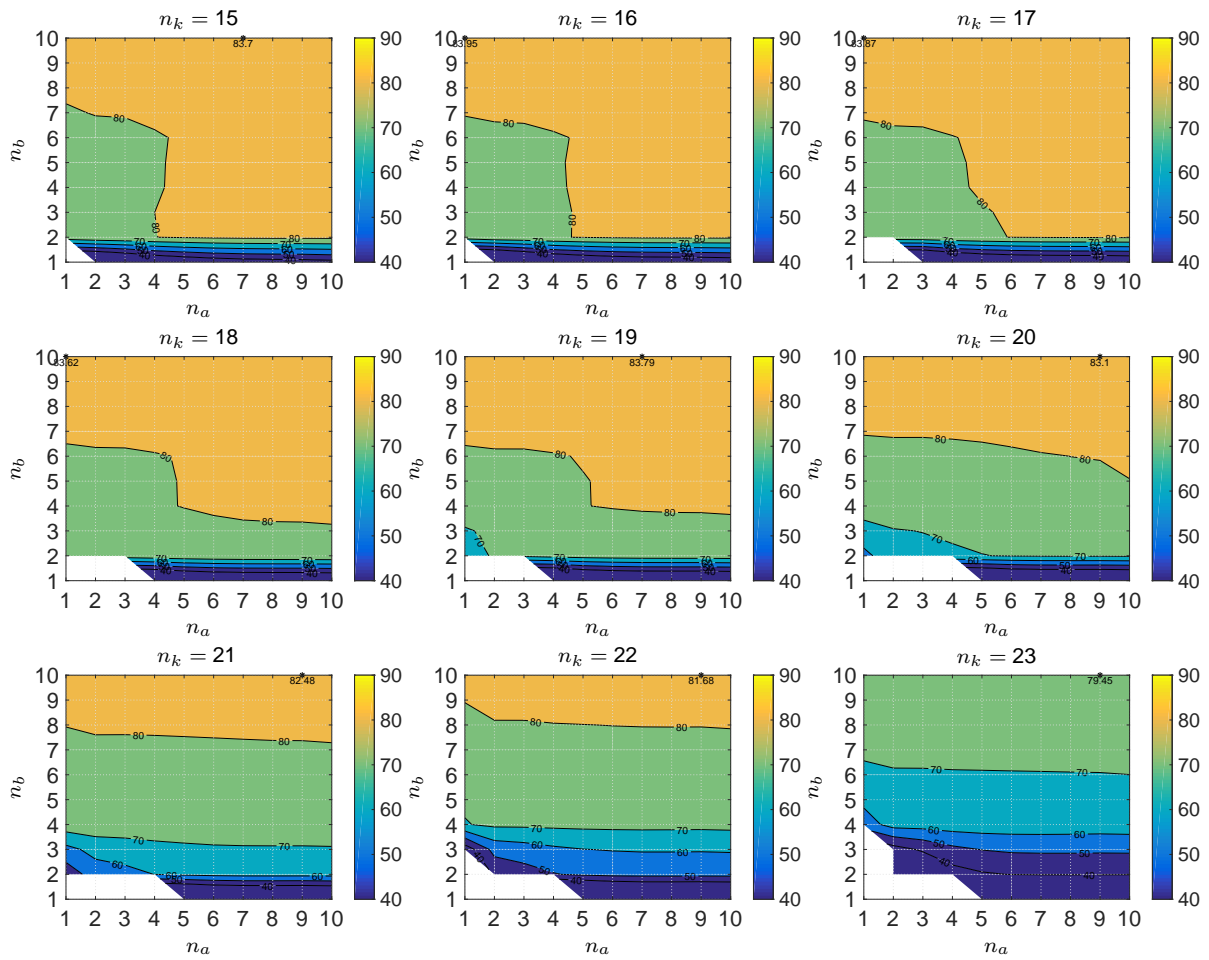


Figure C.2 (continued)

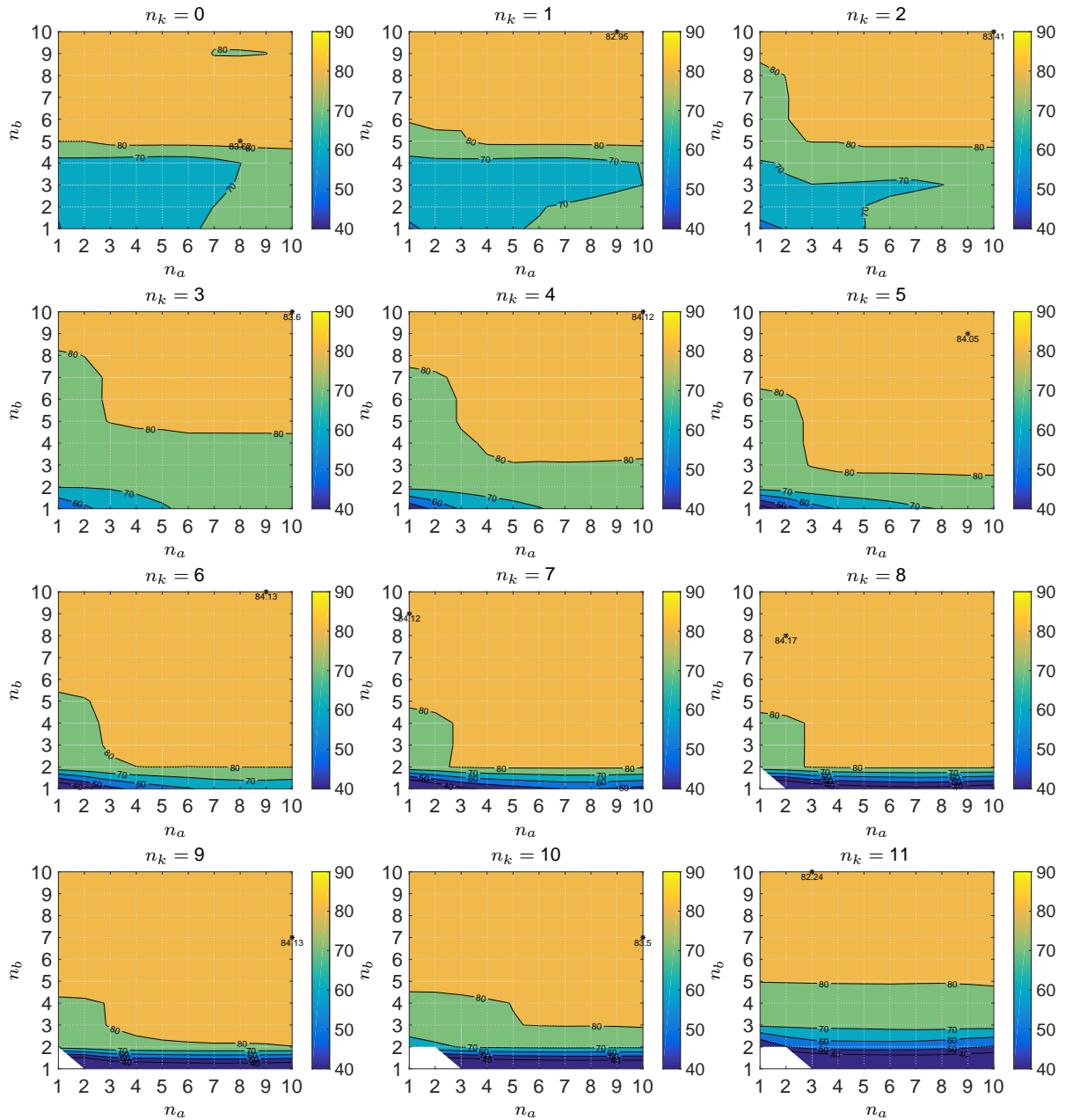


Figure C.3 VAF-contour plots: input-output signals decimated with $d = 4$ ($P_n = 0.15$).

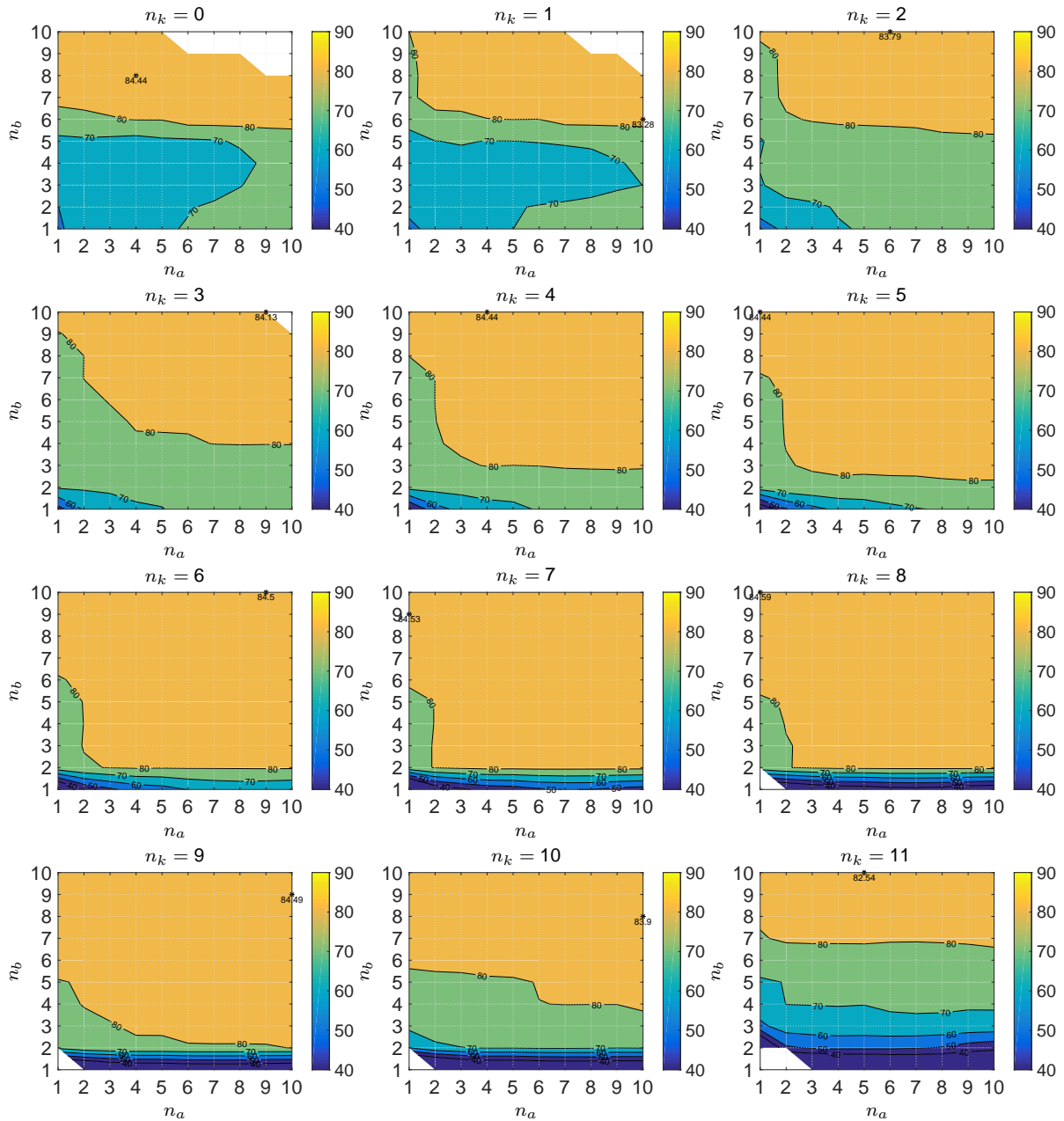


Figure C.4 VAF-contour plots: input-output signals filtered and decimated with $d = 4$ ($P_n = 0.15$).

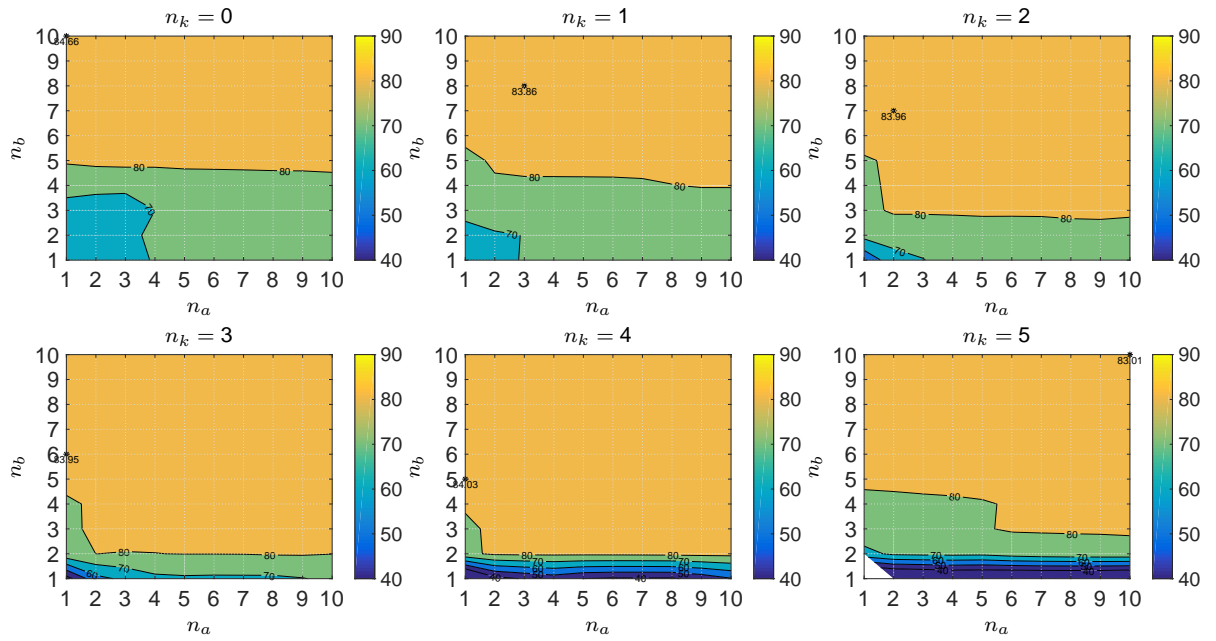


Figure C.5 VAF-contour plots: input-output signals decimated with $d = 8$ ($P_n = 0.15$).

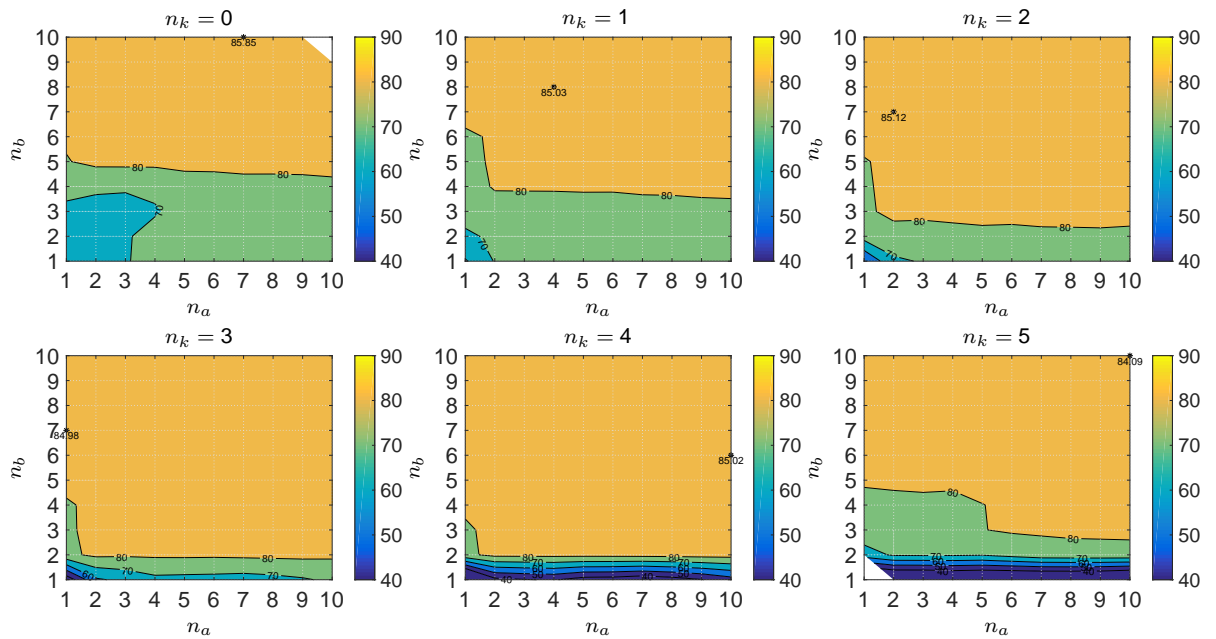


Figure C.6 VAF-contour plots: input-output signals filtered and decimated with $d = 8$ ($P_n = 0.15$).

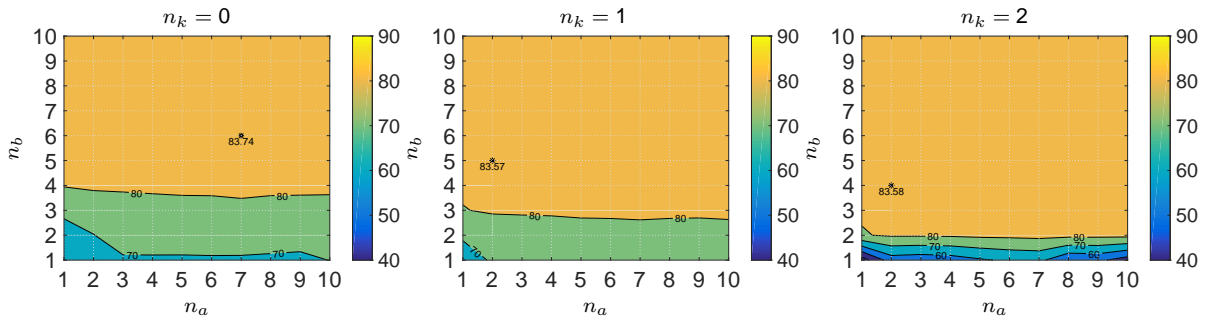


Figure C.7 VAF-contour plots: input-output signals decimated with $d = 16$ ($P_n = 0.15$).

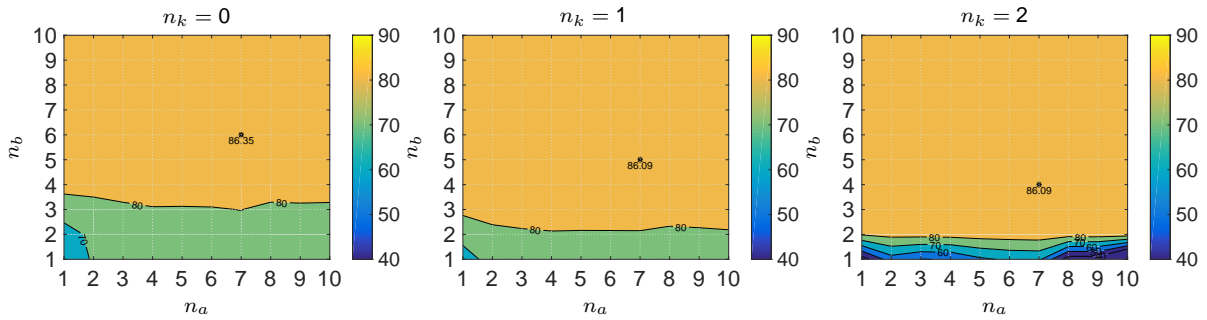


Figure C.8 VAF-contour plots: input-output signals filtered and decimated with $d = 16$ ($P_n = 0.15$).

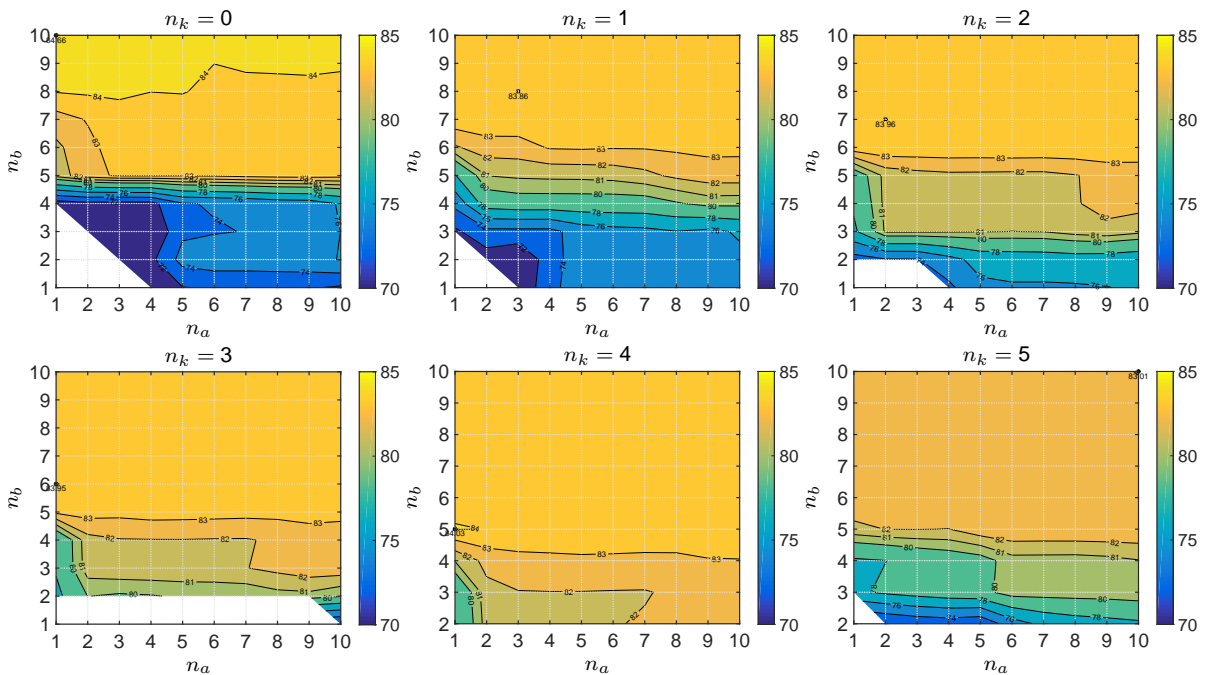


Figure C.9 High-valued VAF-contour plots: input-output signals decimated with $d = 8$ ($P_n = 0.15$).

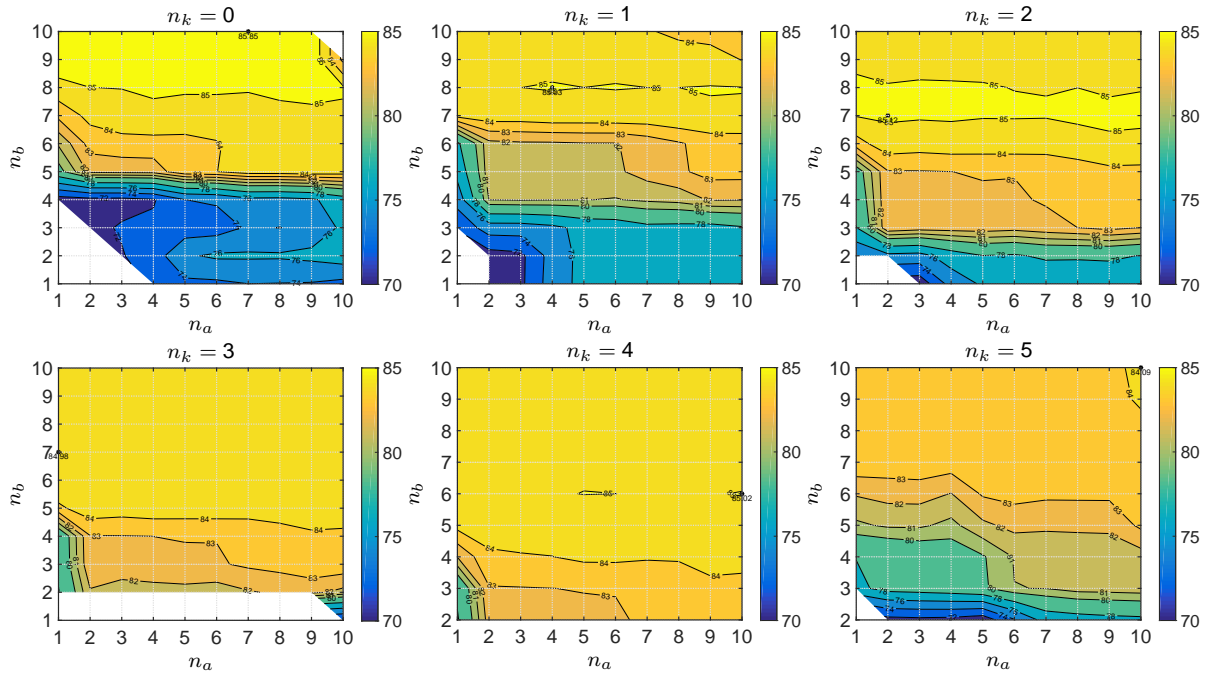


Figure C.10 High-valued VAF-contour plots: input-output signals filtered and decimated with $d = 8$ ($P_n = 0.15$).

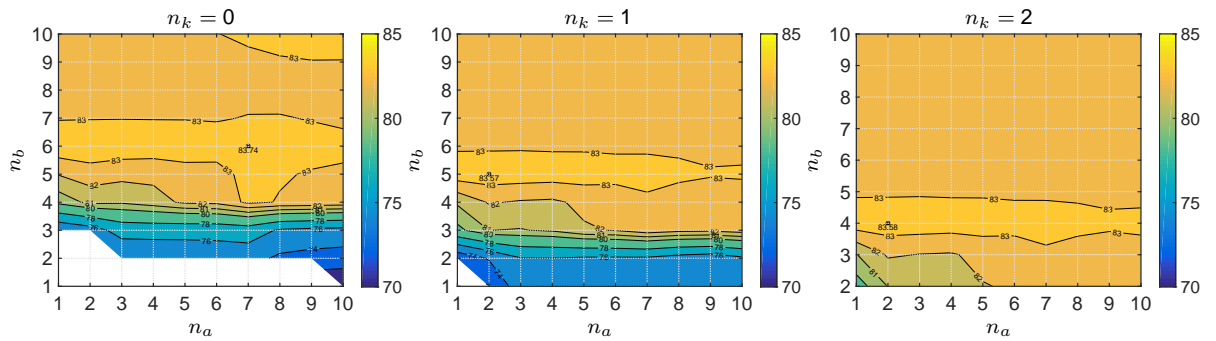


Figure C.11 High-valued VAF-contour plots: input-output signals decimated with $d = 16$ ($P_n = 0.15$).

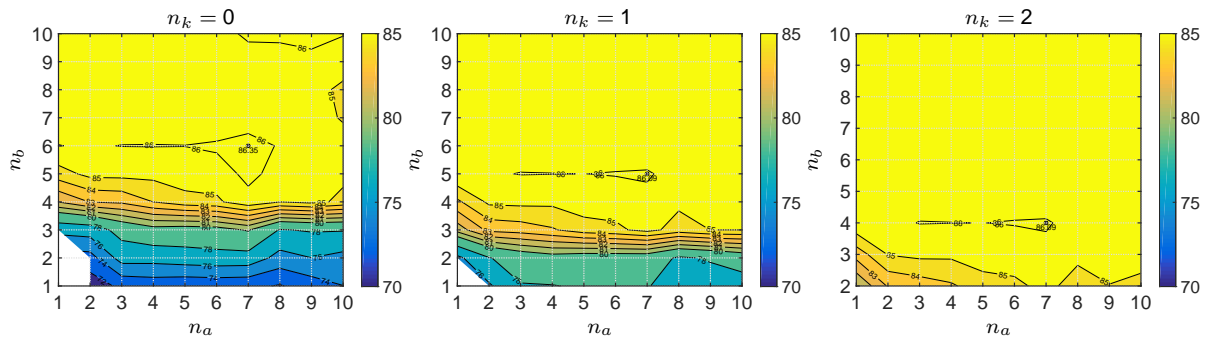
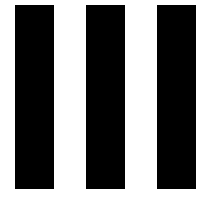


Figure C.12 High-valued VAF-contour plots: input-output signals filtered and decimated with $d = 16$ ($P_n = 0.15$).



Final report appendices

D

Simulation setup of the compensatory manual-control model

Chapter 3 of Part II provided the setup of the single-loop compensatory target-following control task. A block diagram was given and parametric definitions of the controlled-element and the analytical human-operator dynamics were defined. In the further research, the setup of the remnant filter is slightly changed. The updated high-level block diagram of the compensatory manual-control model with time-varying dynamics is shown in Figure D.1. This appendix presents the approach toward a low-level SIMULINK implementation, in which attention is paid to the model's capability of simulating both time-invariant as well as time-varying dynamics.

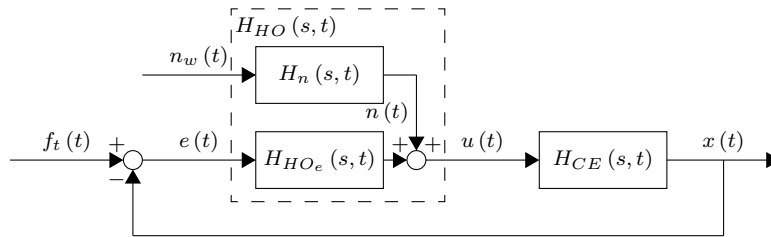


Figure D.1 Block diagram of a single-loop compensatory manual-control model.

D.1 Human-operator dynamics

Analytical human-operator dynamics The time-varying analytical human-operator dynamics are parametrically defined by

$$H_{HO_e}(s, t) = K_v(t) [T_L(t)s + 1] e^{-s\tau_v} \frac{\omega_{nm}^2}{s^2 + 2\zeta_{nm}\omega_{nm}s + \omega_{nm}^2} \quad (D.1)$$

The above equation should be rewritten as follows, in order to implement it in SIMULINK.

$$H_{HO_e}(s, t) = [K_v(t)T_L(t)s + K_v(t)] e^{-s\tau_v} \frac{\omega_{nm}^2}{s^2 + 2\zeta_{nm}\omega_{nm}s + \omega_{nm}^2} \quad (D.2)$$

$$= \left[K_v(t)T_L(t) \frac{\omega_{nm}^2 s}{s^2 + 2\zeta_{nm}\omega_{nm}s + \omega_{nm}^2} + K_v(t) \frac{\omega_{nm}^2}{s^2 + 2\zeta_{nm}\omega_{nm}s + \omega_{nm}^2} \right] e^{-s\tau_v} \quad (D.3)$$

Remnant filter Based on studies performed by Pool et al. (2011b, 2012), the following m th-order remnant filter is considered

$$H_n(s, t) = \frac{K_n(t)}{(T_n s + 1)^m} \quad (D.4)$$

in which the remnant gain $K_n(t)$ can vary in time. The remnant-time constant T_n is set equal to 0.06 s. Analogous to the values of the parameters of the controlled-element dynamics and the operator's equalization dynamics, the value of $K_n(t)$ will vary according a sigmoid function.

In addition, the following specific remnant filter is considered.

$$H_n(s, t) = K_n(t) H_{nm}(s) \quad (\text{D.5})$$

This one is similar to the human operator's neuromuscular-actuation dynamics $H_{nm}(s)$.

D.2 Controlled-element dynamics

The time-varying controlled-element dynamics are parametrically defined by

$$H_{CE}(s, t) = \frac{K_{CE}(t)}{s^2 + \omega_b(t) s} \quad (\text{D.6})$$

In order to set up the simulation, Eq. (D.6) should be rewritten as follows.

$$H_{CE}(s, t) = \frac{K_{CE}(t)}{s^2 + \omega_b(t) s} \frac{1}{\frac{1}{s^2}} \quad (\text{D.7})$$

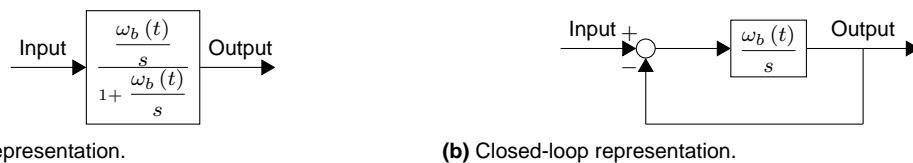
$$= \frac{K_{CE}(t)}{\frac{s^2}{1 + \frac{\omega_b(t)}{s}}} \quad (\text{D.8})$$

$$= \frac{K_{CE}(t) \omega_b(t)}{s^2 \frac{\omega_b(t)}{s} \left(1 + \frac{\omega_b(t)}{s}\right)} \quad (\text{D.9})$$

$$= \frac{K_{CE}(t) \omega_b(t) \frac{1}{s}}{\omega_b(t) \frac{s}{1 + \frac{\omega_b(t)}{s}} \frac{1}{s}} \quad (\text{D.10})$$

$$= \frac{K_{CE}(t)}{\omega_b(t)} \underbrace{\frac{\omega_b(t)}{1 + \frac{\omega_b(t)}{s}}}_{\square} \frac{1}{s} \quad (\text{D.11})$$

The controlled-element dynamics part represented by the square \square can be expressed in an open-loop block diagram as in Figure D.2(a). A closed-loop representation of this, suitable for implementation in SIMULINK, is shown in Figure D.2(b).



(a) Open-loop representation.

(b) Closed-loop representation.

Figure D.2 Equivalent block diagrams of a part of the controlled-element dynamics.

D.3 SIMULINK implementation

Figure D.3 shows the SIMULINK block diagram of the compensatory manual-control model with the possibility to simulate both time-invariant and time-varying dynamics. The gray blocks represent the analytical human-operator dynamics and the controlled-element dynamics, which were set up using Eqs. (D.3) and (D.11). In order to avoid integrator windup, it is very important to perform most of the setpoint calculations before signals enter the integrator blocks. The operator's visual time delay is modeled with a (discrete) "Delay" block.

In order to compute the states of the model during the simulation, the fixed-step solver `ode4` is selected with the step size set to $\Delta t = 1/f_s$. This solver uses the fourth-order Runge-Kutta (RK4) formula.

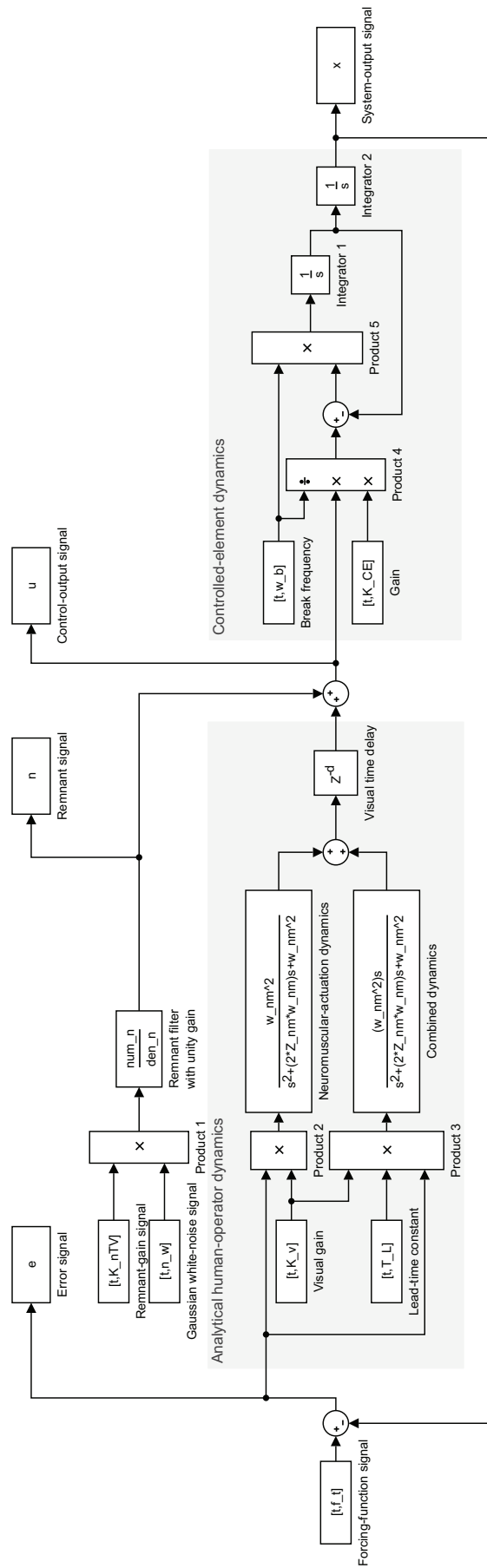


Figure D.3 SIMULINK implementation of the compensatory manual-control model with the possibility to simulate both time-invariant and time-varying dynamics.

E

Remnant-free simulations of the compensatory manual-control model

This appendix illustrates the time traces of the signals that are obtained when simulating the compensatory manual-control model in different conditions without taking into account remnant (see Figure E.1). Both the time traces in the measurement window and the transition window are provided. Table E.1 presents an overview of the different conditions and lists the references to the figures. For conditions with controlled-element transitions, the maximum rate of transition G was set around $M = 40.96$ s, i.e., around the midpoint of the measurement window. This midpoint is indicated in the corresponding figures. Time traces of the forcing function $f_t(t)$ are shown in Figure E.2.

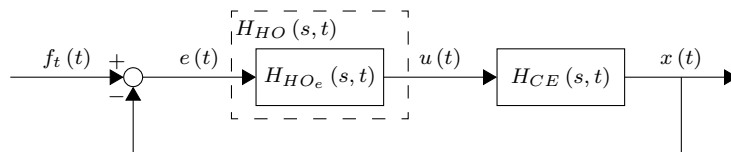
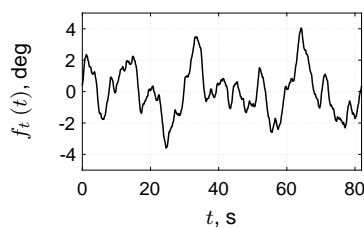


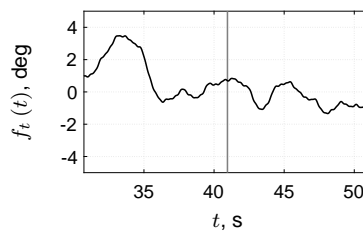
Figure E.1 Block diagram of the single-loop compensatory target-following control task excluding remnant.

Table E.1 Simulated conditions and overview of figures.

Condition	$H_{CE}(s)$	G, s^{-1}	Measurement window	Transition window
C1	$H_{CE,1}(s)$	n/a	Figure E.3	Figure E.9
C2	$H_{CE,2}(s)$	n/a	Figure E.4	Figure E.10
C3	$H_{CE,1}(s) \rightarrow H_{CE,2}(s)$	0.5	Figure E.5	Figure E.11
C4	$H_{CE,1}(s) \rightarrow H_{CE,2}(s)$	100	Figure E.6	Figure E.12
C5	$H_{CE,2}(s) \rightarrow H_{CE,1}(s)$	0.5	Figure E.7	Figure E.13
C6	$H_{CE,2}(s) \rightarrow H_{CE,1}(s)$	100	Figure E.8	Figure E.14



(a) Measurement window.



(b) Transition window.

Figure E.2 Time traces of the forcing function.

E.1 Measurement window

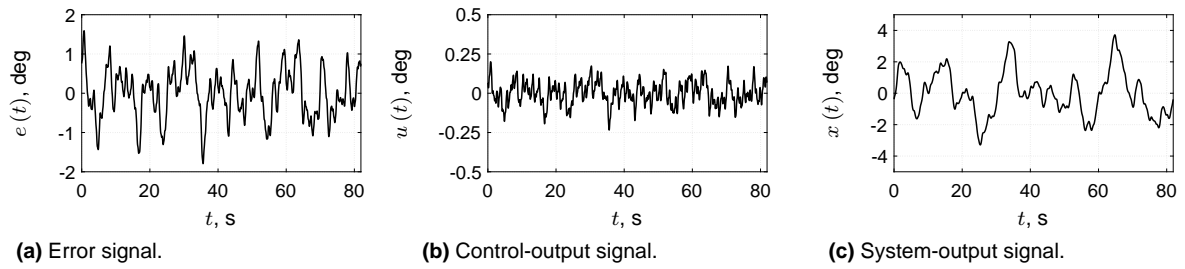


Figure E.3 Measurement-time traces for condition C1.

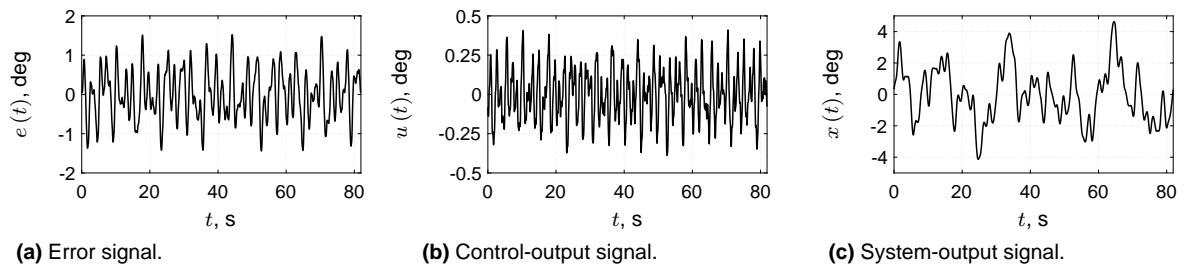


Figure E.4 Measurement-time traces for condition C2.

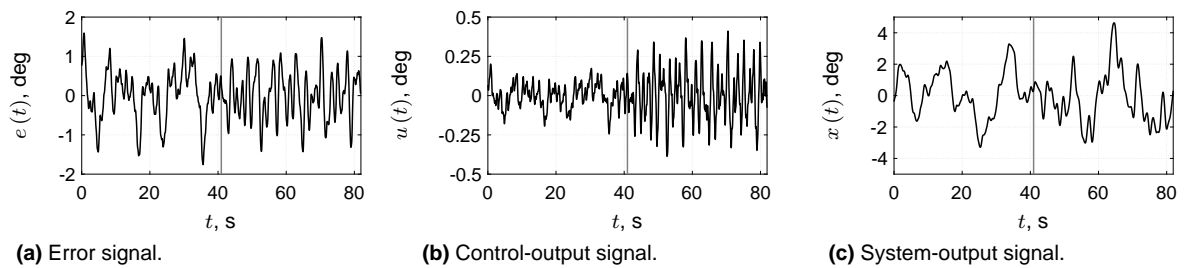


Figure E.5 Measurement-time traces for condition C3.

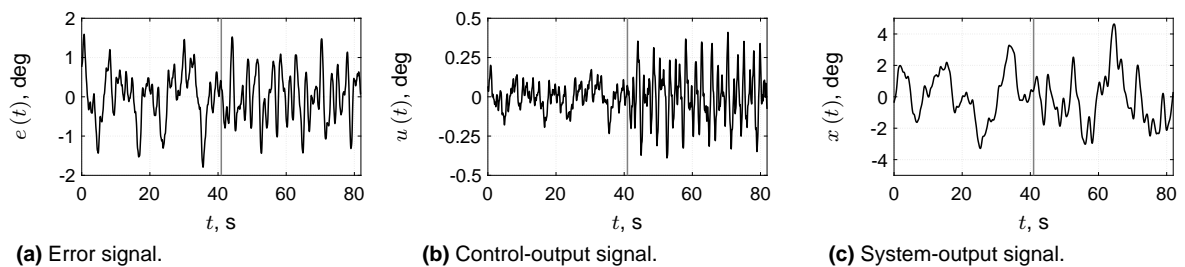


Figure E.6 Measurement-time traces for condition C4.

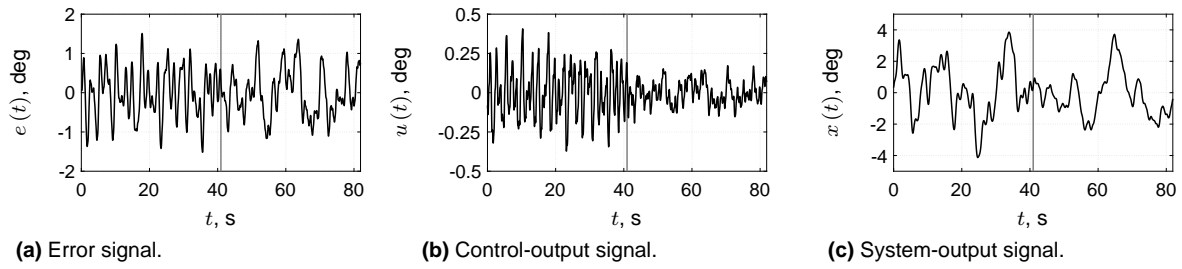


Figure E.7 Measurement-time traces for condition C5.

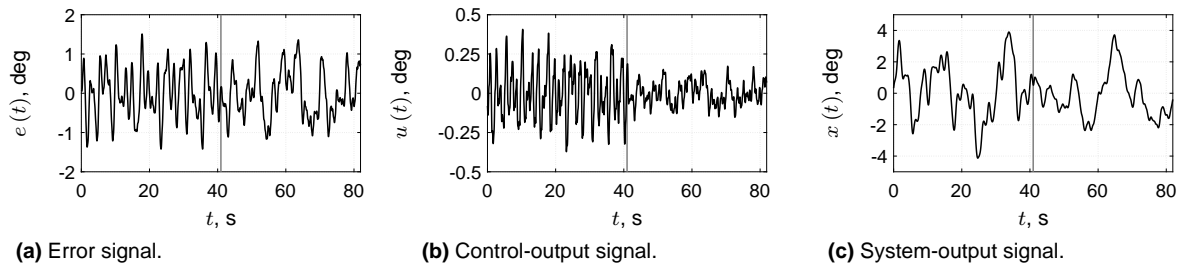


Figure E.8 Measurement-time traces for condition C6.

E.2 Transition window

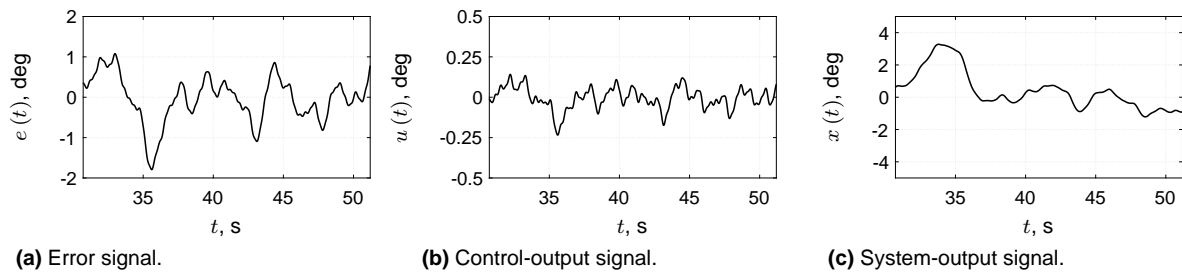


Figure E.9 Transition-time traces for condition C1.

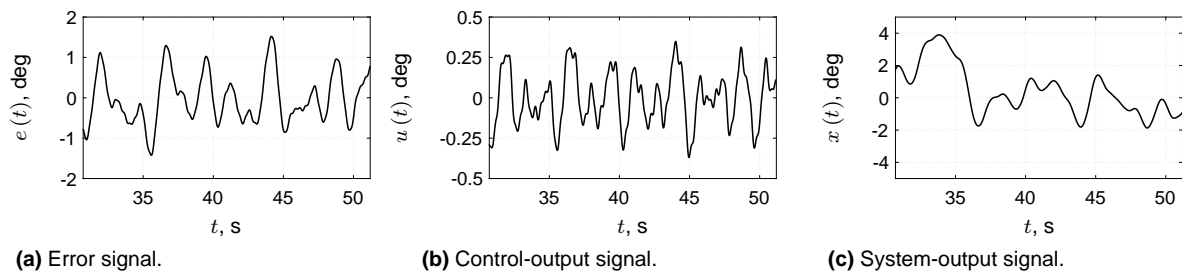


Figure E.10 Transition-time traces for condition C2.

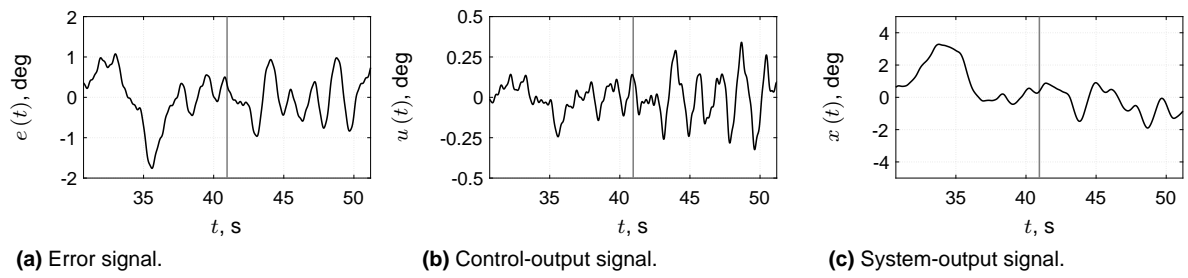


Figure E.11 Transition-time traces for condition C3.

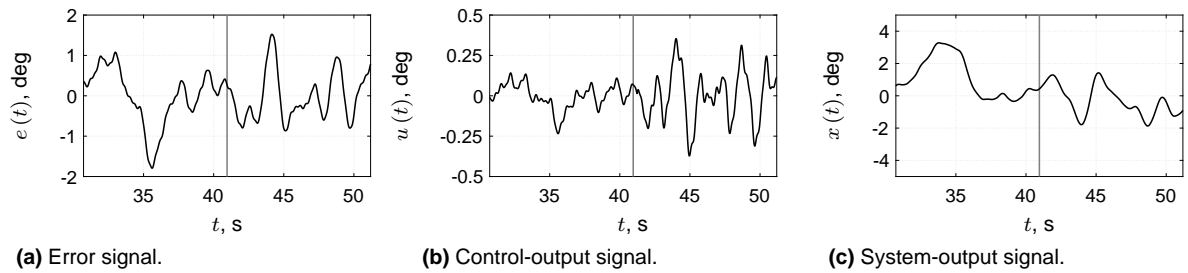


Figure E.12 Transition-time traces for condition C4.

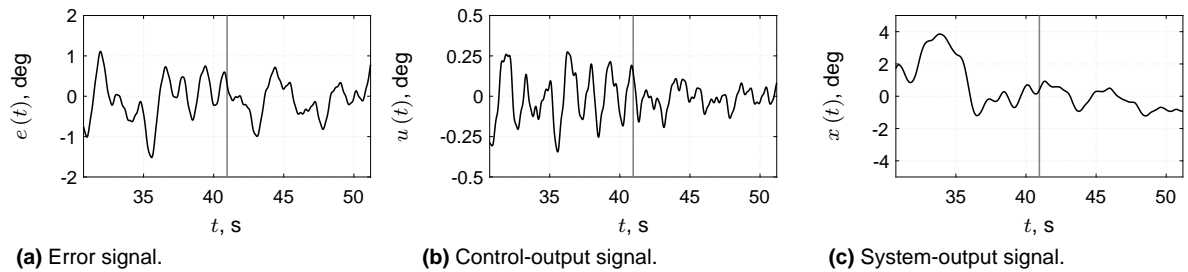


Figure E.13 Transition-time traces for condition C5.

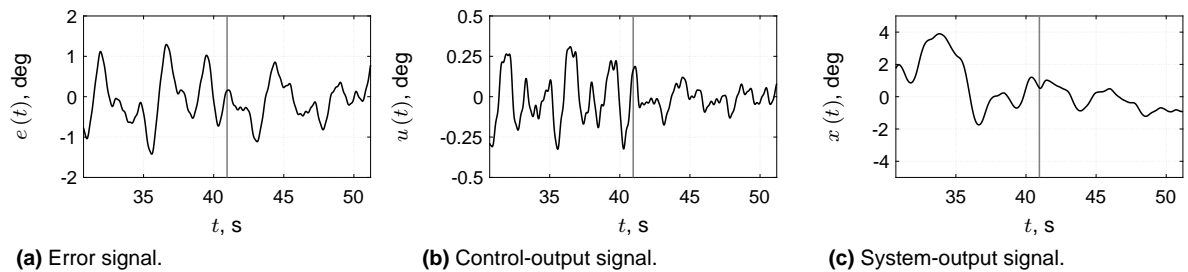
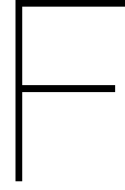


Figure E.14 Transition-time traces for condition C6.



ZOH discretization of the analytical human-operator dynamics

In the simulation study (cf., Chapter 5 of Part II), the following analytical human-operator model is considered

$$H_{HO_e}(j\omega) = \underbrace{K_v [T_L j\omega + 1]}_{\substack{\text{Gain} \quad \text{Lead term}}} \underbrace{\frac{e^{-j\omega\tau_v}}{(j\omega)^2 + 2\zeta_{nm}\omega_{nm}j\omega + \omega_{nm}^2}}_{\substack{\text{Time delay} \quad \text{Limitations} \\ \text{Neuromuscular-actuation dynamics: } H_{nm}(j\omega)}} \quad (\text{F.1})$$

Without taking into account the time delay τ_v , this continuous-time model is written as

$$H(j\omega) = K_v [T_L j\omega + 1] \frac{\omega_{nm}^2}{(j\omega)^2 + 2\zeta_{nm}\omega_{nm}j\omega + \omega_{nm}^2} \quad (\text{F.2})$$

A discrete-time transfer function $G_d(z)$ can be obtained from a continuous-time transfer function $H_c(s)$ by applying zero-order hold (ZOH) discretization. The following expression summarizes the procedure (Tangirala, 2015):

$$G_d(z) = \frac{Z \left\{ \mathcal{L}^{-1} \left\{ \frac{H_c(s)}{s} \right\} \Big|_{t=kT_s} \right\}}{1 - z^{-1}} \quad (\text{F.3})$$

If the input $e[k]$ is set to a step signal, ZOH results in a step input $e(t)$ to the process. Then, the output $u(t)$ is a step response to $H_c(s)$.

The above model in Eq. (F.2) can be specified using the following rational expression in the discrete-time variable z , in ascending powers of z^{-1} :

$$H(z) = z^{-1} \frac{b_0 + b_1 z^{-1}}{1 + a_1 z^{-1} + a_2 z^{-2}} \quad (\text{F.4})$$

It can be observed that the numerator and the denominator of the above expression have the same conventions as the ARX model's input polynomial $B(q)$ and output polynomial $A(q)$, respectively (cf., Chapter 4 of Part II). Furthermore, a unit-sample input-output delay arises due to discretization. The value of a_0 always equals 1. The actual values of a_1 , a_2 , b_0 , and b_1 , can be found by discretizing Eq. (F.2) (take care about the z-transform convention), once values for the equalization and the (neuromuscular) limitation parameters are substituted. Furthermore, they are dependent on the discretization method and the sampling time T_s . It should be noted that the human-operator model assumes another disturbance than the ARX model (see Figure F.1). Thus, it is necessary to keep in mind that the ARX-model parameters will be estimated biased and inconsistent.

Demonstration The following particular sets of values for the equalization and limitation parameters are taken in this simulation study

$$K_{v,1} = 0.09, \quad T_{L,1} = 0.4 \text{ s} \quad (\text{F.5})$$

$$K_{v,2} = 0.07, \quad T_{L,2} = 1.2 \text{ s} \quad (\text{F.6})$$

$$\tau_v = 0.28 \text{ s}, \quad \omega_{nm} = 11.25 \text{ rad/s}, \quad \zeta_{nm} = 0.35 \quad (\text{F.7})$$

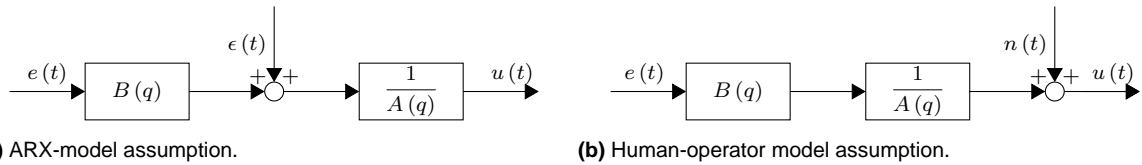


Figure F.1 Comparison of the ARX model and the human-operator model.

Substituting the latter two values listed in Eq. (F.7), and, in turn, the values listed in Eqs. (F.5) and (F.6), into Eq. (F.2), will lead to the following two continuous-time models:

$$H_1(j\omega) = \frac{4.556j\omega + 11.39}{(j\omega)^2 + 7.875j\omega + 126.6} \quad (\text{F.8})$$

$$H_2(j\omega) = \frac{10.63j\omega + 8.859}{(j\omega)^2 + 7.875j\omega + 126.6} \quad (\text{F.9})$$

Table F.1 shows the ARX model's parameter values when employing the ZOH discretization with different sampling times on Eqs. (F.8) and (F.9). They will be treated as the true parameters θ_0 . Table F.1 also lists the decimation factors d as a means of reference in case $T_s = 0.01$ s is considered as no decimation (i.e., $d = 1$). Accompanying Bode plots of the different discrete-time models $H_1(z)$ and $H_2(z)$ are shown in Figures F.2(a) and (b), respectively. They also include the analytical continuous-time human-operator models $H_{HO_{e,1}}(j\omega)$ and $H_{HO_{e,2}}(j\omega)$. The Bode phase-angle plots of the discrete-time models are adjusted with $-\frac{180}{\pi}\omega\tau_v$ as the delay was left out during discretization. The frequency range of each discrete-time model depends on the Nyquist frequency $\omega_N(d)$.

Table F.2 lists for different decimation factors, the variance accounted for (VAF) values when using the parameter values in Table F.1 as true ARX model. The higher the decimation, the lower the VAF. Analogously, Table F.3 presents the true parameter values if data is sampled with 200 Hz (no resampling). Then, VAF_{ZOH} , % for condition C1 and C2 with $n_k^0 = 57$ equal 99.9182 and 99.9525, respectively.

Table F.1 Values of the ARX-model coefficients for different sampling times T_s once ZOH discretization is employed.

T_s , s	d	$H_1(z); H_2(z)$		$H_1(z)$		$H_2(z)$	
		a_1^0	a_2^0	b_0^0	b_1^0	b_0^0	b_1^0
0.01	1	-1.9121	0.9243	0.0443	-0.0432	0.1024	-0.1016
0.02	2	-1.8076	0.8543	0.0858	-0.0816	0.1967	-0.1935
0.04	4	-1.5590	0.7298	0.1592	-0.1438	0.3589	-0.3470
0.08	8	-0.9709	0.5326	0.2636	-0.2130	0.5715	-0.5322
0.16	16	0.1226	0.2837	0.3065	-0.1799	0.5942	-0.4957

Table F.2 VAF values when using ARX-model coefficients for different sampling times T_s once ZOH discretization is employed, $f_s = 100$ Hz, $n_k^0 = 29$.

T_s , s	d	$H_1(z)$	$H_2(z)$
		VAF_{ZOH} , %	VAF_{ZOH} , %
0.01	1	99.9104	99.9423
0.02	2	99.8966	99.9475
0.04	4	99.7140	99.7271
0.08	8	98.9185	98.4915
0.16	16	96.5235	92.1485

Table F.3 Values of the ARX-model coefficients for different sampling times T_s once ZOH discretization is employed.

T_s , s	$H_1(z); H_2(z)$		$H_1(z)$		$H_2(z)$	
	a_1^0	a_2^0	b_0^0	b_1^0	b_0^0	b_1^0
0.005	-1.9583	0.9614	0.0225	-0.0222	0.0522	-0.0520

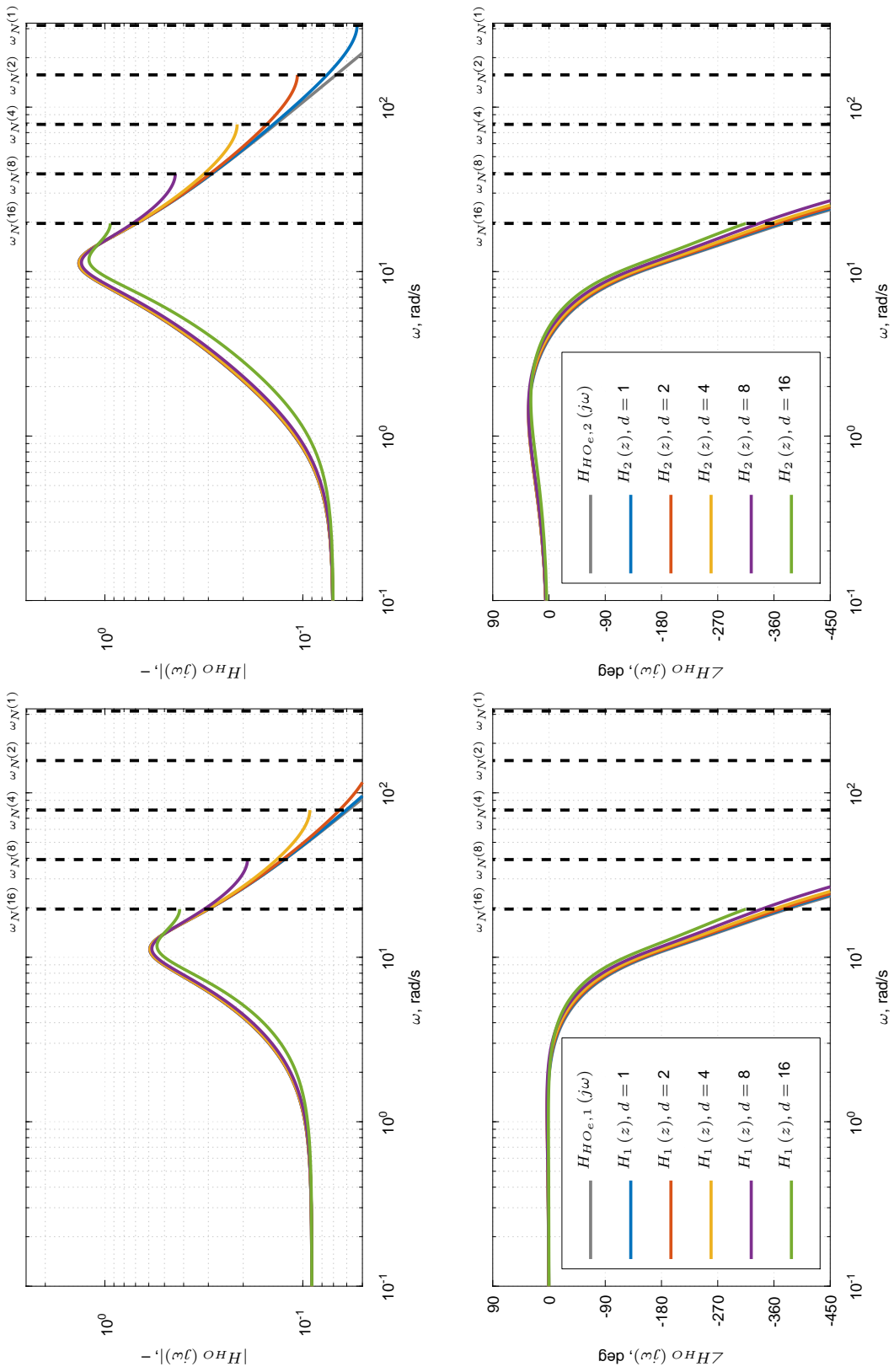


Figure F.2 Bode plots of the continuous-time human-operator model $H_{HOe,1}(j\omega)$ and the discrete-time human-operator models $H_1(z)$ including the time delay for different decimation factors d .

G

Influence of the remnant-filter type on ARX-model estimation

In the scientific paper the influence of the variable delay estimation n_k^* and remnant-filter type $H_n^m(s)$ was only shown for C1. This appendix shows for C1 and C2 (see Table E.1), the box plot results for $M = 100$ Monte Carlo replications and seven remnant intensities P_n , i.e., 0, 0.05, 0.10, 0.15, 0.20, 0.25, 0.30. In addition the results are shown for open-loop input-output data. Remnant-free error signals $e(t)$ are taken and the open-loop control-output signals $u(t)$ are obtained by

$$u(t) = u'(t) + n(t) \quad (\text{G.1})$$

with $u'(t)$ the remnant-free control-output signal (see Appendix E).

Table G.1 lists the optimized K_n values for different remnant-filter types $H_n^m(s)$, for conditions C1 and C2.

Table G.1 Optimized K_n values for different remnant-filter types $H_n^m(s)$, for conditions C1 and C2.

P_n	K_n									
	$H_n^1(s)$		$H_n^2(s)$		$H_n^3(s)$		$H_n^4(s)$		$H_n^{nm}(s)$	
	C1	C2	C1	C2	C1	C2	C1	C2	C1	C2
0.05	0.006	0.013	0.008	0.019	0.010	0.022	0.010	0.024	0.006	0.013
0.10	0.009	0.020	0.012	0.029	0.014	0.034	0.015	0.038	0.009	0.020
0.15	0.011	0.026	0.016	0.039	0.018	0.047	0.020	0.053	0.011	0.026
0.20	0.013	0.032	0.019	0.051	0.022	0.063	0.024	0.073	0.013	0.033
0.25	0.015	0.039	0.023	0.066	0.026	0.088	0.029	0.110	0.016	0.040
0.30	0.018	0.046	0.026	0.091	0.031	0.150	0.034	0.339	0.018	0.050

G.1 Variable delay estimation

G.1.1 Condition 1

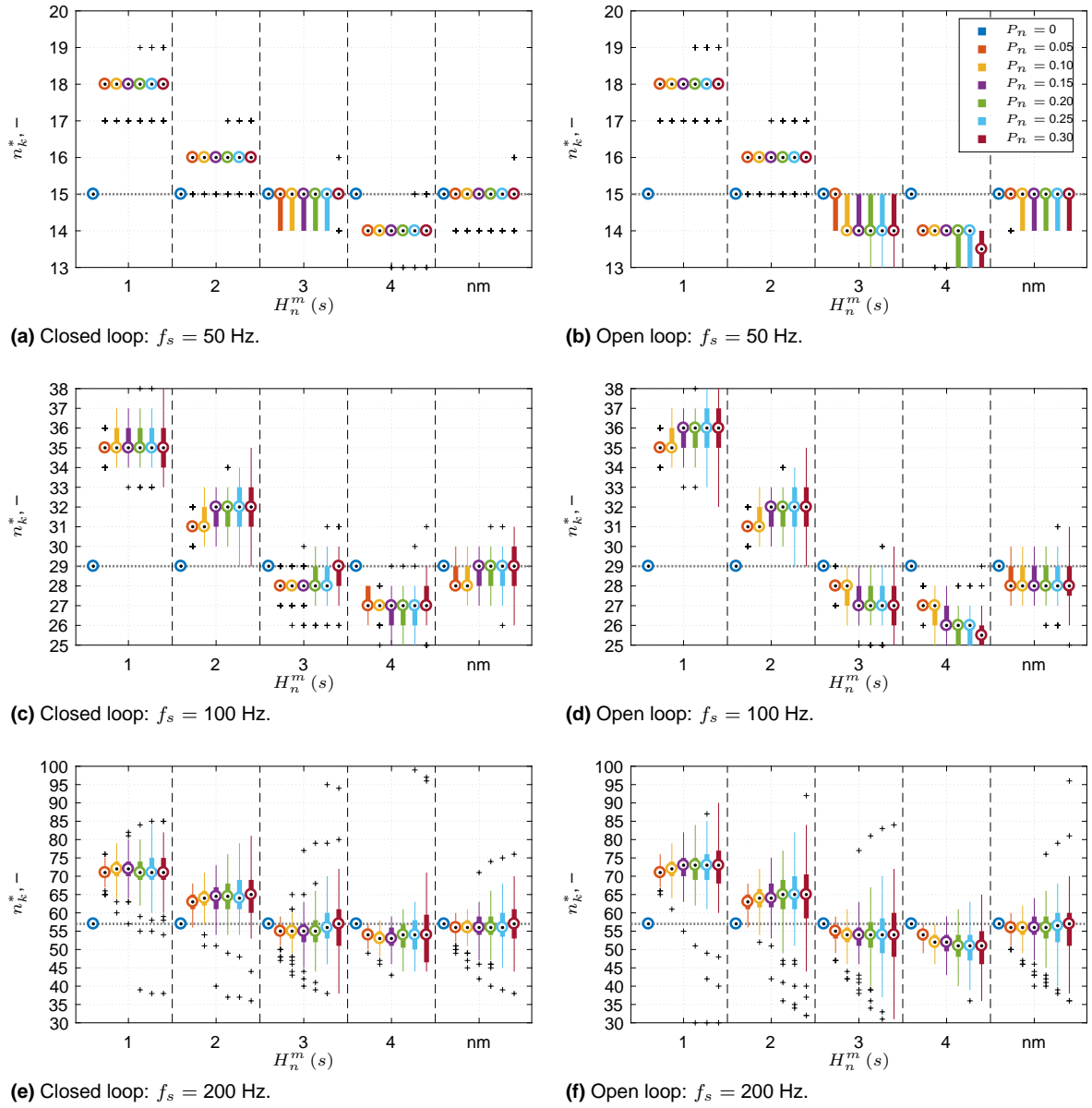


Figure G.1 Variable n_k^* estimation for condition C1, for different H_n^m (s).

G.1.2 Condition 2

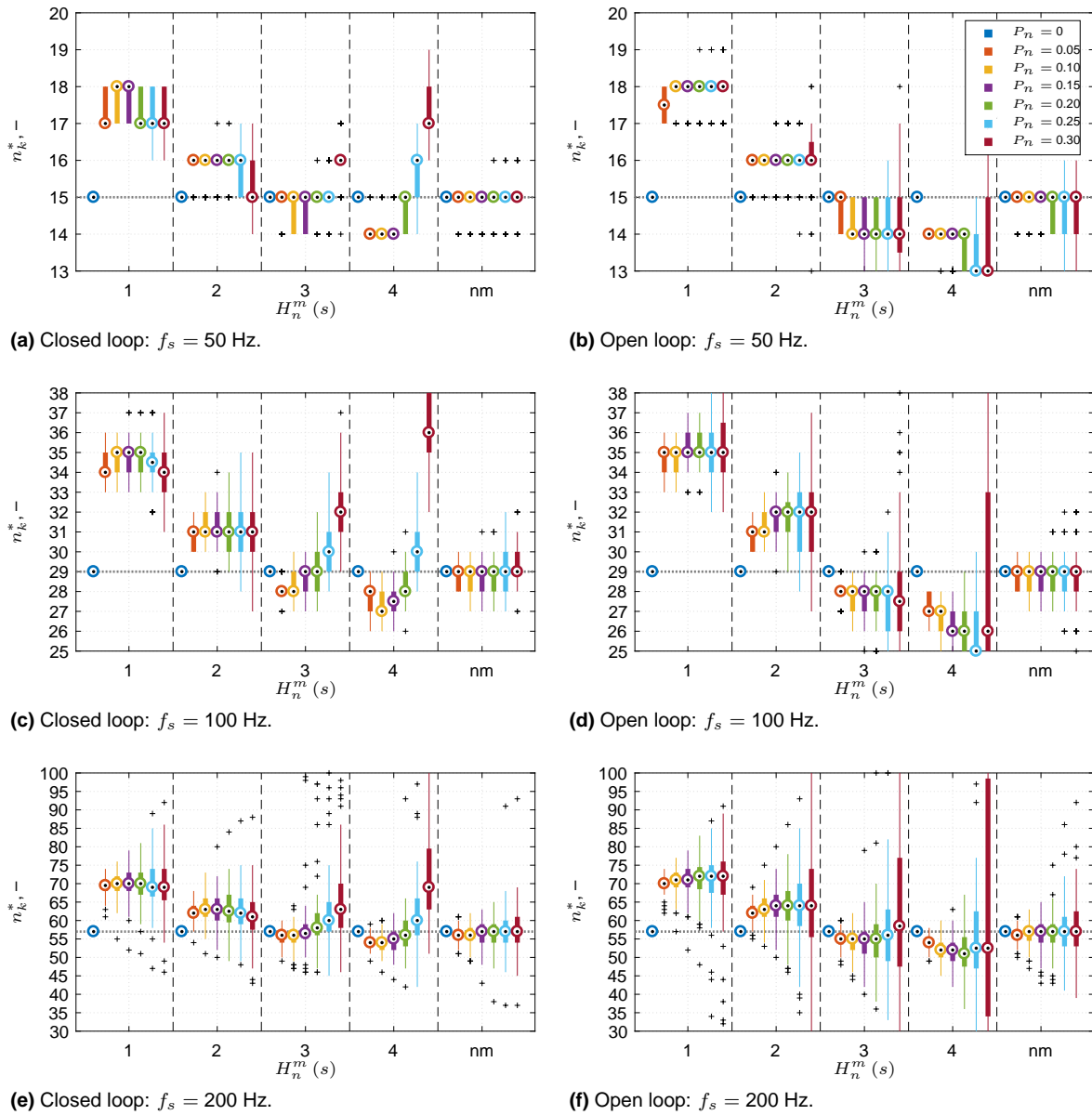


Figure G.2 Variable n_k^* estimation for condition C2, for different H_n^m (s).

G.2 Relative bias

G.2.1 Condition 1

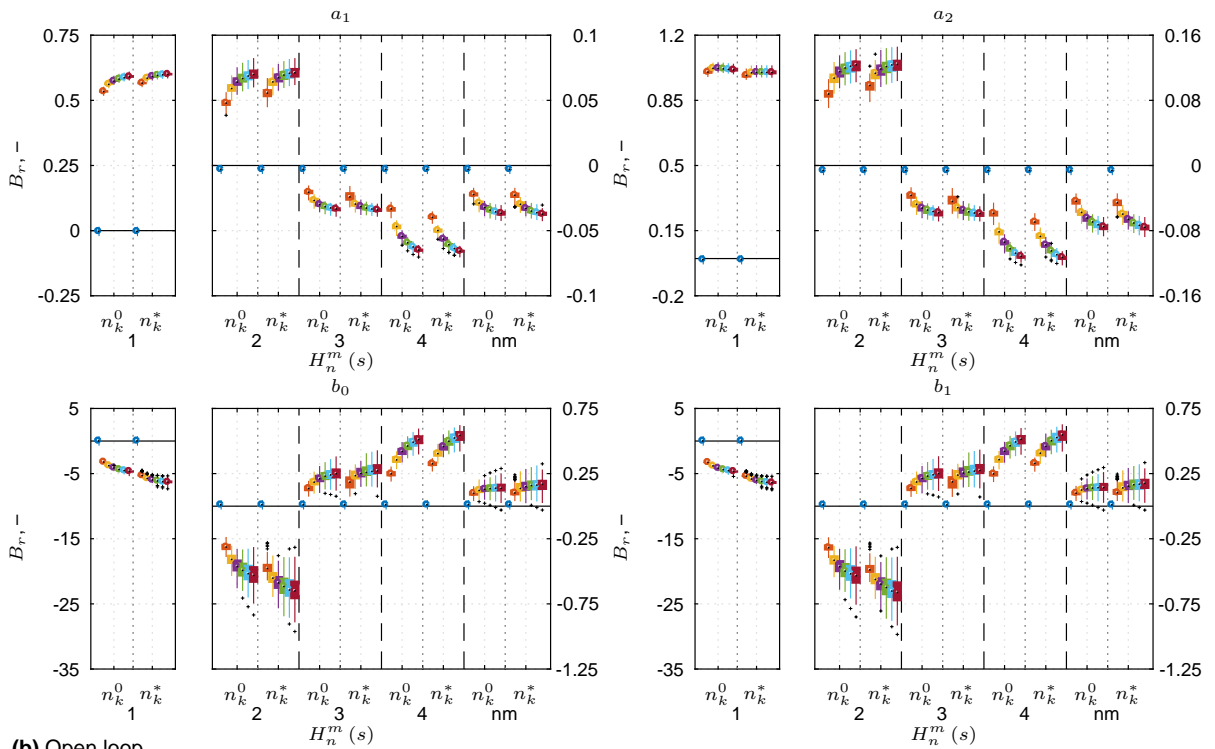
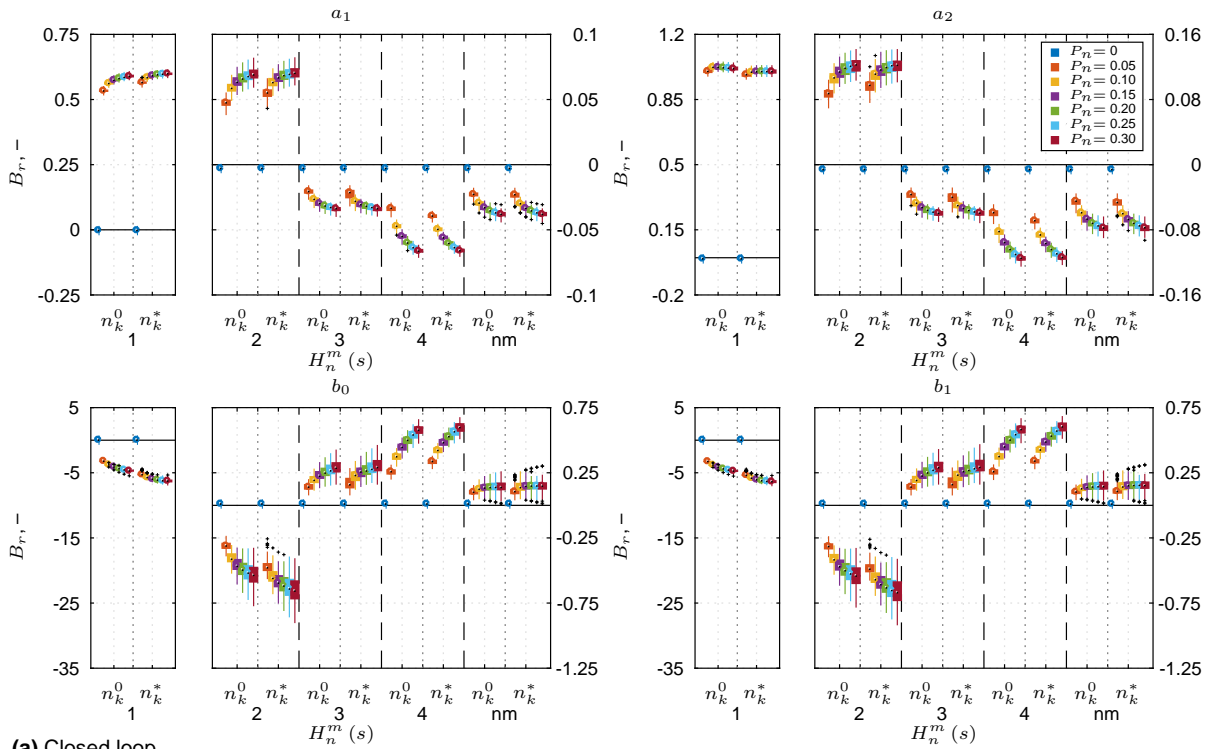


Figure G.3 Relative bias in ARX-model parameters for condition C1, for different $H_n^m(s)$, when using n_k^0 and n_k^* for $f_s = 50$ Hz.

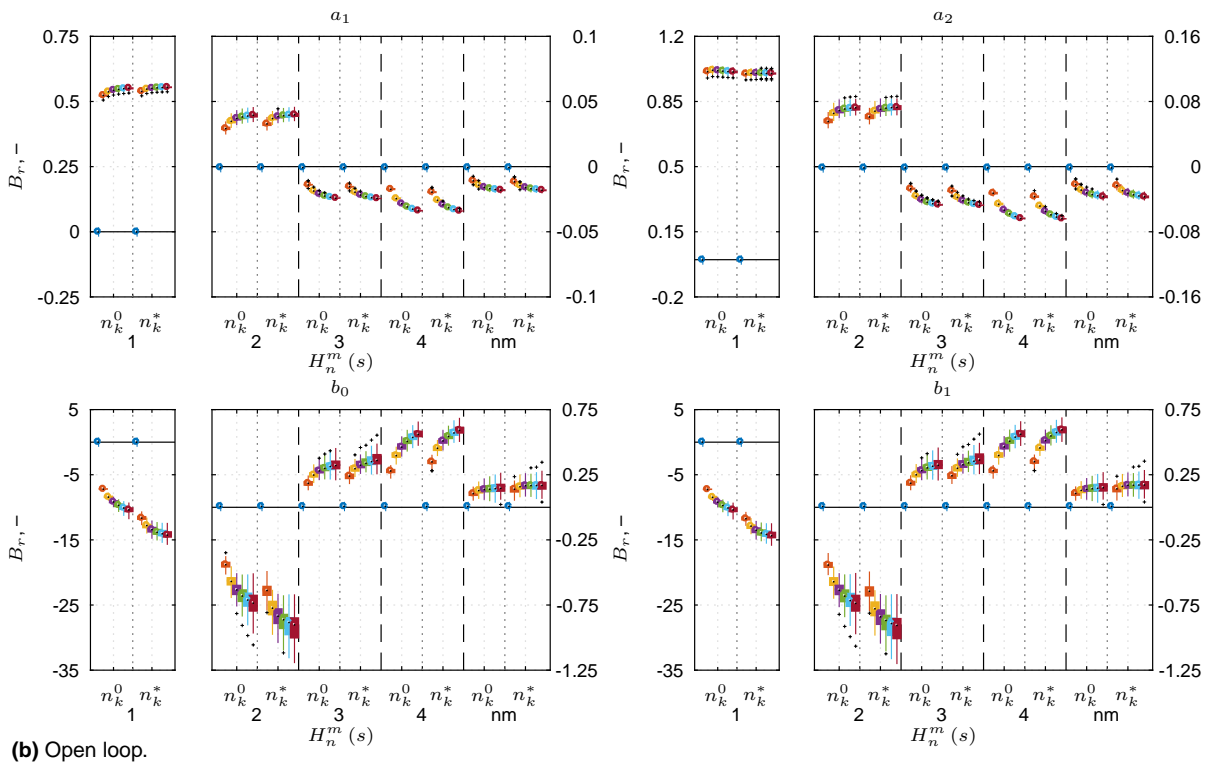
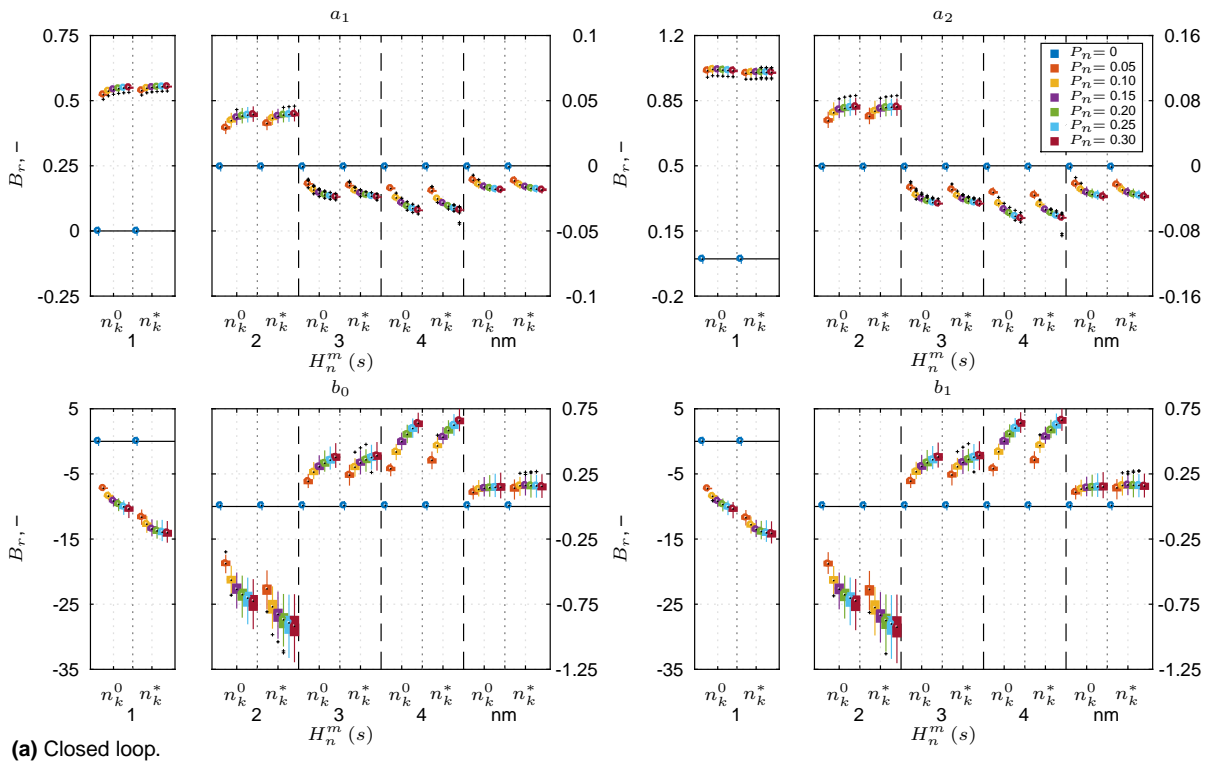


Figure G.4 Relative bias in ARX-model parameters for condition C1, for different $H_n^m(s)$, when using n_k^0 and n_k^* for $f_s = 100$ Hz.

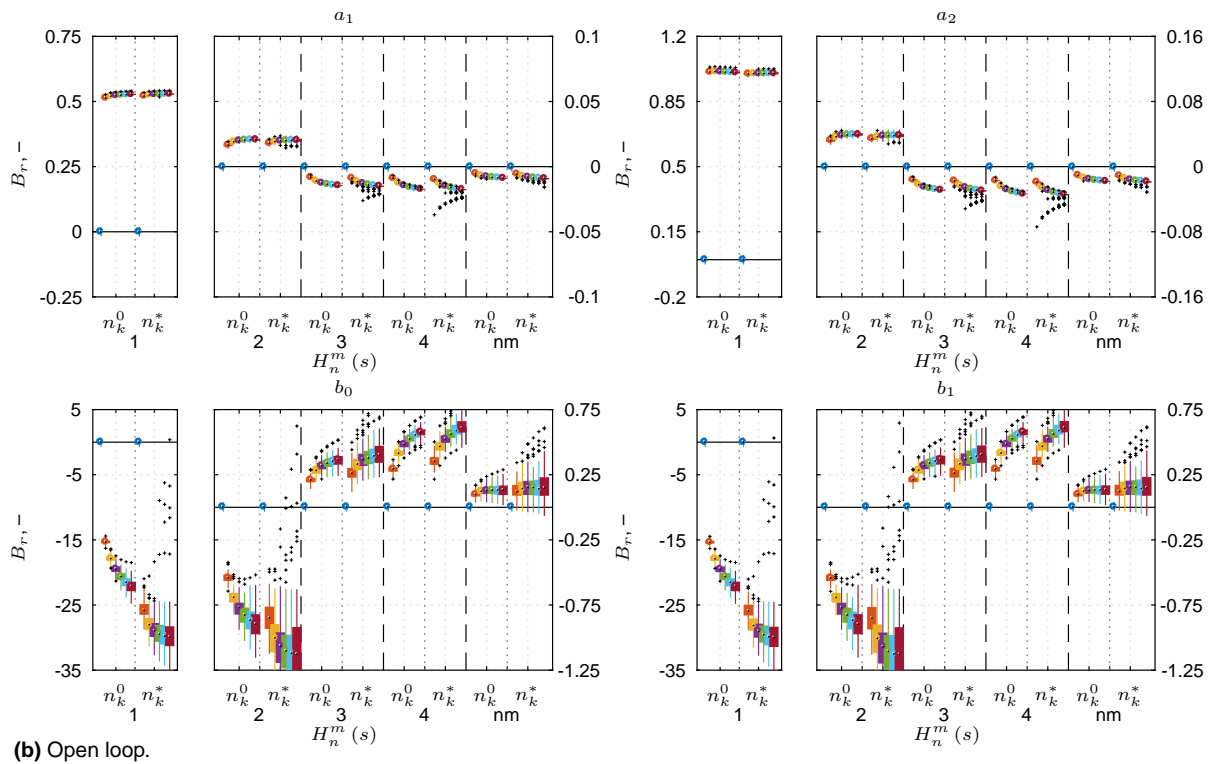
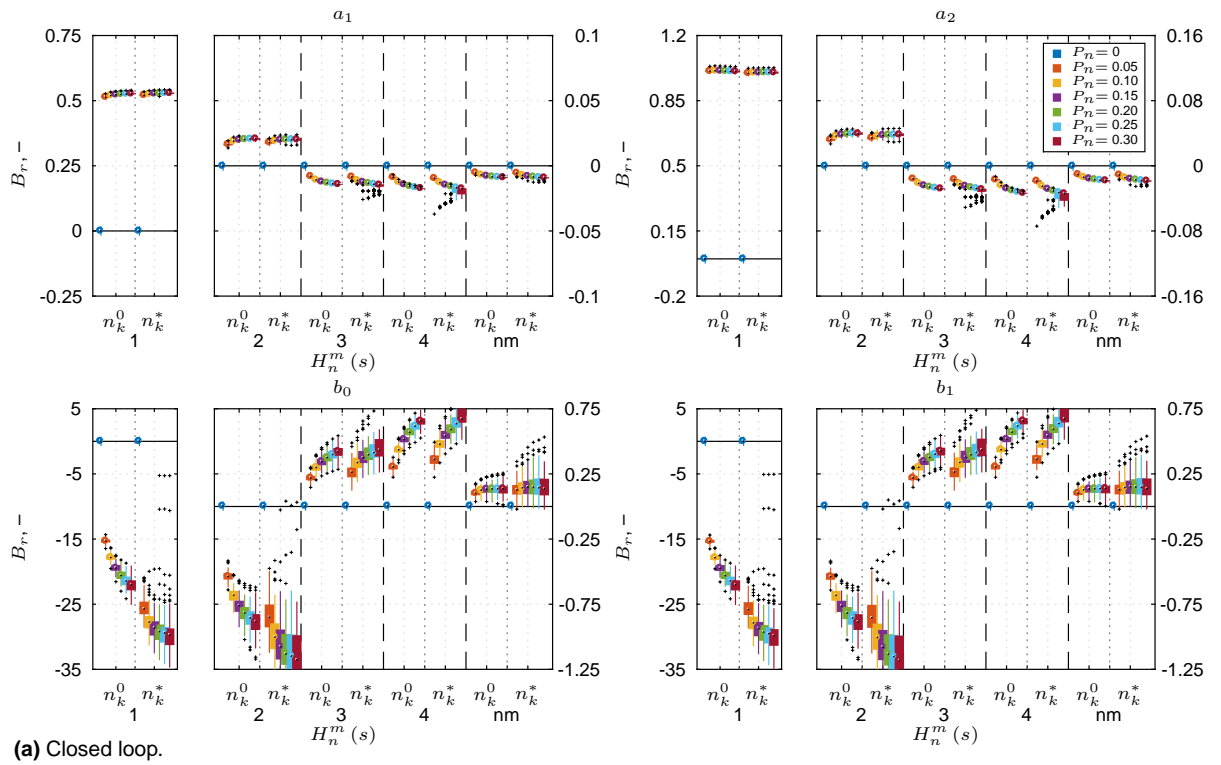


Figure G.5 Relative bias in ARX-model parameters for condition C1, for different $H_n^m(s)$, when using n_k^0 and n_k^* for $f_s = 200$ Hz.

G.2.2 Condition 2

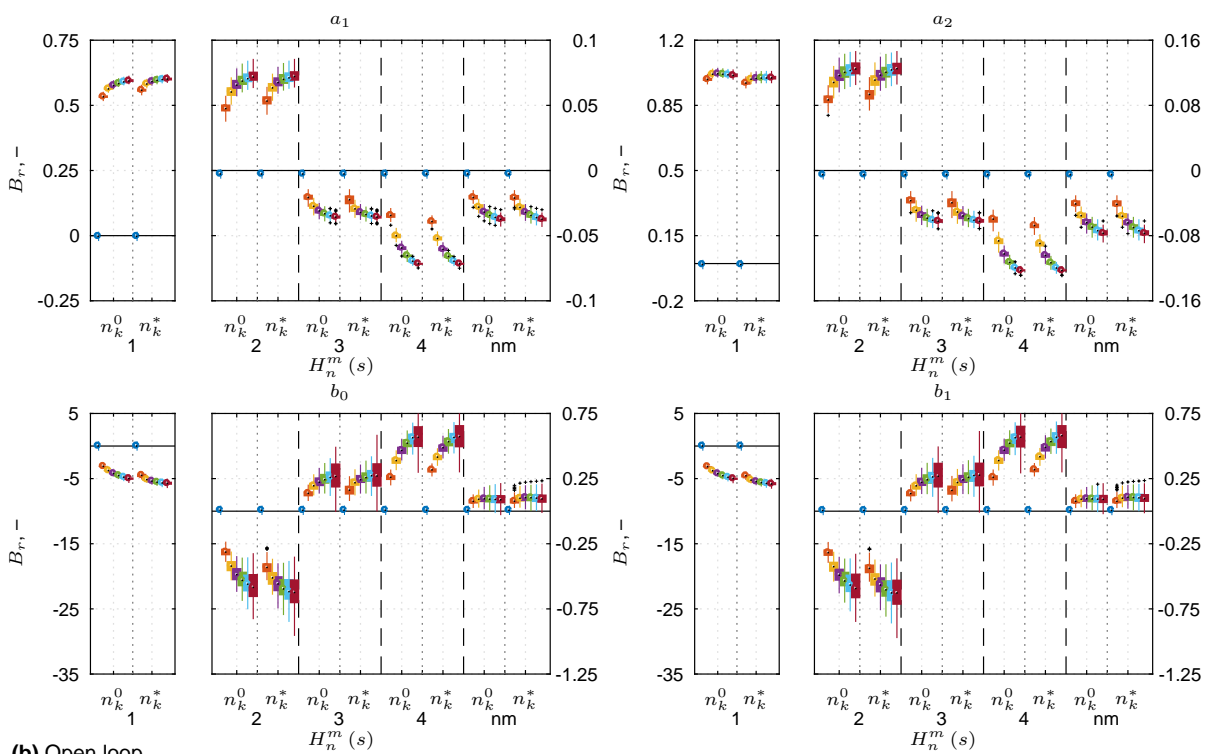
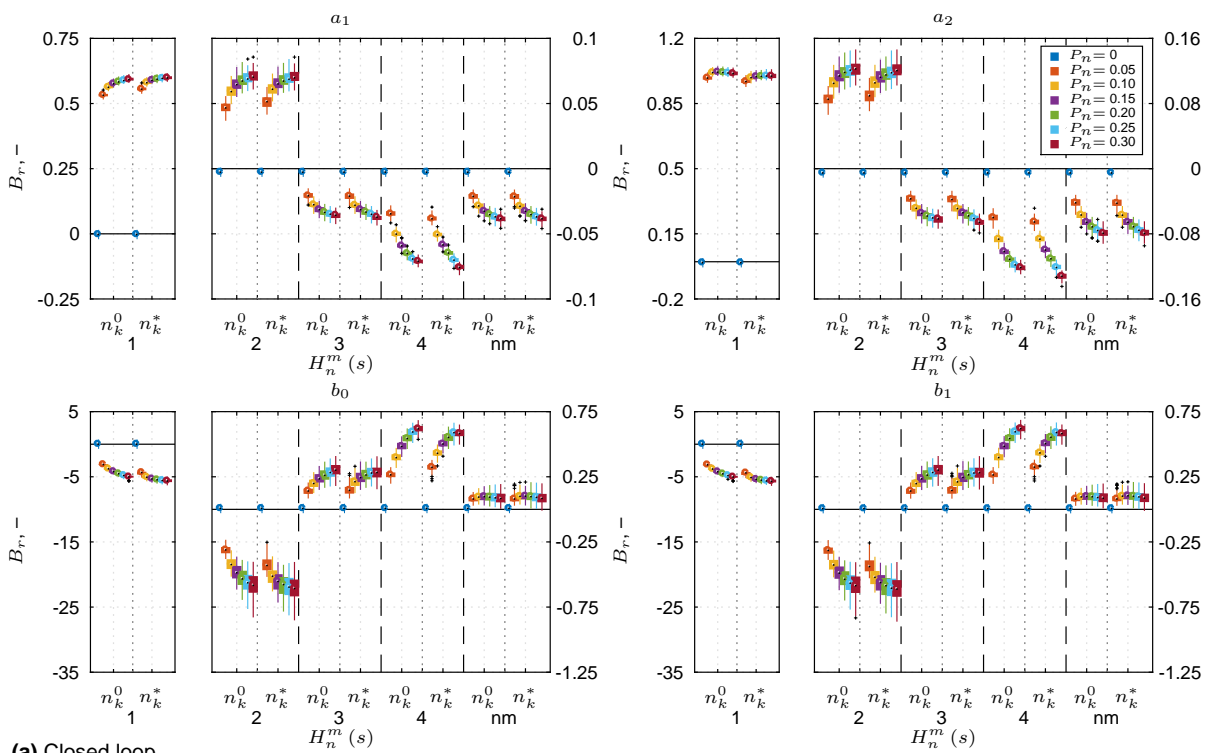


Figure G.6 Relative bias in ARX-model parameters for condition C2, for different $H_n^m(s)$, when using n_k^0 and n_k^* for $f_s = 50$ Hz.

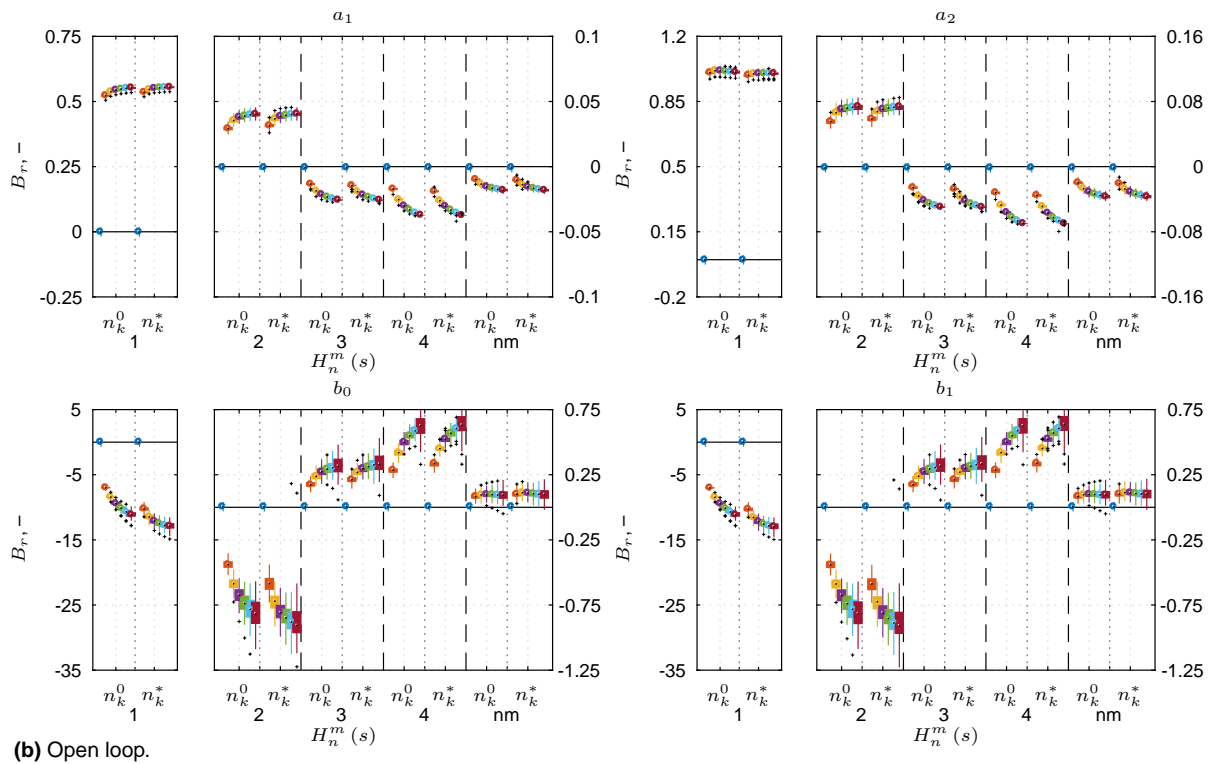
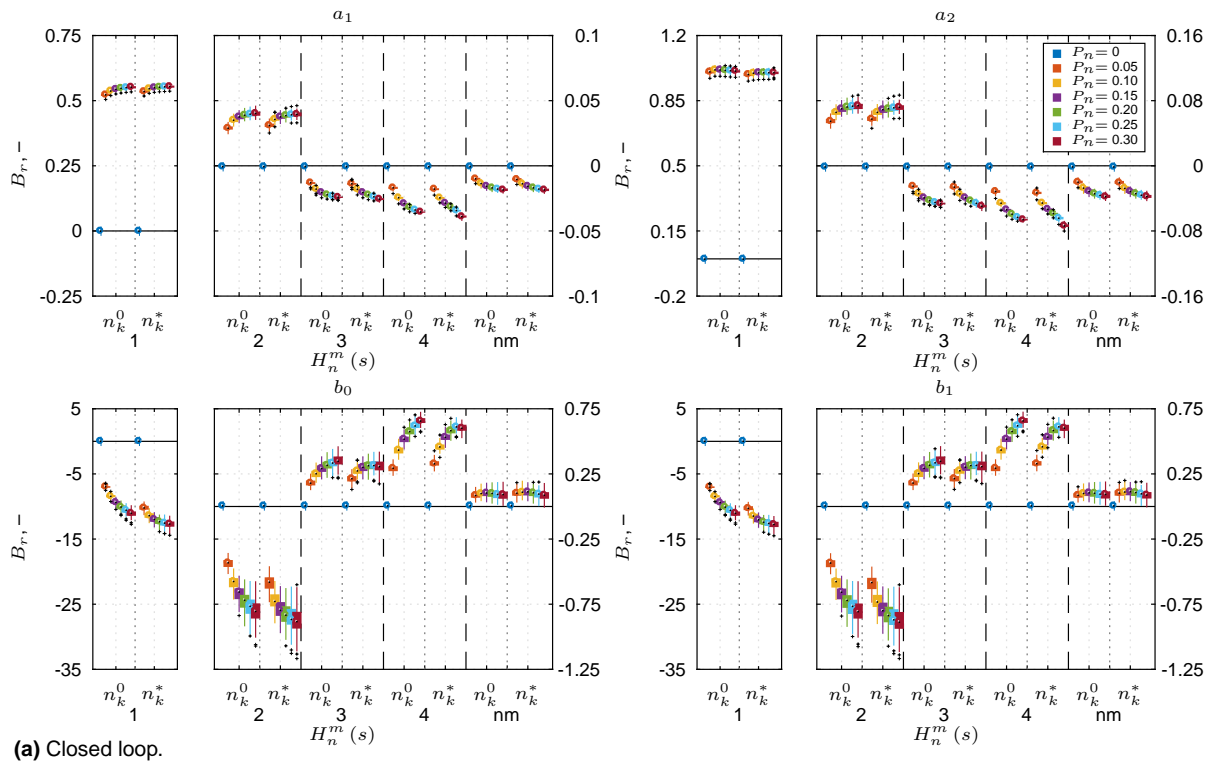


Figure G.7 Relative bias in ARX-model parameters for condition C2, for different $H_n^m(s)$, when using n_k^0 and n_k^* for $f_s = 100$ Hz.

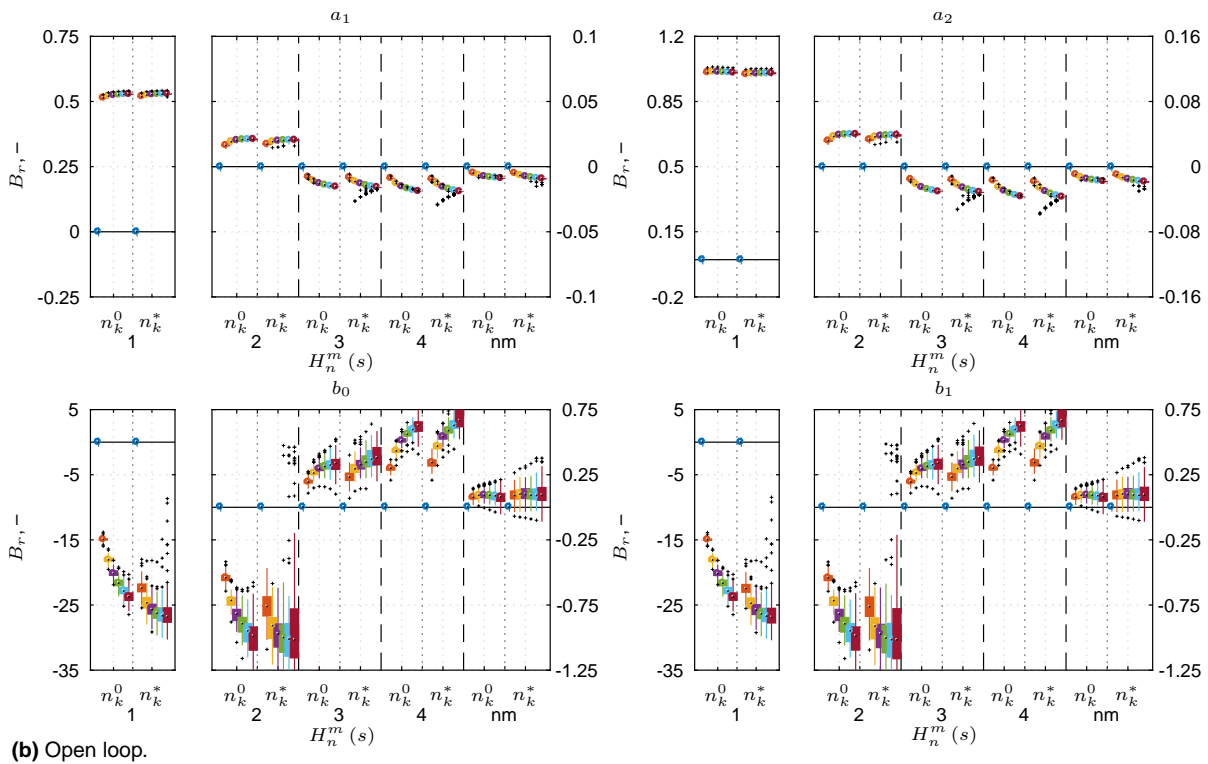
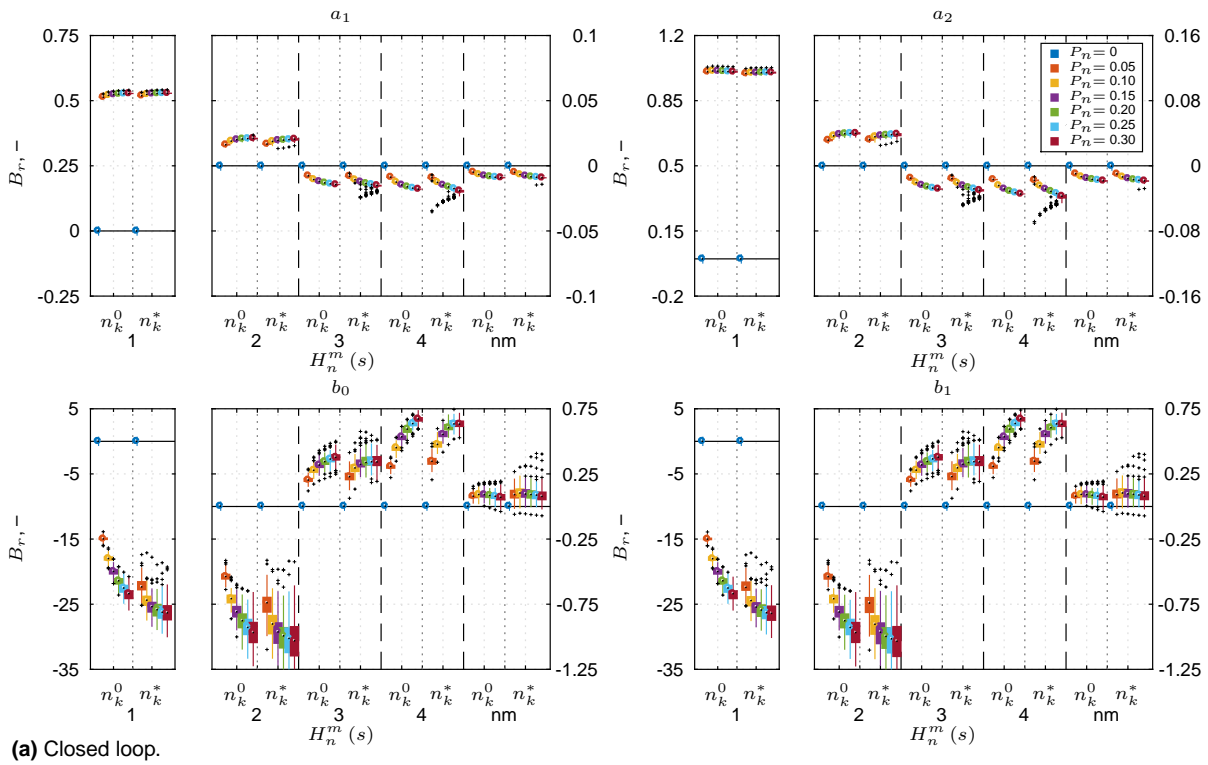
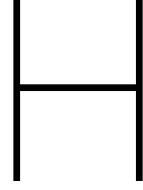


Figure G.8 Relative bias in ARX-model parameters for condition C2, for different $H_n^m(s)$, when using n_k^0 and n_k^* for $f_s = 200$ Hz.



Frequency-response statistics and accuracies

H.1 Ensemble statistics

In order to calculate the average magnitude and the average phase angle of the frequency response $\bar{H}(j\omega_k; Z)$, at a given frequency ω_k , for a set Z of n realizations ζ_i , the real and imaginary parts of the estimated frequency responses $\hat{H}(j\omega_k; Z)$, i.e., $\text{Re}\{\hat{H}(j\omega_k; Z)\}$ and $\text{Im}\{\hat{H}(j\omega_k; Z)\}$, should be averaged first:

$$\text{Re}\{\bar{H}(j\omega_k; Z)\} = \frac{1}{n} \sum_{i=1}^n \text{Re}\{\hat{H}(j\omega_k; \zeta_i)\} \quad (\text{H.1})$$

$$\text{Im}\{\bar{H}(j\omega_k; Z)\} = \frac{1}{n} \sum_{i=1}^n \text{Im}\{\hat{H}(j\omega_k; \zeta_i)\} \quad (\text{H.2})$$

The average magnitude and the average phase angle are then computed, respectively, using

$$|\bar{H}(j\omega_k; Z)| = \sqrt{\text{Re}\{\bar{H}(j\omega_k; Z)\}^2 + \text{Im}\{\bar{H}(j\omega_k; Z)\}^2} \quad (\text{H.3})$$

$$\angle \bar{H}(j\omega_k; Z) = \arctan \frac{\text{Im}\{\bar{H}(j\omega_k; Z)\}}{\text{Re}\{\bar{H}(j\omega_k; Z)\}} \quad (\text{H.4})$$

Similarly, in order to calculate the standard deviations of the magnitude and the phase angle of the frequency response $\bar{H}(j\omega_k; Z)$, the standard deviations of the real and imaginary parts should be computed first:

$$\sigma_{\text{Re}\{\bar{H}\}(j\omega_k; Z)} = \sqrt{\frac{1}{n-1} \sum_{i=1}^n \left| \text{Re}\{\hat{H}(j\omega_k; \zeta_i)\} - \text{Re}\{\bar{H}(j\omega_k; Z)\} \right|^2} \quad (\text{H.5})$$

$$\sigma_{\text{Im}\{\bar{H}\}(j\omega_k; Z)} = \sqrt{\frac{1}{n-1} \sum_{i=1}^n \left| \text{Im}\{\hat{H}(j\omega_k; \zeta_i)\} - \text{Im}\{\bar{H}(j\omega_k; Z)\} \right|^2} \quad (\text{H.6})$$

The standard deviation of the magnitude is then obtained by

$$\sigma_{|\bar{H}|(j\omega_k; Z)} = \sqrt{\sigma_{\text{Re}\{\bar{H}\}(j\omega_k; Z)}^2 + \sigma_{\text{Im}\{\bar{H}\}(j\omega_k; Z)}^2} \quad (\text{H.7})$$

The standard deviation of the phase angle (in rad) is calculated as (van der Vaart, 1992, pp. 234–235):

$$\sigma_{\angle \bar{H}(j\omega_k; Z)} = \begin{cases} \pi & \text{if } \frac{\sigma_{|\bar{H}|(j\omega_k; Z)}}{|\bar{H}(j\omega_k; Z)|} > 1 \\ \arctan \frac{\sigma_{|\bar{H}|(j\omega_k; Z)}}{|\bar{H}(j\omega_k; Z)|} & \text{otherwise} \end{cases} \quad (\text{H.8})$$

A graphical interpretation of the above is given in Figure H.1. The standard deviation of the phase angle equals π (i.e., 180°) if the standard deviation of the magnitude is larger than the average magnitude itself.

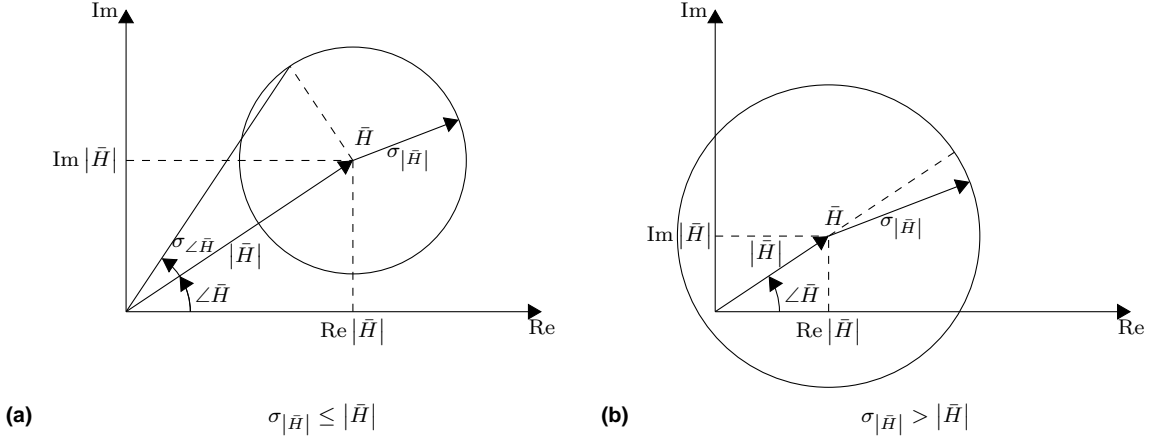


Figure H.1 Standard deviations $\sigma_{|\bar{H}|}$ and $\sigma_{\angle \bar{H}}$ in the complex plane, adapted from van der Vaart (1992).

H.2 Frequency-response accuracies

As presented in Nieuwenhuizen et al. (2008) [note the typo in Eq. (16) corrected here], the analytical variances of the magnitude and the phase angle (in rad) of the frequency response $\hat{H}(j\omega_k; \zeta_i)$, at a given frequency ω_k , are computed, respectively, as (omitting $(j\omega_k; \zeta_i)$ for readability)

$$\sigma_{|\hat{H}|}^2 = \frac{1}{|\hat{H}|^2} \left(\text{Re}(\hat{H})^2 C_1 + 2 \text{Re}(\hat{H}) \text{Im}(\hat{H}) C_{12} + \text{Im}(\hat{H})^2 C_2 \right) \quad (\text{H.9})$$

$$\sigma_{\angle \hat{H}}^2 = \frac{1}{|\hat{H}|^4} \left(\text{Im}(\hat{H})^2 C_1 - 2 \text{Re}(\hat{H}) \text{Im}(\hat{H}) C_{12} + \text{Re}(\hat{H})^2 C_2 \right) \quad (\text{H.10})$$

In the above, C_1 is the variance of the real part of \hat{H} , i.e., $\sigma_{\text{Re}\{\hat{H}\}}^2$, C_{12} is the covariance between the real and imaginary parts of \hat{H} , i.e., $C_{\text{Re}\{\hat{H}\}, \text{Im}\{\hat{H}\}}$, and C_2 is the variance of the imaginary part of \hat{H} , i.e., $\sigma_{\text{Im}\{\hat{H}\}}^2$. Letting $*$ denote the complex conjugate transpose, these elements are determined using Gauss' approximation formula as

$$C_1 = \text{Re} \left(\frac{d\hat{H}}{d\theta} \right) P_\theta \text{Re} \left(\frac{d\hat{H}}{d\theta} \right)^* \quad (\text{H.11})$$

$$C_{12} = \text{Re} \left(\frac{d\hat{H}}{d\theta} \right) P_\theta \text{Im} \left(\frac{d\hat{H}}{d\theta} \right)^* \quad (\text{H.12})$$

$$C_2 = \text{Im} \left(\frac{d\hat{H}}{d\theta} \right) P_\theta \text{Im} \left(\frac{d\hat{H}}{d\theta} \right)^* \quad (\text{H.13})$$

where $\frac{d\hat{H}}{d\theta}$ is the sensitivity of $d\hat{H}$ with respect to the parameter set θ and P_θ is the covariance matrix.

Considering an ARX model's frequency response at a given frequency ω and sampling time T_s (not taking into account the input-output delay n_k)

$$\hat{H}(\omega) = \frac{b_0 + b_1 e^{-j\omega T_s} + \dots + b_{n_b} e^{-(i)j(n_b-1)\omega T_s}}{1 + a_1 e^{-j\omega T_s} + \dots + a_{n_a} e^{-jn_a \omega T_s}} \quad (\text{H.14})$$

the sensitivity is expressed as (omitting ω for readability)

$$\frac{d\hat{H}}{d\theta} = \left[\frac{d\hat{H}}{da_1} \quad \frac{d\hat{H}}{da_2} \quad \dots \quad \frac{d\hat{H}}{da_{n_a}} \quad \frac{d\hat{H}}{db_0} \quad \frac{d\hat{H}}{db_1} \quad \dots \quad \frac{d\hat{H}}{db_{n_b}} \right] \quad (\text{H.15})$$

with (considering no input-output delay n_k)

$$\frac{d\hat{H}}{da_i} = -\frac{\hat{H}}{1 + a_1 e^{-j\omega T_s} + \dots + a_{n_a} e^{-jn_a \omega T_s}} e^{-(i)j\omega T_s} \quad (\text{H.16})$$

$$\frac{d\hat{H}}{db_i} = \frac{1}{1 + a_1 e^{-j\omega T_s} + \dots + a_{n_a} e^{-jn_a \omega T_s}} e^{-(i)j\omega T_s} \quad (\text{H.17})$$



Frequency-response estimation with FCs, and batch and recursive ARX models

This appendix presents frequency-response estimates of the human operator (HO) dynamics for condition C1 (mostly $1/s$ dynamics) and C2 (mostly $1/s^2$ dynamics) (see Table E.1) for $M = 100$ Monte Carlo replications and seven remnant intensities P_n , i.e., 0, 0.05, 0.10, 0.15, 0.20, 0.25, 0.30. The remnant dynamics were defined according $H_n^2(s)$. Both the methods of Fourier coefficients (FCs), batch and recursive ARX models are considered. The ARX-model structure is specified with $n_a = n_b = 2$. Continuous-time delay is estimated with n_k^* (see procedure in scientific paper). For the RLS estimation, the initial parameter estimate $\hat{\theta}_0$ is set to $\hat{\theta}^{\text{OLS}}$ estimated on the initial 30.72 s, and the initial scaled covariance matrix P_0 is set to I . Constant dynamics are considered so the forgetting factor λ is set to 1. The final RLS estimation is used to obtain the frequency-response estimates. For the different P_n , Bode plots of the frequency responses for condition C1 and C2 are shown in Figures I.1 and I.2, respectively. The ensemble-average mean and ensemble standard deviation is shown for the frequency responses based on the FCs. Both the analytical and ensemble standard deviations (see Appendix H) are included in Bode plots of the batch and recursive ARX models. These ARX models are consistent.

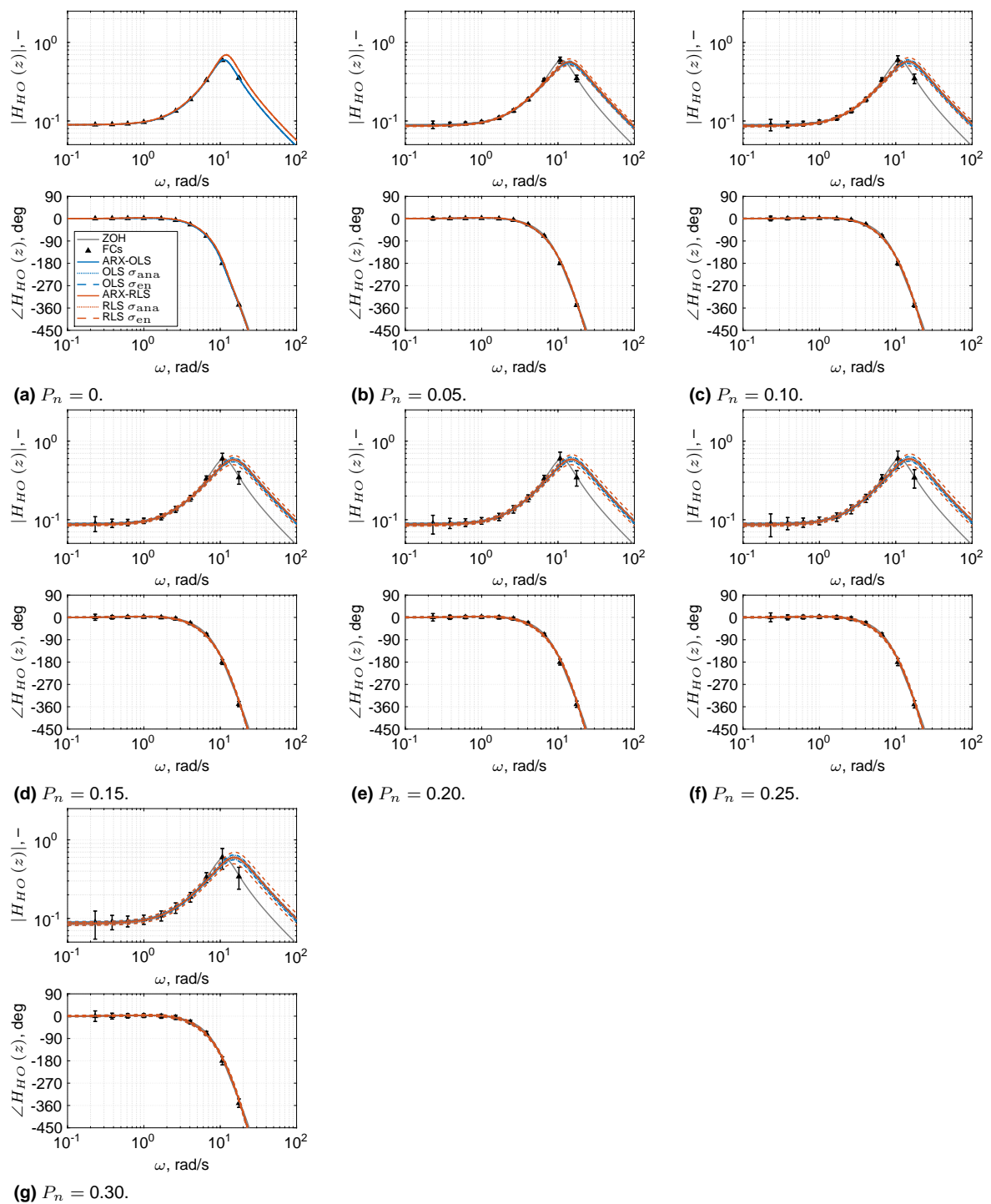


Figure I.1 Bode plots for condition 1.

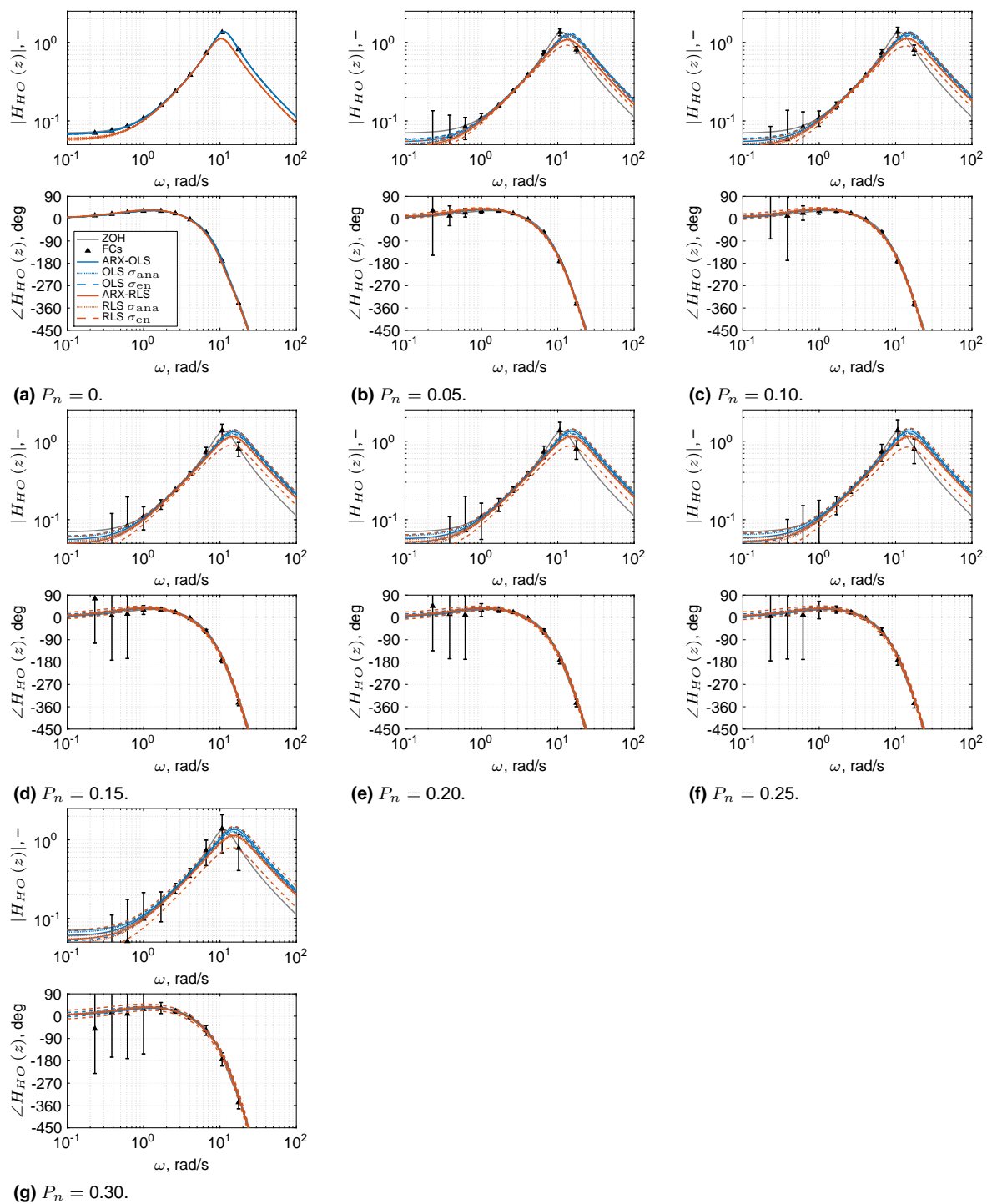


Figure I.2 Bode plots for condition 2.

J

VAF-results

This appendix contains additional results of the variance accounted for (VAF) calculations in the transition window of 20.48 s, for all conditions and remnant intensities. In the scientific paper the actual VAF values were not shown. Figures J.1 and J.2 present the estimation data and validation data VAFs, respectively. Figures J.3 and J.4 shows the average overfit that can be calculated based on these estimation data and validation data VAFs. Figure J.3 expresses the overfit as a subtraction:

$$\Delta \text{VAF}^\lambda = \text{VAF}_e^\lambda - \text{VAF}_v^\lambda \quad (\text{J.1})$$

$$\Delta \text{VAF}^\Lambda = \text{VAF}_e^\Lambda - \text{VAF}_v^\Lambda \quad (\text{J.2})$$

J.4 shows the overfit as a ratios:

$$\frac{\text{VAF}_e^\lambda}{\text{VAF}_v^\lambda} \quad (\text{J.3})$$

and

$$\frac{\text{VAF}_e^\Lambda}{\text{VAF}_v^\Lambda} \quad (\text{J.4})$$

An alternative measure to trade off the tracking ability versus noise sensitivity is given by.

$$\frac{\text{VAF}_v^\lambda}{\text{VAF}_v^{\lambda=1}} \quad (\text{J.5})$$

and

$$\frac{\text{VAF}_v^\Lambda}{\text{VAF}_v^{\Lambda=I}} \quad (\text{J.6})$$

The results of these ratios are shown in Figure J.5.

J.1 Estimation data VAFs

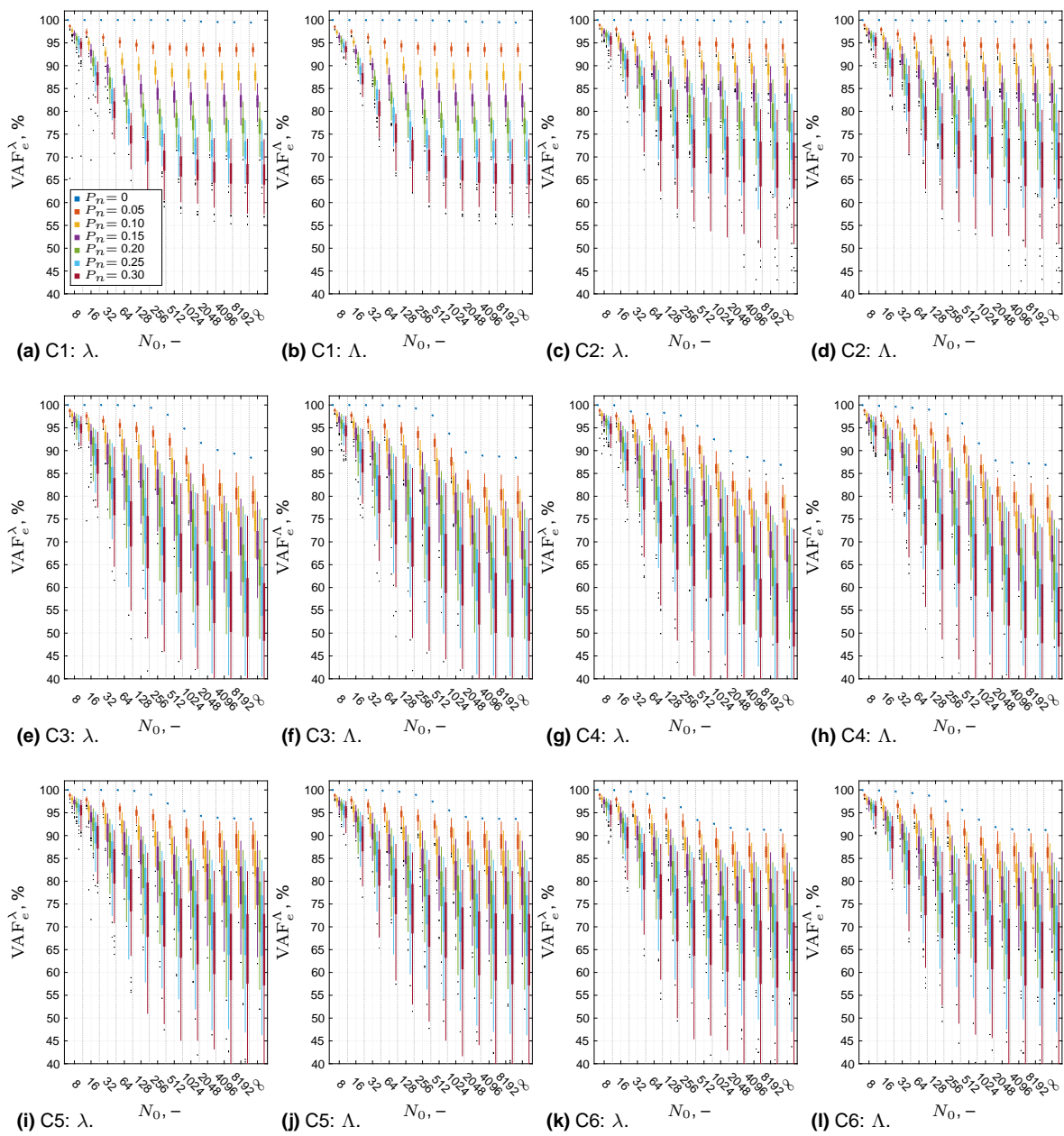


Figure J.1 Estimation data VAFs.

J.2 Validation data VAFs

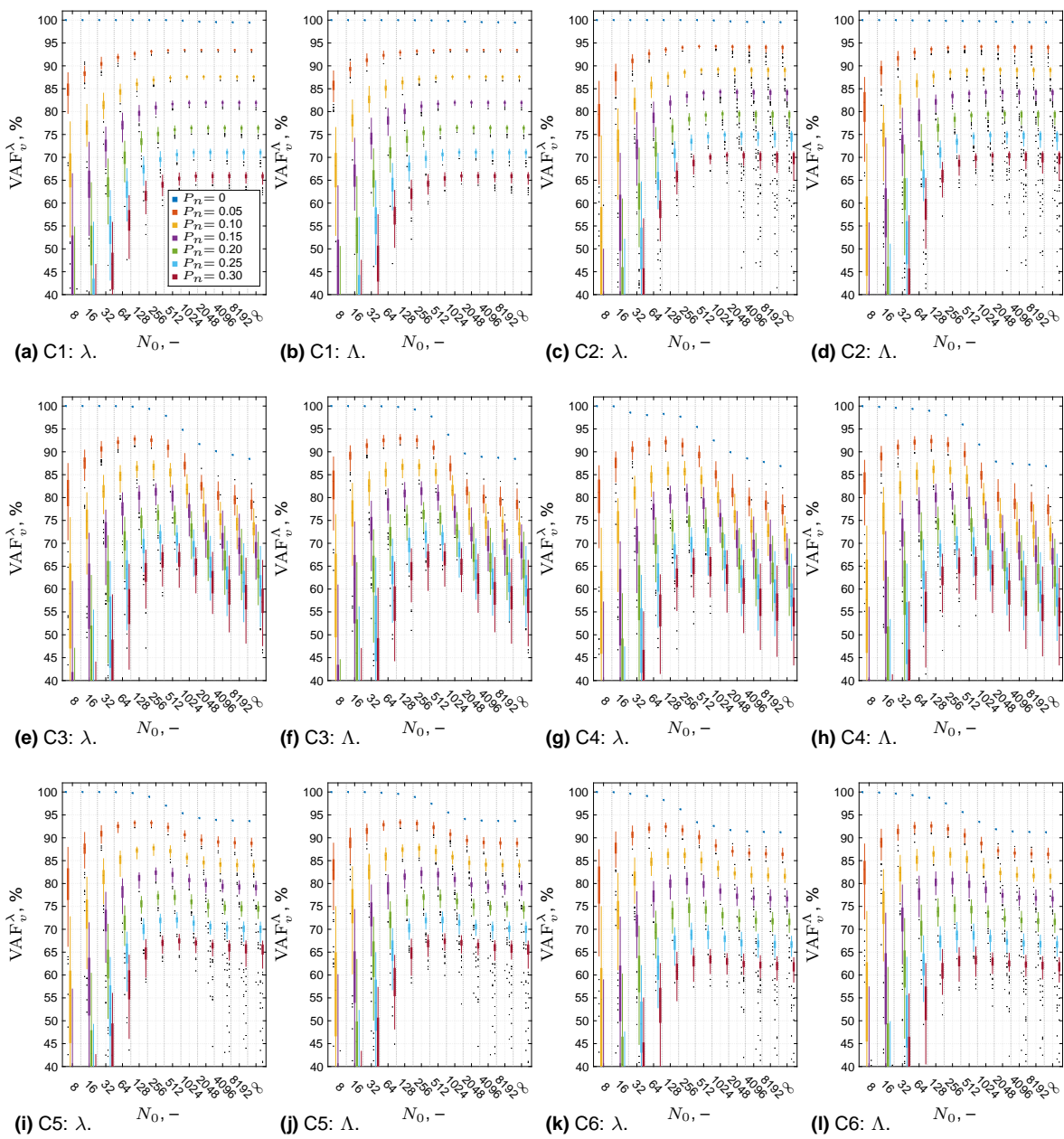


Figure J.2 Validation data VAFs.

J.3 Overfit measures

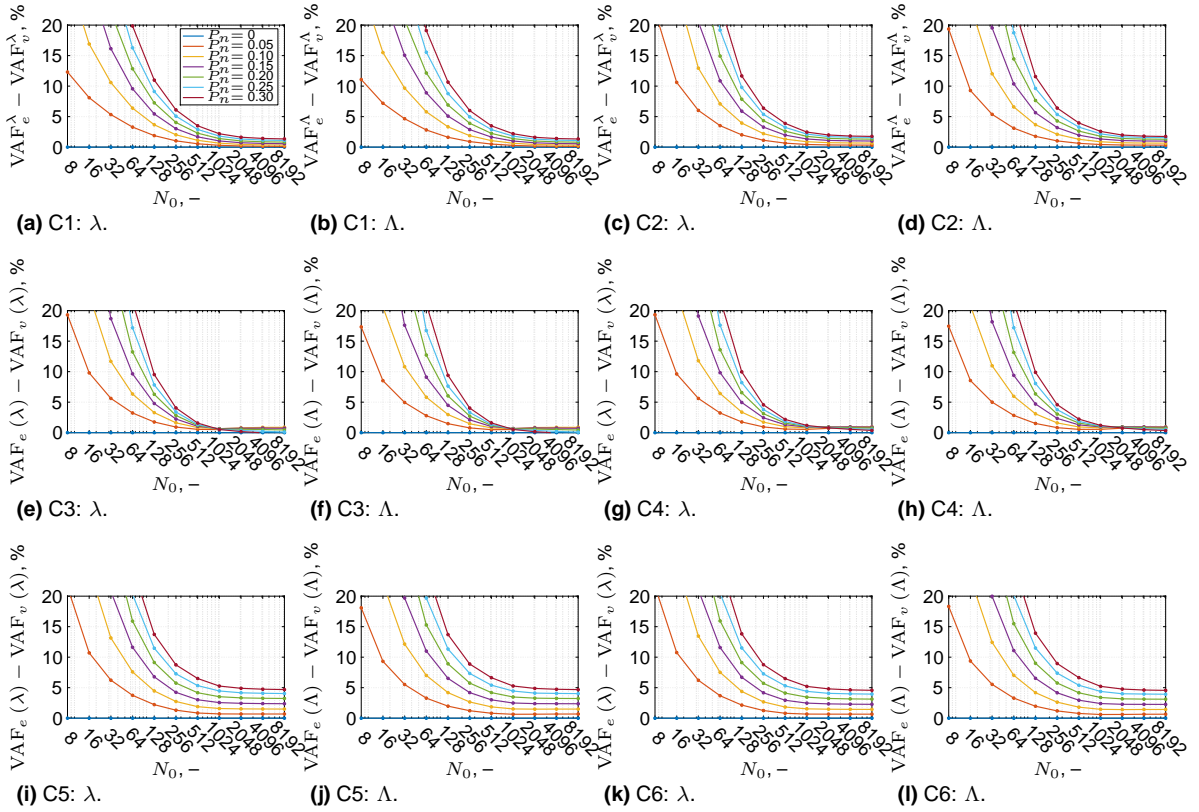


Figure J.3 Overfit as subtraction.

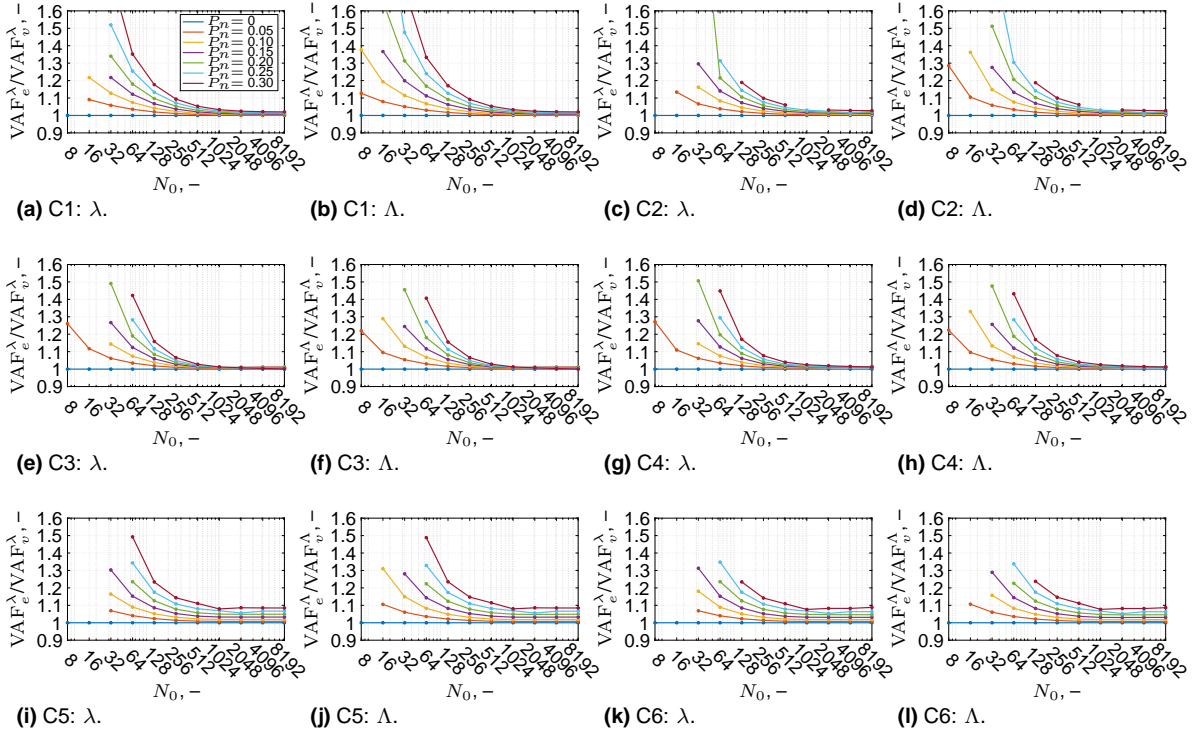


Figure J.4 Overfit as a ratio, ratios for low N_0 approach infinity.

J.4 Tracking ability versus noise sensitivity

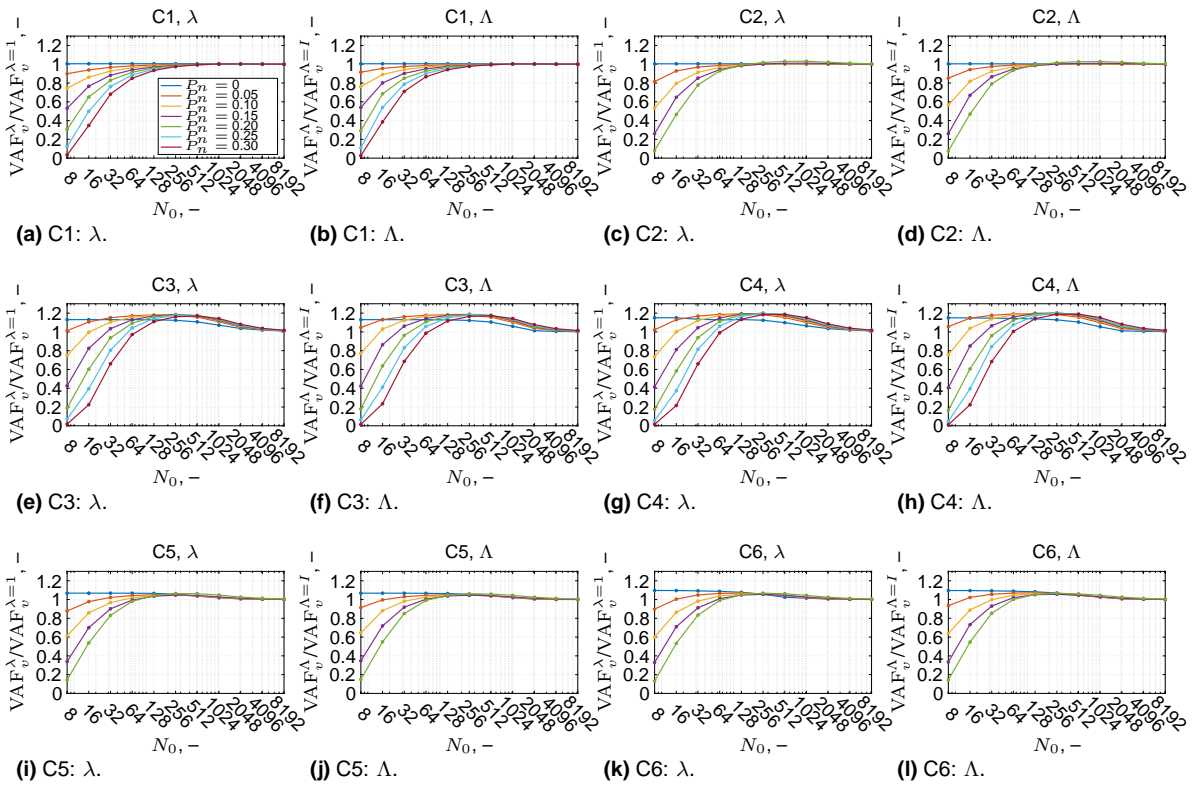
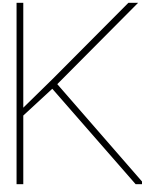


Figure J.5 Ratio to trade off between tracking ability and noise sensitivity.



Time traces of the ARX-model parameters

The subsequent pages show figures with the time traces of the ARX-model parameters $a_1(t)$, $a_2(t)$, $b_0(t)$, and $b_1(t)$, for the different conditions and remnant intensities considered. The results are based on $M = 100$ Monte Carlo replications. Time traces are shown for the initial and final (constant) batch ARX-model estimates with green lines and the recursive ARX-model estimates with black lines. For both the batch and recursive estimates the mean and standard deviations are presented. In addition the ZOH discretized true parameter values are presented in red line. The instant of the sigmoid time of maximum rate of change is shown with a gray line. Memory horizons of powers of two ranging between 2 and 8 192 samples are considered. The results are shown for both the scalar forgetting factor λ and the forgetting matrix Λ , with λ_{a_1} and λ_{a_2} set equal to 1. In addition the case of no forgetting, i.e., $N_0 = \infty$ is given for each condition.

Table K.1 Simulated conditions and overview of figures.

Condition	$H_{CE}(s)$	G, s^{-1}	Measurement window
C1	$H_{CE,1}(s)$	n/a	Figure K.1
C2	$H_{CE,2}(s)$	n/a	Figure K.2
C3	$H_{CE,1}(s) \rightarrow H_{CE,2}(s)$	0.5	Figure K.3
C4	$H_{CE,1}(s) \rightarrow H_{CE,2}(s)$	100	Figure K.4
C5	$H_{CE,2}(s) \rightarrow H_{CE,1}(s)$	0.5	Figure K.5
C6	$H_{CE,2}(s) \rightarrow H_{CE,1}(s)$	100	Figure K.6

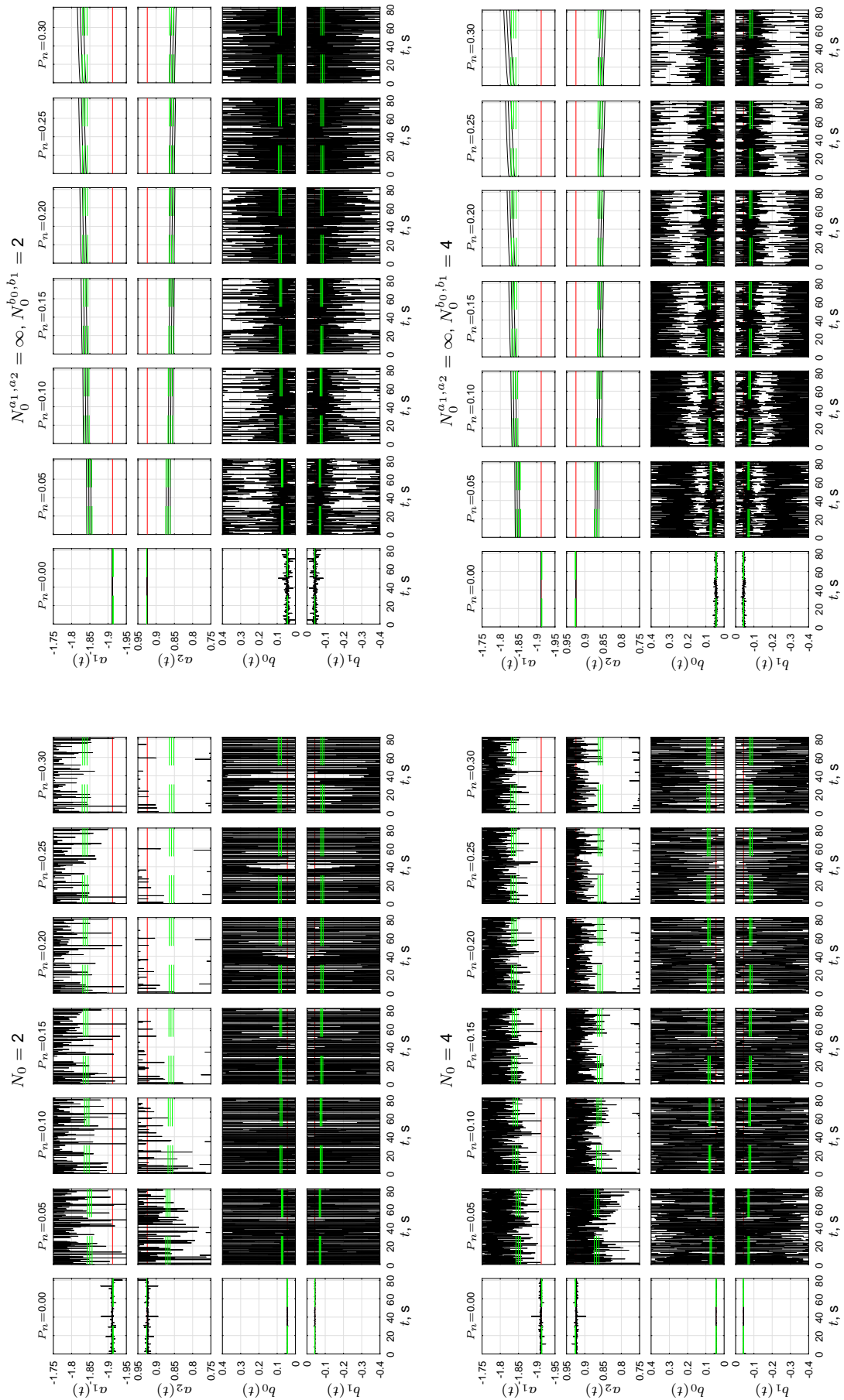


Figure K.1 Time traces of ARX-model parameters for condition C1.

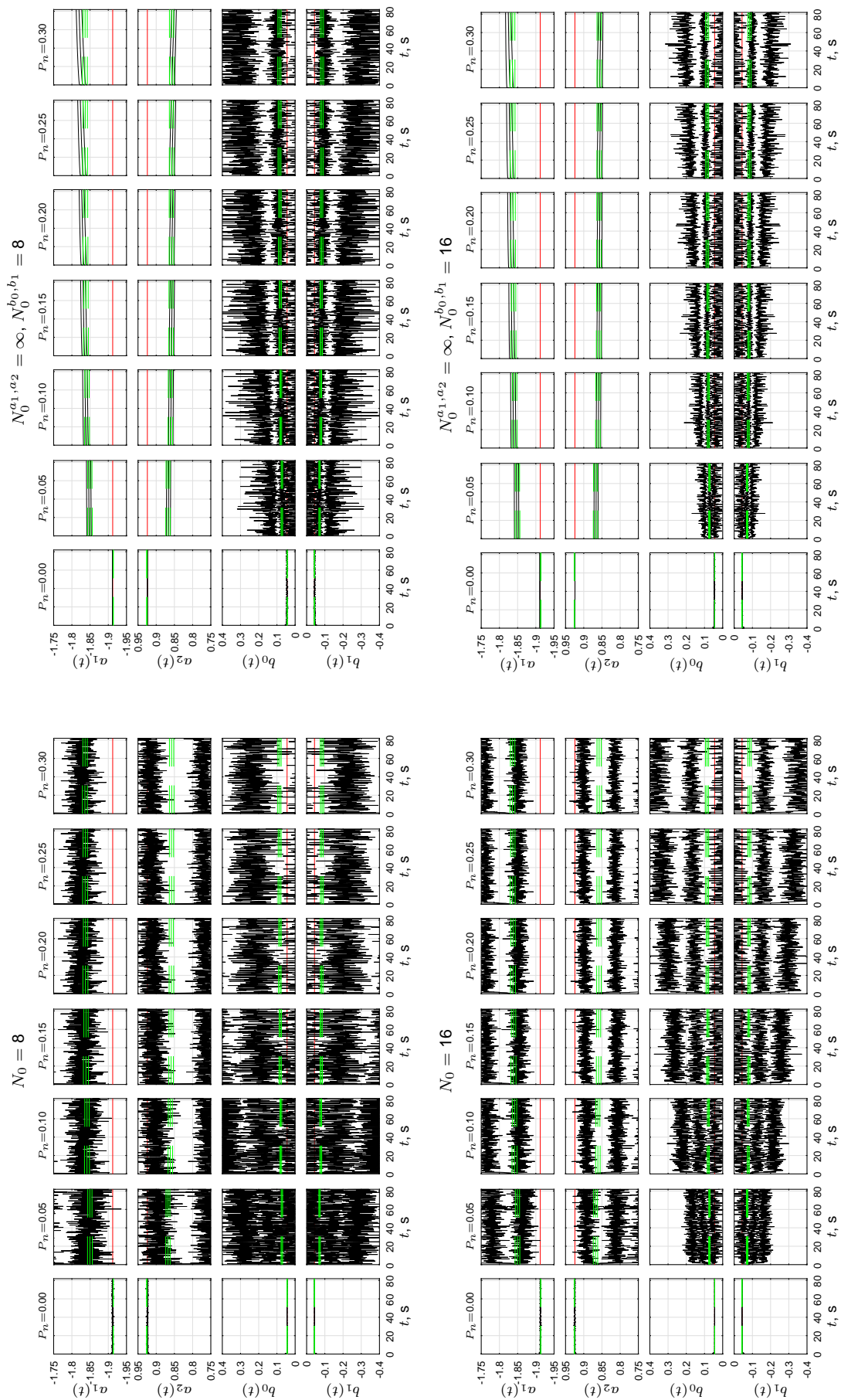


Figure K.1 (continued)

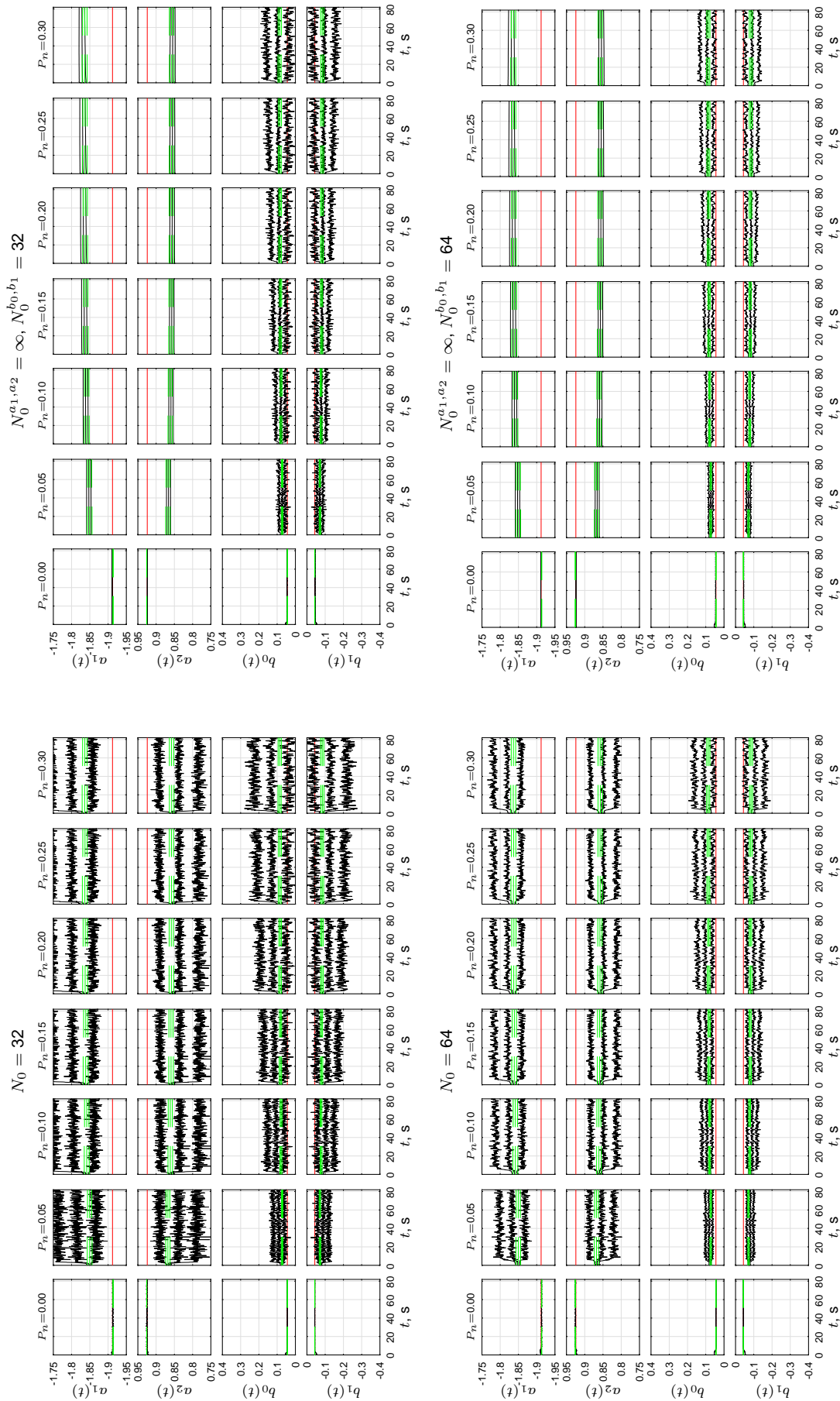


Figure K.1 (continued)

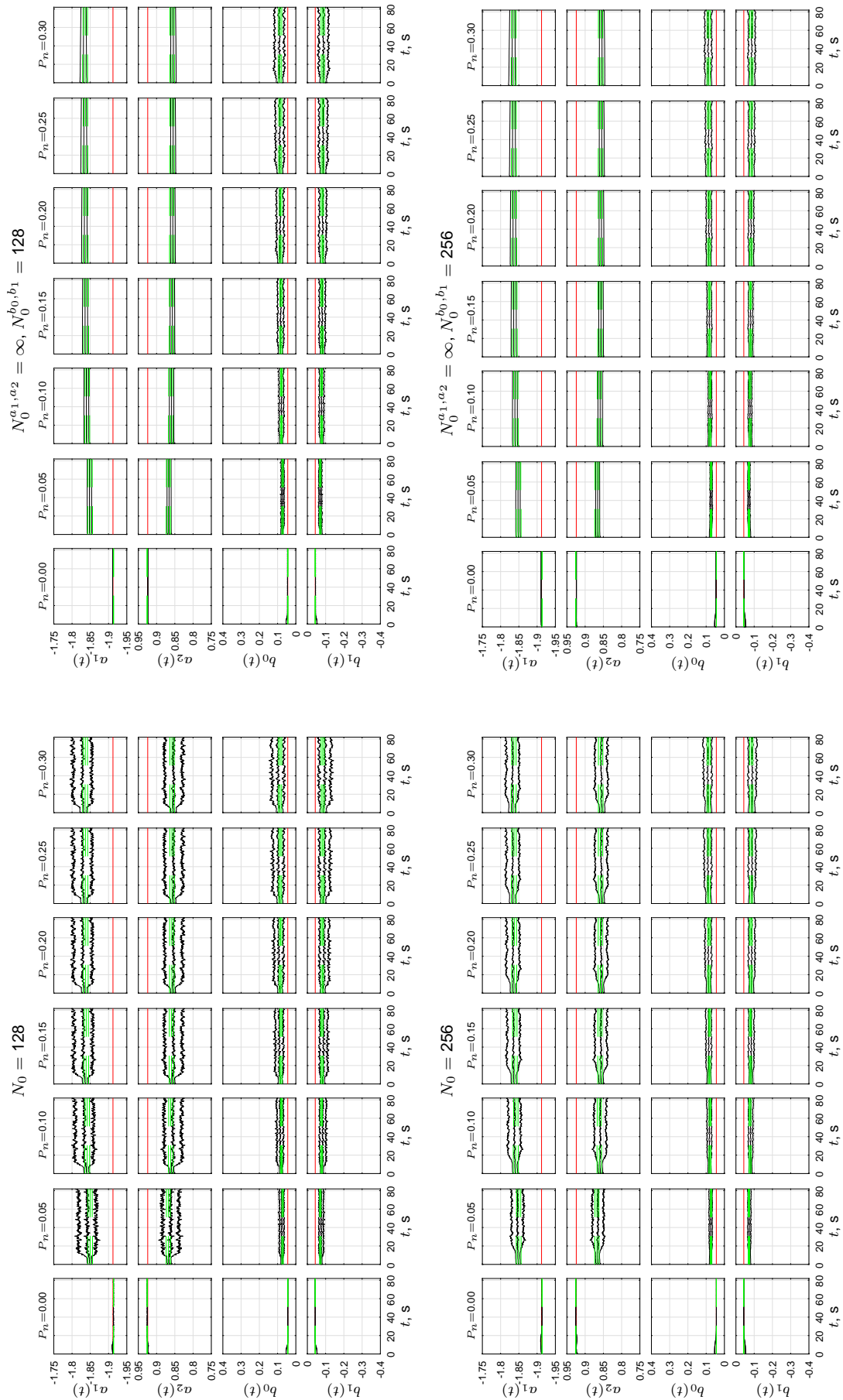


Figure K.1 (continued)

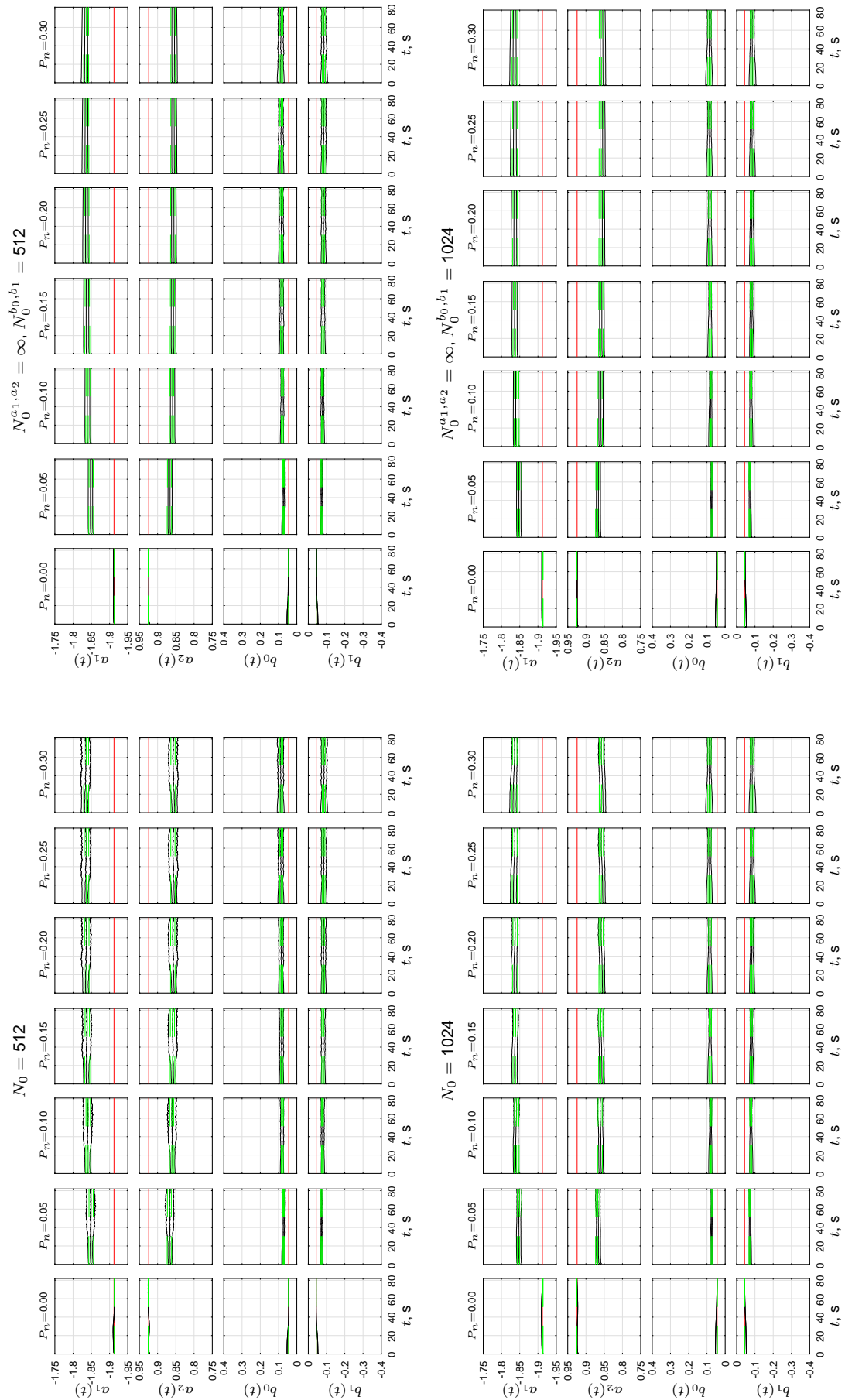


Figure K.1 (continued)

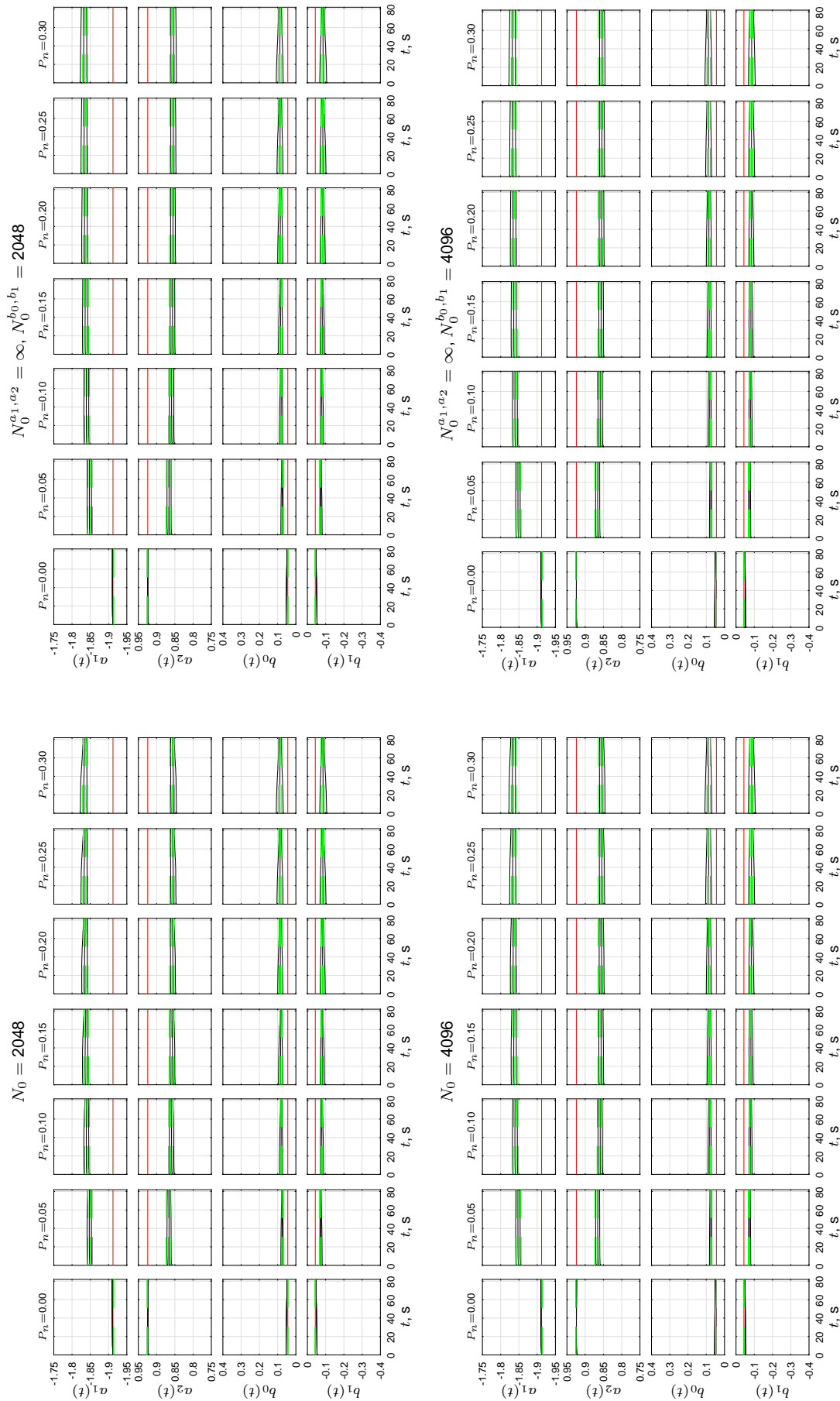


Figure K.1 (continued)

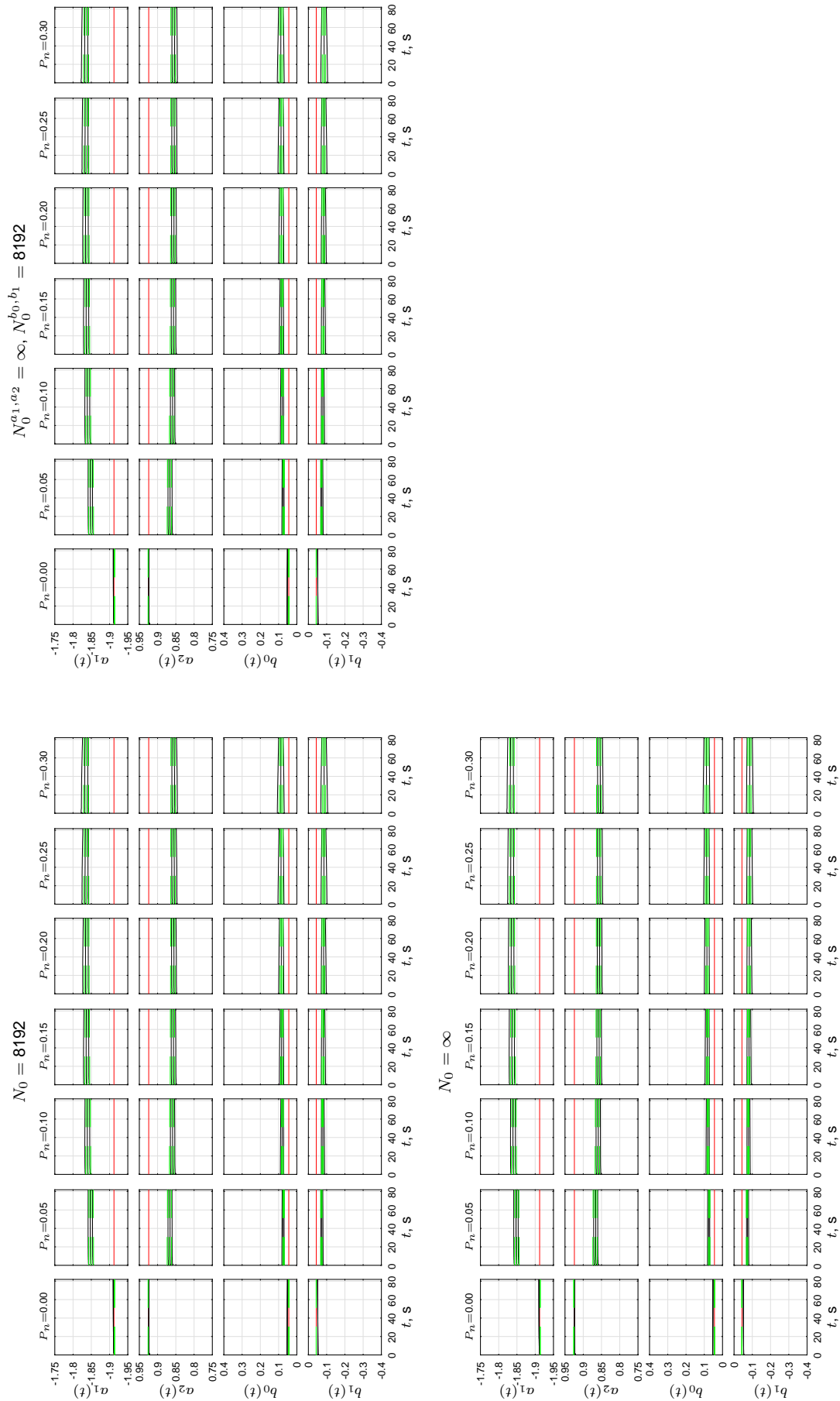


Figure K.1 (continued)

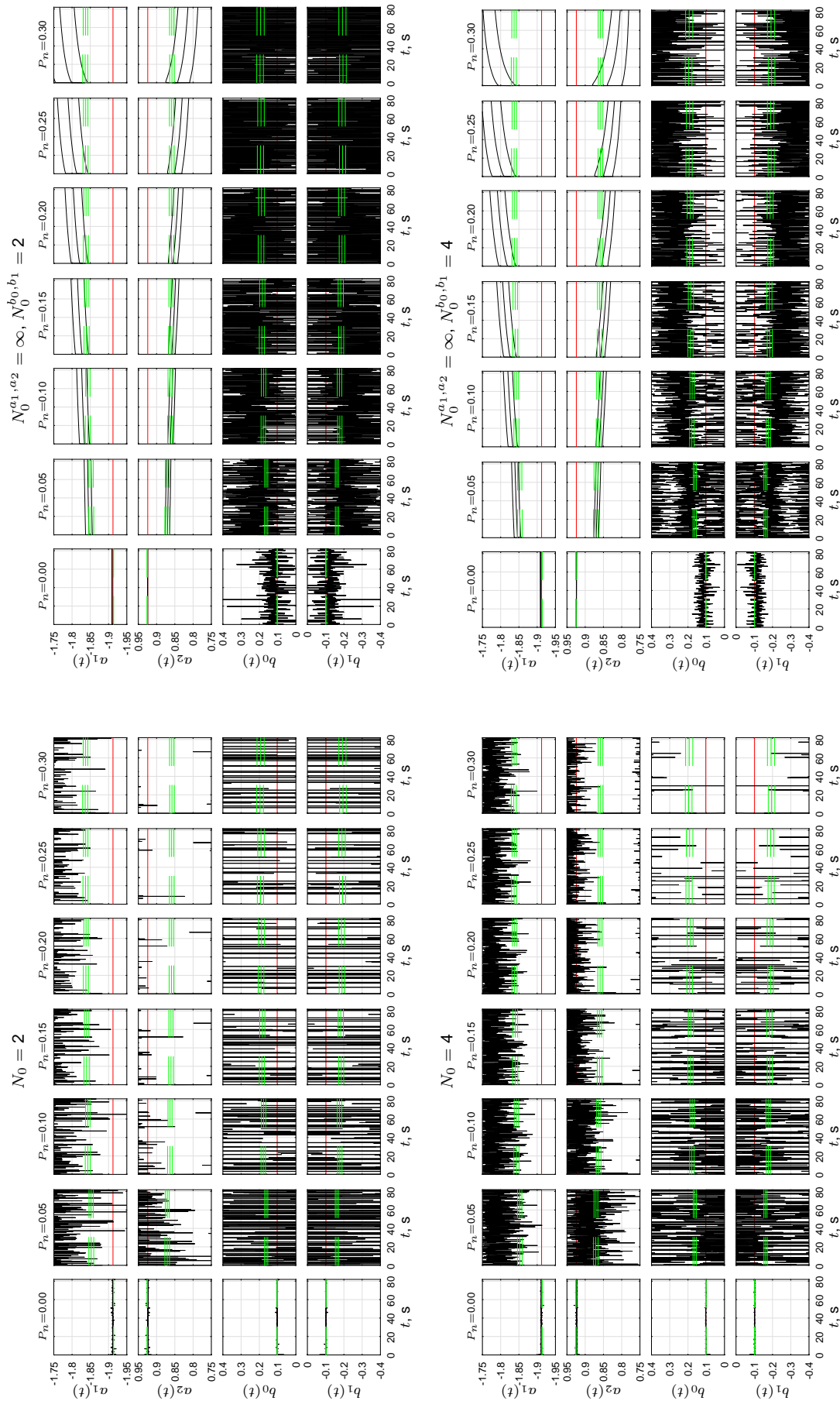


Figure K.2 Time traces of ARX-model parameters for condition C2.

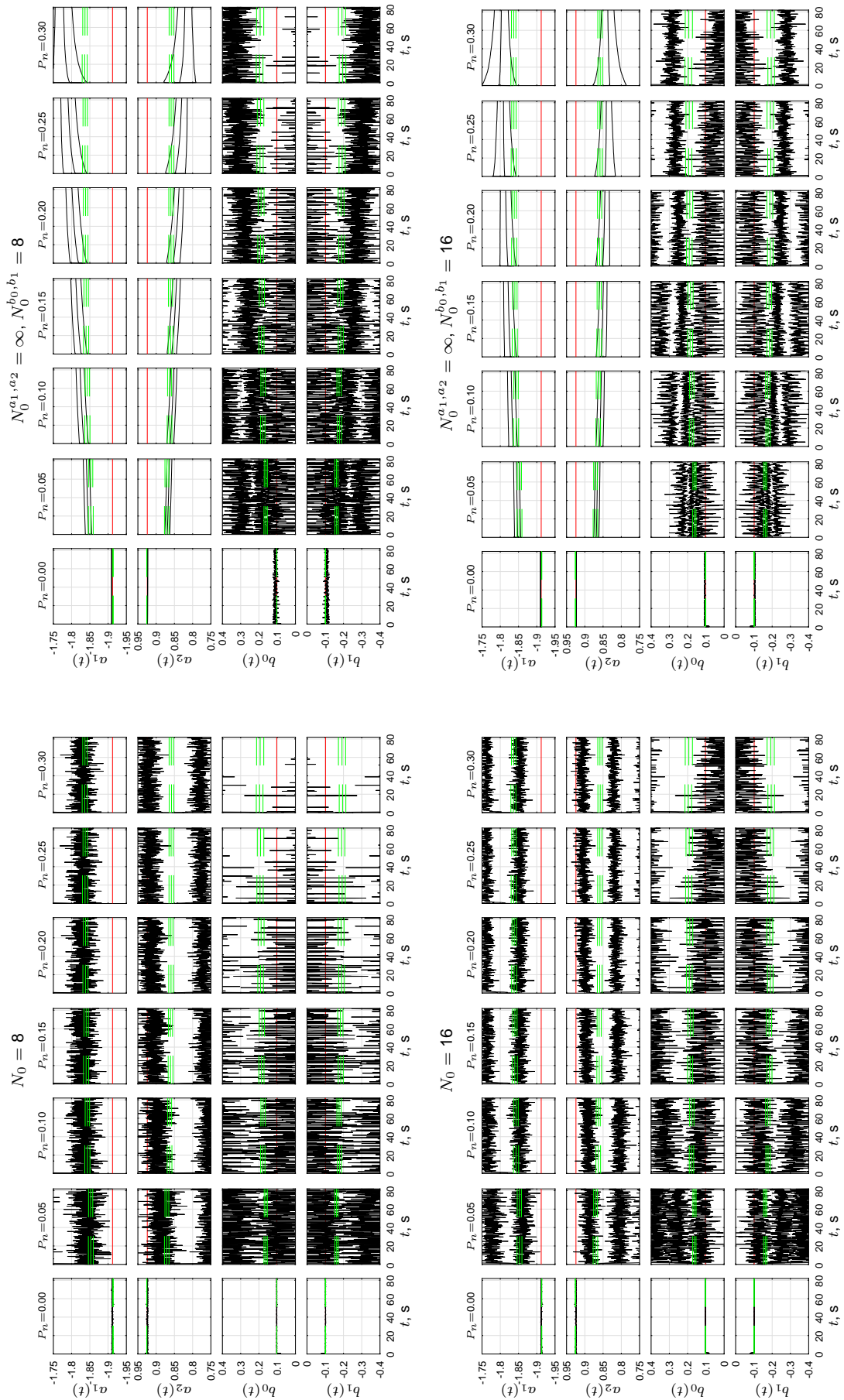


Figure K.2 (continued)

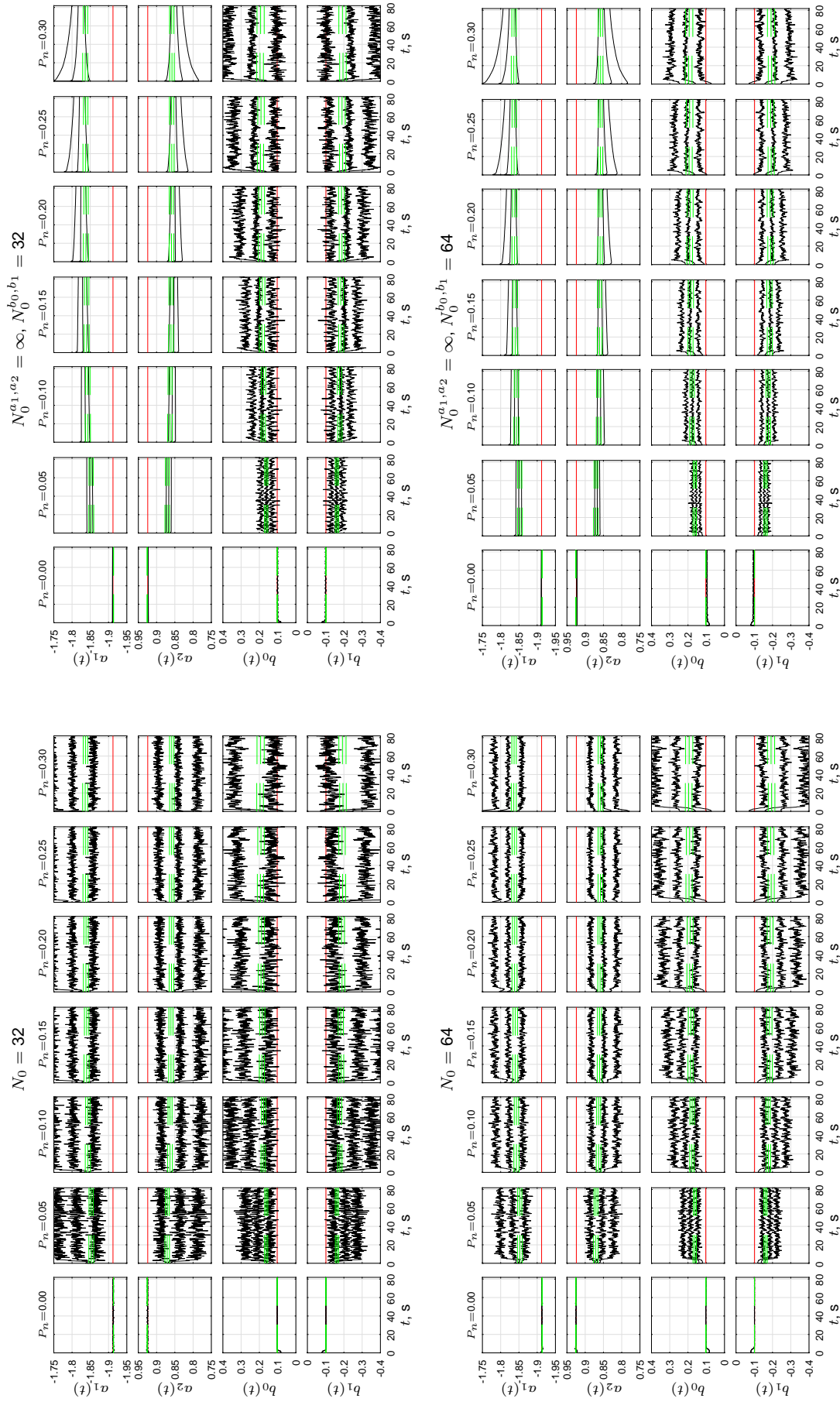


Figure K.2 (continued)

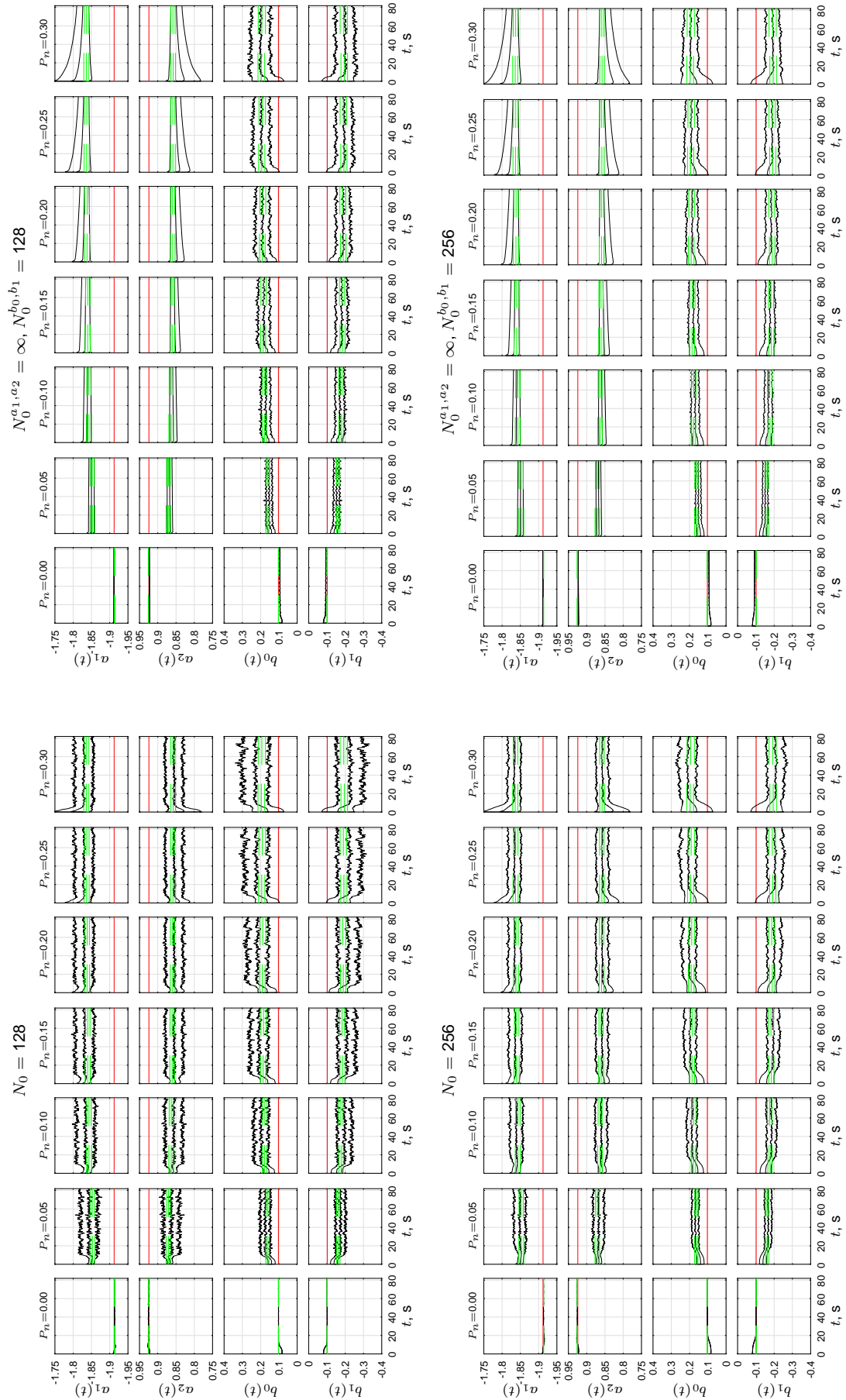


Figure K.2 (continued)

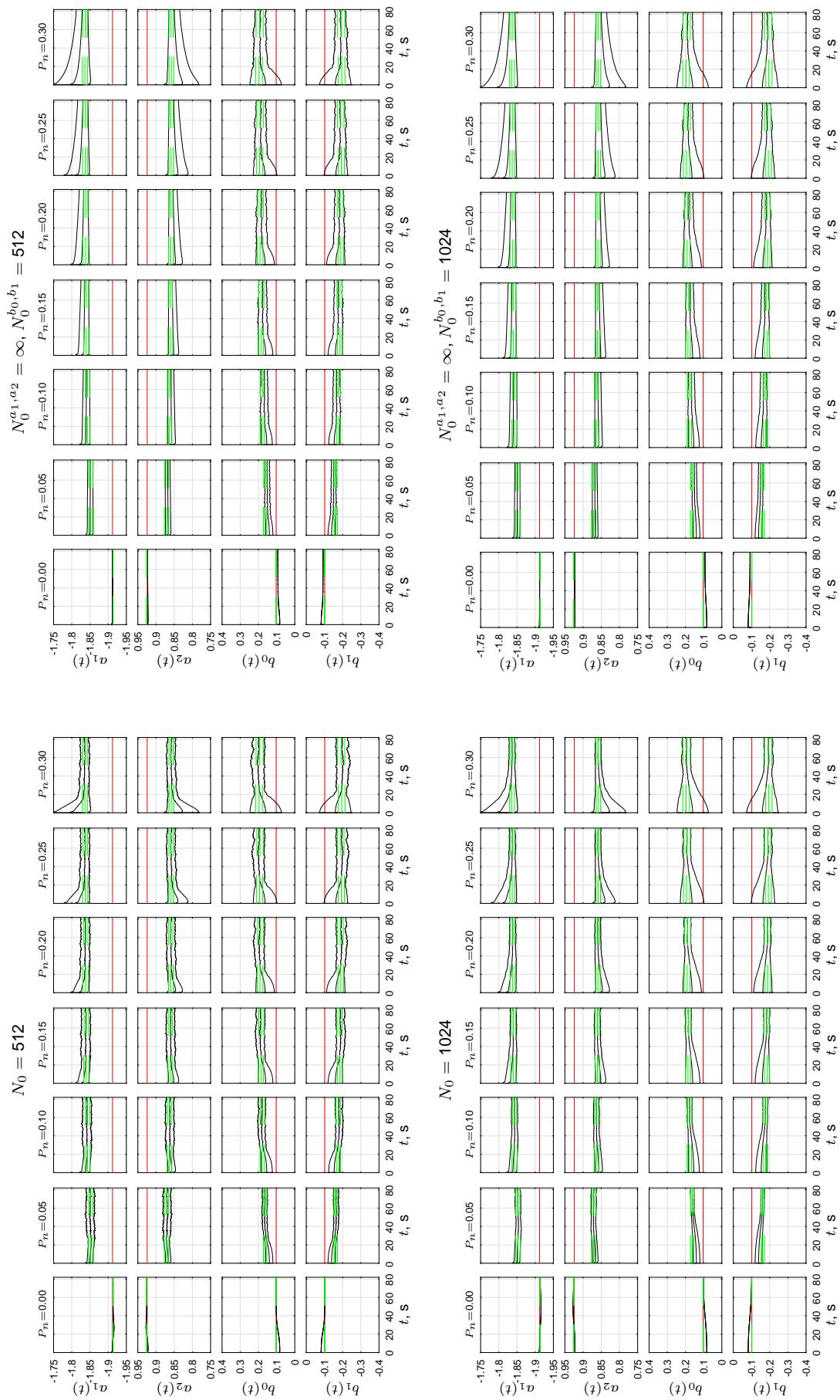


Figure K.2 (continued)

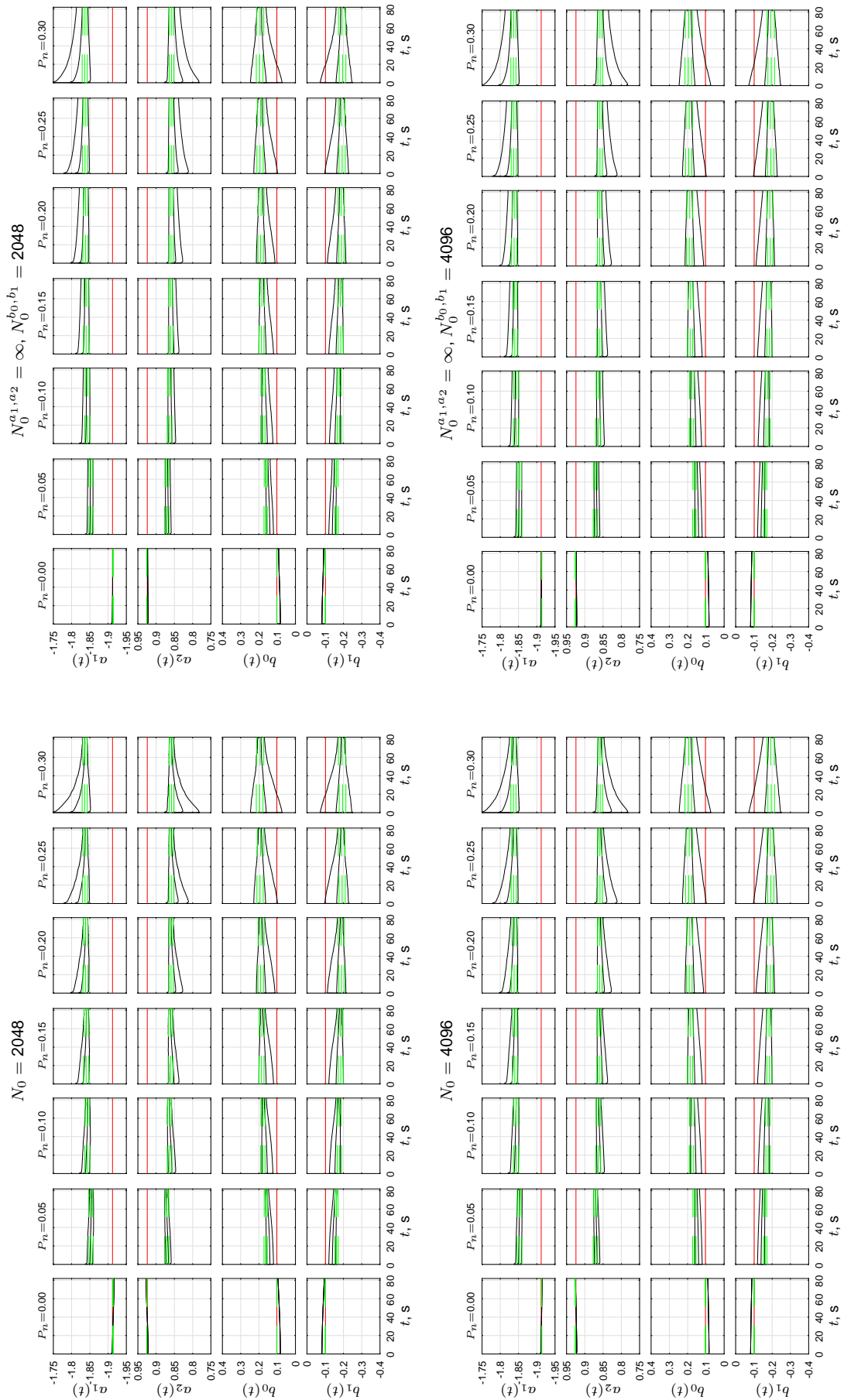


Figure K.2 (continued)

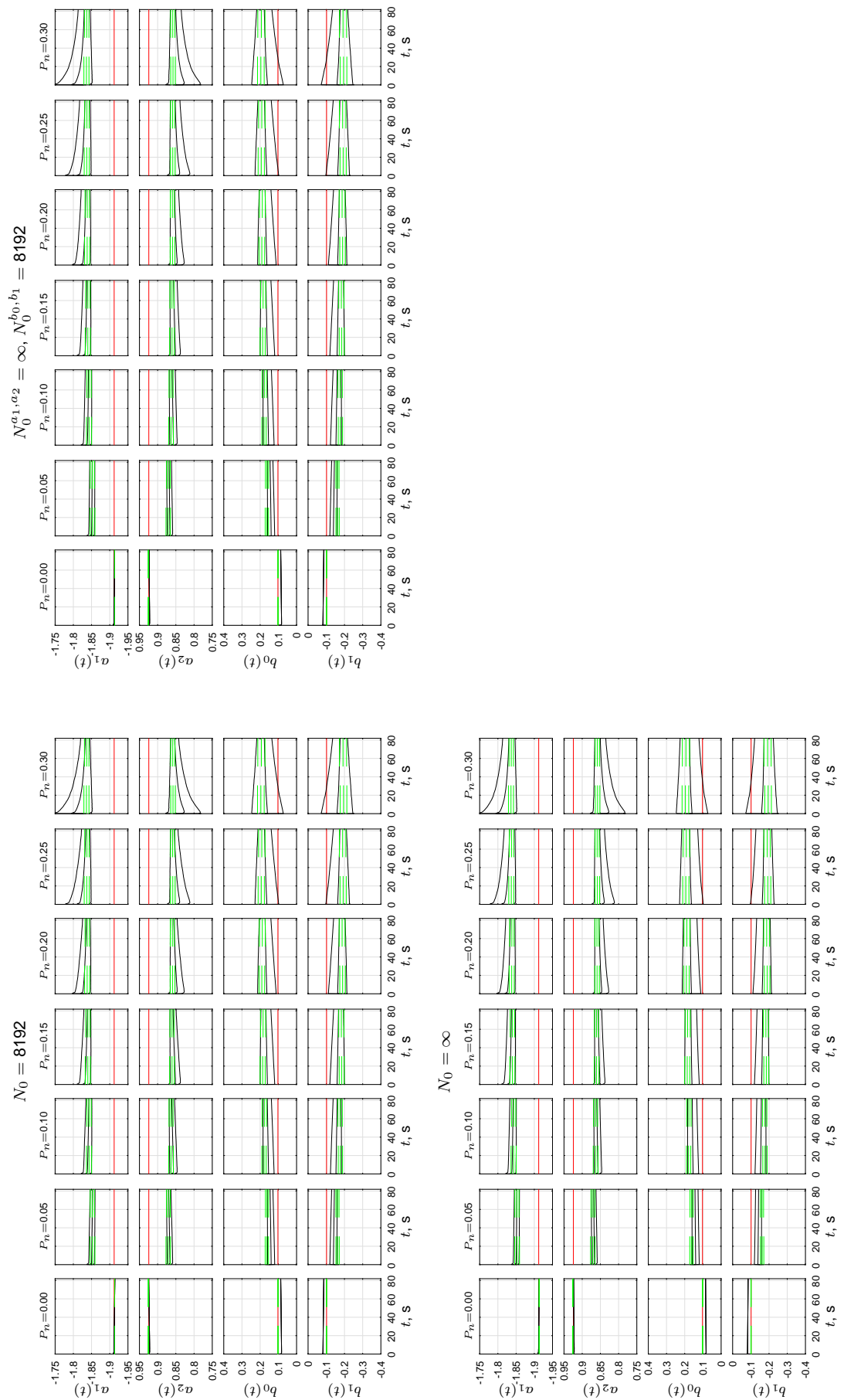


Figure K.2 (continued)

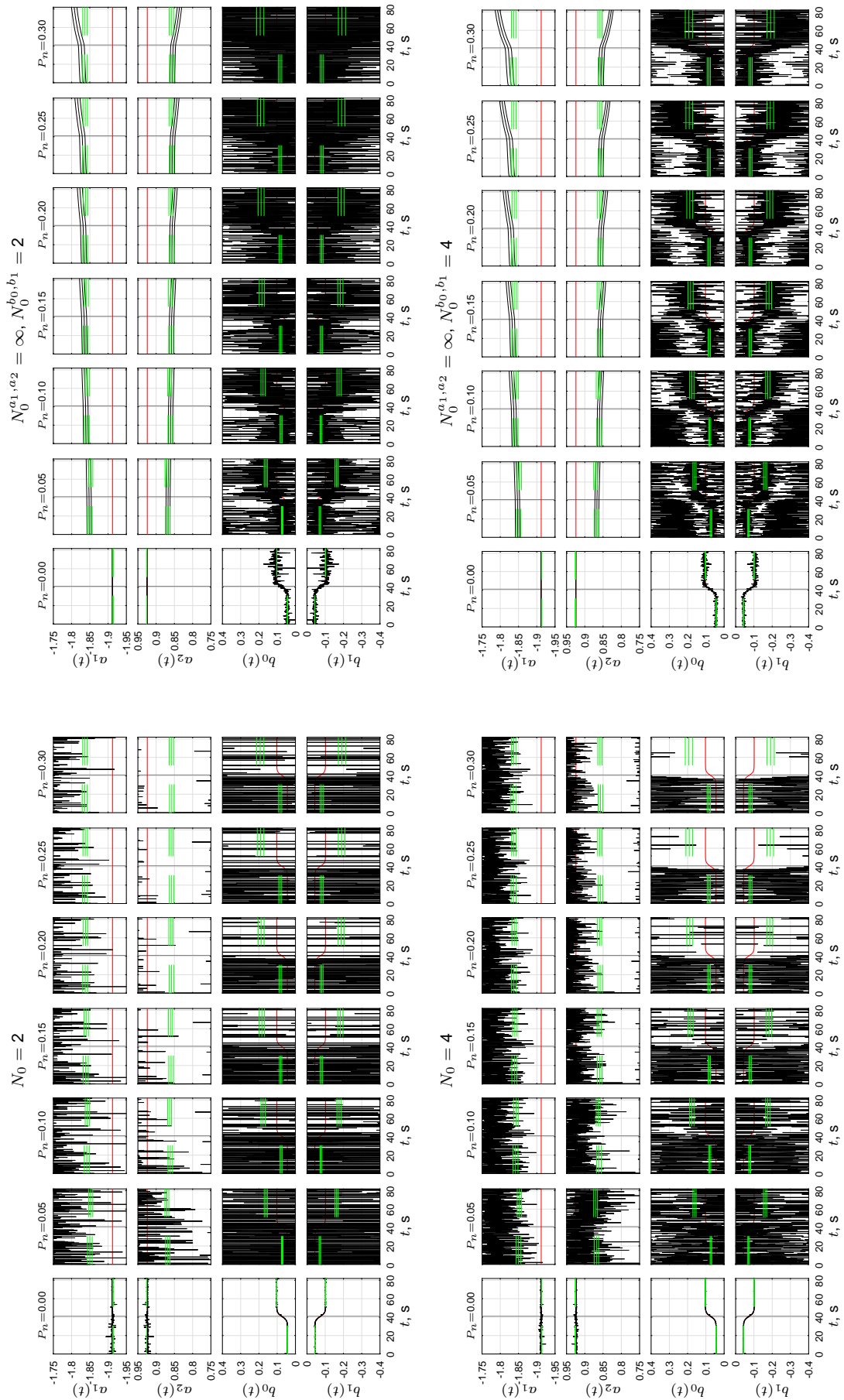


Figure K.3 Time traces of ARX-model parameters for condition C3.

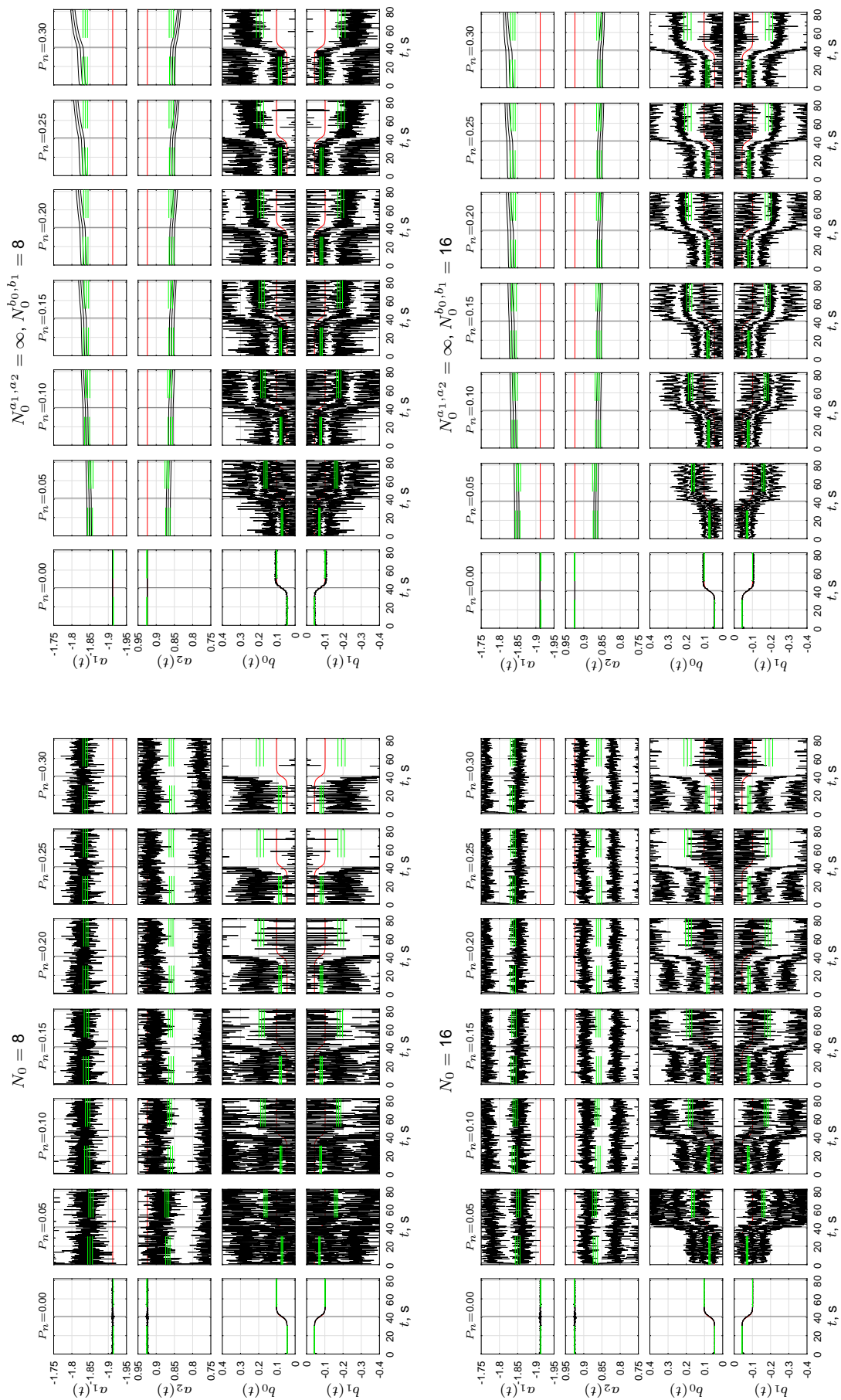


Figure K.3 (continued)

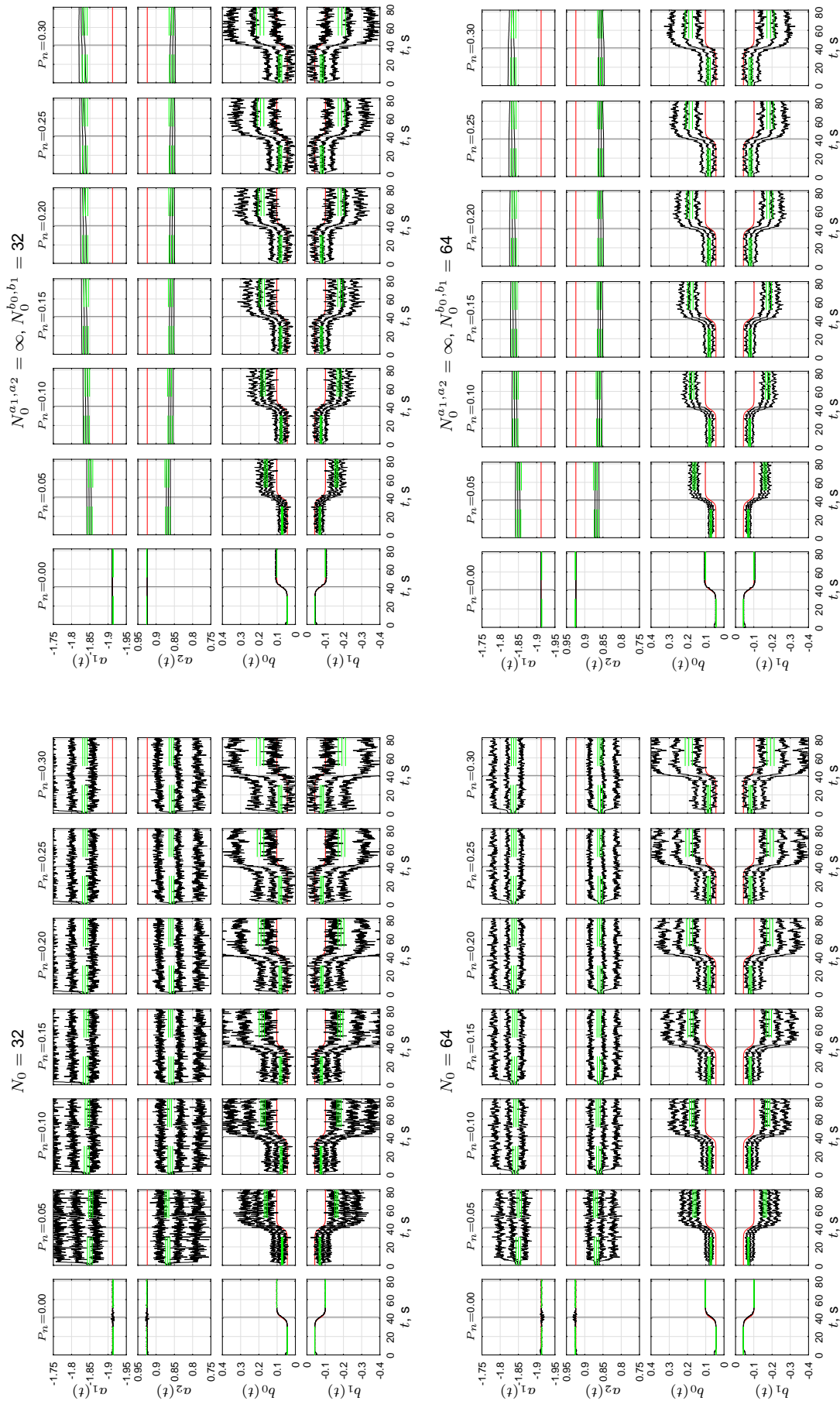


Figure K.3 (continued)

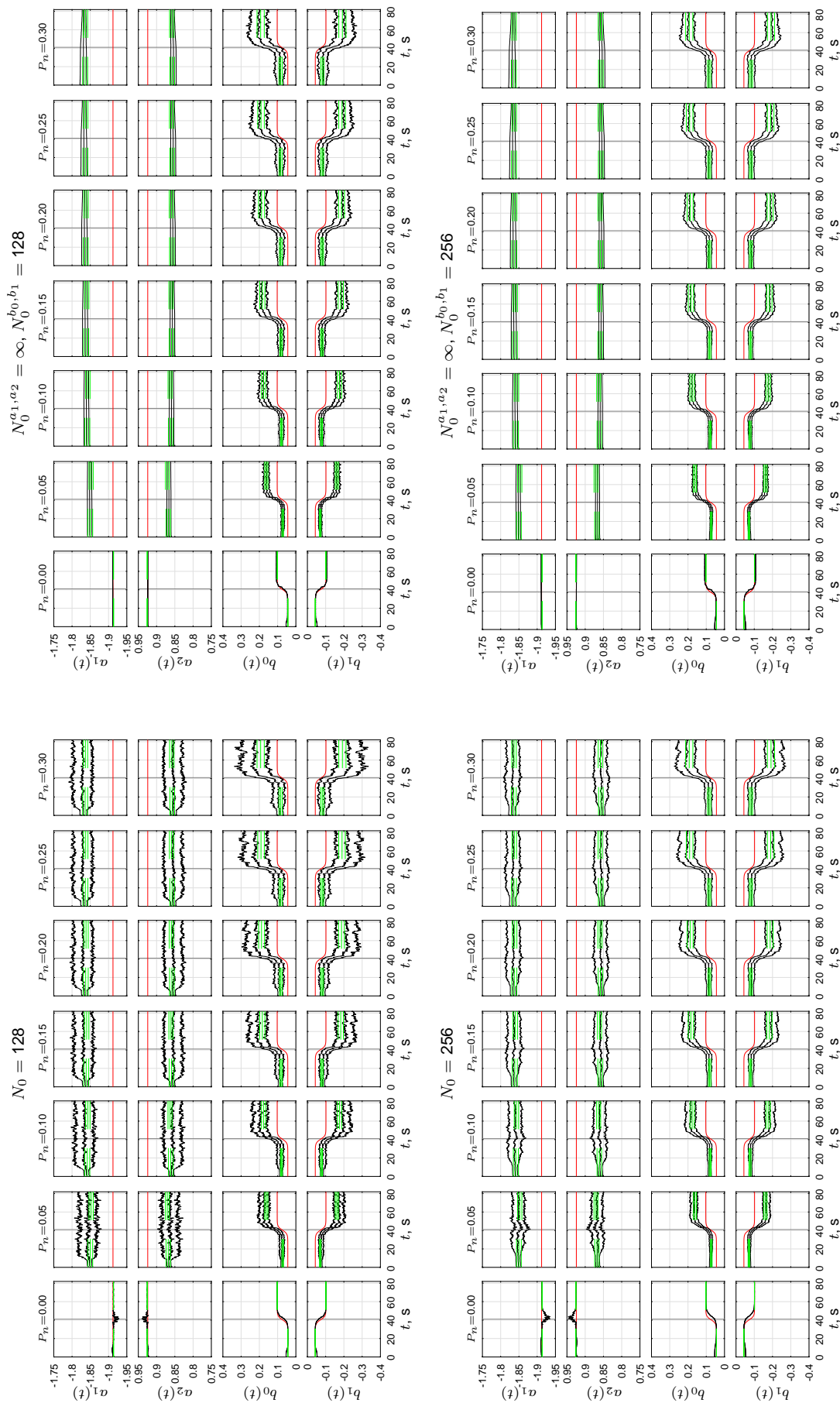


Figure K.3 (continued)

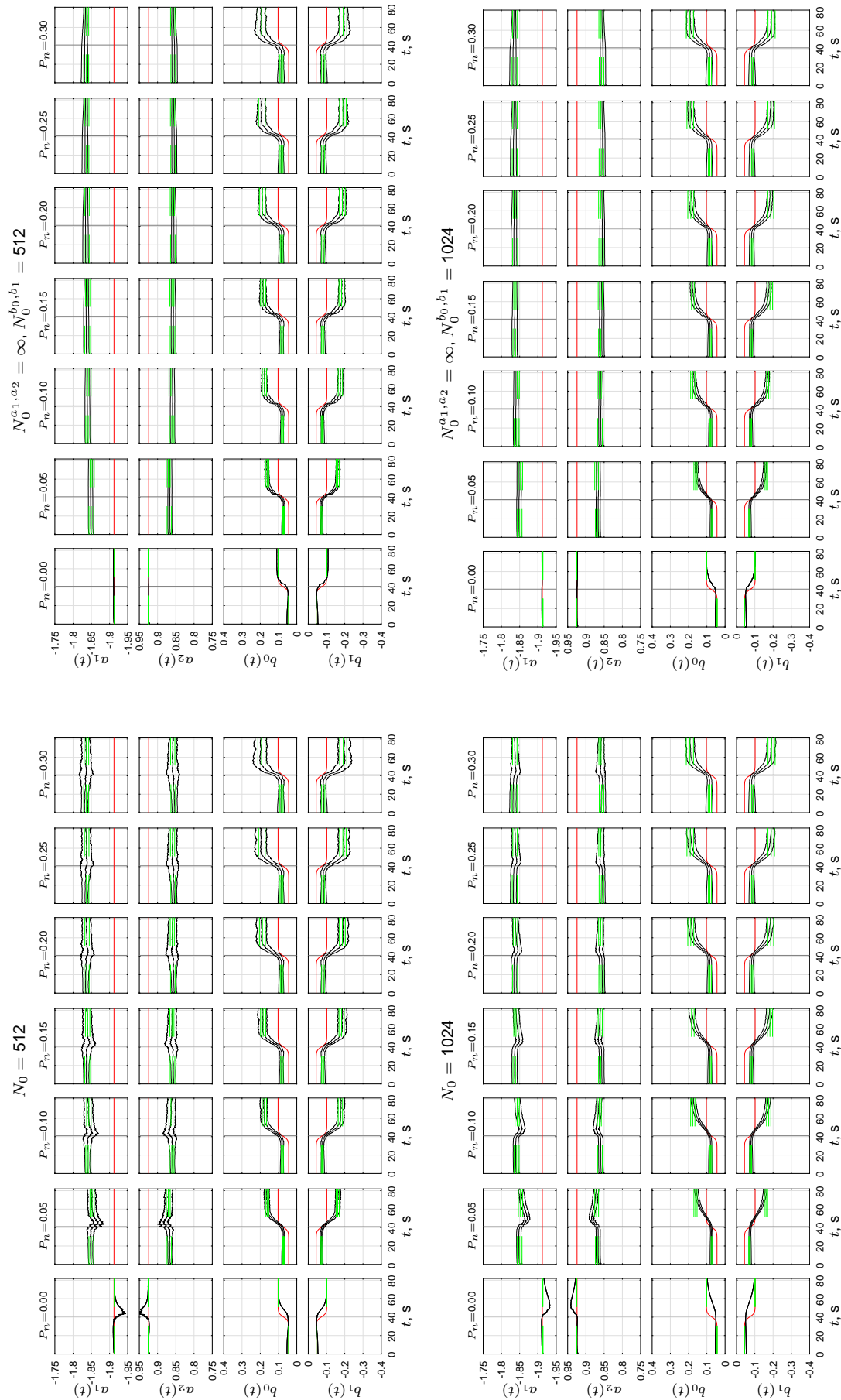


Figure K.3 (continued)

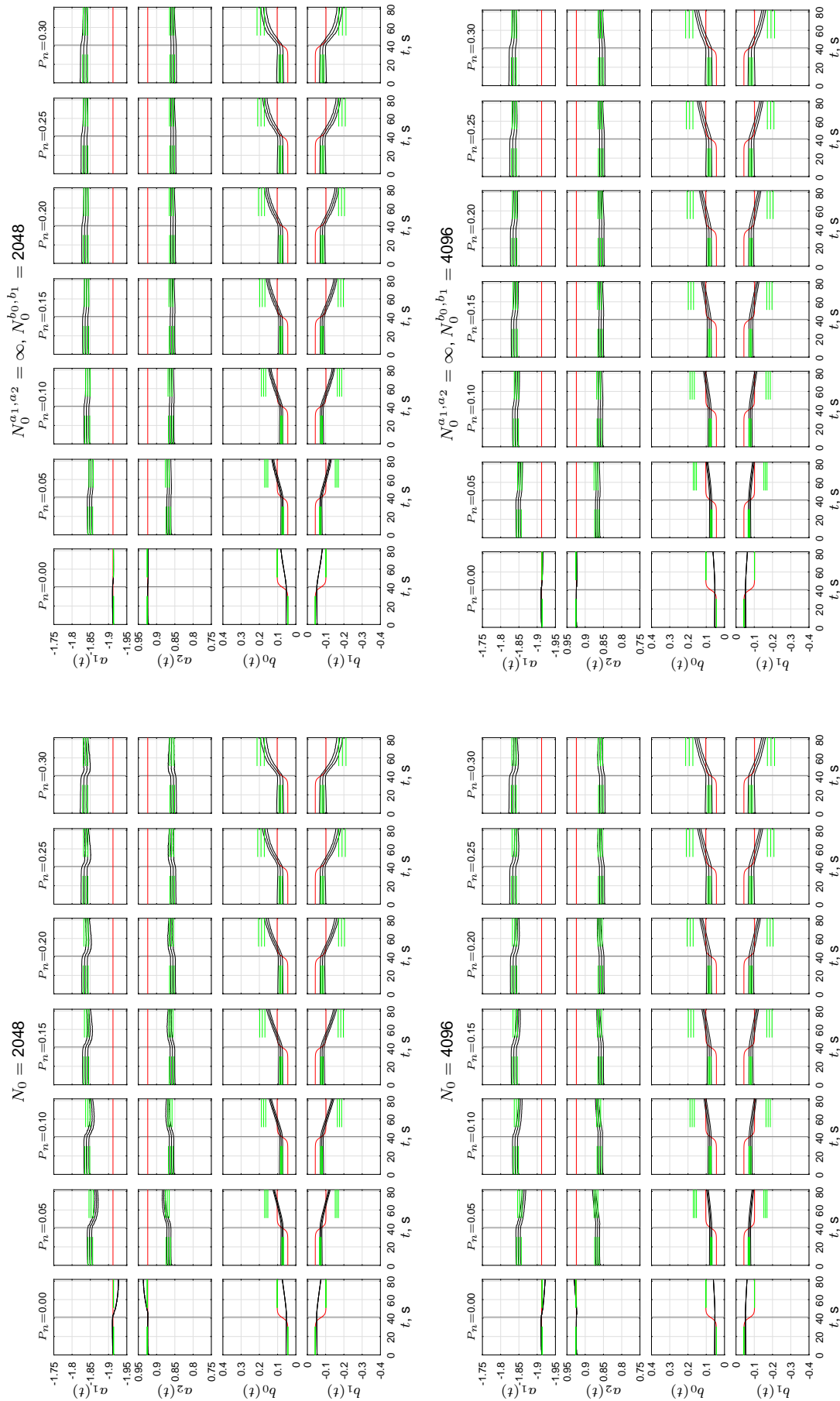


Figure K.3 (continued)

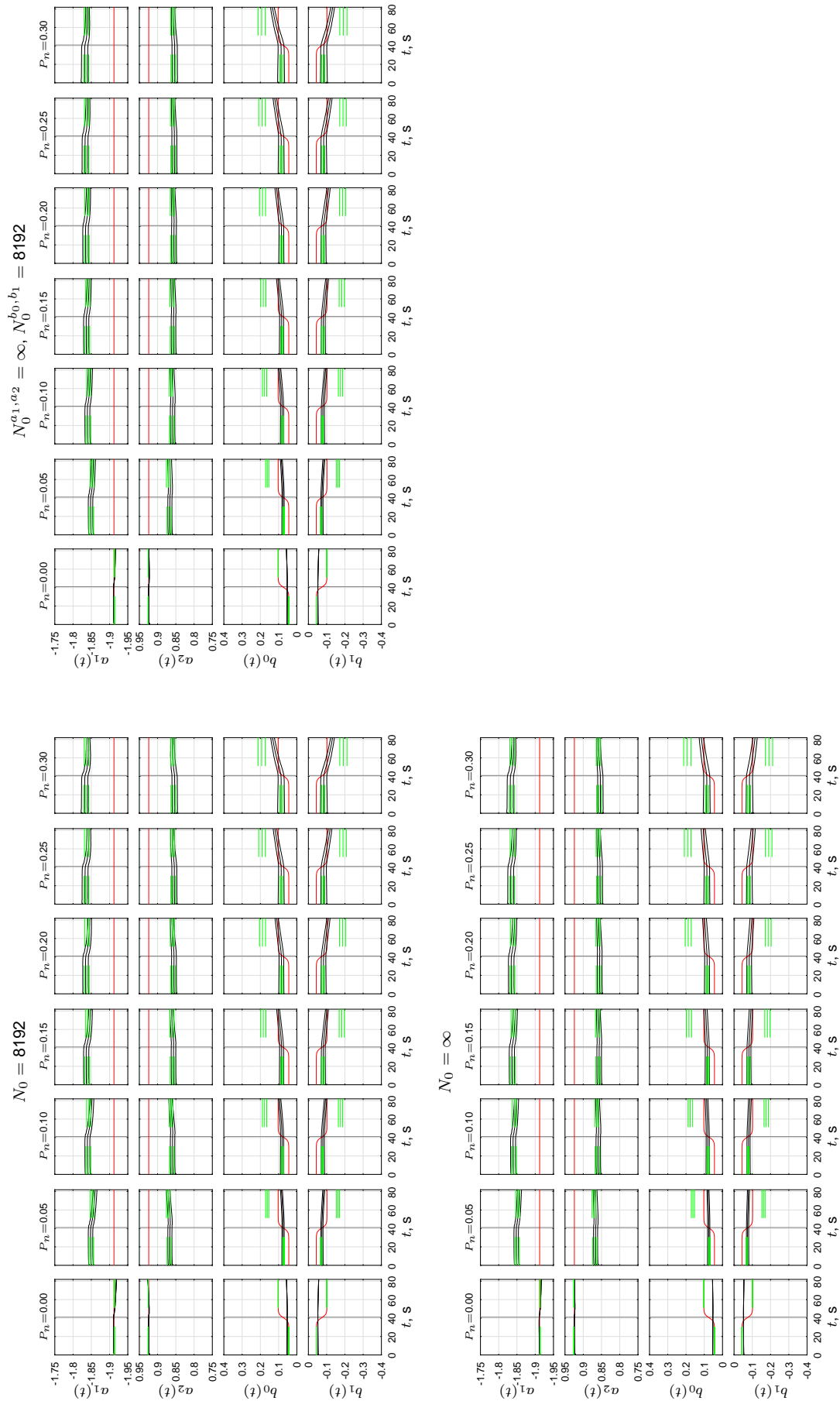


Figure K.3 (continued)

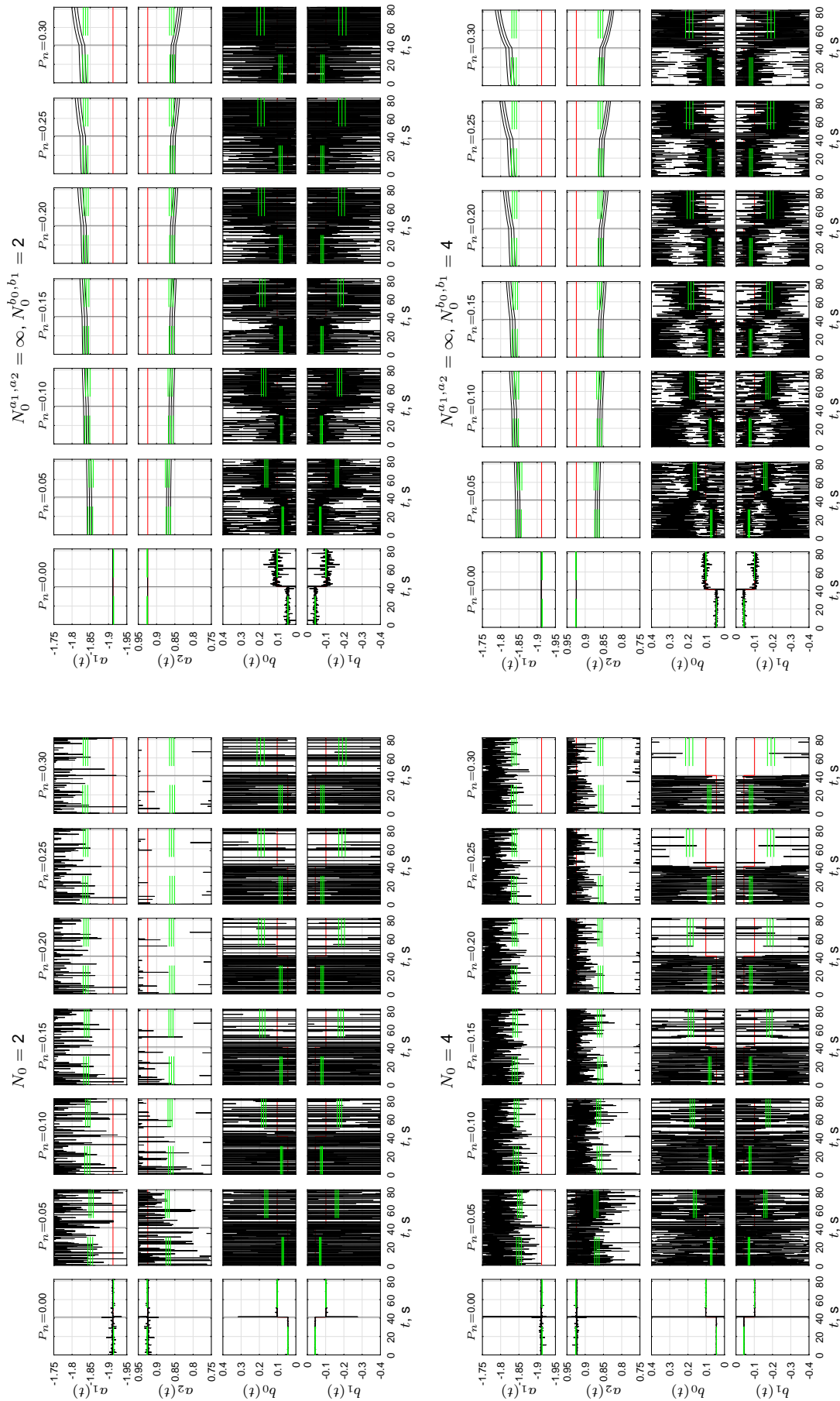


Figure K.4 Time traces of ARX-model parameters for condition C4.

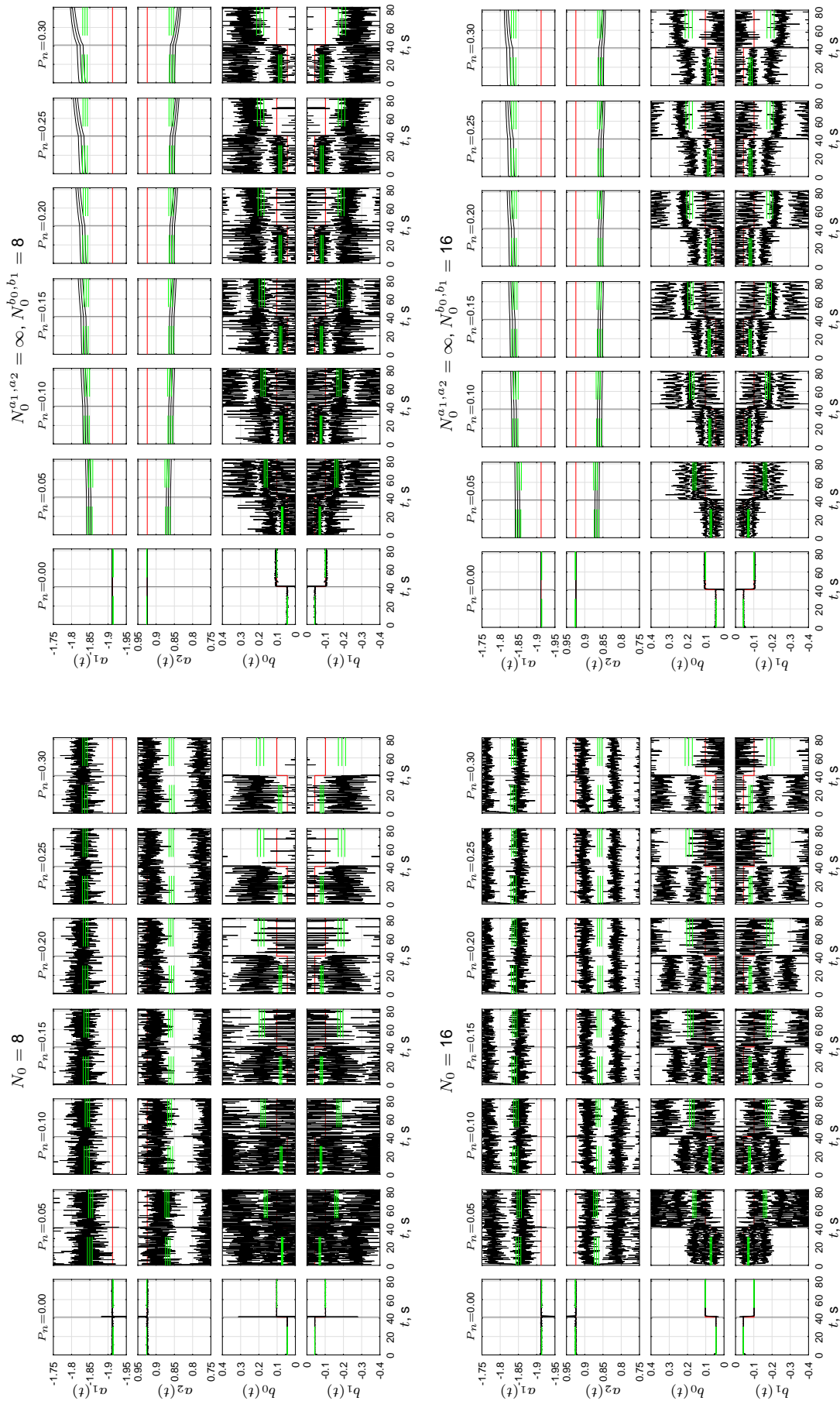


Figure K.4 (continued)

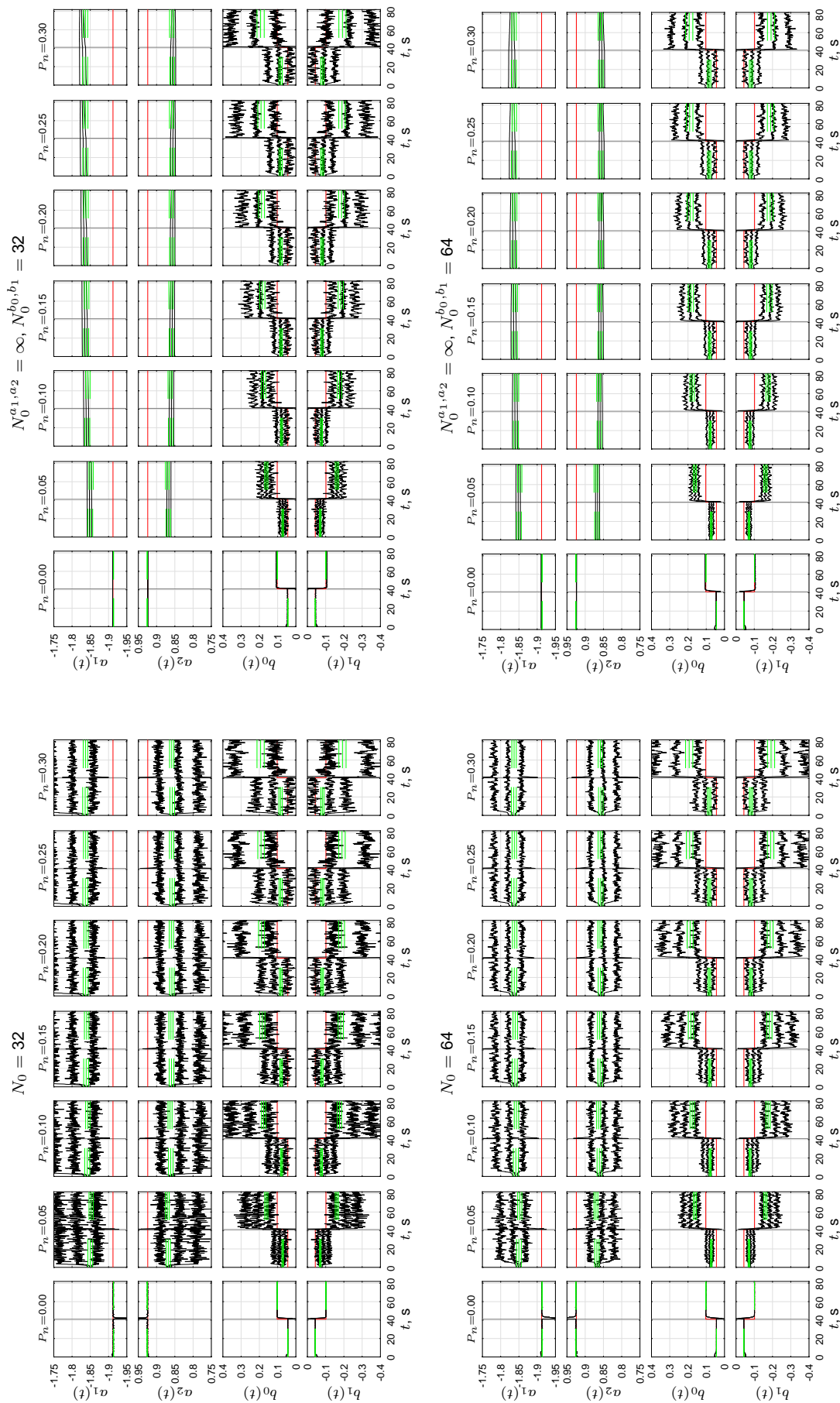


Figure K.4 (continued)

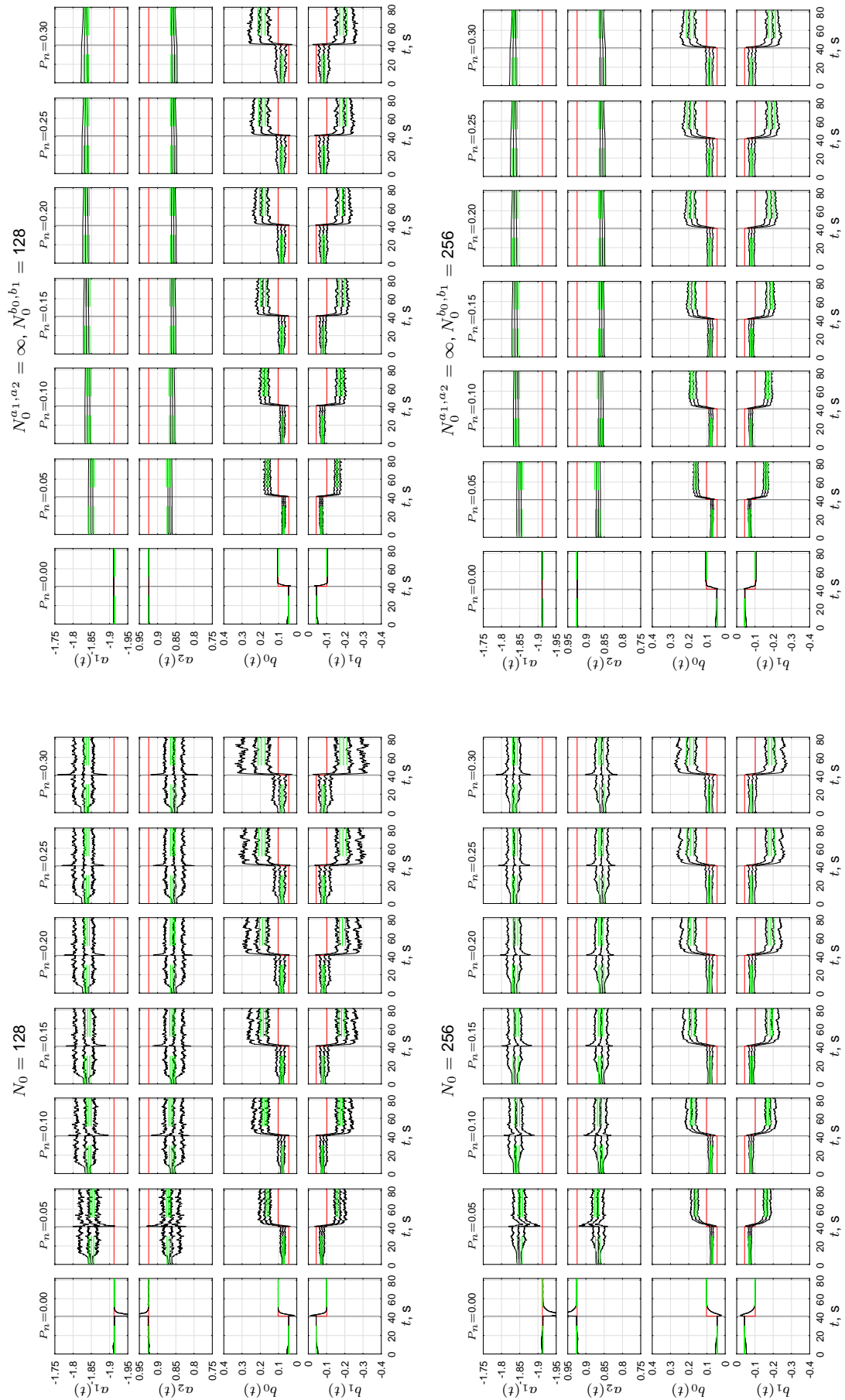


Figure K.4 (continued)

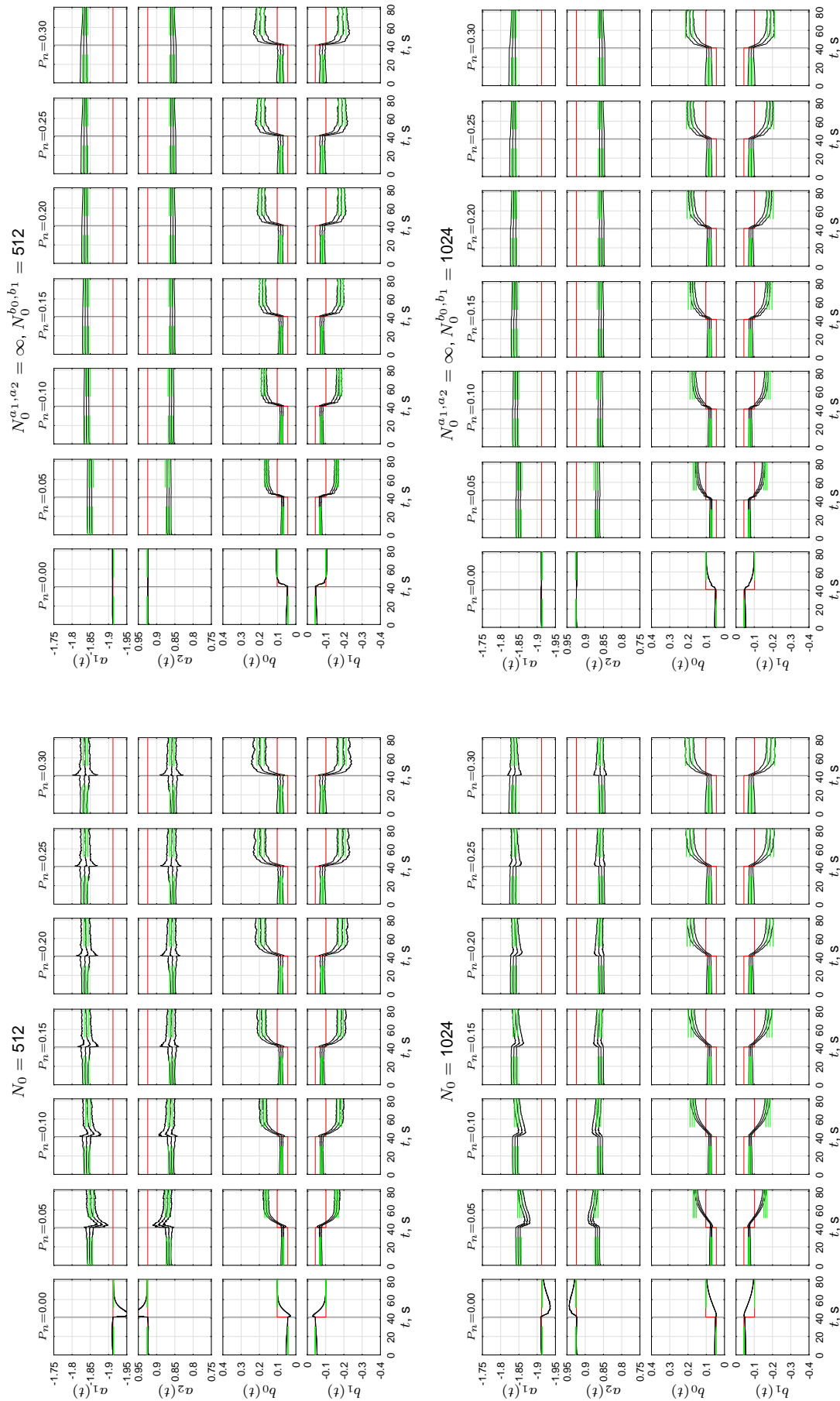


Figure K.4 (continued)

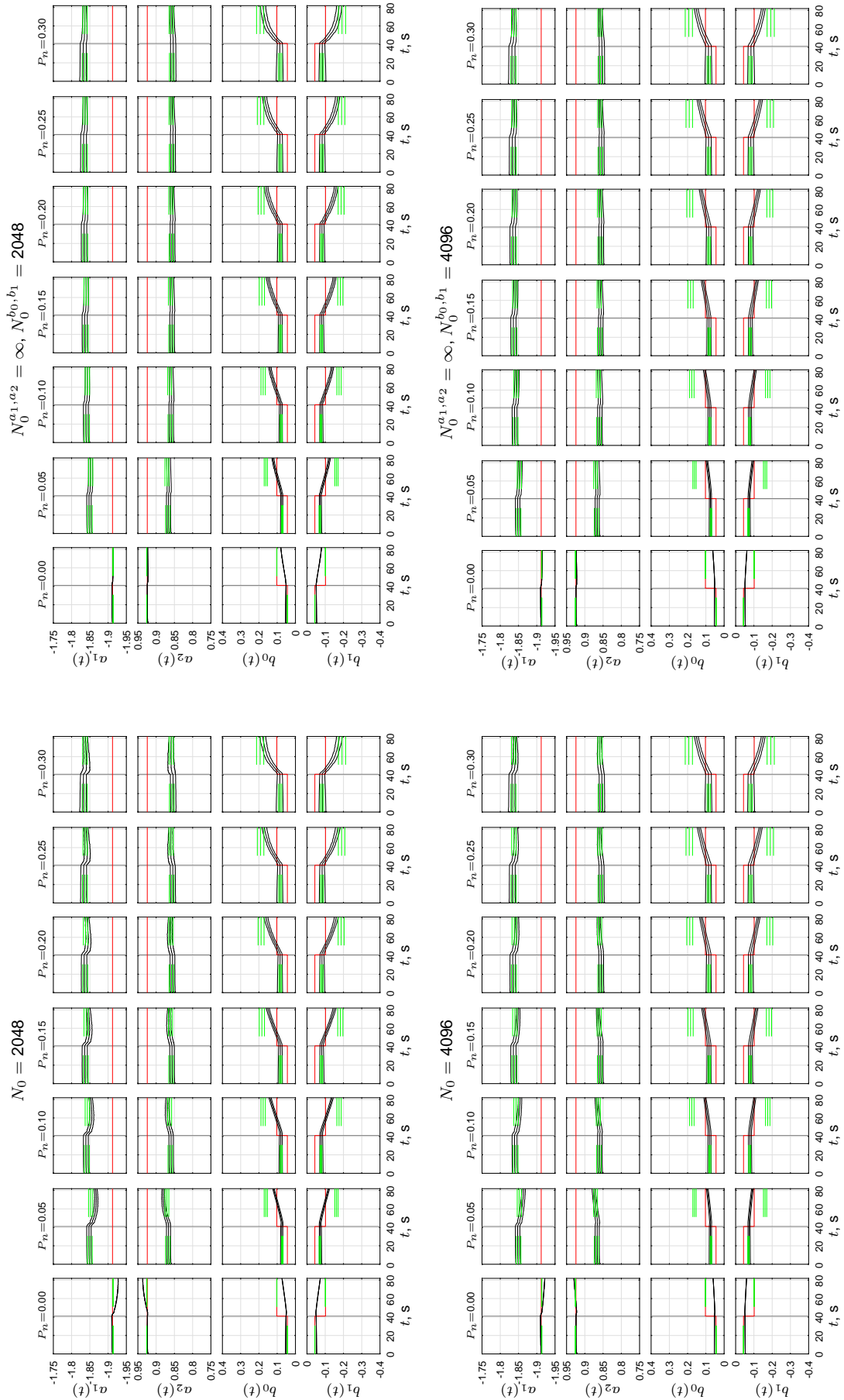


Figure K.4 (continued)

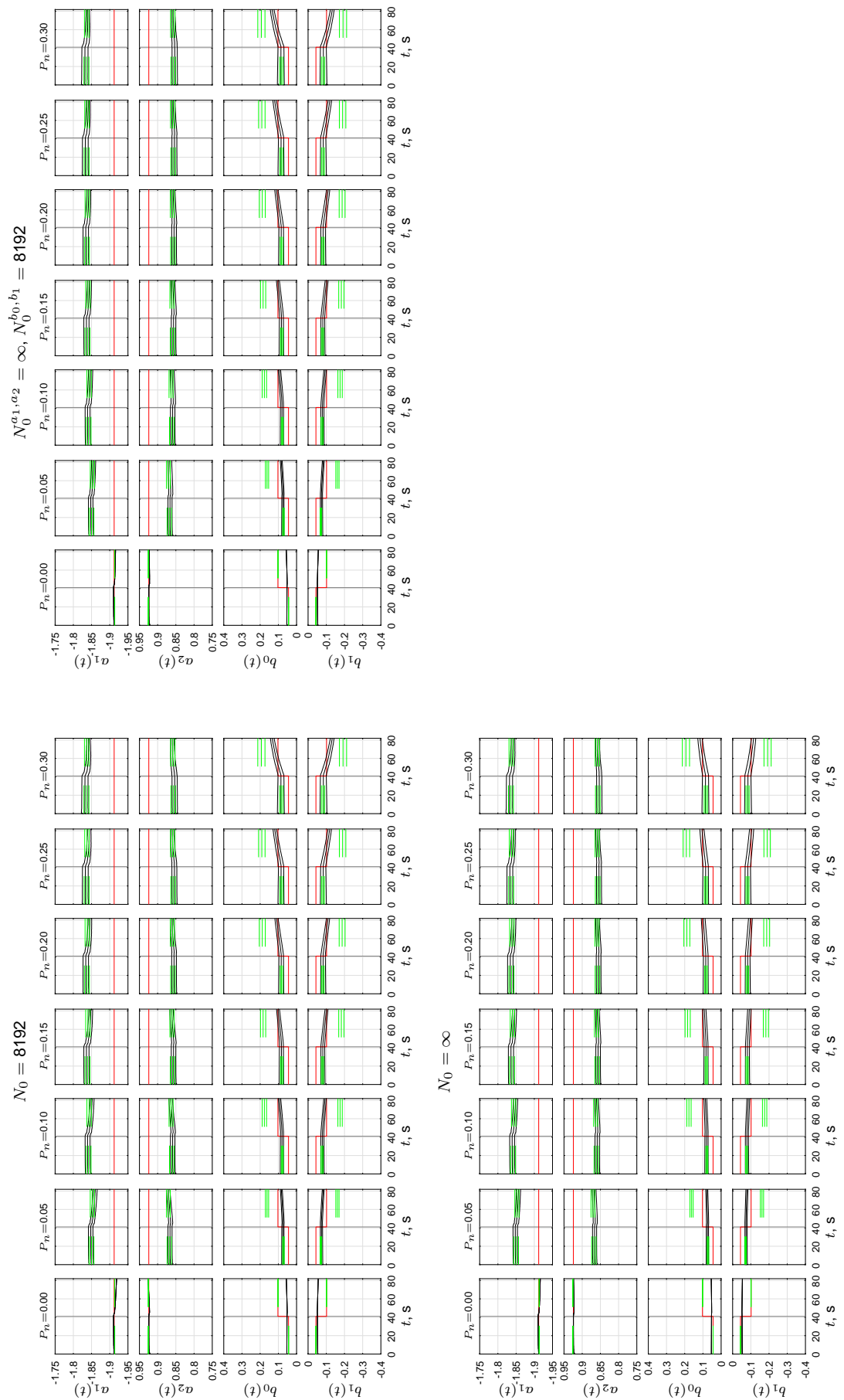


Figure K.4 (continued)

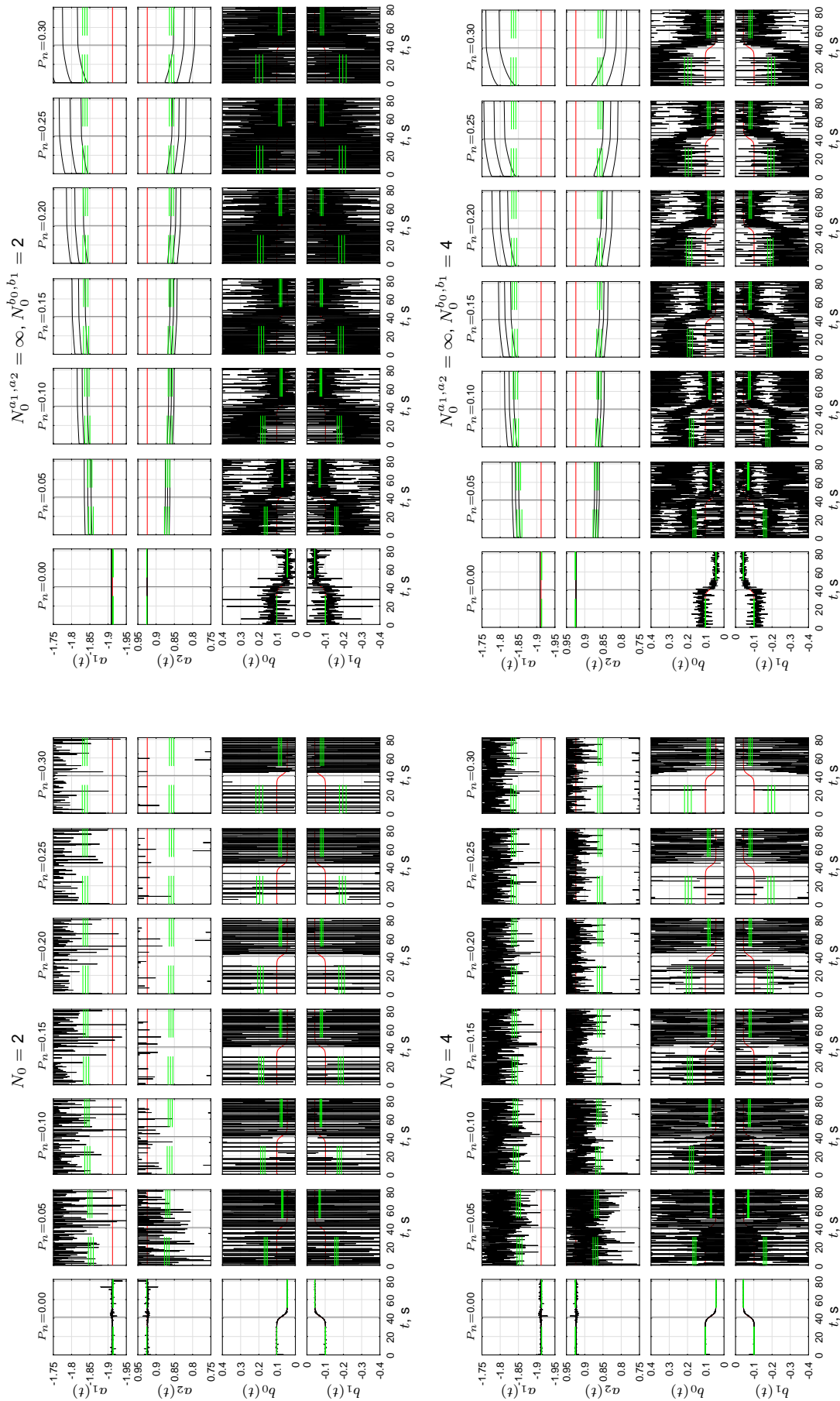


Figure K.5 Time traces of ARX-model parameters for condition C5.

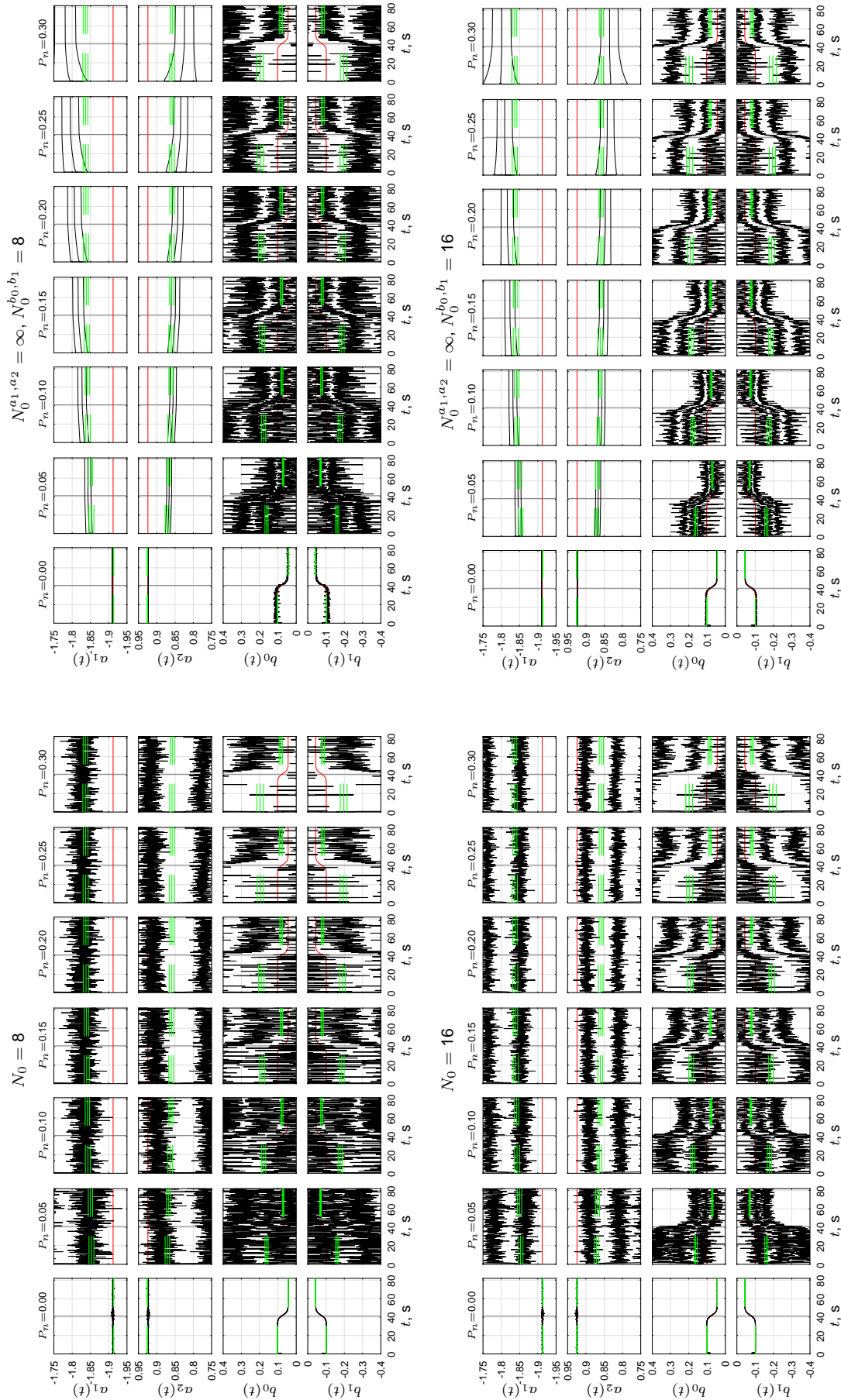


Figure K.5 (continued)

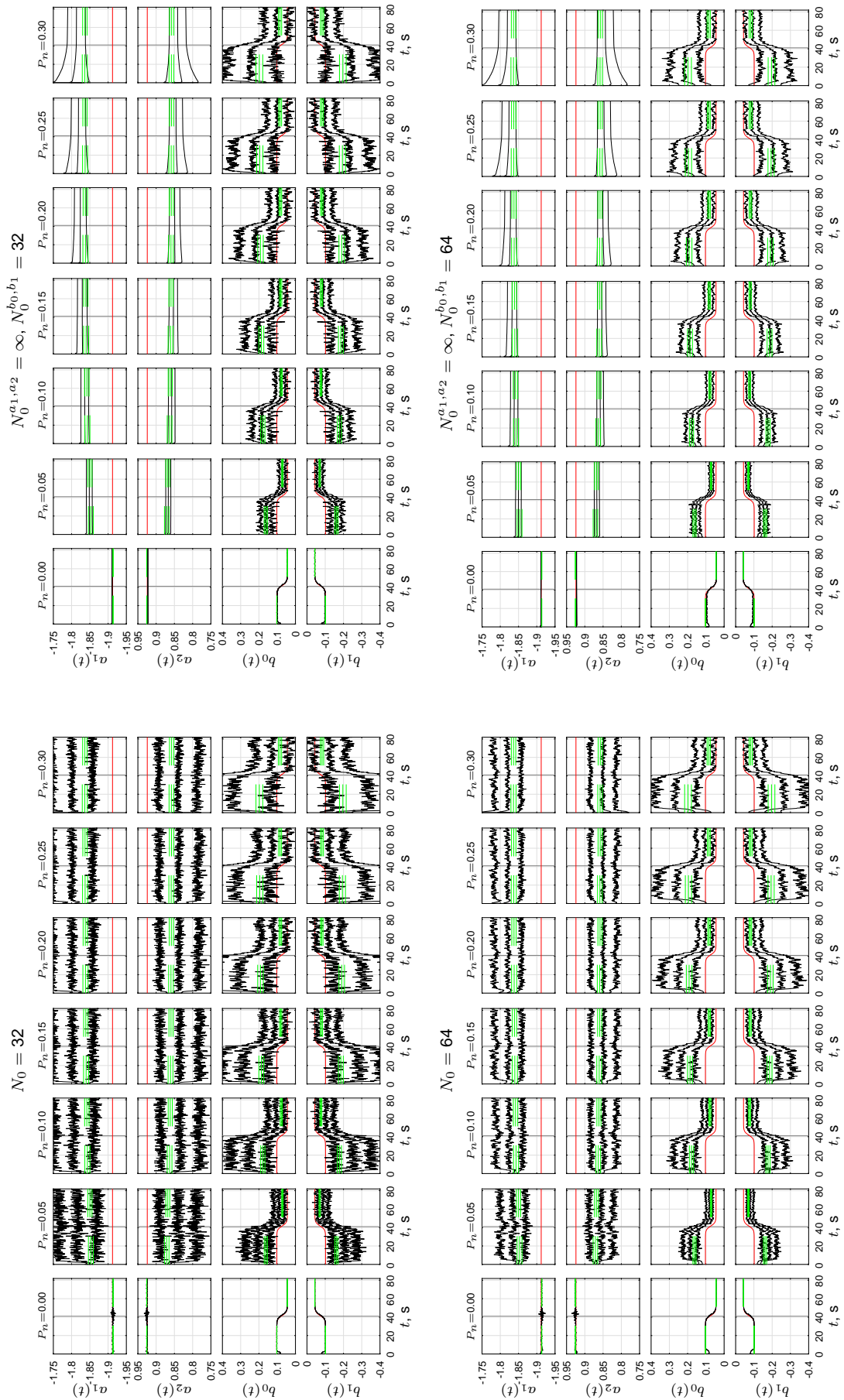


Figure K.5 (continued)

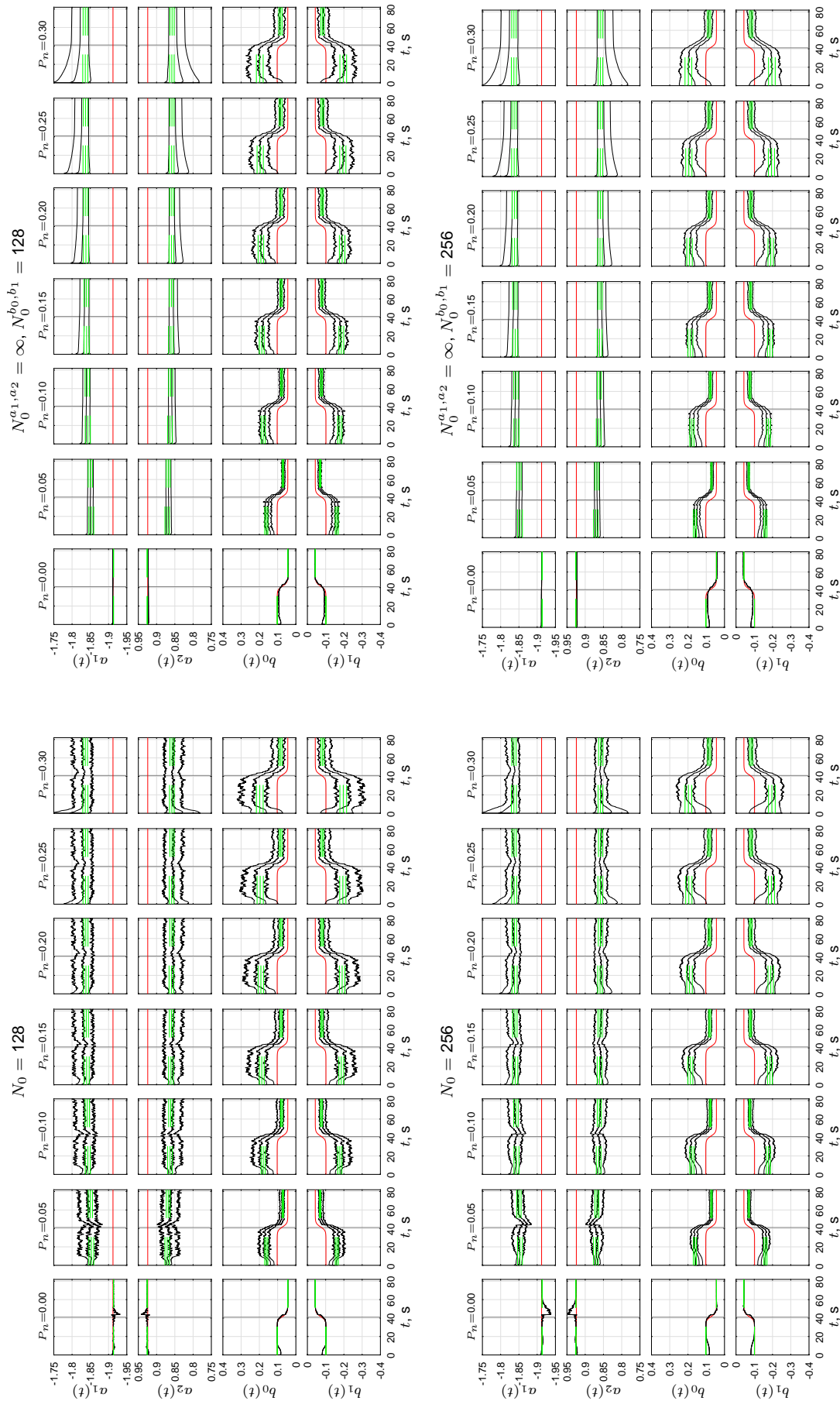


Figure K.5 (continued)

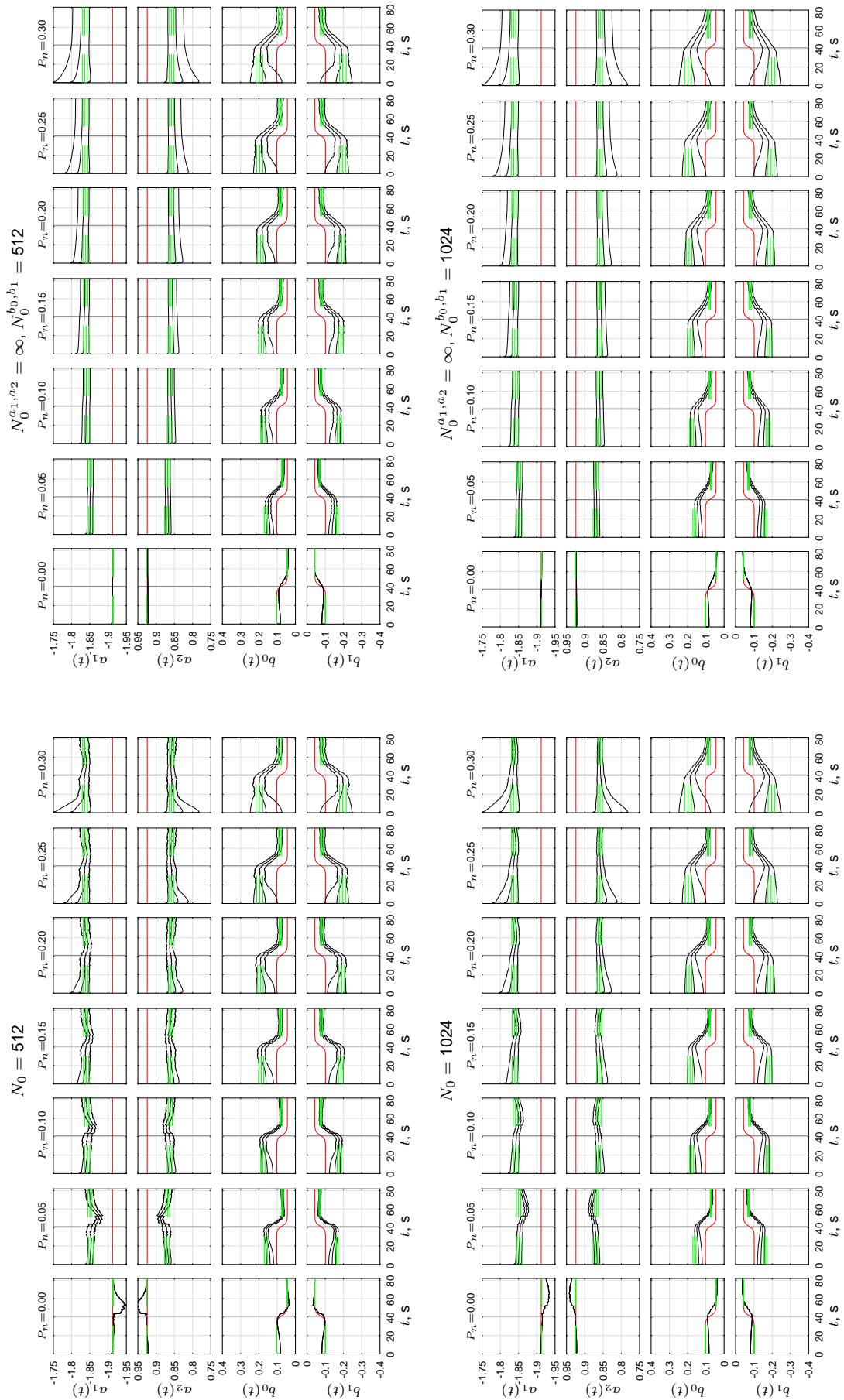


Figure K.5 (continued)

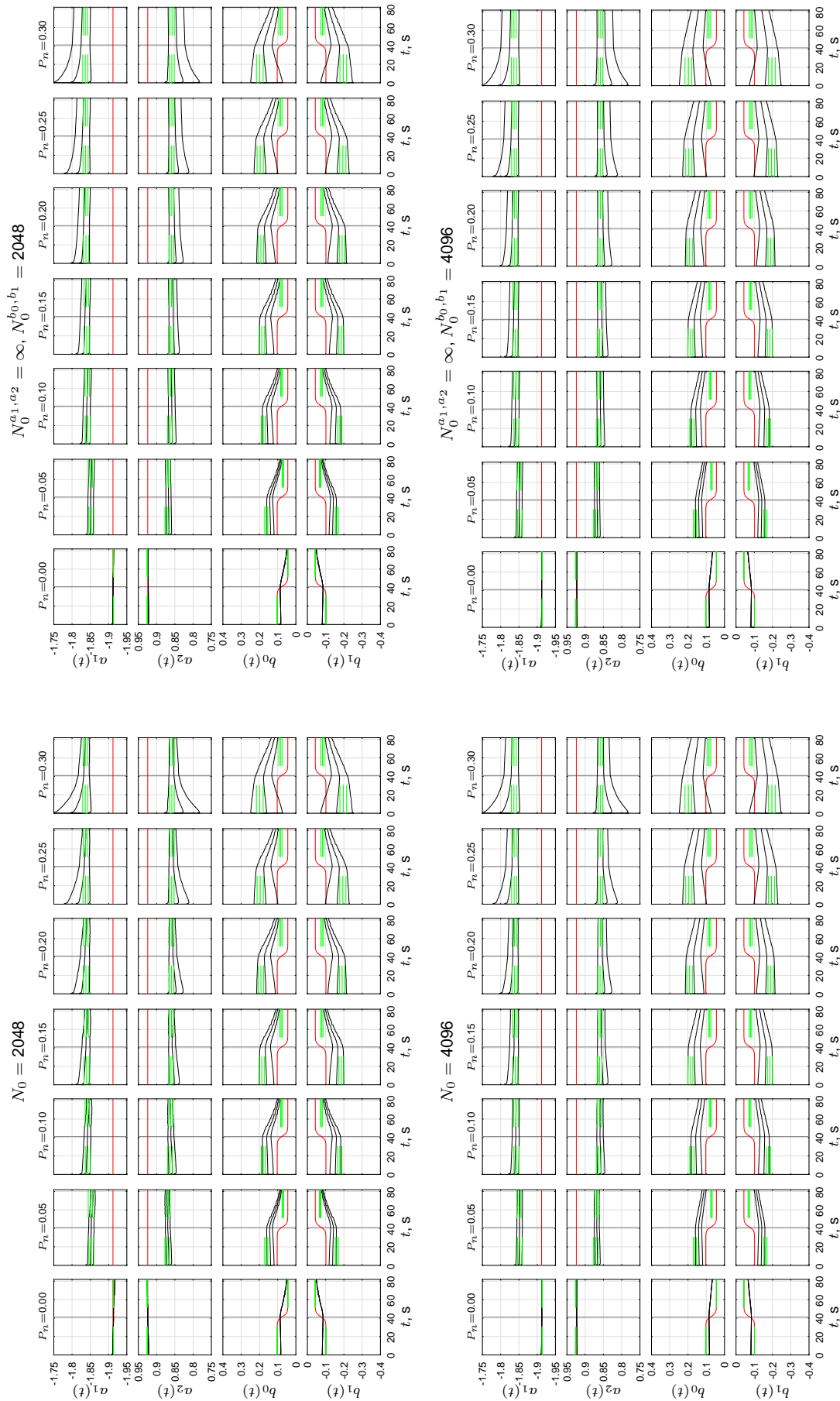


Figure K.5 (continued)

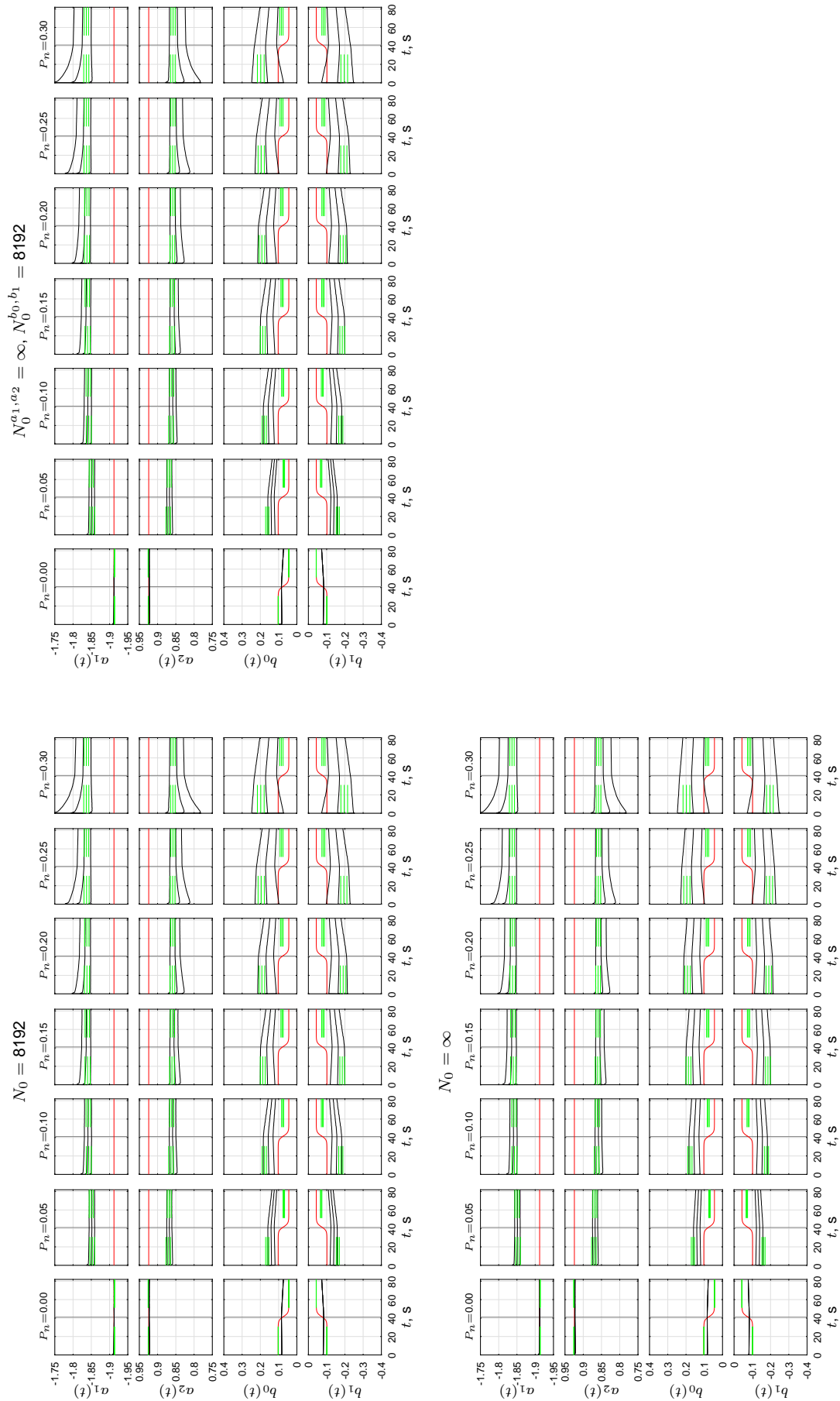


Figure K.5 (continued)

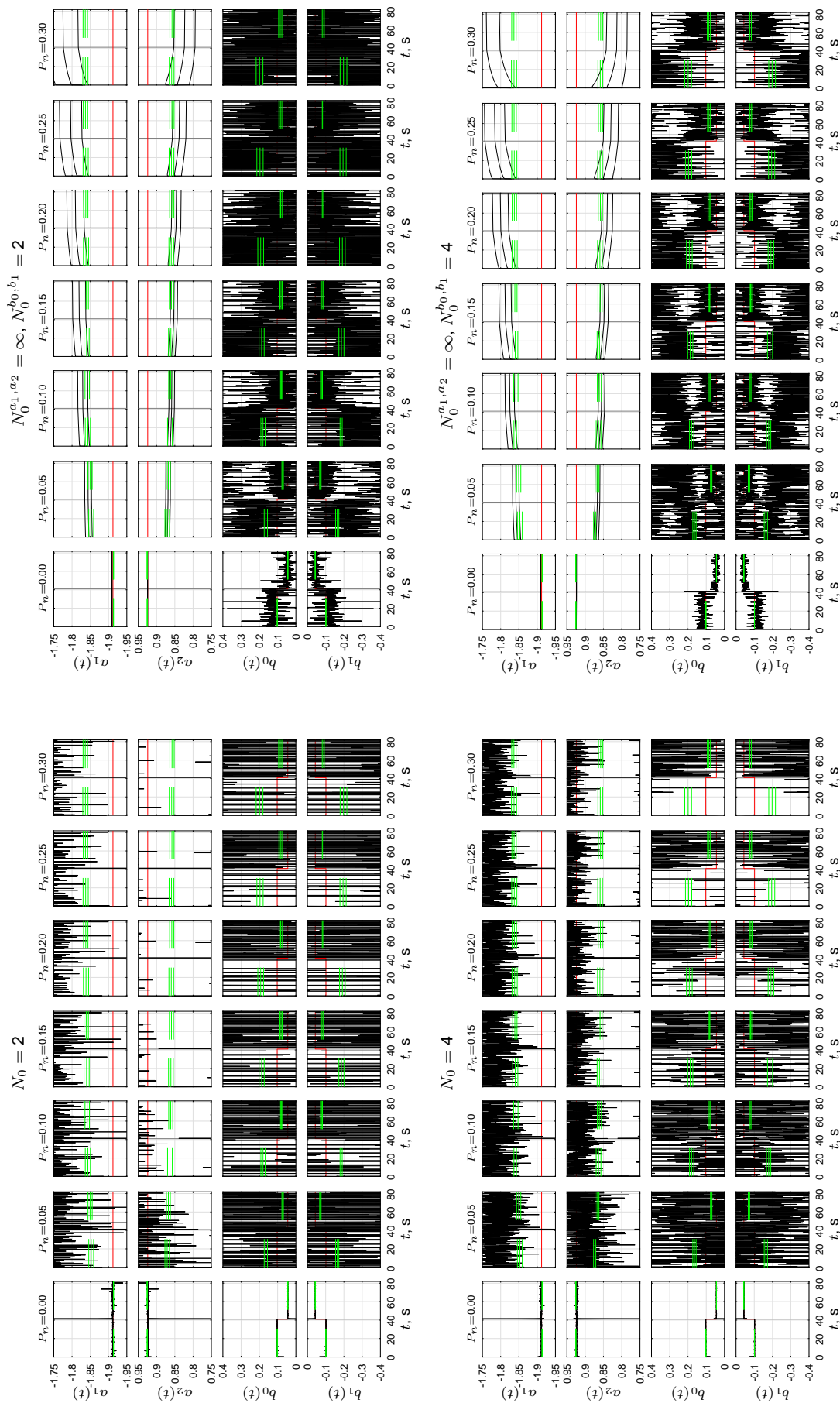


Figure K.6 Time traces of ARX-model parameters for condition C6.

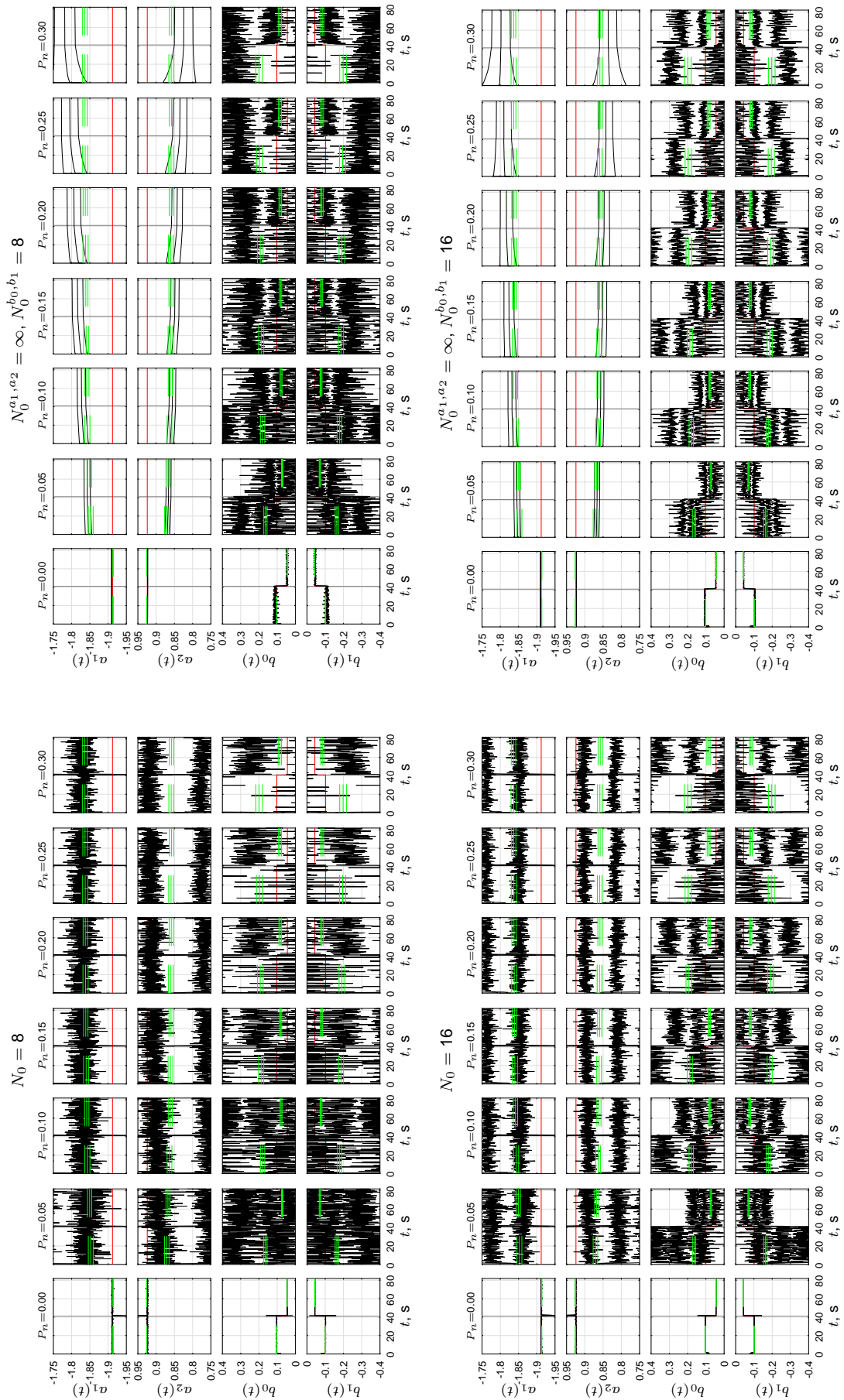


Figure K.6 (continued)

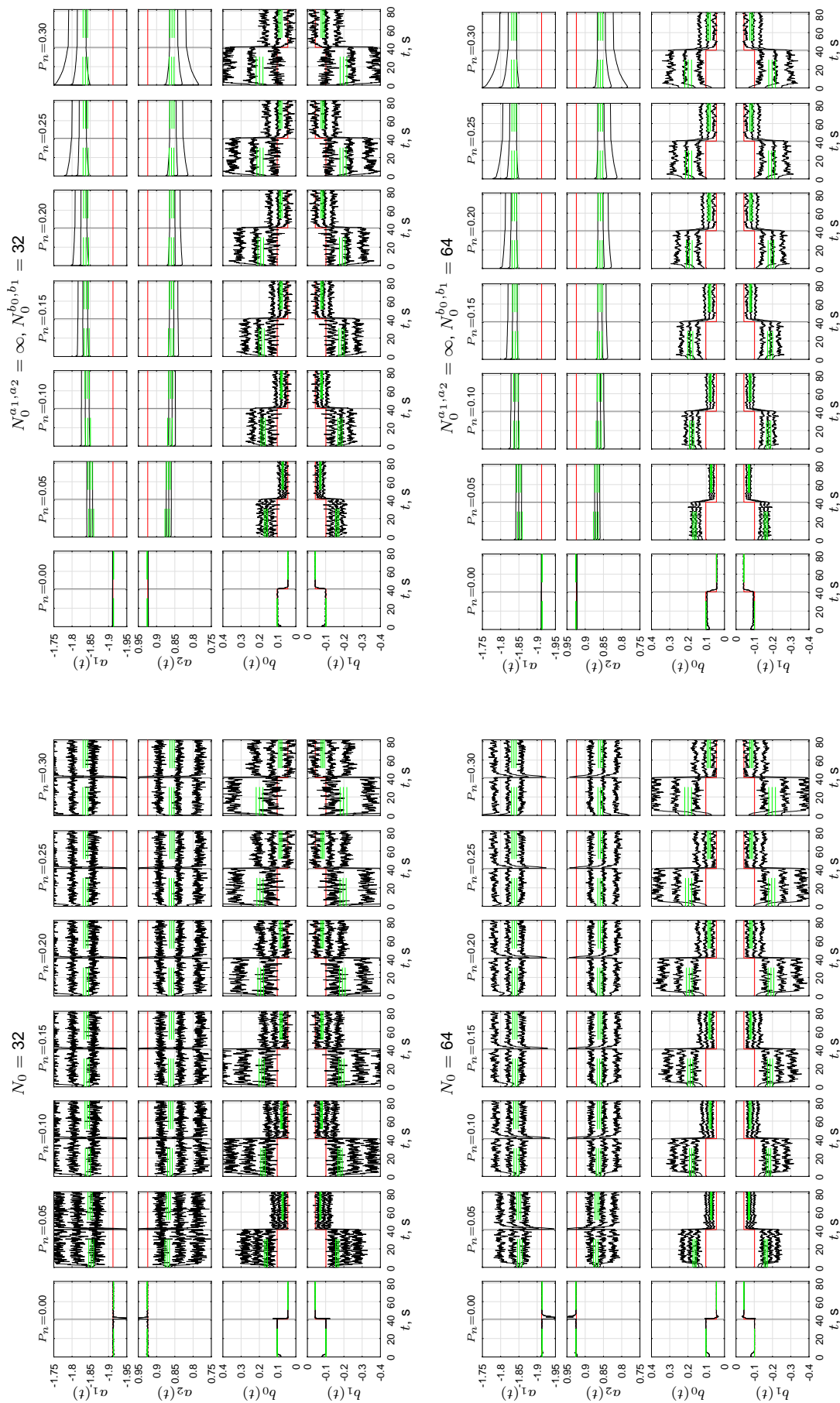


Figure K.6 (continued)

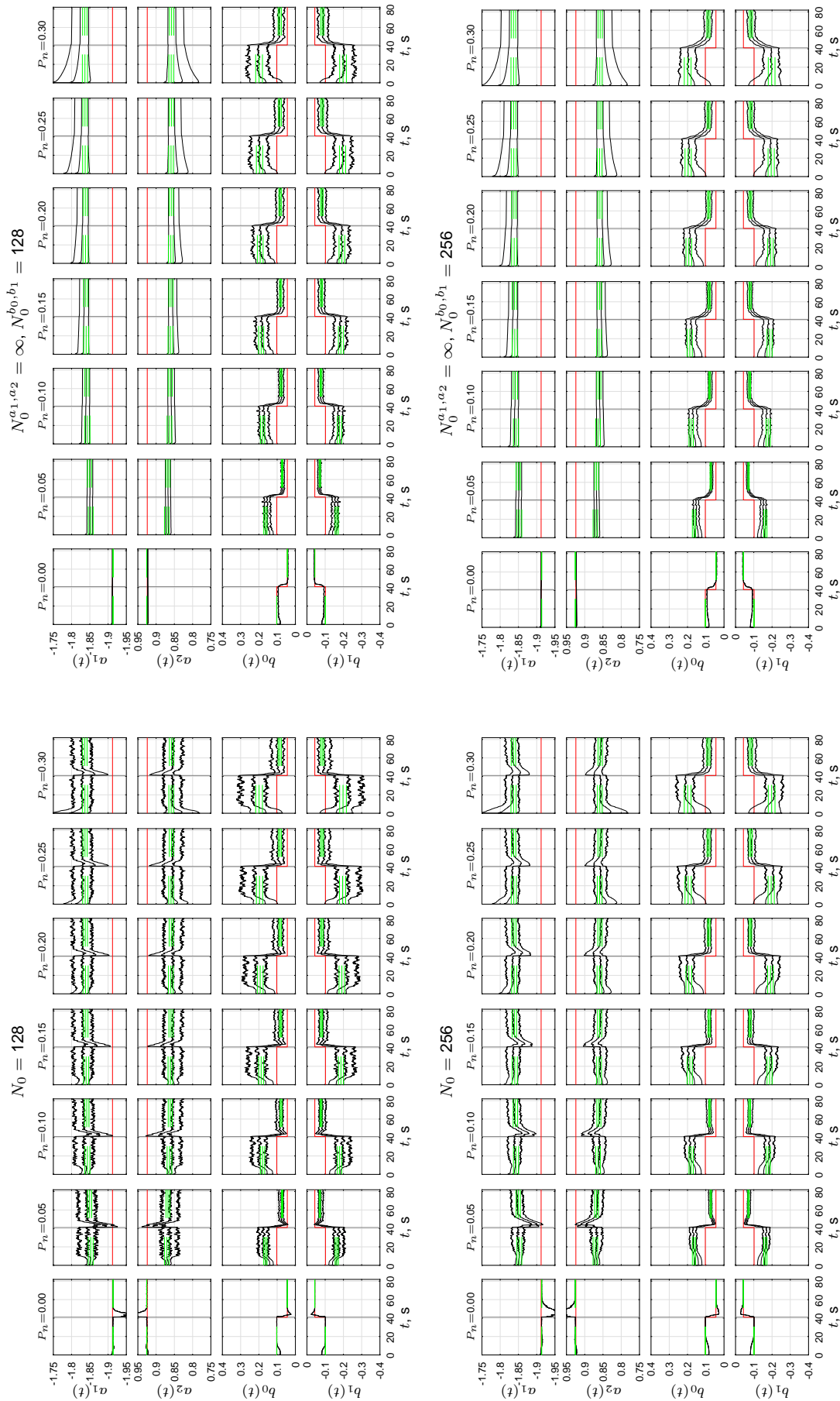


Figure K.6 (continued)

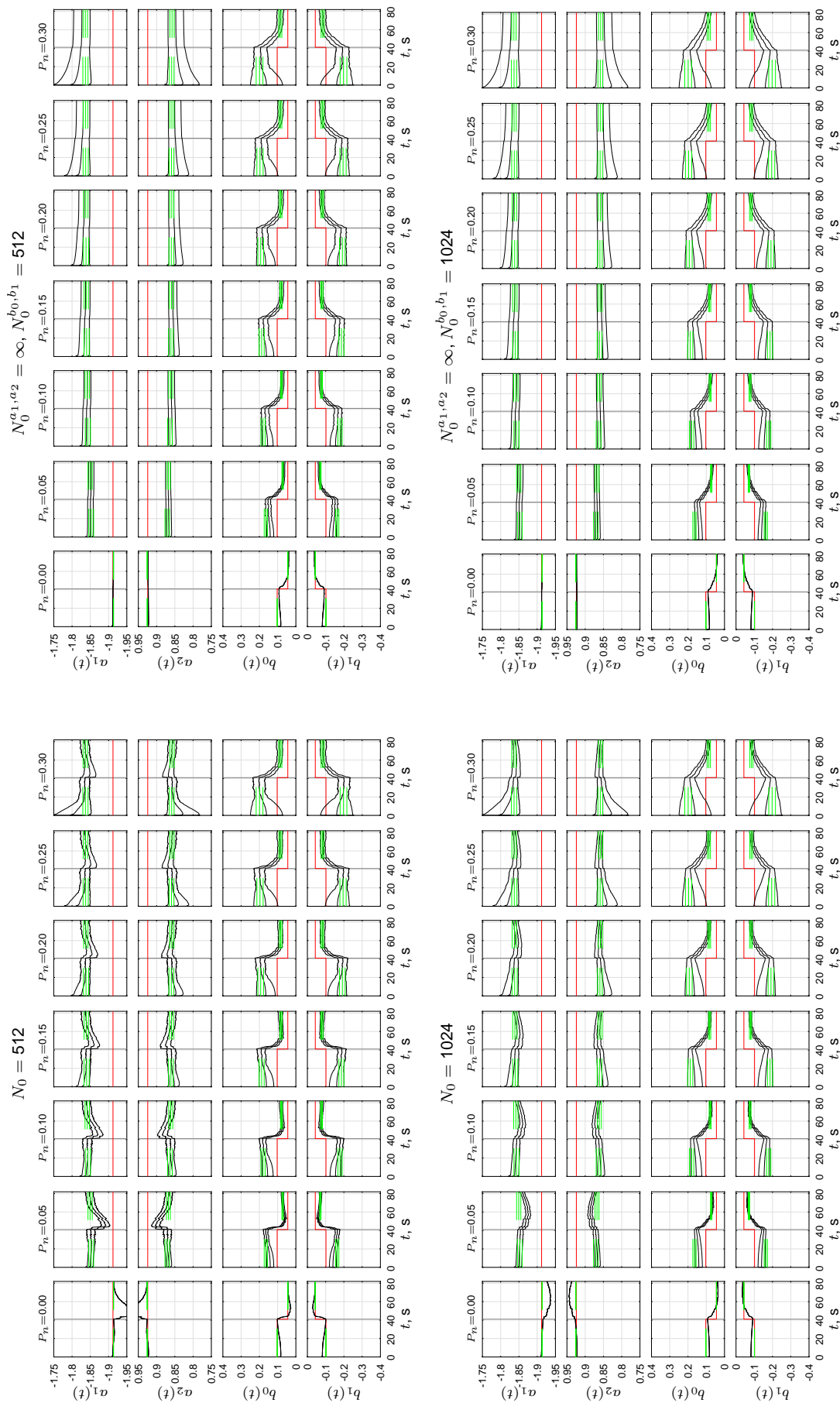


Figure K.6 (continued)

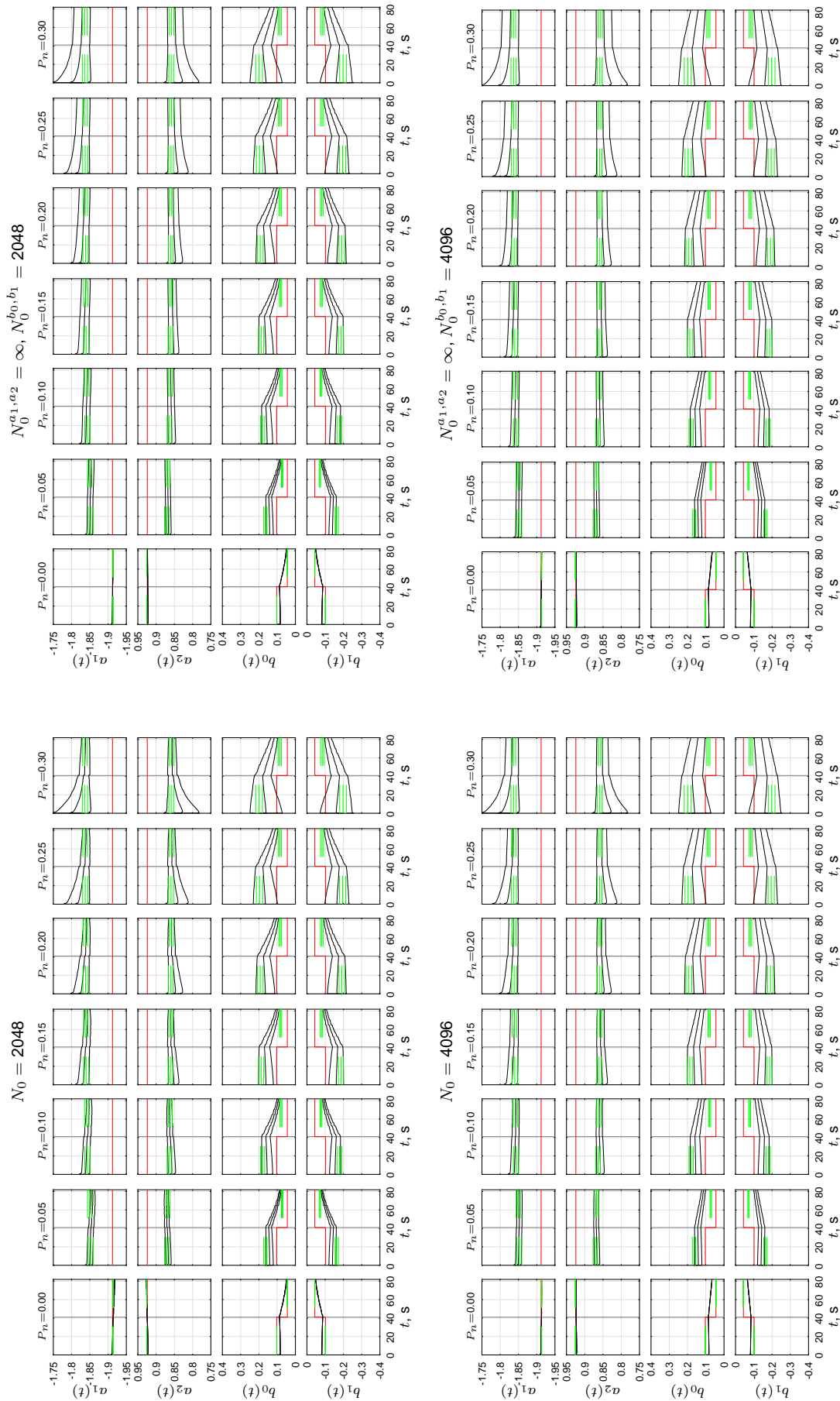


Figure K.6 (continued)

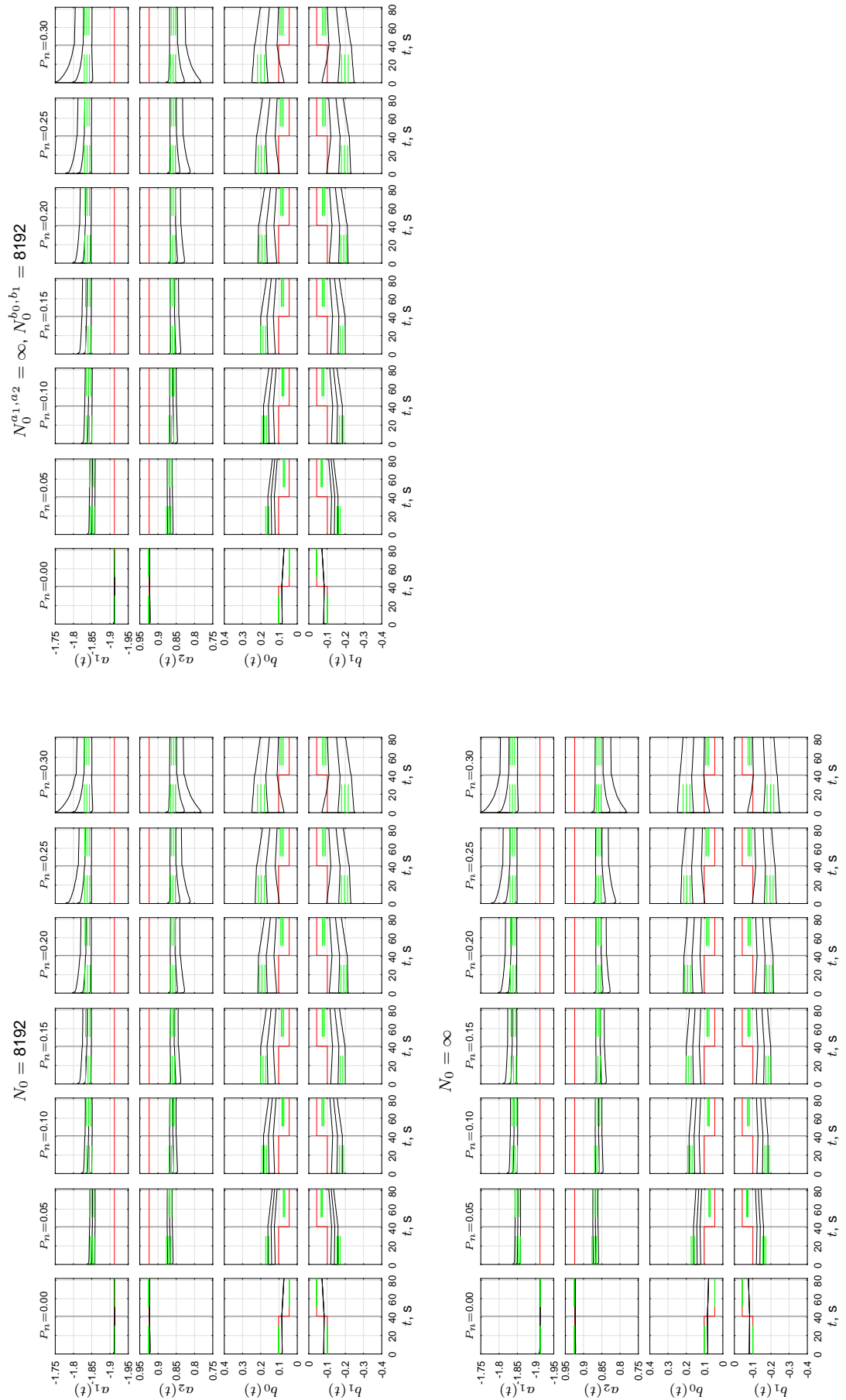


Figure K.6 (continued)



Time traces of the human-operator model parameters

The subsequent pages show figures with the time traces of the HO-model parameters $T_L(t)$, $K_{\dot{e}}(t)$, $\omega_{nm}(t)$, $\zeta_{nm}(t)$. These figures are in accordance with the figures shown in Appendix K. Only the results are shown for optimal scalar forgetting factor λ of 0.99609 (for data sampled with $f_s = 100$ Hz), and for the forgetting matrix Λ , with $\lambda_{a_1} = \lambda_{a_2} = 1$ and $\lambda_{a_1} = \lambda_{a_2} = 0.99609$. ARX models were only converted to the HO model structure at instants where the corresponding discrete ARX model's transfer function had complex-conjugate poles.

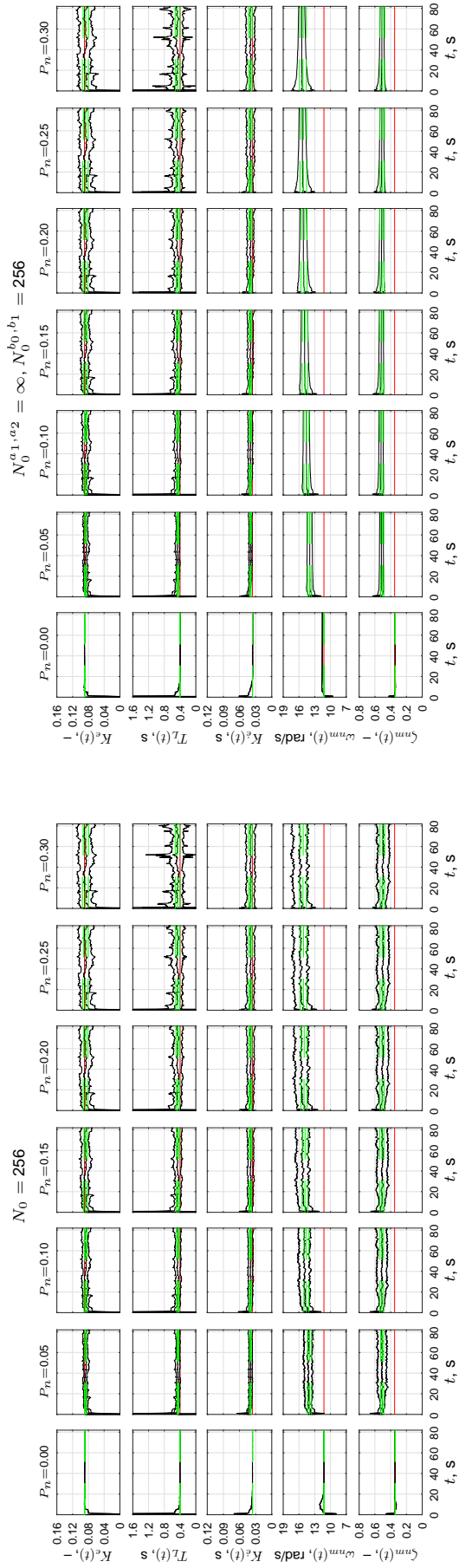


Figure L.1 Human-operator model parameters for condition C1.

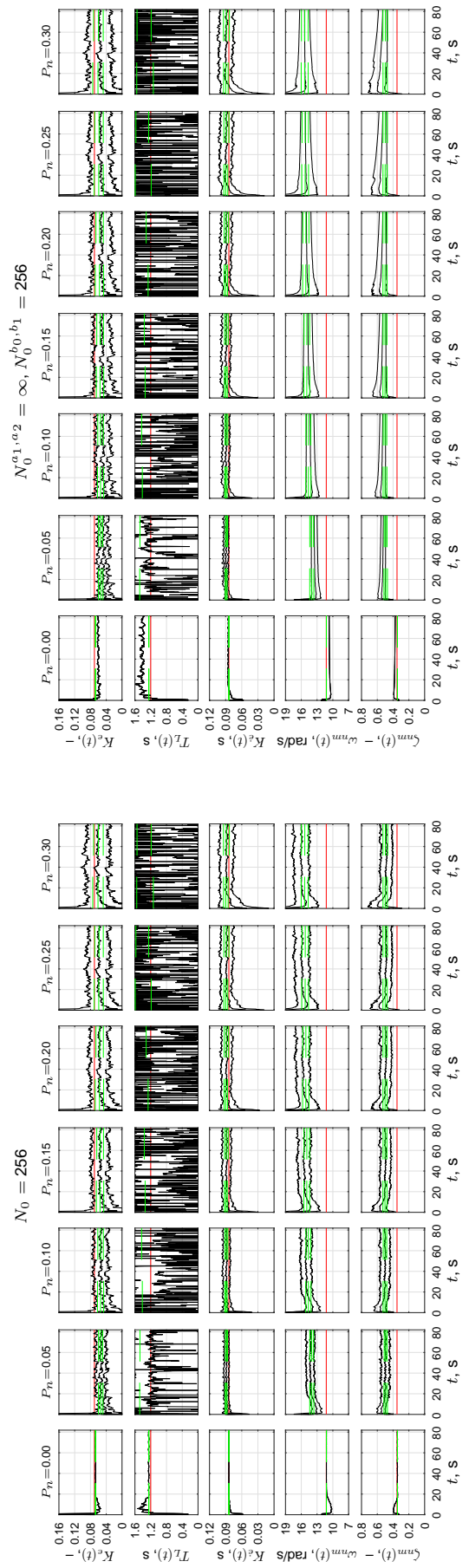


Figure L.2 Human-operator model parameters for condition C2.

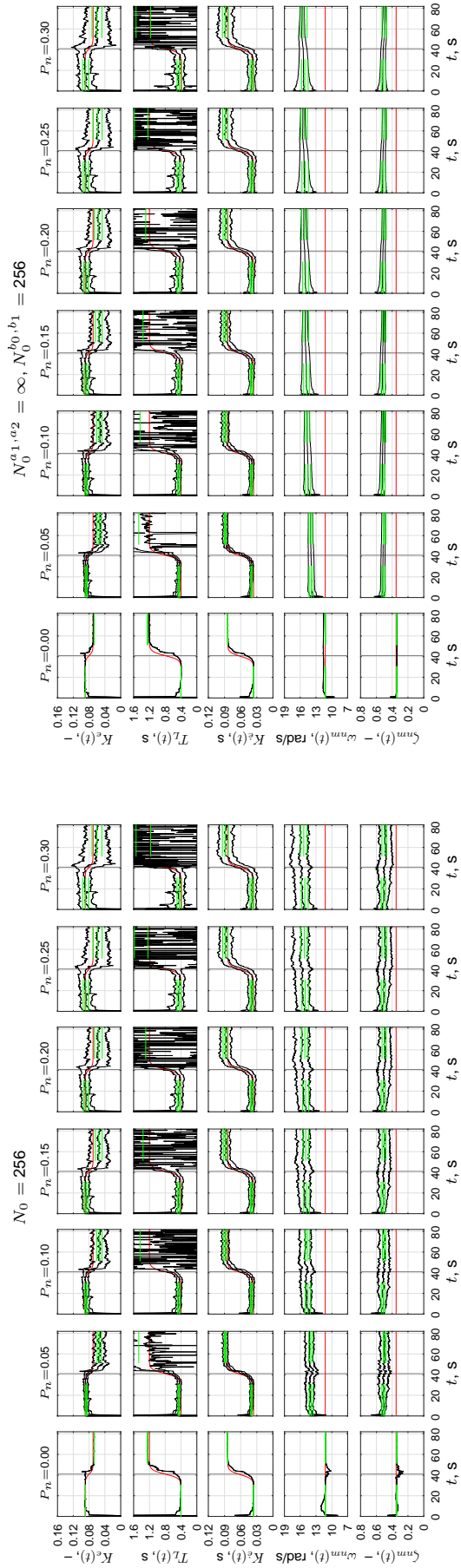


Figure L.3 Human-operator model parameters for condition C3.

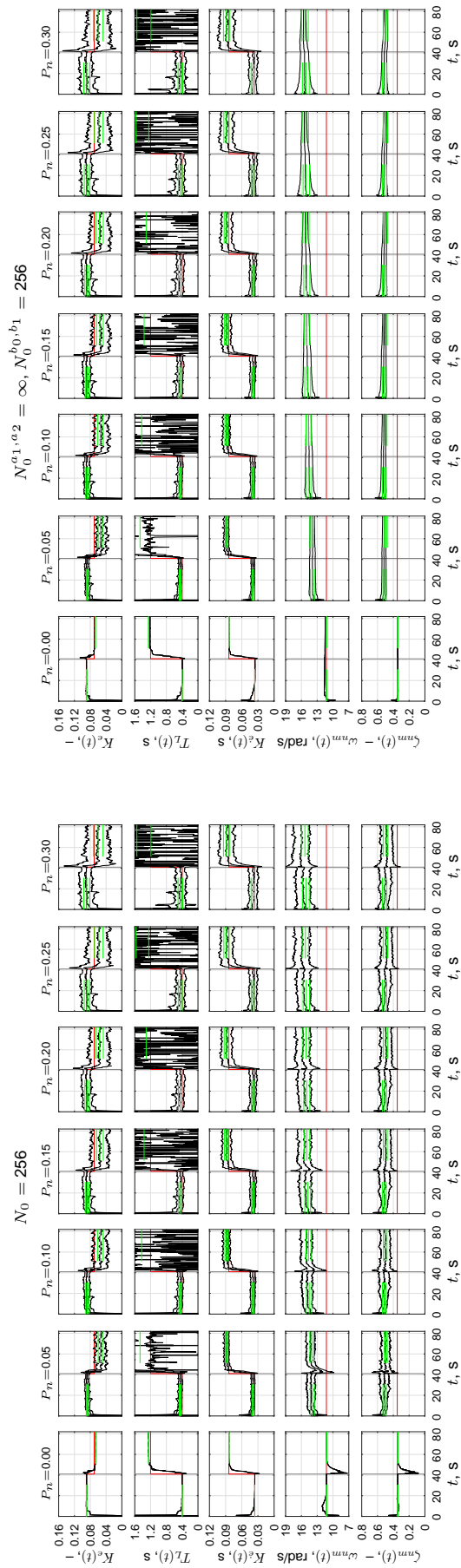


Figure L.4 Human-operator model parameters for condition C4.

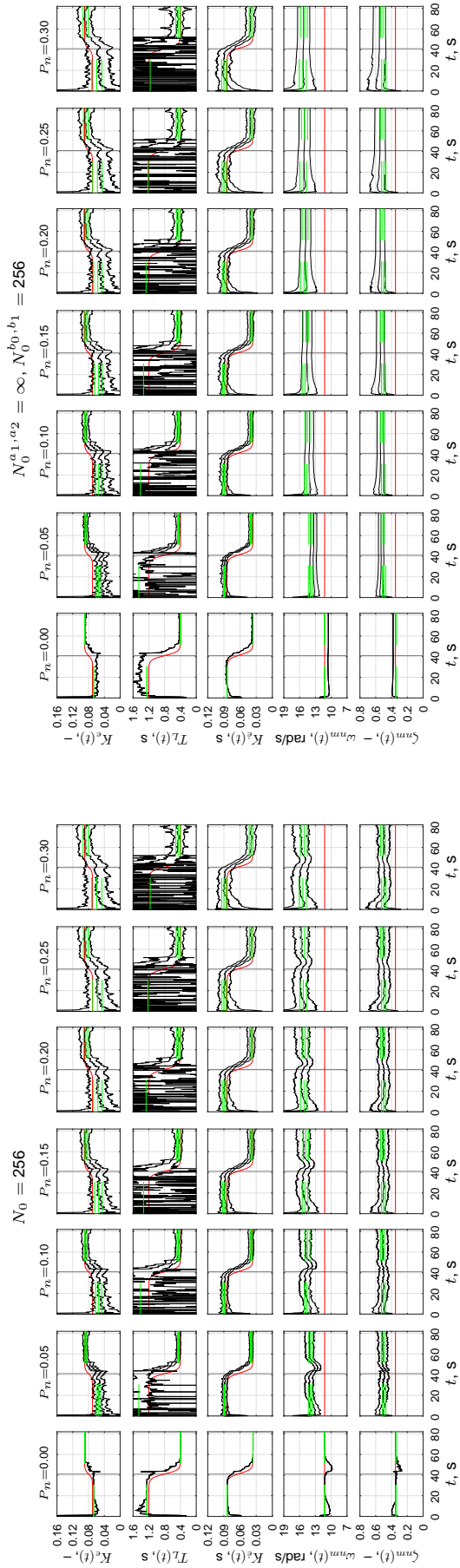


Figure L.5 Human-operator model parameters for condition C5.

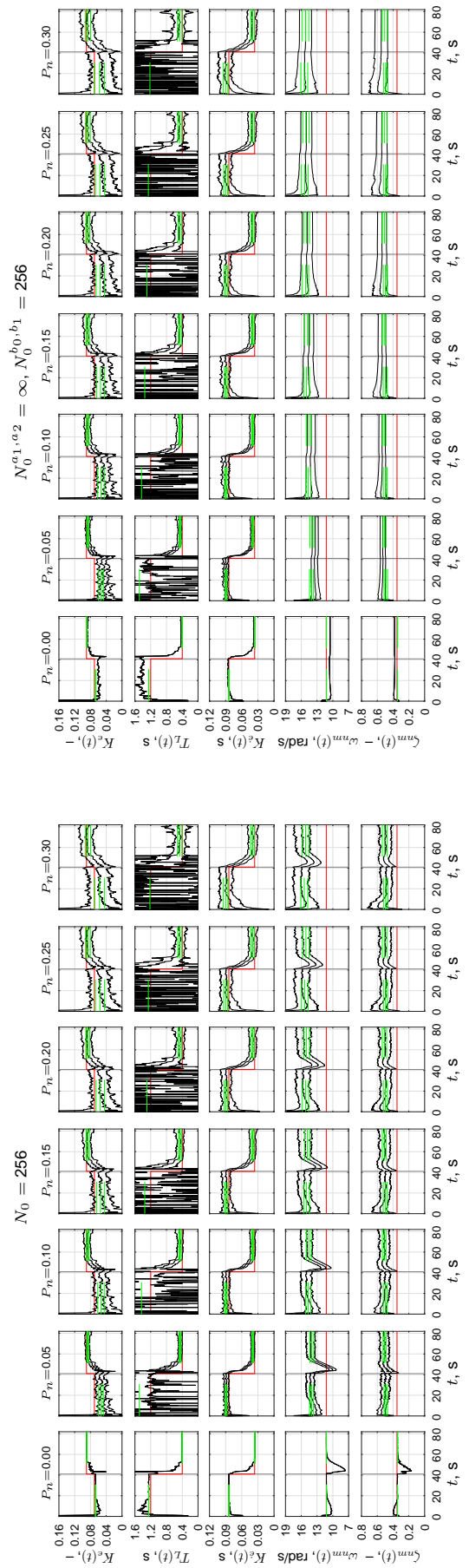


Figure L.6 Human-operator model parameters for condition C6.

M

Real measurements

This appendix shows the application of the identification procedure outlined in this research on real experimental manual-control data.

An experiment was conducted in the SIMONA Research Simulator (SRS) at Delft University of Technology, in fixed-base setting. Three subjects (average age 24 years) performed the single-axis compensatory manual-control task that was studied in this research by means of the Monte Carlo simulations. The conditions are listed in Table M.1. The conditions C3–C6 contained time-varying controlled-element (CE) dynamics in which the rate of change of the parameters was varied. Subjects 1 and 2 also performed the task with constant controlled element (CE) dynamics. In each condition multiple runs were performed. The length of the runs was set to 90.00 s. A measurement time T_m of 81.92 s was used for the identification. The maximum rate of transition M in conditions C3–C6 was set to 50.00 s (i.e., at 42.93 s in the measurement window). Data was samples with $f_s = 100$ Hz.

Table M.1 Experiment conditions.

Condition	$H_{CE}(s)$	G, s^{-1}	Subjects	Figure
C1	$H_{CE,1}(s)$	n/a	1, 2	Figure M.1
C2	$H_{CE,2}(s)$	n/a	1, 2	Figure M.2
C3	$H_{CE,1}(s) \rightarrow H_{CE,2}(s)$	0.5	1, 2, 3	Figure M.3
C4	$H_{CE,1}(s) \rightarrow H_{CE,2}(s)$	100	1, 2, 3	Figure M.4
C5	$H_{CE,2}(s) \rightarrow H_{CE,1}(s)$	0.5	1, 2, 3	Figure M.5
C6	$H_{CE,2}(s) \rightarrow H_{CE,1}(s)$	100	1, 2, 3	Figure M.6

The ARX-model identification approach, as outlined in the scientific paper, was adopted. Input-output data were recorded with $f_s = 100$ Hz, and $f_t(t)$ was set up with the properties listed in Table 5.1. Similar to the Monte Carlo analysis, the ARX-model structure was set to $n_a = n_b = 2$. Visual delay was assumed to be constant and estimated using n_k^* . Batch ARX models were fit on the initial and final 30.72 s of the measurement window. The recursive ARX-model estimations were initialized with the initial $\hat{\theta}^{OLS}$ and P_0 set to I . In accordance with the results from the Monte Carlo analysis, N_0 was set to 256 samples. Both the scalar forgetting factor λ and the forgetting matrix Λ (with $\lambda_{a_1} = \lambda_{a_2} = 1$) were considered.

Table M.1 also gives a reference overview of the figures with time traces of ARX-model estimates and corresponding HO-model parameters. The figures show batch ARX-model estimates fit on the initial and final 30.72 s and are indicated with thick green lines. Recursive ARX-model estimates are shown with thick black lines. The sigmoid's instant t_M is indicated with the gray line. All figures also include the five recursive single-run ARX-model estimates (thin colored lines). No extreme outliers are observed in these single-run estimates.

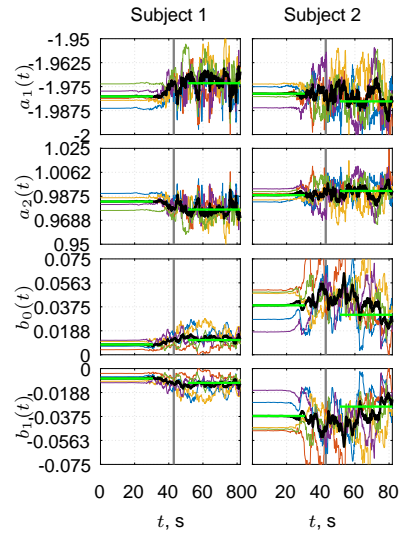
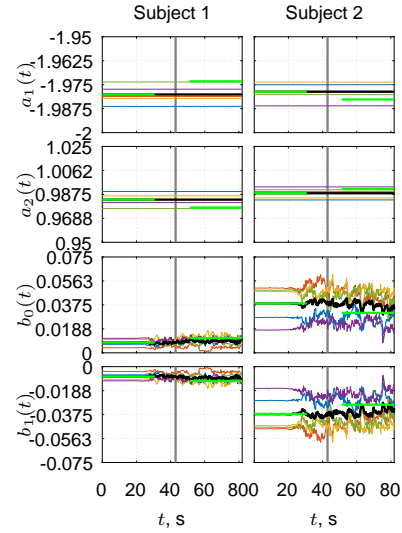
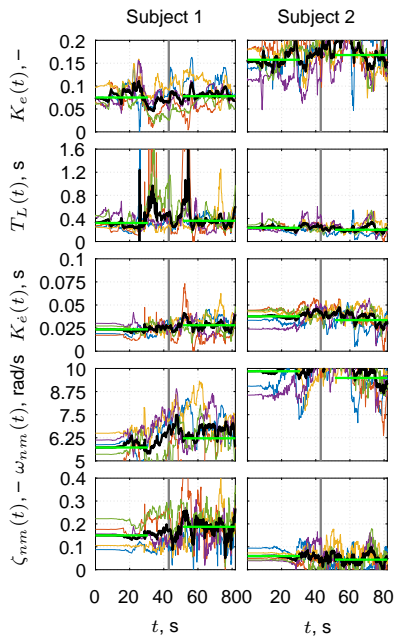
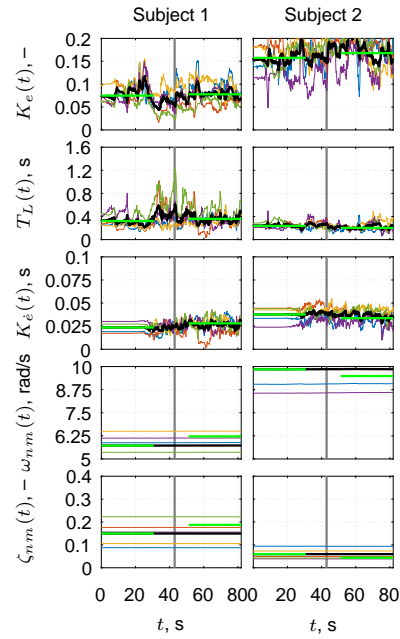
(a) ARX-model parameters, $T_0 = 256$.(b) ARX-model parameters, $T_0^{a_1, a_2} = \infty$, $T_0^{b_0, b_1} = 256$.(c) HO-model parameters, $T_0 = 256$.(d) HO-model parameters, $T_0^{a_1, a_2} = \infty$, $T_0^{b_0, b_1} = 256$.

Figure M.1 Estimated ARX-model parameters and HO-model parameters for condition C1.

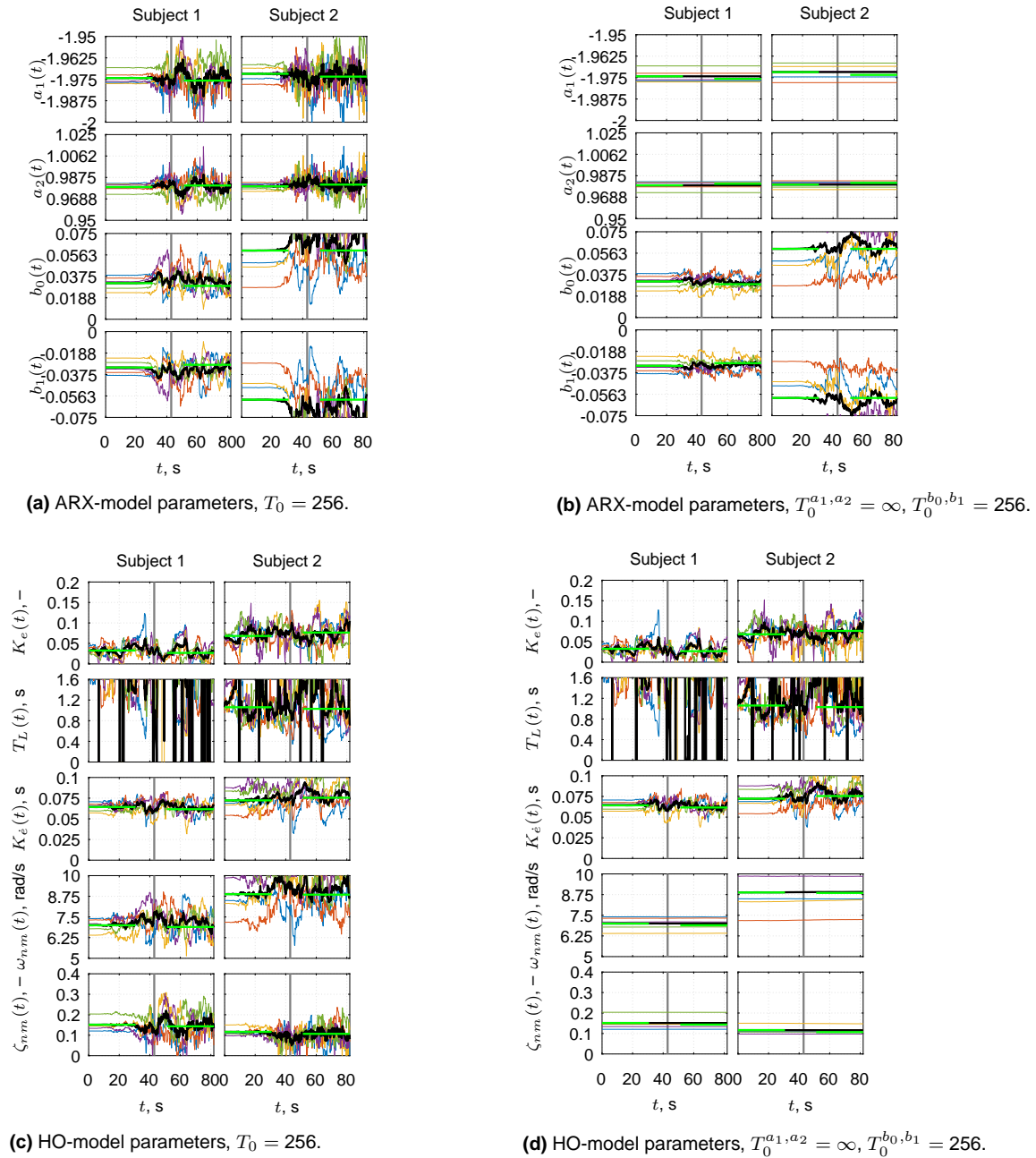
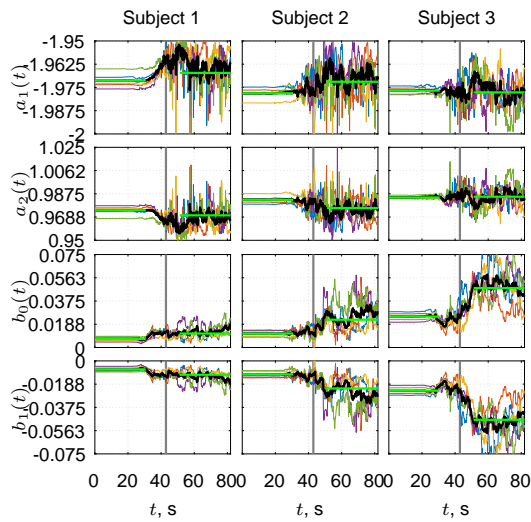
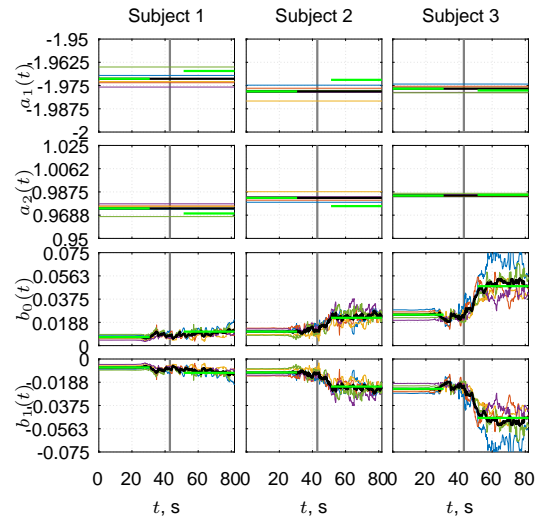


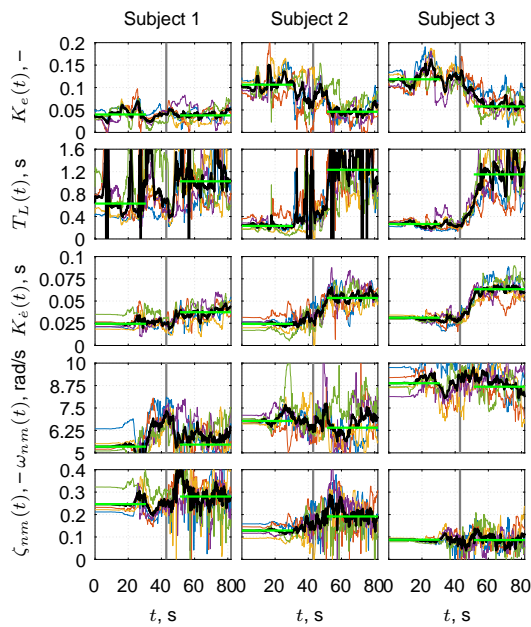
Figure M.2 Estimated ARX-model parameters and HO-model parameters for condition C2.



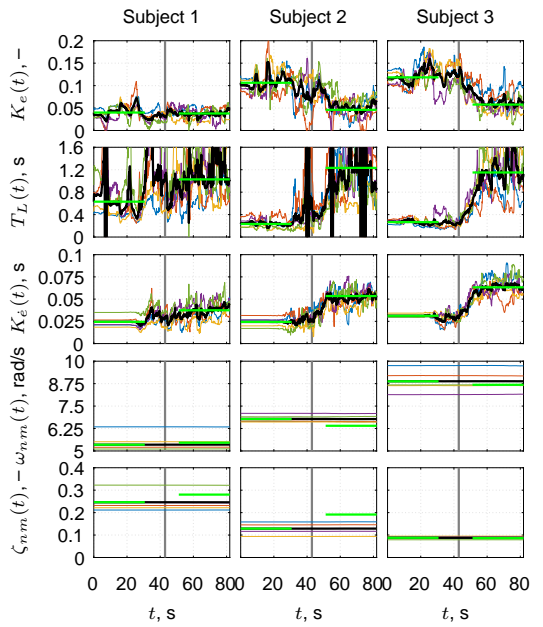
(a) ARX-model parameters, $T_0 = 256$.



(b) ARX-model parameters, $T_0^{a_1, a_2} = \infty, T_0^{b_0, b_1} = 256$.

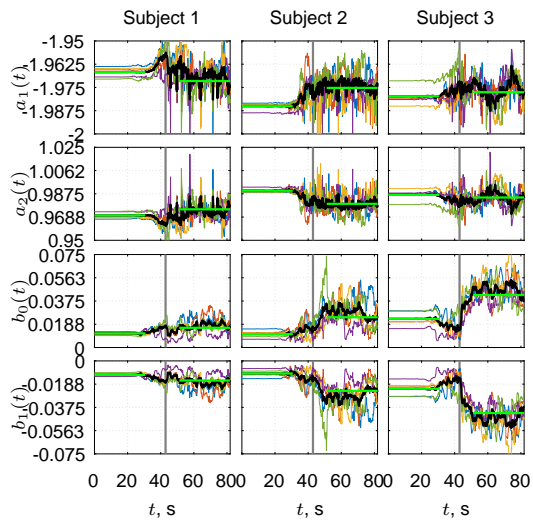
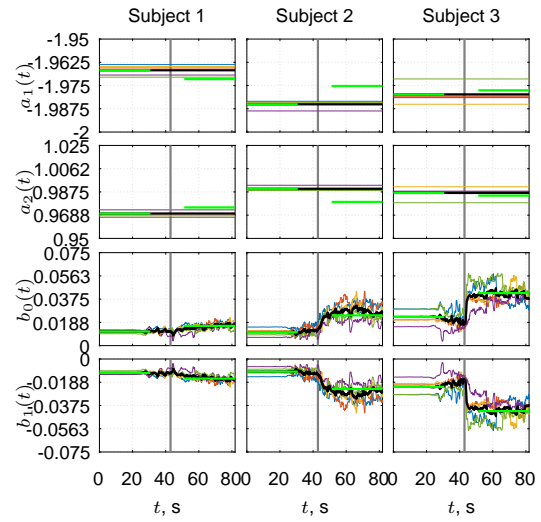
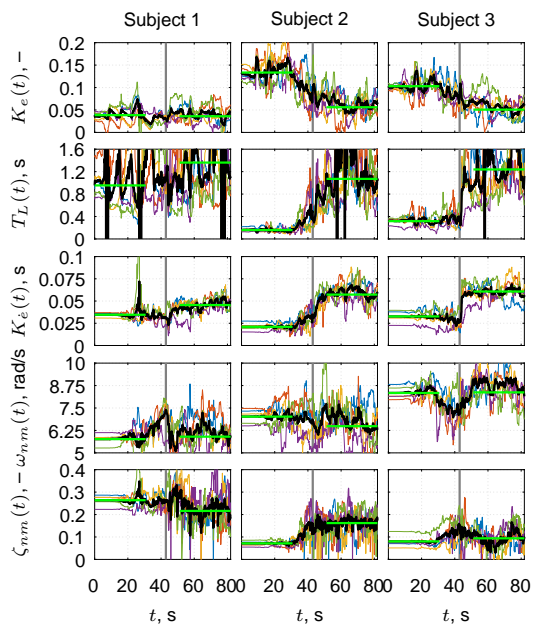
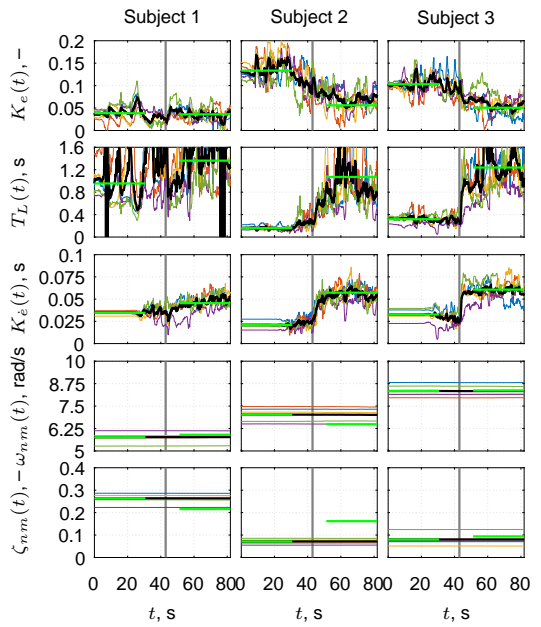


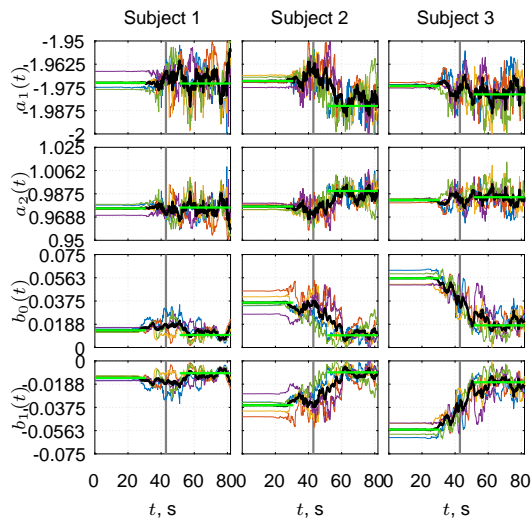
(c) HO-model parameters, $T_0 = 256$.



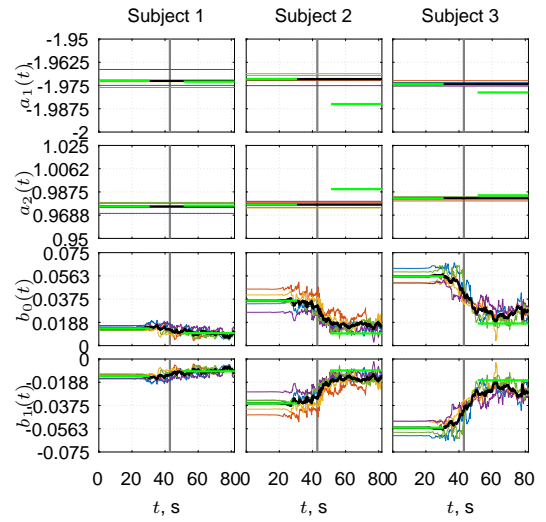
(d) HO-model parameters, $T_0^{K_e, K_{\dot{\phi}}} = \infty, T_0^{b_0, b_1} = 256$.

Figure M.3 Estimated ARX-model parameters and HO-model parameters for condition C3.

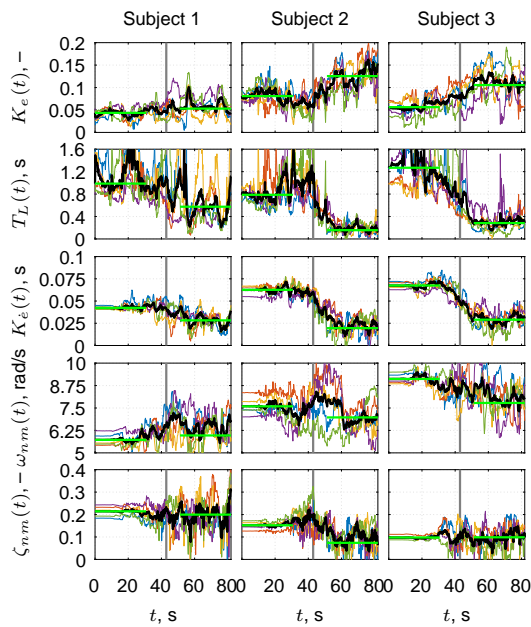
(a) ARX-model parameters, $T_0 = 256$.(b) ARX-model parameters, $T_0^{a_1, a_2} = \infty$, $T_0^{b_0, b_1} = 256$.(c) HO-model parameters, $T_0 = 256$.(d) HO-model parameters, $T_0^{a_1, a_2} = \infty$, $T_0^{b_0, b_1} = 256$.**Figure M.4** Estimated ARX-model parameters and HO-model parameters for condition C4.



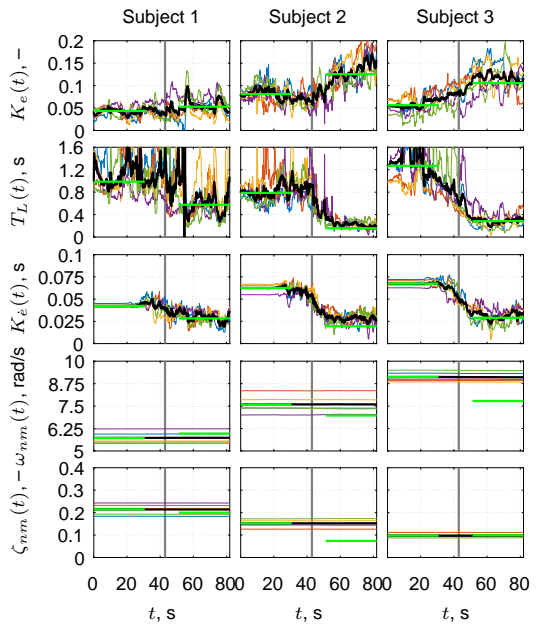
(a) ARX-model parameters, $T_0 = 256$.



(b) ARX-model parameters, $T_0^{a_1, a_2} = \infty, T_0^{b_0, b_1} = 256$.

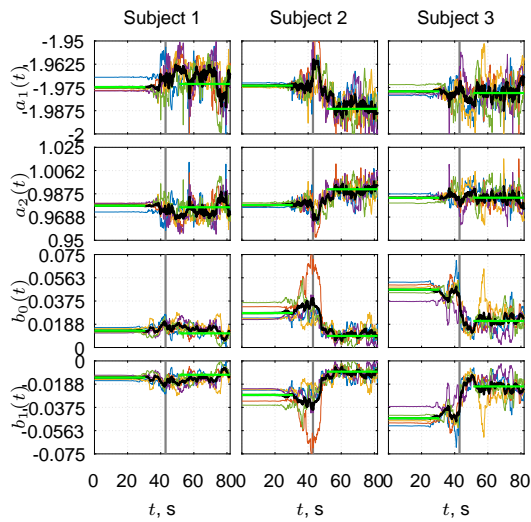
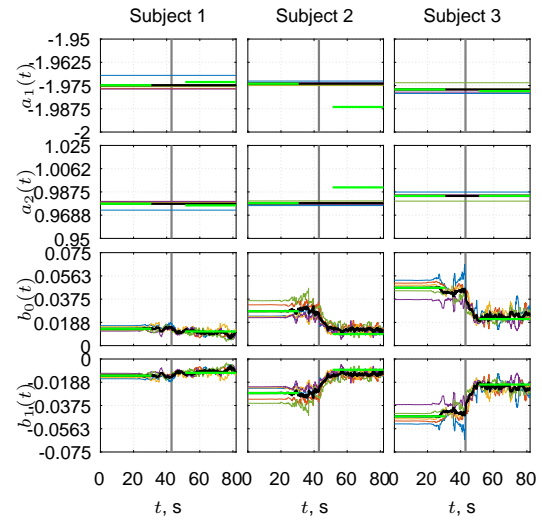
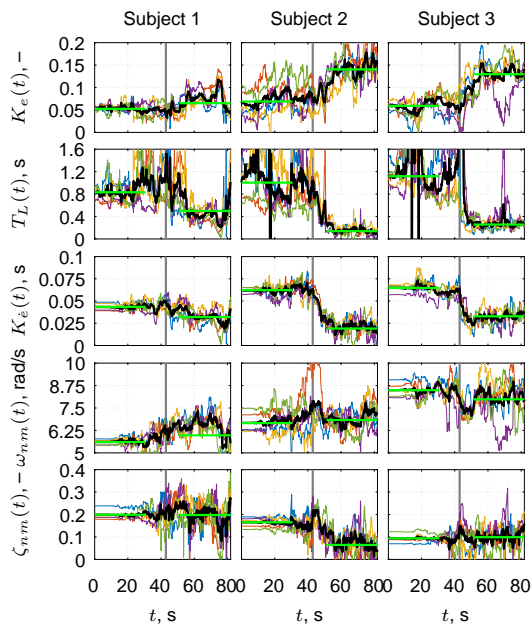
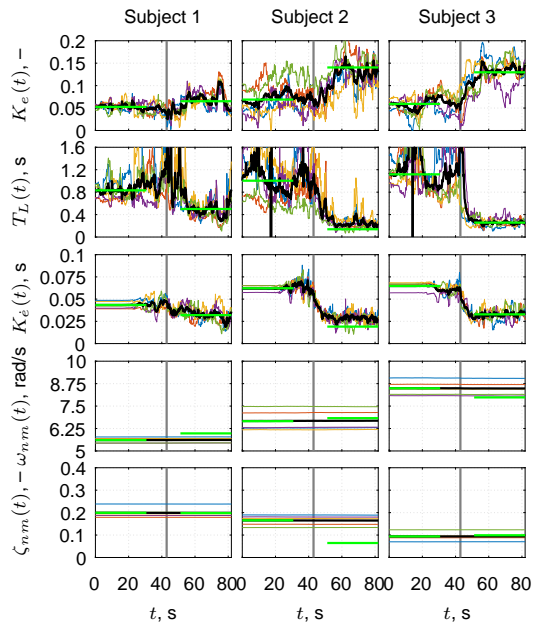


(c) HO-model parameters, $T_0 = 256$.



(d) HO-model parameters, $T_0^{a_1, a_2} = \infty, T_0^{b_0, b_1} = 256$.

Figure M.5 Estimated ARX-model parameters and HO-model parameters for condition C5.

(a) ARX-model parameters, $T_0 = 256$.(b) ARX-model parameters, $T_0^{a_1, a_2} = \infty$, $T_0^{b_0, b_1} = 256$.(c) HO-model parameters, $T_0 = 256$.(d) HO-model parameters, $T_0^{a_1, a_2} = \infty$, $T_0^{b_0, b_1} = 256$.**Figure M.6** Estimated ARX-model parameters and HO-model parameters for condition C6.

References

- Ameyoe, A., Chevrel, P., Le-Carpentier, E., Mars, F., and Illy, H. (2015). Identification of a linear parameter varying driver model for the detection of distraction. *IFAC-PapersOnLine*, 48(26):37–42. 1st IFAC Workshop on Linear Parameter Varying Systems, Grenoble, France.
- Balakrishna, S. (1976). Time domain and time series models for human activity in compensatory tracking experiments. Technical report TN-50, National Aeronautical Laboratory, Bangalore, India.
- Balakrishna, S., Raol, J. R., and Rajamurthy, M. S. (1983). Contributions of congruent pitch motion cue to human activity in manual control. *Automatica*, 19(6):749–754.
- Biezad, D. J. and Schmidt, D. K. (1985). Normalized predictive deconvolution: A time series algorithm for modeling human operator dynamics. *Journal of Guidance, Control, and Dynamics*, 8(6):768–776.
- Boer, E. R. (1995). Identification of time varying systems with applications to adaptive human control. PhD thesis, University of Illinois at Chicago.
- Boer, E. R. and Kenyon, R. V. (1998). Estimation of time-varying delay time in nonstationary linear systems: an approach to monitor human operator adaptation in manual tracking tasks. *IEEE Transactions on Systems, Man and Cybernetics, Part A: Systems and Humans*, 28(1):89–99.
- Celik, O. and Ertugrul, S. (2010). Predictive human operator model to be utilized as a controller using linear, neuro-fuzzy and fuzzy-ARX modeling techniques. *Engineering Applications of Artificial Intelligence*, 23(4):595–603.
- Drop, F. M., Pool, D. M., Damveld, H. J., van Paassen, M. M., and Mulder, M. (2013). Identification of the feedforward component in manual control with predictable target signals. *IEEE Transactions on Cybernetics*, 43(6):1936–1949.
- Drop, F. M., Pool, D. M., Mulder, M., and Bülthoff, H. H. (2016a). Constraints in identification of multi-loop feedforward human control models. *IFAC-PapersOnLine*, 49(19):7–12. 13th IFAC Symposium on Analysis, Design, and Evaluation of Human-Machine Systems, Kyoto, Japan.
- Drop, F. M., Pool, D. M., van Paassen, M. M., Mulder, M., and Bülthoff, H. H. (2016b). Objective model selection for identifying the human feedforward response in manual control. *IEEE Transactions on Cybernetics*. Advance online publication.
- Duarte, R. F. M. (2016). Human operator identification in the LPV system framework. Unpublished master's thesis, Delft University of Technology, Faculty of Aerospace Engineering.
- Fracaroli, F., Peruffo, A., and Zorzi, M. (2015). A new recursive least squares method with multiple forgetting schemes. In *54th IEEE Conference on Decision and Control*, pages 3367–3372, Osaka, Japan.
- Goto, N. and Matsuo, T. (1988). Identification of pilot dynamics in a system with a choice of feedback structures. *Journal of Guidance, Control, and Dynamics*, 11(2):159–166.
- Grant, P. R. and Schroeder, J. A. (2010). Modeling pilot control behavior for flight simulator design and assessment. In *AIAA Modeling and Simulation Technologies Conference*, number AIAA 2010-8356 in *Guidance, Navigation, and Control and Co-located Conferences*, Toronto, Canada.
- Hanson, G. D. and Jewell, W. F. (1983). Non-intrusive parameter identification procedure user's guide. Technical report NASA-CR-170398, Systems Technology, Inc., Mountain View, CA.
- Harashima, F. and Suzuki, S. (2006). Human adaptive mechatronics - interaction and intelligence. In *9th IEEE International Workshop on Advanced Motion Control*, Istanbul, Turkey.

- Hess, R. A. (1990). Identification of pilot-vehicle dynamics from simulation and flight test. In Leondes, C. T., editor, *Advances in Aerospace Systems Dynamics and Control Systems*, volume 33, part 3 of *Control and Dynamic Systems: Advances in Theory and Applications*, pages 151–175. Academic Press, San Diego, CA.
- Hess, R. A. (2009). Modeling pilot control behavior with sudden changes in vehicle dynamics. *Journal of Aircraft*, 46(5):1584–1592.
- Hess, R. A. (2014). A model for pilot control behavior in analyzing potential loss-of-control events. *Proceedings of the Institution of Mechanical Engineers, Part G: Journal of Aerospace Engineering*.
- Hess, R. A. (2016). Modeling human pilot adaptation to flight control anomalies and changing task demands. *Journal of Guidance, Control, and Dynamics*, 39(5):655–666.
- Hess, R. A. and Mnich, M. A. (1986). Identification of pilot-vehicle dynamics from in-flight tracking data. *Journal of Guidance, Control, and Dynamics*, 9(4):433–440.
- Jategaonkar, R. V., Raol, J. R., and Balakrishna, S. (1982). Determination of model order for dynamical system. *IEEE Transactions on Systems, Man, and Cybernetics*, 12(1):56–62.
- Johnson, W. A. and Weir, D. H. (1969). Pilot's response to stability augmentation system failures and implications for design. *Journal of Aircraft*, 6(6):504–509.
- Kulhavý, R. and Zarrop, M. B. (1993). On a general concept of forgetting. *International Journal of Control*, 58(4):905–924.
- Ljung, L. (1999). *System Identification: Theory for the User*. Prentice Hall PTR, Upper Saddle River, NJ, 2nd edition.
- Lone, M. and Cooke, A. (2014). Review of pilot models used in aircraft flight dynamics. *Aerospace Science and Technology*, 34:55–74.
- McRuer, D. T. (1980). Human dynamics in man-machine systems. *Automatica*, 16(3):237–253.
- McRuer, D. T., Graham, D., and Krendel, E. S. (1967). Manual control of single-loop systems: Part I & II. *Journal of the Franklin Institute*, 283(1;2):1–29;145–168.
- McRuer, D. T. and Jex, H. R. (1967). A review of quasi-linear pilot models. *IEEE Transactions on Human Factors in Electronics*, HFE-8(3):231–249.
- McRuer, D. T. and Krendel, E. S. (1974). *Mathematical models of human pilot behavior*. Technical report AGARD-AG-188, Advisory Group for Aerospace Research and Development, Paris, France.
- Miller, D. C. and Elkind, J. I. (1967). The adaptive response of the human controller to sudden changes in controlled process dynamics. *IEEE Transactions on Human Factors in Electronics*, HFE-8(3):218–223.
- Mulder, M. (1999). *Cybernetics of Tunnel-in-the-Sky Displays*. PhD thesis, Delft University of Technology, Faculty of Aerospace Engineering.
- Mulder, M., van Paassen, M. M., Flach, J. M., and Jagacinski, R. J. (2006). Fundamentals of manual control. In Marras, W. S. and Karwowski, W., editors, *Fundamentals and Assessment Tools for Occupational Ergonomics*, *The Occupational Ergonomics Handbook*, chapter 12, pages 12–1–12–26. CRC Press, Boca Raton, FL, 2nd edition.
- Mulder, M., Verspecht, T., Abbink, D. A., van Paassen, M. M., Balderas Silva, D. A., Schouten, A., de Vlugt, E., and Mulder, M. (2011). Identification of time variant neuromuscular admittance using wavelets. In *IEEE International Conference on Systems, Man, and Cybernetics*, pages 1474–1480, Anchorage, AK.
- Mulder, M., Zaal, P. M. T., Pool, D. M., Damveld, H. J., and van Paassen, M. M. (2013). A cybernetic approach to assess simulator fidelity: Looking back and looking forward. In *AIAA Modeling and Simulation Technologies Conference*, number AIAA 2013-5225 in *Guidance, Navigation, and Control and Co-located Conferences*, Boston, MA.

- Navrátil, P. and Ivanka, J. (2014). Recursive estimation algorithms in Matlab & Simulink development environment. *WSEAS Transactions on Computers*, 13:691–702.
- Niedźwiecki, M. (2000). *Identification of Time-varying Processes*. Wiley, Chichester, England.
- Nieuwenhuizen, F. M., Zaal, P. M. T., Mulder, M., van Paassen, M. M., and Mulder, J. A. (2008). Modeling human multichannel perception and control using linear time-invariant models. *Journal of Guidance, Control, and Dynamics*, 31(4):999–1013.
- Olivari, M., Nieuwenhuizen, F. M., Bühlhoff, H. H., and Pollini, L. (2014). Pilot adaptation to different classes of haptic aids in tracking tasks. *Journal of Guidance, Control, and Dynamics*, 37(6):1741–1753.
- Olivari, M., Nieuwenhuizen, F. M., Bühlhoff, H. H., and Pollini, L. (2015a). Identifying time-varying neuromuscular response: Experimental evaluation of a RLS-based algorithm. In *AIAA Modeling and Simulation Technologies Conference*, number AIAA 2015-0658 in AIAA SciTech Forum, Kissimmee, FL.
- Olivari, M., Nieuwenhuizen, F. M., Venrooij, J., Bühlhoff, H. H., and Pollini, L. (2015b). Methods for multi-loop identification of visual and neuromuscular pilot responses. *IEEE Transactions on Cybernetics*, 45(12):2780–2791.
- Olivari, M., Venrooij, J., Nieuwenhuizen, F. M., Pollini, L., and Bühlhoff, H. H. (2016). Identifying time-varying pilot responses: a regularized recursive least-squares algorithm. In *AIAA Modeling and Simulation Technologies Conference*, number AIAA 2016-1182 in AIAA SciTech Forum, San Diego, CA.
- Osafo-Charles, F., Agarwal, G. C., O'Neill, W. D., and Gottlieb, G. L. (1980). Application of time-series modeling to human operator dynamics. *IEEE Transactions on Systems, Man and Cybernetics*, 10(12):849–860.
- Phatak, A. V. and Bekey, G. A. (1969). Model of the adaptive behavior of the human operator in response to a sudden change in the control situation. *IEEE Transactions on Man-Machine Systems*, 10(3):72–80.
- Pool, D. M. (2012). *Objective Evaluation of Flight Simulator Motion Cueing Fidelity Through a Cybernetic Approach*. PhD thesis, Delft University of Technology, Faculty of Aerospace Engineering.
- Pool, D. M., Valente Pais, A. R., de Vroome, A. M., van Paassen, M. M., and Mulder, M. (2012). Identification of nonlinear motion perception dynamics using time-domain pilot modeling. *Journal of Guidance, Control, and Dynamics*, 35(3):749–763.
- Pool, D. M., Zaal, P. M. T., Damveld, H. J., van Paassen, M. M., van der Vaart, J. C., and Mulder, M. (2011a). Modeling wide-frequency-range pilot equalization for control of aircraft pitch dynamics. *Journal of Guidance, Control, and Dynamics*, 34(5):1529–1542.
- Pool, D. M., Zaal, P. M. T., van Paassen, M. M., and Mulder, M. (2011b). Identification of multimodal pilot models using ramp target and multisine disturbance signals. *Journal of Guidance, Control, and Dynamics*, 34(1):86–97.
- Pronker, A. J. (2016). *Estimating an LPV model of neuromuscular admittance with grip force as scheduling parameter*. Unpublished master's thesis, Delft University of Technology, Faculty of Aerospace Engineering.
- Qin, P., Nishii, R., Nakagawa, T., and Nakamoto, T. (2010). ARX models for time-varying systems estimated by recursive penalized weighted least squares method. *Journal of Math-for-Industry*, 2(A-11):109–114.
- Raol, J. R., Girija, G., and Singh, J. (2004). *Modelling and Parameter Estimation of Dynamic Systems*. Number 65 in IET Control Engineering Series. Institution of Electrical Engineers, London, England.

- Roggenkämper, N., Pool, D. M., Drop, F. M., van Paassen, M. M., and Mulder, M. (2016). Objective ARX model order selection for multi-channel human operator identification. In *AIAA Modeling and Simulation Technologies Conference*, number AIAA 2016-4299 in *AIAA Aviation*, Washington, DC.
- Rojer, J. (2016). Understanding human adaptation: Time varying pilot model identification. Unpublished preliminary graduation presentation, Delft University of Technology, Faculty of Aerospace Engineering.
- Sheridan, T. B. (1960). Human operator's time-varying transfer characteristics in the study of perception and fatigue. In *Symposium on Recent Developments in Automatic Control*, pages 161–165, London, England. British Institution of Mechanical Engineers.
- Sheridan, T. B. (1985). Forty-five years of man-machine systems: History and trends. In *Analysis, Design and Evaluation of Man–Machine Systems*, IFAC Symposia Series, Varese, Italy. Pergamon.
- Sheridan, T. B. and Ferrell, W. R. (1974). *Man-Machine Systems: Information, Control, and Decision Models of Human Performance*. The MIT Press, Cambridge, MA.
- Shinners, S. M. (1974). Modeling of human operator performance utilizing time series analysis. *IEEE Transactions on Systems, Man and Cybernetics*, SMC-4(5):446–458.
- Stanković, S. S. and Kouwenberg, N. G. M. (1973). Some aspects of human operator identification in real time. In Eykhoff, P., editor, *Identification and System Parameter Estimation*, volume 1, pages 247–250. North-Holland Publishing Company, Amsterdam, The Netherlands. 3rd IFAC Symposium, The Hague/Delft, The Netherlands.
- Stapleford, R. L., McRuer, D. T., and Magdaleno, R. E. (1967). Pilot describing function measurements in a multiloop task. *IEEE Transactions on Human Factors in Electronics*, HFE-8(2):113–125.
- Tangirala, A. K. (2015). *Principles of System Identification: Theory and Practice*. CRC Press, Boca Raton, FL.
- Tervo, K., Palmroth, L., and Koivo, H. (2010). Skill evaluation of human operators in partly automated mobile working machines. *IEEE Transactions on Automation Science and Engineering*, 7(1):133–142.
- Thompson, P. M., Klyde, D. H., and Brenner, M. J. (2001). Wavelet-based time-varying human operator models. In *AIAA Atmospheric Flight Mechanics Conference and Exhibit*, number AIAA 2001-4009 in *Guidance, Navigation, and Control and Co-located Conferences*, Montreal, Canada.
- Trujillo, A. C. and Gregory, I. M. (2016). Pilot stick input estimates from attitude commands as indicator of systemic changes. *Journal of Guidance, Control, and Dynamics*. Advance online publication.
- Trujillo, A. C., Gregory, I. M., and Hempley, L. E. (2014). Adaptive controller effects on pilot behavior. Technical report NF1676L-18398, NASA Langley Research Center, Hampton, VA.
- van der Vaart, J. C. (1992). *Modelling of Perception and Action in Compensatory Manual Control Tasks*. PhD thesis, Delft University of Technology, Faculty of Aerospace Engineering.
- van Paassen, M. M. and Mulder, M. (1998). Identification of human operator control behaviour in multiple-loop tracking tasks. In Inoue, K. and Nishida, S., editors, *Analysis, Design and Evaluation of Man-Machine Systems*, pages 515–520. Pergamon Press, Oxford, England. 7th IFAC/IFIP/IFORS/IEA Symposium, Kyoto, Japan.
- van Wingerden, J. W. and Verhaegen, M. (2009). Subspace identification of bilinear and LPV systems for open- and closed-loop data. *Automatica*, 45(2):372–381.
- Verhaegen, M. and Verdult, V. (2007). *Filtering and System Identification: A Least Squares Approach*. Cambridge University Press, Cambridge, United Kingdom.
- Xi, B. and de Silva, C. W. (2015). System identification in human adaptive mechatronics. In de Silva, C. W., Khoshnoud, F., Li, M., and Halgamuge, S. K., editors, *Mechatronics: Fundamentals and Applications*, chapter 7, pages 253–293. CRC Press, Boca Raton, FL.

- Young, L. R. (1969). On adaptive manual control. *Ergonomics*, 12(4):635–674.
- Zaal, P. M. T. (2016). Manual control adaptation to changing vehicle dynamics in roll-pitch control tasks. *Journal of Guidance, Control, and Dynamics*, 39(5):1046–1058.
- Zaal, P. M. T. and Pool, D. M. (2014). Multimodal pilot behavior in multi-axis tracking tasks with time-varying motion cueing gains. In *AIAA Modeling and Simulation Technologies Conference*, number AIAA 2014-0810 in *AIAA SciTech Forum*, National Harbor, MD.
- Zaal, P. M. T., Pool, D. M., Chu, Q. P., Mulder, M., van Paassen, M. M., and Mulder, J. A. (2009). Modeling human multimodal perception and control using genetic maximum likelihood estimation. *Journal of Guidance, Control, and Dynamics*, 32(4):1089–1099.
- Zaal, P. M. T. and Sweet, B. T. (2011). Estimation of time-varying pilot model parameters. In *AIAA Modeling and Simulation Technologies Conference*, number AIAA 2011-6474 in *Guidance, Navigation, and Control and Co-located Conferences*, Portland, OR.